DANISH NATIONAL SPACE CENTER

Combination of Spaceborne, Airborne and In-Situ Gravity Measurements in Support of Arctic Sea Ice Thickness Mapping

R. Forsberg, H. Skourup, O. B. Andersen, P. Knudsen, S. W. Laxon, A. Ridout, J. Johannesen, F. Siegismund, H. Drange, C. C. Tscherning, D. Arabelos, A Braun, and V. Renganathan

Danish National Space Center
Technical report No. 7, 2007

UNIVERSITY OF CALGARY

NERSC

esa

cpom

UCL University College London

DTU

Combination of Spaceborne, Airborne and In-Situ Gravity Measurements in Support of Arctic Sea Ice Thickness Mapping

R. Forsberg, H. Skourup, O. B. Andersen, P. Knudsen, S. W. Laxon, A. Ridout, J. Johannesen, F. Siegismund, H. Drange, C. C. Tscherning, D. Arabelos, A Braun, and V. Renganathan

Danish National Space Center
Technical report No. 7, Copenhagen, 2007

ISBN-10: 87-91694-09-4
ISBN-13: 978-87-91694-09-7
http://www.space.dtu.dk

ARCGICE

Combination of Spaceborne, Airborne and In-Situ Gravity Measurements in Support of Arctic Sea Ice Thickness Mapping

Final Report
May 2007

by

R. Forsberg[1], H. Skourup[1], O. B. Andersen[1], P. Knudsen[1], S. W. Laxon[2], A. Ridout[2], J. Johannesen[3], F. Siegismund[3], H. Drange[3], C. C. Tscherning[4], D. Arabelos[4], A. Braun[5], and V. Renganathan[5]

[1]Danish National Space Centre, Denmark (DNSC)
[2]Centre for Polar Observation and Modeling, Univ.College London, UK (UCL)
[3]Nansen Environmental and Remote Sensing Center, Norway (NERSC)
[4]Niels Bohr Institute of Astronomy, Physics and Geophysics (KU)
[5]Department of Geomatics Engineering, University of Calgary, Canada (UoC)

ESA STUDY CONTRACT REPORT

ESA CONTRACT NO 18753 / 05 / NL / CB	**SUBJECT** Combination of Spaceborne, Airborne and In-Situ Gravity Measurements in Support of Arctic Sea Ice Thickness Mapping		**CONTRACTOR** Danish National Space Center (DNSC)
ESA CR No	**STAR CODE**	**No of volumes** 1 **This is Volume No** 1	**CONTRACTORS REFERENCE** ArcGICE

ABSTRACT

This report is a quantitative study of gravity field and geoid, mean sea surface, mean ocean dynamic topography and tides for the Arctic Ocean, for a large range of existing and new models. The report gives quantitative assessments of errors and error covariances of the different fields, mainly for use of understanding total errors in the mean sea surface (MSS).

The error studies are especially directed towards the CryoSat sea-ice freeboard processor, where the MSS is the basic reference surface, especially in order to quantify if this processor will benefit from adaptive "smart" interpolation, where the varying error covariances of the MSS are taken into account.

As part of the studies a new Arctic gravity field model and geoid has been derived, based on all available terrestrial and airborne gravity data and GRACE satellite data, augmented with gravity field information from ICESat. Rigorous error and covariance of studies of the computed geoid model have been done, showing that the new Arctic geoid is accurate to better than 10 cm over most of the region.

Mean dynamic ocean topography is estimated from remote sensing by combining ERS and ICESat altimetry with the geoid, and compared to four different oceanographic models. The comparison shows large differences between the different oceanographic models, and a reasonable agreement to the results from remote sensing. This part of the study illustrates the potential of future radar altimetry missions such as Cryosat for determining ocean dynamic topography and its temporal changes, in addition to the sea ice freeboard heights.

A number of tidal models are intercompared, and compared to tide gauge data in the Canadian Arctic. The presence of sea-ice is found to damp the tidal amplitudes and it appears that tidal errors will be a major regionally-dependent error source in sea surface determination for CryoSat.

The error covariances and model comparisons are used in a "smart" adaptive estimator scheme, where a linear interpolator operator, similar to the future CryoSat freeboard estimator, is used to quantify errors of the interpolator. Some suggestions for utilization of GOCE data are included in the report, as well as recommendations and a future outlook.

The work described in this report was done under ESA Contract.
Responsibility for the contents resides in the author or organisation that prepared it.

Authors:

R. Forsberg, H. Skourup, O. B. Andersen, P. Knudsen, S. W. Laxon, A. Ridout, J. Johannesen, F. Siegismund, H. Drange, C. C. Tscherning, D. Arabelos, A. Braun, and V. Renganathan

NAME OF ESA STUDY MANAGER Mark Drinkwater Division: Mission Science Division Directorate: Earth Observations Programmes	**ESA BUDGET HEADING**

LIST OF CONTENTS

Executive Summary

This report outlines for the first time a comprehensive comparison of geoid, mean sea surface (MSS), mean ocean dynamic topography (MDT) and tides for the Arctic Ocean, for a large range of existing and new models, and gives quantitative assessments of errors and error covariances of the different fields, mainly for use of understanding total errors in the MSS. The error studies are especially directed towards the CryoSat sea-ice freeboard processor, where the MSS is the basic reference surface, especially in order to quantify if this processor will benefit from adaptive "smart" interpolation, where the error covariances of the MSS are taken into account.

The geoid and its errors are modeled from an updated Arctic gravity data set, based on surface and airborne gravity data from Arctic Gravity Project, gravity anomalies derived from ICESat, and different GRACE-based spherical harmonic models. Geoids are computed by both spherical Fast Fourier Transform (FFT) methods, and least-squares collocation methods, applied both in an Arctic wide "regional" solution, using a solvable subset of data (57,000 equations) and a "blocked" computation where more detailed data are used. The error estimations show that the geoid models over much of the Arctic Ocean are accurate at the 10 cm level. Error covariance functions are derived, showing that apart from a scaling factor the error covariances of the geoid are somewhat similar over the Arctic Ocean. The principles of an integrated method, taking into account covariance information of geoid, DT, sea-ice freeboard and tides are proposed, and illustrated on a limited example in the Fram Strait.

Errors in MDT are illustrated by using four different oceanographic models (OCCAM, MICOM, Univ. of Washington and PIPS). The oceanographic models show very large differences. A composite MDT from ERS 1995-2003 and 7 epochs of ICESat laser altimetry is constructed, showing a reasonable comparison with some of the oceanographic models, and highlighting the importance of CryoSat and GOCE for improving the determination of MDT in the future.

A number of different tidal models are intercompared, and compared to tide gauge data in the Canadian Arctic. For the Arctic is seems that the AOTIM-5 model fit the tide gauges best. The presence of sea-ice is found to damp the tidal amplitudes and it appears that tidal errors will be a major regionally-dependent error source in MSS determination for CryoSat.

The error covariances and model comparisons are used in a "smart" adaptive estimator scheme, where a linear interpolator operator similar to the future CryoSat freeboard estimator is used to quantify errors of the interpolator. The interpolator is based on a linear interpolation scheme between leads, and used with ERS altimetry. Various widths are used in the estimation, with the goal to see if there are optimal operator widths, as a function of spatial and temporal parameters. It appears in some cases, such as the geoid, that a constant operator across the Arctic would give good results as an adaptive operator, whereas for other quantities, notably tides, results show than an adaptive filter is optimal. Since the geoid error estimates will be much improved after GOCE, the conclusion for the geoid might not be valid when CryoSat is launched. Some suggestions for utilization of GOCE data are included in the report, as well as recommendations and a future outlook.

Introduction

This report contains the final report for the ESA-study "Combination of Spaceborne, Airborne and In-Situ Gravity Measurements in Support of Arctic Sea Ice Thickness Mapping". The main goal of the study was to get quantitative estimates of the geoid, mean sea surface heights, tides and mean dynamic topography of the Arctic Ocean, including the characteristics of errors and error correlations of the quantities, in order to be able to produce an optimal sea-surface height estimator for potential use with CryoSat-2.

It has been widely accepted that the Arctic is particularly sensitive to climate variability and that sea ice is a potential indicator and a forcing mechanism for climate change (Rind et al., 1997; Rothrock et al., 2003). Model simulations indicate a warming in the polar regions with increasing emissions of greenhouse gases (Houghton et al., 2001, IPCC report, 2007). In fact, Arctic sea ice is sensitive to small changes in vertical oceanic heat flux, i.e. a flux of 10 W/m^2 would melt ~1 m of sea ice in a year. Because sea ice governs the interaction between ocean and atmosphere, its thickness is its most important property. Ice thickness not only controls the rate of energy transfer from ocean to atmosphere, but also determines the ice strength, which controls its resistance to motion and deformation (Tucker et al., 1992).

Starting in the mid-1970's, Arctic sea ice extent and concentration have been documented using satellite passive microwave observations (Gloersen et al., 1999; Parkinson et al., 1999). Studies associated with Arctic sea ice thinning are reported by Tucker et al. (1992); Rothrock et al. (1999) and (2003), Wadhams and Davis (2000) and Laxon et al. (2003). However, there are still too few observations of sea ice thickness available, and particularly data of the annual, and inter-annual variations is lacking (Copley, 2000). The use of radar altimetry (Peacock and Laxon, 2004; Laxon et al., 2003) to measure sea ice thickness change is a new methodology, and it is expected that CryoSat-2 with its SIRAL data will provide more accurate measurements. In addition, ICESat equipped with a precise laser altimeter allows for accurate measurement of sea ice surface height (relative to the Earth's center of mass) (Kwok et al., 2004; Forsberg and Skourup, 2005).

While recent radar altimetry (ERS-1/2 and ENVISAT) have been used for Arctic sea ice thickness change observations (Laxon et al., 2003; Peacock and Laxon, 2004), conventional radar altimeters have footprint diameters of several km and ERS-1's Ice Mode measurements are limiting the resolution and accuracy of sea ice surface height measurements. ICESat's GLAS laser altimeter has an along-track spatial resolution of 172 m and a footprint of 70 m in diameter, and is currently the most accurate altimeter system for measuring the detailed sea ice surface height with respect to the Earth' center (Zwally et al., 2002; Schutz et al., 2005). With CryoSat's SAR processing of radar altimetry, a similar narrow effective footprint will be possible over the sea ice.

The measurement of thickness of the sea ice from space thus ultimately relies on the determination of a mean sea surface (MSS), and the deviations of the ice surface from this (the "freeboard").

A MSS, i.e. the heights of the ocean above a reference ellipsoid, is necessary in order to estimate freeboard sea ice heights, and thus thickness, by satellite altimetry. The basic equation is

$$F = H - R - N - \zeta - \Delta h \qquad (1)$$

where F is the freeboard, H the satellite ellipsoidal height, R the measured range, N the geoid, ζ the ocean topography (consisting of the mean dynamic topography MDT, and the tides), and Δh the errors. The basic principle is illustrated in Figure 1. In this figure F is shown as the

freeboard including snow, as e.g. measured by satellite or airborne laser; it should be noted that F for radar measurements – such as CryoSat or ERS – is usually understood as the height of the top of the ice over sea level, as the snow on top of the ice is assumed to be transparent for the radar measurements (at least for dry snow). In this report it follows from the context which type of freeboard is discussed.

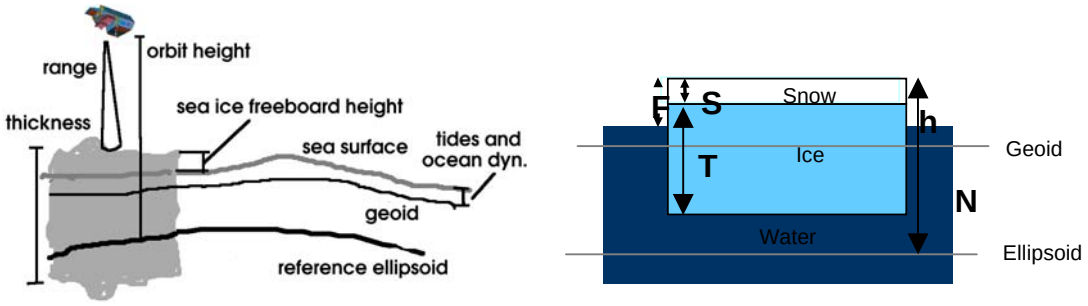

Fig. 1. Principle of satellite measurement of sea ice freeboard and thickness

Measurement of the free-board heights allows the ice thickness to be determined by assumptions on the snow depth, ice and ocean densities. The typical relationship between freebord and thickness is a factor around 6-8, dependent on ice type, snow load and seasons (Warren et al, 1999).

The Sea Surface Height SSH (= N + ζ) is by far dominated by the geoid variations. For the Arctic Ocean the utilization of geoid models derived from satellite, airborne and surface data should be an advantage, since the a priori subtraction of an accurate, static geoid model from satellite altimetry would make the signal from the freeboard relatively larger (compared to the combined signal from residual geoid errors, ocean dynamic topography and tides).

Up to now the determination of sea ice freeboard heights have been based on detection of specular returns in radar altimetry (Peacock and Laxon, 2004), or by using lowest-level filtering algorithms for laser data (Hvidegaard and Forsberg, 2002; Forsberg and Skourup, 2005). Such algorithms are necessary to detect trends in ice freeboard at the accuracies required for CryoSat (mission goal is 1.6 cm/year at spatial averages over 10^5 km^2). However, with the cm-accuracy of long-wavelength geoid information from satellite gravity field missions (GRACE and soon GOCE) it should in principle be possible to directly measure freeboards, at least at longer wavelengths, if sufficiently accurate models of MDT and tides were available. Such models are improving, due to both improvements in modelling methods and data availability. In the coming years such models are expected to be much improved, as CTD profiles and other data from ice-tethered buoys and underwater drifters, planned to be deployed in the coming years as part of both European (Damocles) and US (SEARCH) efforts, become available. However, as illustrated in this report, current MDT and tidal models differ by many 10's of cm, and combined with the local errors in the geoid the concept of directly measuring the freeboard heights from space without the "calibration" from open leads is still far away in the future.

The studies of the present report therefore focuses on the basic errors encountered in the basic quantities: geoid, sea surface height (SSH), mean dynamic ocean topography (MDT) and tides. We will especially focus on how the use of a priori models of these quantities allows the relaxation of needs for open water or thin ice leads for recovering the freeboard. In the report we will focus on the above problems, following more or less the work package structure of the original call for proposals for the ArcGICE project.

We will thus in Chapter 1 focus on basic observational data, including the available terrestrial gravimetric data necessary to determine an accurate geoid and its error covariances; we will focus on the MSS data, as estimated from satellite missions ERS and ICESat, including the

mission-specific ways to remove the effect of the sea ice (specular returns for ERS, and lowest level filtering for ICESat). Special emphasis will be given on the determination of an MSS for ICESat, since these data are new, and for the first time provide a coverage of central parts of the Arctic Ocean (ERS data are limited to 81°N whereas ICESat extends to 86°N). For pointing out future improvements in methodology in separating the signals of the fundamental equation (1) we will in Section 1.5 outline a proposed "optimal" estimation method, and apply on a more limited region of the Arctic (the Fram Strait region).

In Chapter 2 we will focus on derived products: the geoid and its accuracy, and a merged SSH product made by integrating ERS, ICESat and geoid-based SSH's.

In Chapter 3 the MDT determined from various oceanographic models will be outlined, with focus on differences in time and space. The "remote sensing" MDT derived from the geoid and the composite SSH is compared to the different oceanographic models, for the first time illustrating the possibility to map the Arctic Ocean MDT directly by space methods, but also illustrating some of the major differences of oceanographic models, and the need for improved space (GOCE) and terrestrial data to improve the geoid.

Finally in Chapter 4 a qualitative investigation will be done on the magnitudes of the errors which can be expected for an operational MSS recovery algorithm for CryoSat, representing a first attempt to quantify the errors from geoid, tides and MDT models in terms of allowing longer distances between leads and open water in the recovery of the freeboard for CryoSat.

An important issue, which is addressed through out the report, is the reference system. With orbits of satellites, altimeter range measurements and long-wavelength geoid potentially accurate at the few cm level, it is a major challenge to have equation (1) match in an absolute sense. We have selected in this report to do individual computations in different "conventional" reference systems (typically the system in which the different data are given), either referring to a "best fit" earth ellipsoid like the Topex system of ICESat (semimajor axis a = 6,371,136.3 m), or the WGS84 system of ERS (a = 6,371,137 m) and terrestrial gravimetry. Oceanographic models use a different implicit reference system ("level of zero motion" in the oceans), which make oceanographic MDT estimates to correspond to a "best fit" earth (which in practice means that the MDT may be viewed as in the Topex system).

Issues like treatment of permanent polar tides and biases between different ICESat epochs complicates the matters further, and in the comparisons it has not been possible to reach consistencies better than the 20 cm level, which is, however, a first step in the right direction. Hopefully some of the many comparisons of the present report will inspire additional research, and reach better accuracy levels of – say 5 cm – in the not too distant future. Such an accuracy level would correspond to 30-40 cm ice thickness.

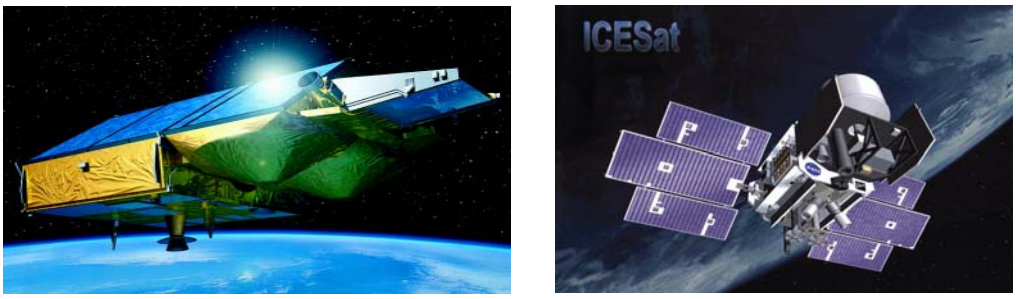

Fig. 2. CryoSat-2 (left) and ICESat (right) – complementary interferometric radar and laser missions, both with the possibility to map sea ice freeboard in the central Arctic Ocean. The results of the present study will hopefully add information on the accuracy of the freeboard recovery for both missions (ESA and NASA illustrations).

1 Gravity, geoid and sea surface height data

1.1 Collection and survey of existing gravity field data

The Arctic Gravity Project has since 1998 collected more or less all available gravity field data of the Arctic Region north of 64°N (Forsberg and Kenyon, 2005). The effort has allowed the compilation of both classified US data, first and foremost recent airborne data, as well as previously unavailable Russian data. The ArcGP has been compiled into a 5' grid of free-air anomalies, with only this grid available in the public domain. The grid compilation has been done at the US National Geospatial-Intelligence Agency, in close cooperation with DNSC. Some major data sets entered into ArcGP include:

Airborne Gravity Surveys:
- Long range of the US Naval Research Laboratory (NRL) 1992-99.
- Long range, high-altitude airborne gravity over Greenland 1991-92 (NRL).
- Danish-Norwegian airborne data in the coastal regions around Greenland, Svalbard and parts of Canada (1998-2003), including the ESAG-2002 ESA-sponsored airborne survey filling in major gaps in the Arctic Ocean coverage.
- German airborne data in the Fram Strait and north of Greenland
- Russian airborne data north of Frans Josef Land (Polar Marine Geological Expedition, St. Petersburg)

Surface gravity data:
- Canadian gravity data on land, sea and sea ice
- Scandiavian land and marine gravity data (Norwegian, Swedish, Finnish, Icelandic)
- US NGA data holdings, including Alaska
- German shipborne gravity data (Polarstern)
- Russian gravity data from Arctic Ocean on-ice measurements (VNIIO, St. Petersburg)
- Russian land gravity (5' x 7.5' mean values; from Tsniigaik, Moscow)

Submarine data:
- SCICEX US gravity profile data 1993-99 (B. Coakley)

Satellite altimetry data:
- Laxon/McAdoo 1997 retracked ERS altimetry gravity anomalies, filling in a major belt in the Ocean north of Siberia, where no other data could be released.

Coincident with ArcGICE, a new revision of the ArcGP grid have been compiled in two stages: An intermediate grid (October 2004), incorporating as one of the major changes new data from Siberia; and a new "final" grid January 2006, incorporating some additional marine data off Alaska, some additional data from Russia, and a few patches of ICESat and ERS-derived altimetry to correct some errors due to lack of data in the earlier ArcGP grid.

Figure 1.1 shows examples of some major data contributions, and Figure 1.2 the nearly-complete composite non-altimetry data. A thinned-out data set of approximately 55,000 points (about 10% of the original data, at a resolution of 15 km or less) was selected for the collocation error estimate studies in the sequel (WP 1.4), cf. Figures 1.2-1.3. The full point data set could not be used due to classification restrictions in the Arctic Gravity Project data; only 5' gridded data are available. A low-resolution selected sub-set of point data, used for the collocation computations of Sect. 1.4, was released from some central data providers (NGA, NRL) especially for the ArcGICE computations, and is not available for work beyond this project. Figures 1.4-1.5 show some differences between the original ArcGP (2002) data set and the most recent compilation. For this compilation two patches of data (north of Ellesmere Island and in the Fram Strait) have been filled with ICESat derived gravimetry, as outlined in Forsberg and Skourup (2005).

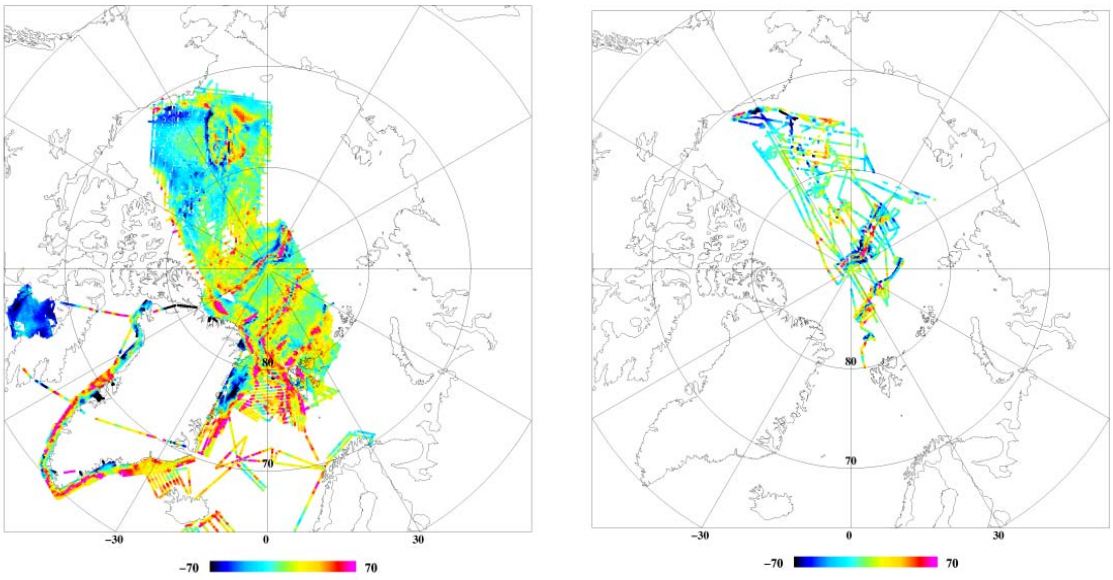

Fig. 1.1: Arctic Gravity Project coverage of NRL and DNSC high-quality airborne gravity data (left); SCICEX submarine data 1993-98 (right). Color scale is free-air gravity anomalies in mGal (10^{-5} m/s^2)

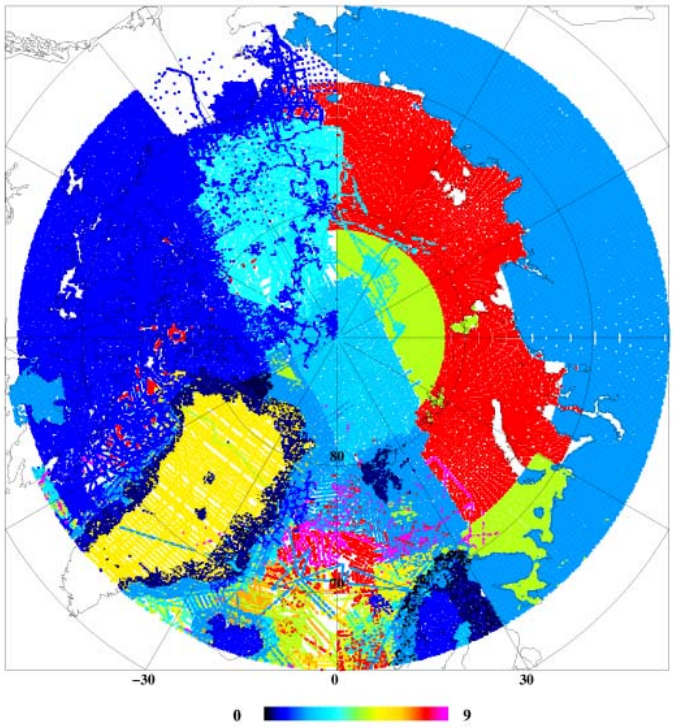

Fig. 1.2: Errors estimated for a subset of the ArcGP data. The red region north of Russia is the ERS altimetry fill-in. Yellow areas in Greenland are downward-continued NRL high altitude aerogravity, downward continued from the nominal 4 km flight elevation by least-sqaures collocation (Forsberg, 2002). Alaska surface data are not shown (but also used in the subset). Unit: mGal.

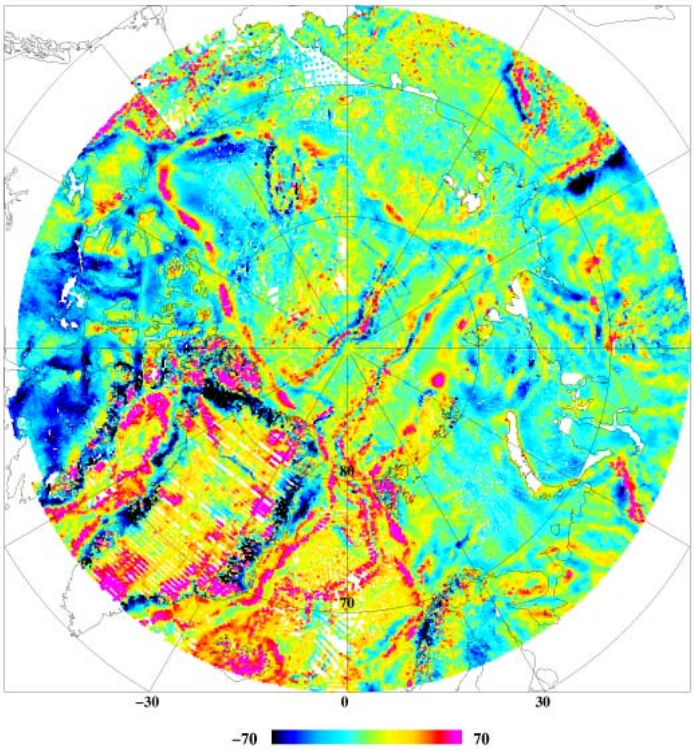

Fig. 1.3: ArcGP data coverage for the selected subset for error studies (October 2004 intermediate data set). Some of the remaining data voids in the Arctic Ocean region and in northern Russia have been filled for the January 2006 ArcGP release. Unit mGal.

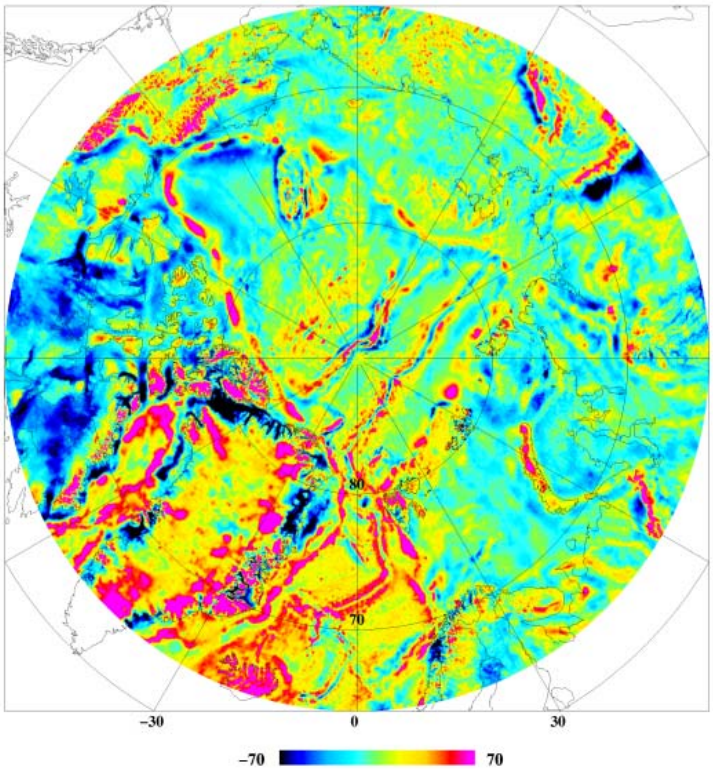

Fig. 1.4: ArcGP grid, January 2006 release. Some ERS and ICESat altimetry has been used to fill in some major data gaps/errors of the original compilation. Unit: mGal.

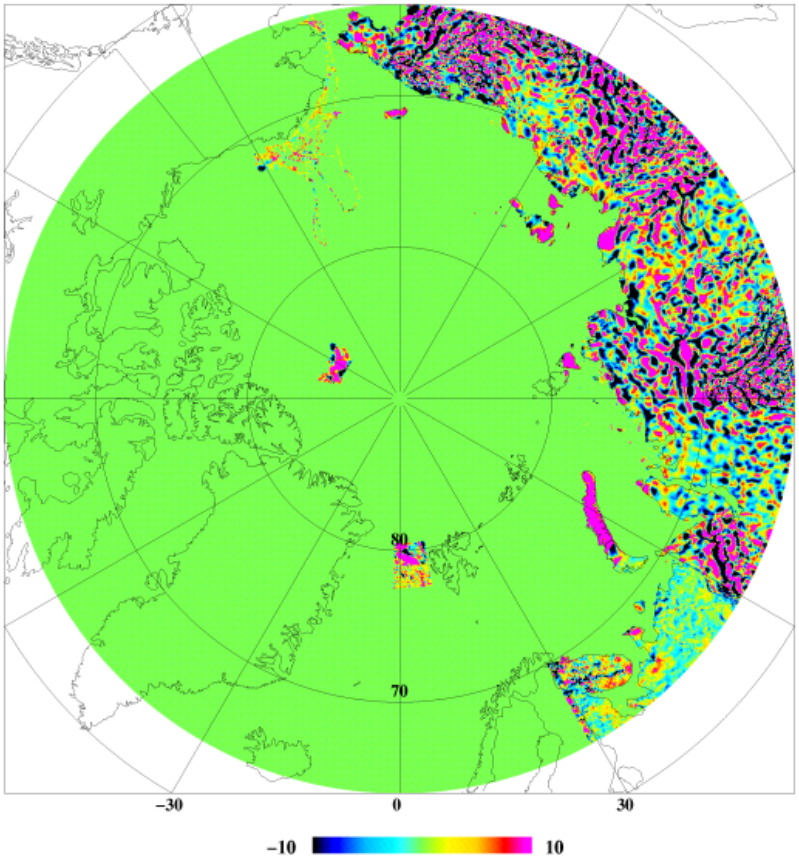

Fig. 1.5: Difference between original ArcGP (Dec. 2002) and the new ArcGP January 2006 release. Unit mGal. The two patches at 80N, 0E and 85N 120W have utilized ICESat gravimetry.

1.2 Collection of MSS heights from ERS-1 and ERS-2

Introduction

The ArcGICE mean sea surface model is created from 8 years of ERS-2 radar altimetry data of UCL using Cycles 01 through to 84 of the mission. This corresponds to the period from 16-May-1995 to 02-Jun-2003. The mean sea surface heights are computed relative to the WGS84 reference ellipsoid and are output on a 0.05 (latitude) by 0.2 (longitude) degree grid. Figure 1.6 shows the final mean sea surface height relative to the WGS84 reference ellipsoid.

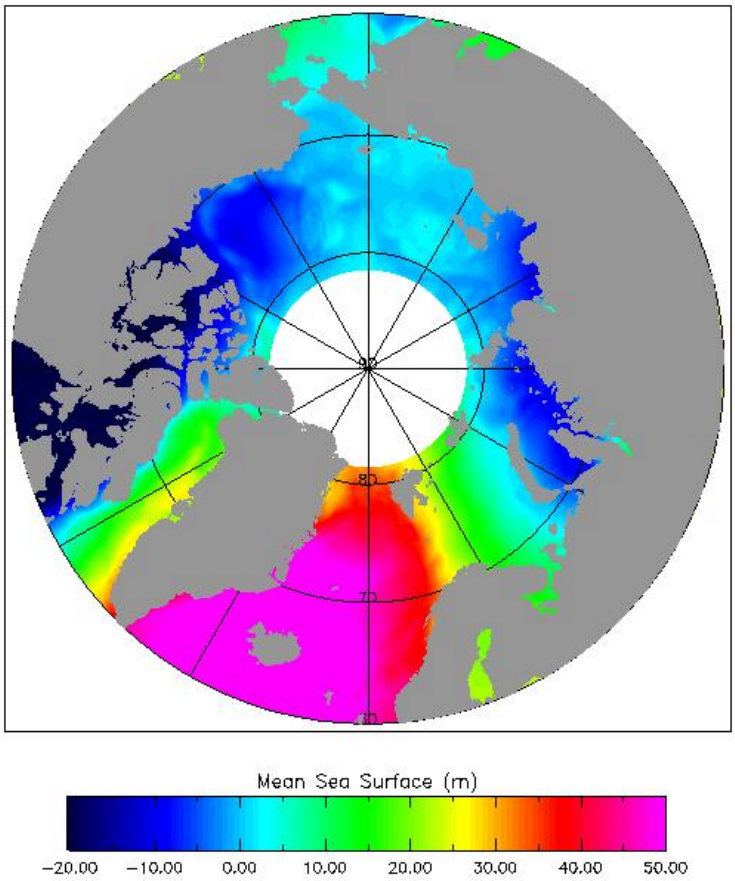

Fig. 1.6: ERS mean sea surface height 1995-2003 relative to the WGS84 reference ellipsoid

Data Processing

Only data collected when ERS-2 was in 'Ocean Mode' has been used to construct the mean sea surface. Over open ocean areas where the altimeter echo have the classic 'ocean like' or diffuse shape, the range to the surface is computed using a 50% OCOG retracking algorithm. Over the sea ice where the echoes frequently become specular due to bright reflections from the ice leads, a 50% threshold retracking algorithm is used. Bad waveforms are removed by applying a series of filters which examine the returning waveform shape. The range to the surface from specular echoes must have a further two corrections applied or they will be biased with respect to the open ocean diffuse echoes: a correction must be applied to compensate for the blurring of specular echoes due to movement of the altimeter's range gate, and a second correction compensates for the fact that the sharper or 'peakier' the echo, the shorter the range to the surface appears to be. The ocean surface height is then computed by deducting the range to the surface from the DGM-E04 orbit reconstruction for ERS-2. The resulting sea surface heights are corrected for tides using the FES95.2.1 tide model, various propagation delays to the radar pulse in the atmosphere, and the depression of the ocean surface at each point due to the local atmospheric pressure. Finally each altimeter track is smoothed and an outlier removal scheme applied.

The result from the above processing is a set of 501 arcs containing sea surface heights for each cycle of ERS-2 data being used. The ground track for a given arc number will be in approximately the same position for each cycle, so for each of the 501 arcs a set of reference locations spaced approximately every 6.7 km along the arc is defined. The 6.7 km corresponds roughly to the 1 sec along-track sampling. The average sea surface height at each

reference location on each arc is then found by extracting the nearest sea surface height measurement to the reference location from each cycle. Once the mean sea surface height at each reference location on each of the 501 arcs has been calculated, the heights are gridded onto a 0.05 (latitude) by 0.2 (longitude) degree grid.

Crossover analysis

In Figure 1.7, each arc used to construct the mean sea surface is taken one at a time. The crossover points between this arc and the grid of 501 averaged arcs are located and the RMS difference in height between the arc and the averaged arcs is computed at the crossover points. Some arcs with very high RMS crossover differences can be seen (e.g. at the start of Cycle 50). This will normally be caused by a poor orbit reconstruction for the arc in question. All arcs with an RMS crossover difference of more than 0.4 metres were removed from the dataset and the mean sea surface height was recomputed.

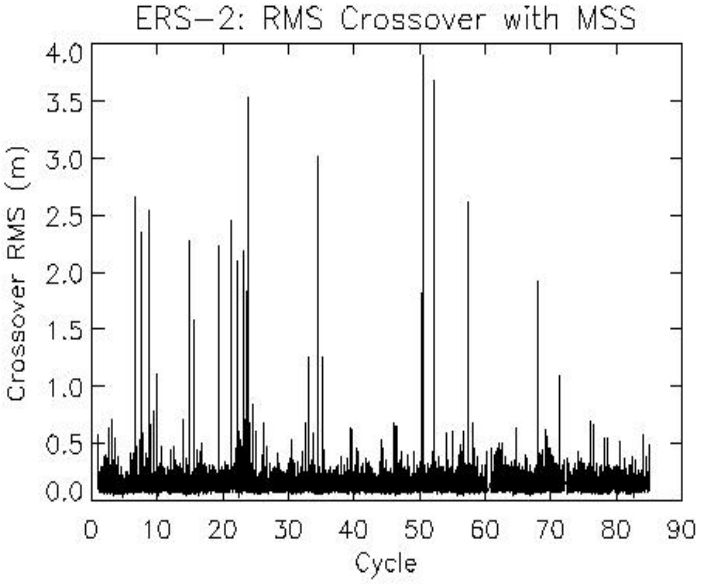

Fig. 1.7: Identification of poor arcs by looking at RMS crossovers differences with the complete set.

Discussion of Errors

Figures 1.8 to 1.10 have been included to give an indication of the possible errors in the mean sea surface. Most errors should decorrelate over the 8 years of data; however a few problems will remain. There will always be an error associated with the satellite orbit which is purely a function of latitude and longitude, the so called 'geographically correlated orbit error'. There is also a 'geographically anti-correlated orbit error' which is a fixed difference between the ascending and descending arcs, again a function of location on the earth's surface. The geographically correlated orbit error folds straight into the mean sea surface and is invisible in all the plots. The geographically anti-correlated orbit error will be visible in the mean crossover differences (Figure 1.8), but should not be present in the actual mean sea surface because ascending and descending arcs are averaged during the gridding. Finally the S2 tide is aliased to infinite period by ERS-2. The difference in S2 tidal error on ascending and descending arcs is seen in the mean crossover difference (Figure 1.8), but this is the part again removed by the gridding. The mean S2 tidal error is unseen and folds directly into the mean sea surface.

An indication of the effect of time variant errors such as in the M2 tidal component is given in Figure 1.9 and Figure 1.10. In particular, assuming a normal distribution of heights at each reference location, the standard deviation of the sea surface heights used to construct the mean (Figure 1.10) indicates that the error in the mean should only be a few centimetres. Figure 1.10 also indicates regions where the sea surface height error will be higher due to variability in the input data.

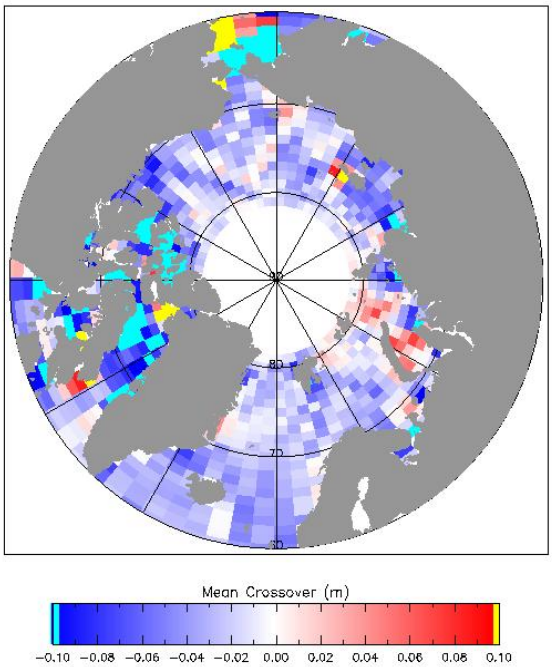

Fig. 1.8: Mean height difference between ascending/descending arcs at all crossover points of the 501 averaged arcs used to construct the MSS

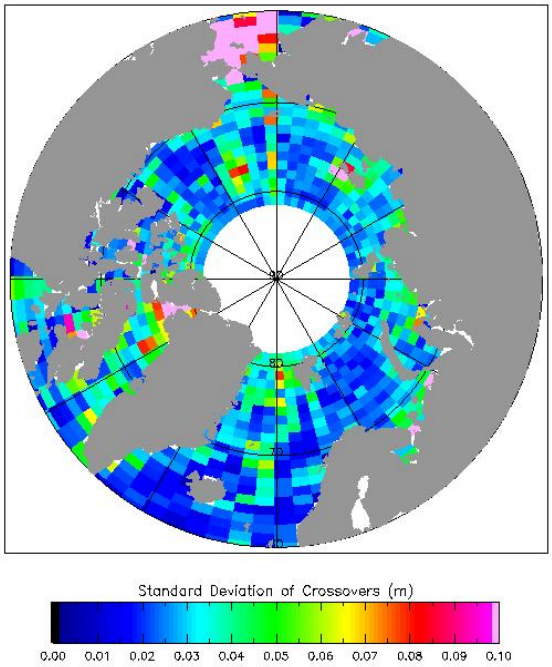

Fig. 1.9: SD of height difference between ascending and descending arcs at all crossover points of the 501 averaged arcs used to construct the mean sea surface.

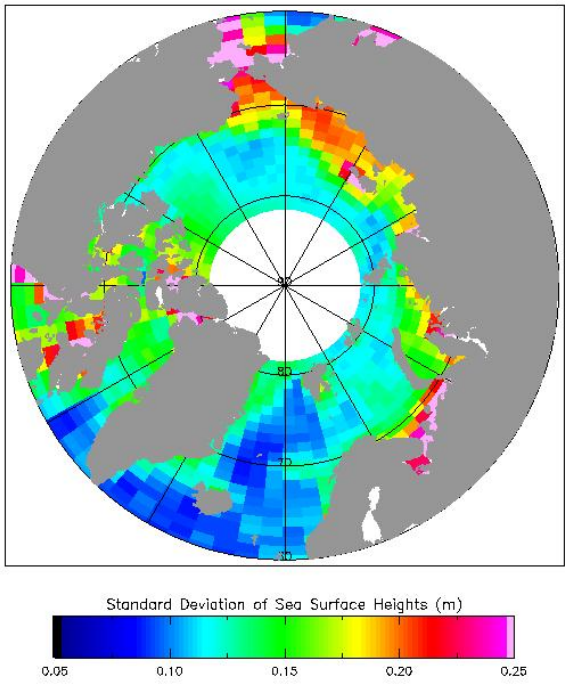

Fig. 1.10: Gridded standard deviation of sea surface heights averaged to construct the mean sea surface.

1.3 Collection of ICESat data and MSS estimation

ICESat data available

In this study 7 epochs (2003-2005) of ICESat GLA13 data release 18 have been used to estimate an Arctic Ocean-wide mean sea surface (MSS) as well as sea ice freeboard heights up to 86°N. The ICESat epochs to be included here are listed in Table 1.1. The mean sea surface has been calculated relative to the TOPEX/Poseidon (T/P) ellipsoid, and has been gridded in GRAVSOFT format, stored row-wise from north to south, with spacings 0.1° x 0.2°. A lowest level algorithm has been developed to estimate the MSS and this method are validated by comparing ICESat derived sea ice freeboards to high resolution airborne lidar profiles, as well as Arctic Ocean wide sea ice freeboard maps are validated by QuikSCAT backscatter maps.

Table 1.1: Available ICESat data.

LASER	Period	Year
1	February 20 – March 29	2003
2A	September 25 – November 18	2003
2B	February 17 – March 21	2004
2C	May 18 – June 21	2004
3A	October 3 – November 8	2004
3B	February 17 – March 24	2005
3C	May 20 – June 23	2005

The used ICESat data has been reduced for tides using the Padman AOTIM-5 model for Arctic tides, rather than the tidal model given on the ICESat geophysical data records.

ICESat snow freeboard and SSH

The basic equation for the measurement of snow sea ice freeboard (F_S) is the earlier mentioned fundamental equation

$$F_S = h - N - MDT - \Delta h \qquad (2)$$

where the altimeter measurement of ellipsoidal heights h (h = H-R in equation 1) is assumed to be corrected for tides, N is the geoid heights, MDT is the mean dynamic topography, and Δh is the errors from measurement, models and uncertainties in reference systems.

The sea ice thickness in the Arctic is between 2 and 6 meters with annual variations on the order of a fraction of a meter. Based on isostatic equilibrium and snow/ice/water densities of 290, 890, 1024 kg/m^3, respectively, a sea ice freeboard height of 1 m corresponds to a sea ice thickness of about 7 m. An example of the annual cycle of sea ice thickness is shown in Figure 1.11. This data has been obtained from sea ice thickness stations along the coast of Canada (NRCan/CRYSYS, Brown and Cote, 1992).

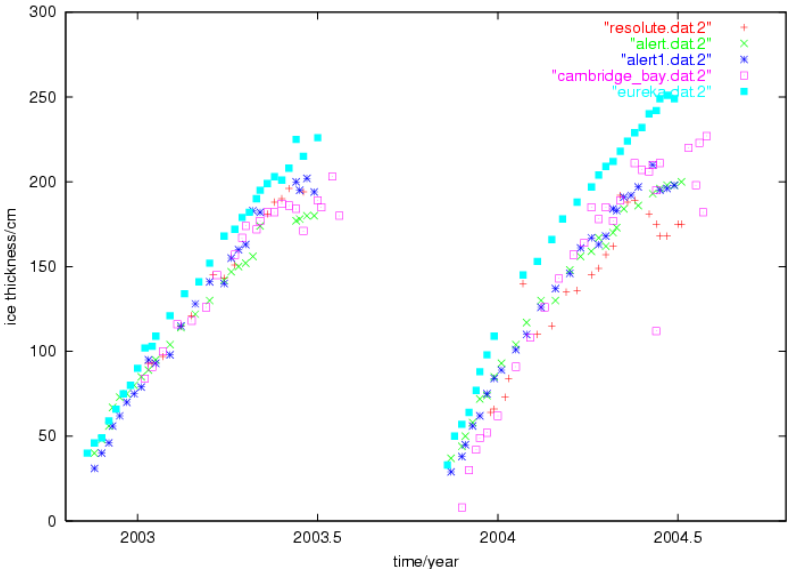

Figure 1.11: Sea ice thickness at five Canadian monitoring stations (Alert I/II, Resolute, Cambridge Bay, Eureka, from NRCan/CRYSYS Project, Brown and Cote (1992)). Sea ice develops in October and disappears in May the following year.

Evaluation of ICESat MSS by global geoid models

This section describes the estimation of sea ice freeboard height using the following approach: The sea ice surface is determined using ICESat GLA13 ellipsoidal height of the ice surface, and is subtracted from a high-resolution global geoid model. This approach is a direct attempt at qualitatively estimating the freeboard, assuming that geoid and SSH are in a consistent reference system. Mean dynamic topography and inverse barometric effects are not taken into account, and no lowest level filtering is used in this approach.

Current models of the mean dynamic topography (MDT) in the Arctic have differences of several tens of centimeters, making them inappropriate for accurate sea ice freeboard height determination using the method described here. Furthermore, the MDT shows annual and inter-annual variations of several tenths of centimeters, so that MDT models are definitively required. Consequently, this is the major limitation of the approach followed here. All errors associated with the geoid and tide models are passed into the sea ice freeboard height estimate.

The approach was tested with different releases of ICESat data and different geoid and tide models. The results do not differ significantly between different ICESat releases. The geoid model, however, has a significant impact. The results are presented for the combined gravity field model EIGEN-GL04C_complete to degree and order 360 from GRACE, Lageos and surface gravity data. The EIGEN-GL04C is the only high-resolution global gravity field model currently including surface gravimetry of the Arctic Gravity Project. The gravity field model was provided by GFZ Potsdam (Förste et al., 2006).

Ocean tides models are nearly global models where altimetry has been assimilated (e.g. GOT00.2, NAO99b, CSR4.0), unfortunately, non sun-syncronous altimetry missions such as Topex or Jason-1 only reach a latitude of 66° latitude and are not useful to constrain tide models in the Arctic. An assessment of tide models is presented in Section 3.4. Geoid models are available from recent dedicated gravity missions GRACE (Tapley et al., 2004), CHAMP (Reigber et al., 2005) as well as terrestrial and airborne data from the Arctic Gravity Project. Ocean circulation models are not reliable at present, partly due to the fact that sea ice

thickness dynamics are poorly known, which may have a significant impact on ocean dynamics.

To summarize, considered in this freeboard/MSS approach:

- geoid – EIGEN-GL04C
- ocean tides – AOTIM-5

Not considered in this approach:

- mean dynamic topography
- barometric effect
- snow cover

ICESat's GLA13 sea ice product of release 26 was used for 3 mission periods 2A, 2B and 2D which are considered the best calibrated mission phases. The 40 Hz data stream along track has been filtered for cloud and unrealistic elevations, then all land data have been deleted based on a 2 by 2 minute land-ocean mask. The data sets have been split into three mission periods as outlined above and are given in ellipsoidal heights above the TOPEX reference ellipsoid. The AOTIM-5 (Padman and Erofeeva, 2004) model was used to estimate the ocean tides for every ICESat footprint. As outlined in Section 3.4, it performs best in the Arctic. Other models which have been included and considered are: NAO99.b, GOT00.2, and CSR4.0.

Results presented here are limited to the best models available at the time of this document, namely the AOTIM-5 tide model and the EIGEN-GL04c geoid model. As the dynamic topography is not included as well as the variability of the dynamic topography, these results must be interpreted very carefully. However, the results are convincing as they give a reasonable overview of the sea ice freeboard height for the specific time periods (Figure 1.12). Known features such as the thicker ice in the western part of the Labrador Sea is visible. Individual patterns north of Svalbard reflect the true distribution of sea ice when compared to independent sea ice concentration data from SSM/I. Thickest sea ice can be found North of Greenland and the Canadian Arctic. In order to validate the freeboard height distribution, SSM/I data for the same time periods has been taken and plotted in the same projection (Figure 1.13). Although it shows sea ice concentration only, the distribution of sea ice is very similar to the one derived in this study.

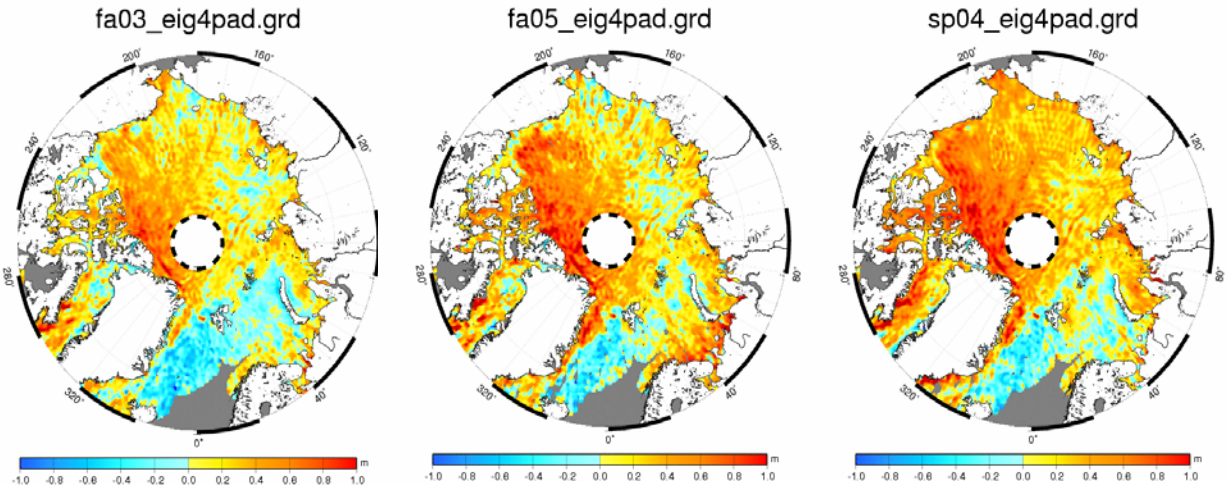

Figure 1.12: Sea ice freeboard height estimated from ICESat GLA13 release 26. Left: September-November 2003, Middle: September-November 2005, Right: February-March, 2004.

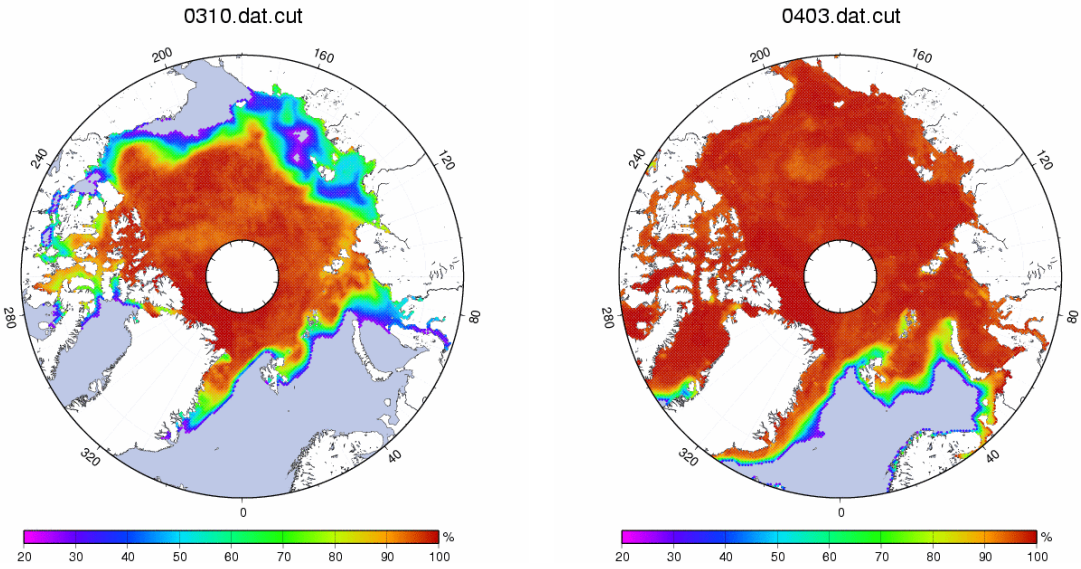

Figure 1.13: Sea ice concentration estimated from SSM/I data for the time periods September-November 2003 and February-March, 2004 as in Figure 1.12.

The approach used to model the instantaneous sea surface rather than measuring it from lowest level filtering has produced reasonable results, but is strongly limited by the uncertainty associated with the mean dynamic topography, which can exceed several decimeters in magnitude, and show seasonal and interannual changes. Improved methods for MSS determination must therefore use some kind of "calibration" of the MSS through direct observation of the MSS over open water or thin ice leads.

Improved ICESat MSS estimation method by lowest level filtering

First attempts for freeboard estimation from ICESat laser altimetry have been described by Kwok et al. (2004), and Forsberg and Skourup (2005). A detailed geoid model is used as a first approximation of the mean sea surface (MSS) above the ellipsoid. To reduce tidal errors, ocean mean dynamic topography, and measurement errors, a lowest-level filtering scheme is used, where the lowest geoid-reduced measured laser ranges are fitted to a smooth curve, supposedly reflecting the instantaneous SSH. For airborne laser data this method was originally described in Hvidegaard and Forsberg (2002), using a polynomial fit scheme to define the smooth SSH surface. In the ICESat investigations here, this scheme has been updated to use a smooth least-squares collocation (optimal estimation) function, yielding nearly equivalent results to the polynomial scheme, but allowing a more flexible fitting to the assumed "lowest level" points (assumed to be open water or leads with thin ice). It is the surface spanned by the lowest levels which is assumed to be the present SSH.

The above method has been applied to each ICESat track to estimate the SSH. In this study we apply the Arctic Ocean regional tide model AOTIM-5 to the ICESat measurements, as this model has shown to represent the best tidal model in the Arctic, see the study of tidal models in Section 3.4. We use the most updated release (January 2006) of the geoid from the Arctic Gravity Project (ArcGP), see Section 2. To remove effects from clouds, heights above/below 1.5 m has been rejected after removal of the geoid (h - N). The SSH has been determined by taking the three lowest levels averaged for each interval of 20 km. Compared to the "direct" estimation of the ICESat freeboards, as outlined in the last section, we have in this subsection used all the 7 ICESat periods shown in Table 1.1.

The estimated SSH shows large variations between the tracks, which can partly be explained by the track biases (e.g. due to errors in orbits, pointing, and inverse barometer effects), and others due to geoid errors. The correction from the inverse barometer (IB) effect can be calculated from the sea level pressure (SLP):

$$IB = \alpha (SLP - 1013.3) \quad (3)$$

where the constant 1013.3 mbar represent the global mean sea level pressure calculated over the oceans, and the proportionality constant α is taken to be -11.2 mm/mbar based on work done by repeated ICESat tracks on the Arctic by Kwok et al. (2006). The sea level pressure fields used here to obtain the IB correction for each ICESat sample is linearly interpolated from 6-hourly NCEP/NCAR reanalysis products provided by the NOAA-ESRL PSD Climate Diagnostics Center Branch, Boulder Colorado. Spatial and temporal differences due to the IB effects are on the order of a few decimeters.

To further limit the orbit-related errors a cross-over adjustment has been applied to these data, estimating a bias for each orbit. Finally the surface has been gridded and filtered. An example of the ICESat SSH of the 2 first ICESat periods (Laser 1 and 2A) is presented in Figure 1.14. To avoid the effect of the large spacing between the satellite groundtracks the map has been cut off south of 80°N. Since the MSS is changing with time, each of the 7 ICESat epochs are treated as independent MSS grids. The combination of these 7 fields and ERS is discussed further in Section 2.4.

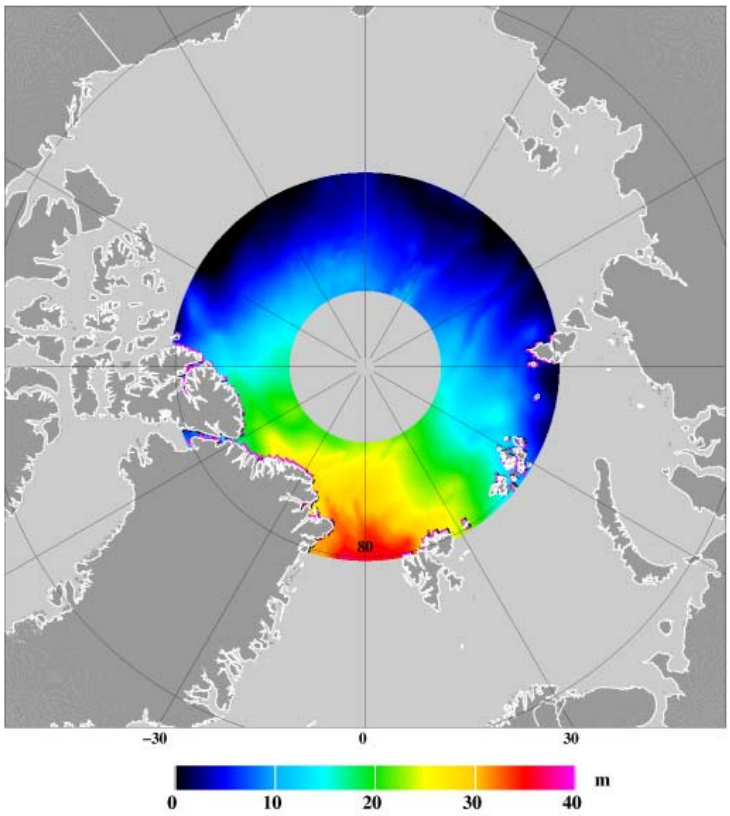

Fig. 1.14: Mean sea surface (MSS) for the Arctic Ocean 80-86°N based on ICESat data from February 20 – March 29, 2003, and September 25 – November 18, 2003. The SSH is based on the Topex reference ellipsoid, as used for the ICESat orbit.

The 7 Arctic Ocean-wide sea ice freeboard maps estimated by the lowest level filtering method are plotted in Figure 1.15. To remove false sea ice freeboard heights over open ocean, originating from the lowest-level algorithm favoring the trough of the waves, an open water mask is applied. The mask is obtained from SeaWinds scatterometer mission QuickSCAT, and combines backscatter and brightness temperatures to define areas with less than 40% sea ice concentration to represent open ocean.

In order to compare the sea ice freeboard distributions in Figure 1.15 to other products backscatter maps obtained from QuikSCAT are plotted in Figure 1.16 for the same periods. Kwok (2004) have shown that high backscatter (σ > -14.5 dB) values obtained from ku-band scatterometer data correspond to multi-year sea ice, explained by enhanced volume scattering. Multi-year sea ice is defined by the World Meteorological Organization (WMO) to be ice thicker than 2 m. Thus, a high backscatter value in the QuikSCAT backscatter maps indicates areas with ice thicker than 2 m. In Figure 1.15 and 1.16 the ICESat estimated freeboards shows qualitatively the same features as in the backscatter data obtained from QuikSCAT, with thicker sea ice north of Greenland (with freeboards up to 1 m, corresponding to a sea ice thickness of 6 m), forced against the coast by the Beaufort Gyre, and thinner sea ice in the Russian Arctic.

In addition the ICESat freeboard maps show seasonal (see Figure 1.11) variations with winter conditions present in the February - March data sets, represented by a larger extent of sea ice, e.g. off the coast of east Greenland. October and November represents fall conditions, just after the minimum sea ice extent in September. The freeboard map shows here much less ice, both in extent but also in freeboard, especially in the Siberian Arctic (Chukchi Sea). The data sets representing summer conditions (May - June) are very noisy. Especially, the mission phase from 2005 show unrealistic thick freeboard heights. This can partly be explained by the data availability, which is very sparse during these periods, see Figure 1.15 lower right showing the tracks available during each of the mission phases. This can be due to the presence of clouds during these warmer periods, with less sea ice resulting in more water vapor in the atmosphere.

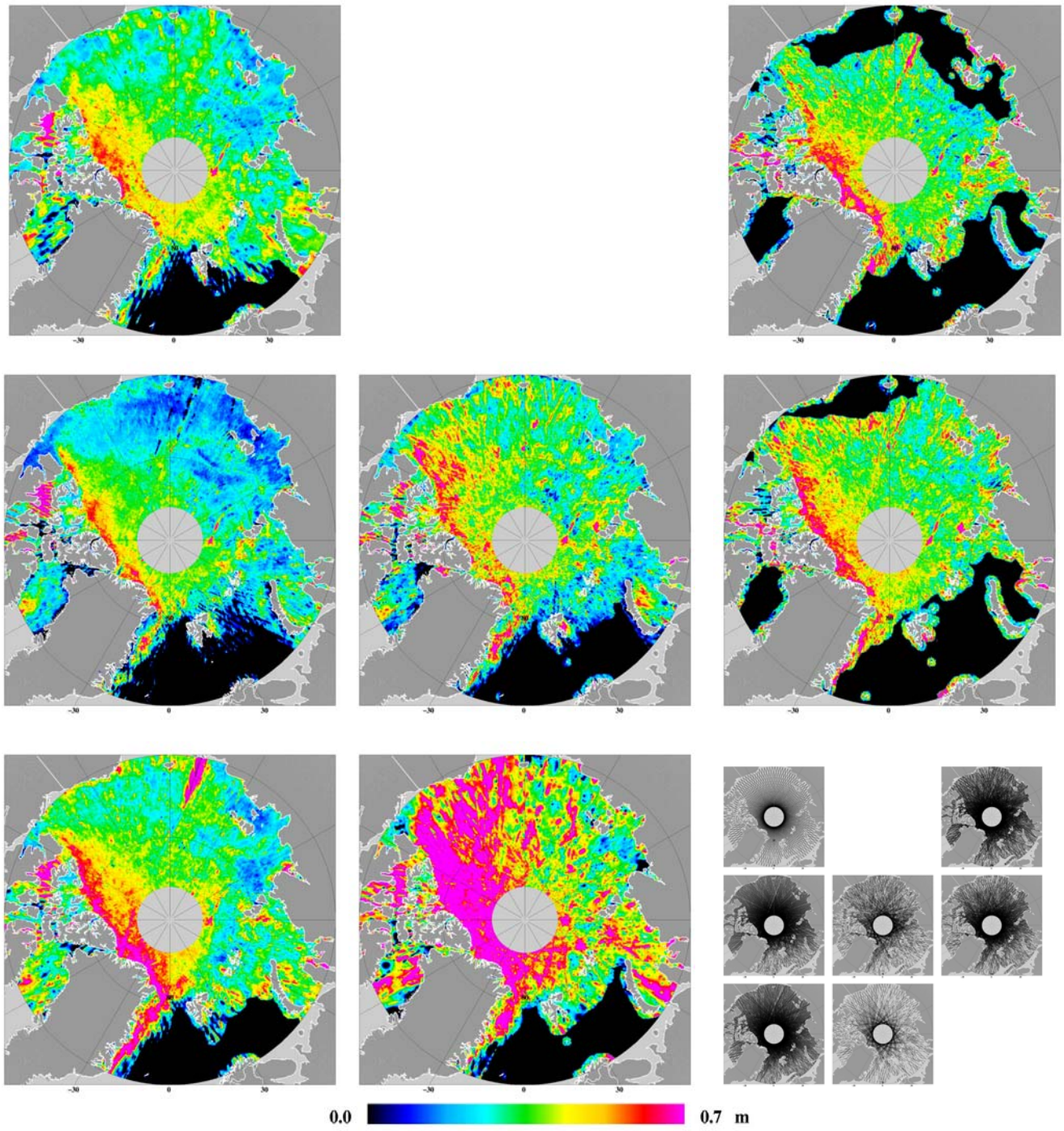

Fig. 1.15: Sea ice freeboard heights estimated by the lowest level filtering method from ICESat (release 18). Top: 2003, Middle: 2004 and Bottom: 2005. From Left: February - March, Middle May - June, and Right: October – November. In the lower right corner the data coverage of the corresponding mission phases.

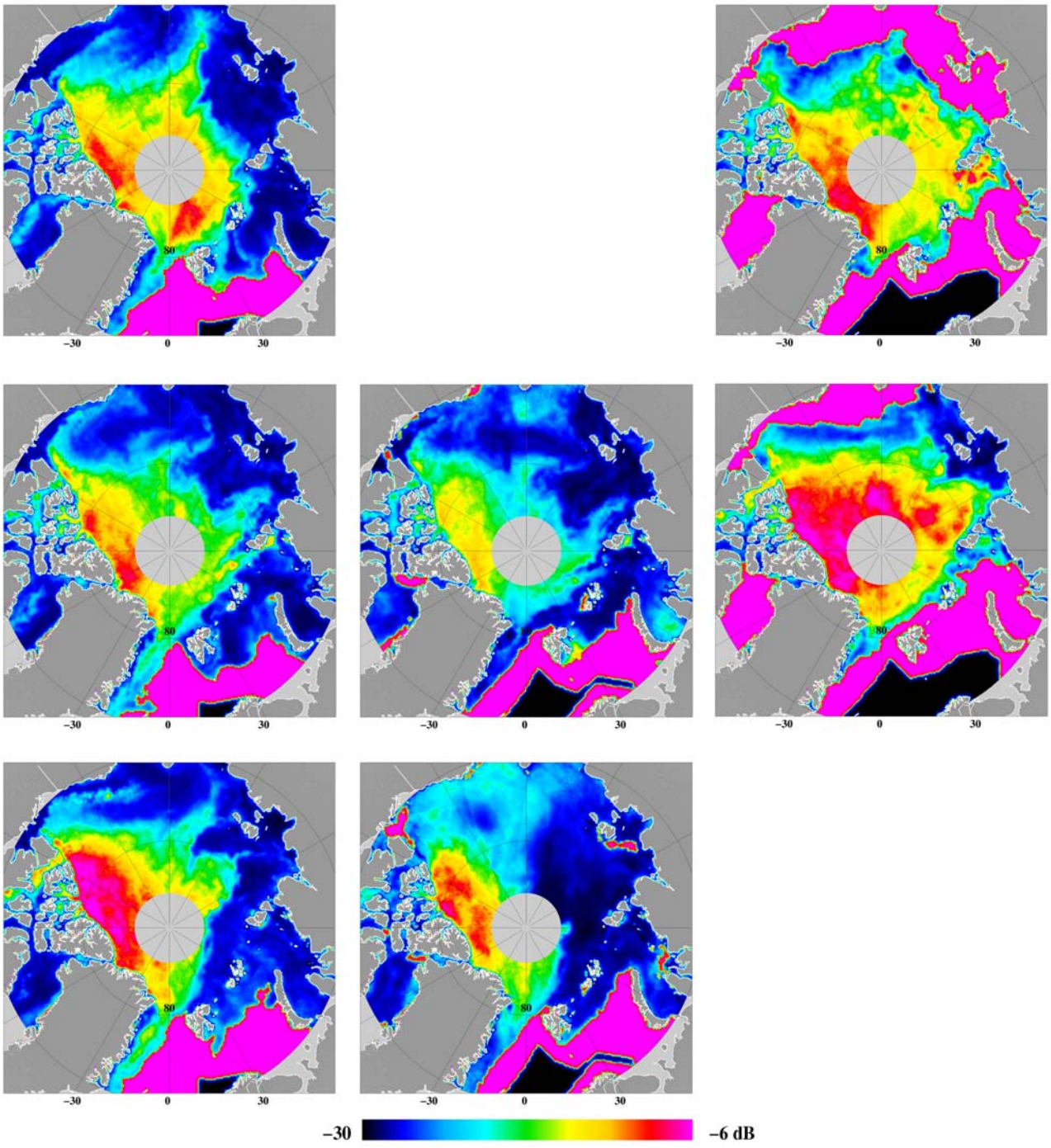

Fig. 1.16: QuikSCAT backscatter maps for the Arctic Ocean with ocean mask (pink), Top: 2003, Middle: 2004 and Bottom: 2005. From Left: February - March, Middle May - June, and Right: October – November.

Validation of ICESat lowest-level filtering by airborne lidar underflight

Because of the fundamental problems with estimating the lowest-level from laser data (no "specular" returns are available to uniquely classify laser measurements as either water or ice), airborne lidar data, with its much higher resolution, is useful to illustrate the problems of the freeboard estimation with ICESat, and thus the corresponding problem of estimating a bias-free MSS.

In connection with DNSC's airborne field activities in May 2004, Arctic sea ice freeboard heights were measured by high resolution airborne laser scanner on dedicated flights in the area north of Greenland. Two lines were flown on May 25 along ICESat ground tracks, in order to do a near-coincident underflight of the ICESat satellite, for track information see Figure 1.17. Airborne scanning laser data was collected from an Air Greenland Twin-Otter. The airborne lidar data has a very small footprint (less than 1 m) and a high horizontal resolution (approximate 1 m at 300 m altitude), compared to ICESat, which has a footprint size approximately 70 m wide and an along-track separation of the centers of the footprints by approximately 172 m.

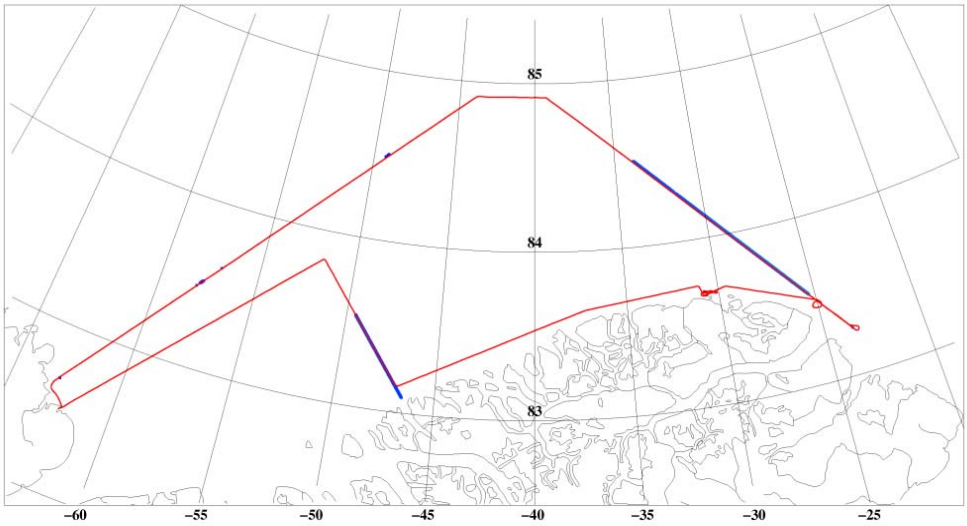

Fig. 1.17: The red line is the Twin-Otter flight track of May 25 north of Greenland, lined up along several ICESat tracks. The blue lines are the cloud-free near-coincident ICESat subtracks.

To estimate the freeboards the lowest level technique as described above was applied to both data-sets, using a 10 km-resolution for lowest level filtering. Figure 1.18 shows the vertical component of the scanner data plotted against the ICESat freeboard, as well as the reflectivity of the surface, as measured by ICESat. An offset of 36 cm for the eastern most track and 37 cm for the western most track were found. The offset is believed to originate from an overestimation of the lowest-level fit points, as the sea ice heights are averaged over the relative large ICESat footprint ~70 m and the lower along-track resolution. We also show the ICESat-measured reflectivity of the ice surface, which can be an indicator of presence of leads; work done by Kwok et al. (2004) shows that the reflectance of open water, and newly formed lead ice has a very low value, which rapidly increases with thickness. Only very few cases of low reflectivity are found in the two ICESat subtracks, indicating that ICESat only picks up very few open or thin-ice leads to represent the lowest levels. We also made tests with 5 km resolution "lowest-level" filtering, yielding changes in the lowest level surface of typically 5 cm. Therefore algorithm-dependent biases in the freeboard results could be at a similar level.

The lowest-level technique used to estimate the sea ice freeboards is highly dependent on the presence of leads with open water or thin ice. North of Greenland the sea ice is primarily thick perennial ice, with heavy ridges and rubble fields with very few or no open leads (Figure 1.19). It is therefore likely that the bias is caused by the fact that the "lowest points" as seen by ICESat include some thick ice in the footprints whereas the airborne laser can resolve the narrow leads. The area under investigation are not representative for the ice conditions seen across the entire Arctic Ocean, but a bias is expected to be found in the Arctic Ocean ICESat freeboard heights, especially where the thickest ice occurs.

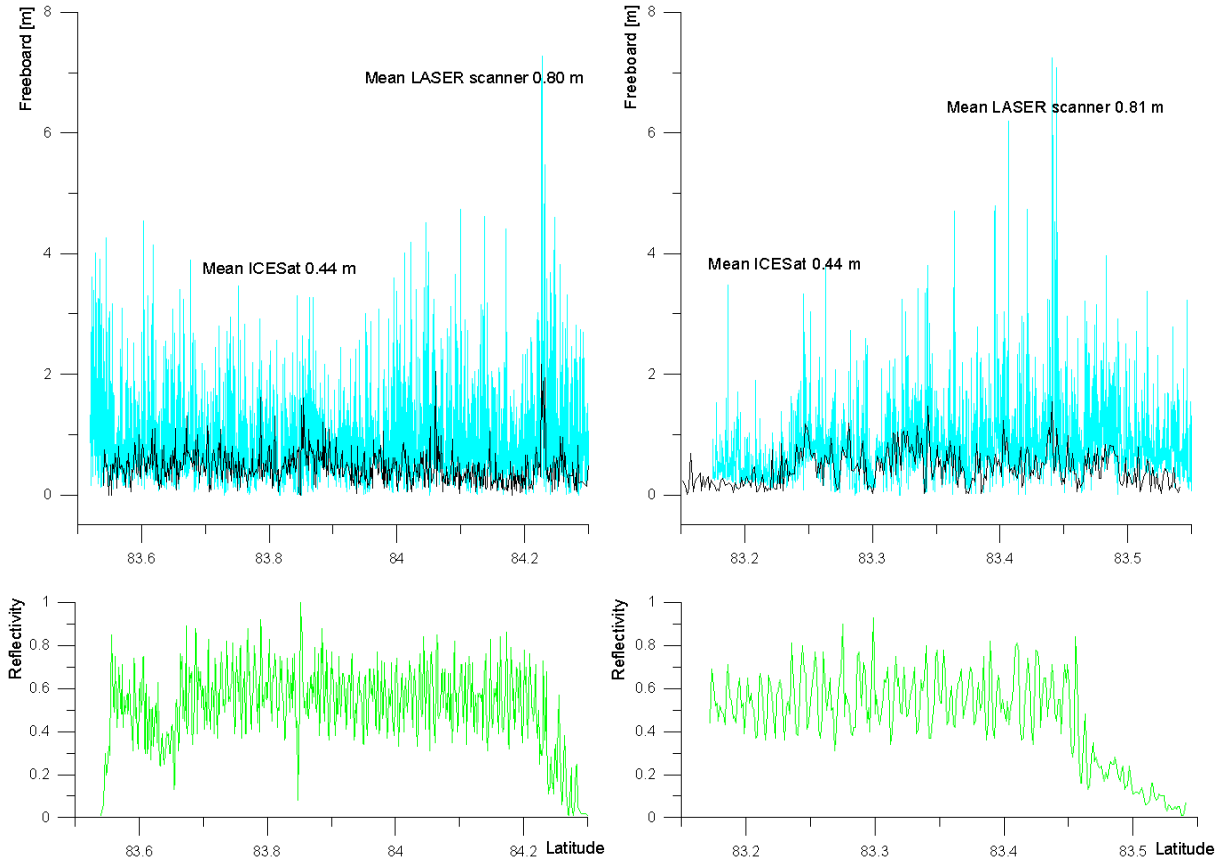

Fig. 1.18: Sea ice freeboard heights from ICESat (black), and the vertical component from airborne lidar (blue) for the eastern flight (to the left) and the western subtrack (to the right). Lower plot in green: reflectivity of ICESat. It is seen that the sea ice region north of Greenland has ridges up to 6 m high.

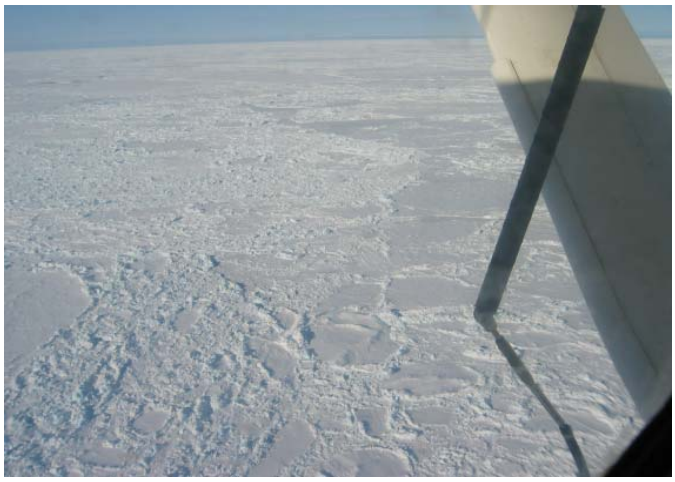

Fig. 1.19: Typical sea ice north of Greenland (eastern subtrack).

The comparison of an airborne underflight of ICESat shows that lowest level filtering techniques for ICESat may produce a bias in the estimated sea ice freeboard heights. We found a bias of approximately 35 cm in the region north of Greenland for 10 km-resolution lowest level filtering. We believe the bias is due to the lower frequency along-track sampling of ICESat, with fewer points to hit the open leads, and also due to averaging the freeboard across the footprint. Research is still undergoing in how distant "tie points" for the lowest level filtering can be separated, as a function of ice conditions and roughness of the gravity field.

Only very few cases of low reflectivity are found in the two ICESat subtracks, indicating that ICESat only picks up very few open or thin-ice leads to represent the lowest levels. This information can be implemented in future sea ice thickness products based on ICESat data, where a combination of lowest level and reflectivity probably would give better results. It is also to be expected that the bias problem is less in other regions of the Arctic Ocean, where ice is thinner and more leads are found.

The ICESat MSS estimated up to 86°N in Figure 1.14, representing the average of 2 ICESat epochs in 2003, will in the next section be updated to include all 7 epochs (2003-2005). This combined MSS will be merged with the ERS MSS of Figure 1.6, to provide a first approximation of an Arctic Ocean wide MSS. It is clear, however, that the MSS estimation is quite uncertain, especially for ICESat, and there is a strong correlation between geoid error and MSS error. In the Section 1.5 we therefore outline a proposal and test case for a joint method to simultaneously estimate all quantities by least squares collocation.

1.4 Gravity and geoid error estimates in spatial and spectral domains

A sea surface height interpolator, ψ must be designed to provide a reconstruction, *h(x)* of the along track sea surface height, *y(x)* from a discrete set of observations *g(n)*. The reconstruction is therefore obtained using (Laxon et al. 2003):

$$h(x) = \Psi(x,n)g(n) \tag{4}$$

The interpolator will be chosen to minimize the mean square error ε^2, given by

$$\varepsilon^2(x) = \left\langle \left(y(t) - \sum_n \Psi(x,n)g(n) \right)^2 \right\rangle \tag{5}$$

The covariance of *g* is obtained from the sum of the covariance of the signal *y*, obtained from the spectrum of sea surface height variability, and the covariance of the errors in *g(n)* (including noise and the covariance of the errors in the geoid, tides and MDT used to interpolate between *x* and *n*).

In the present study, error covariance functions of geoid heights derived from gravity anomalies in the Arctic Ocean were computed, necessary for the construction of the covariance of *g* in equation 5. A solution based on a (signal) covariance function estimated from data from the whole Arctic Ocean and solutions based on covariance functions estimated

from data from smaller blocks were computed. The GRAVSOFT (Tscherning et al, 1994) programs were used in the calculations.

Error covariance estimates

An observation y_i associated with the disturbing potential T through a linear functional L_i may be expressed through the equation

$$y_i = L_i(T) + e_i + A_i^T \cdot X \,, \tag{6}$$

where e_i is an error, X unknown parameters and A a known matrix. Estimates of T and X are obtained as (Moritz, 1980)

$$\widetilde{T}(P) = \{C_{Pi}\}^T \overline{C}^{-1}(y - A^T X) \tag{7}$$

$$\widetilde{X} = (A^T \overline{C}^{-1} A + W)^{-1}(A^T \overline{C}^{-1} y) \tag{8}$$

where W is the a-priori weight matrix for the parameters (generally the zero matrix). C_{Pi} is the covariance between the i-th observation and the value of T in a point P and $\overline{C}$ the variance covariance of the observations with the error-covariances D added.

$$\overline{C} = C + D \tag{9}$$

$$C_{ij} = COV(L_i, L_j) = L_i(L_j(COV(T(P), T(Q)) \tag{10}$$

The observation vector y may contain any combination of ground and satellite data.

Predicted values are obtained by applying the associated linear functional (L) on the estimate of T. Error estimates may also be computed. The mean square error of the parameter vector becomes

$$m_X^2 = ((A^T \overline{C}^{-1} A + W)^{-1} \tag{11}$$

Using

$$H = \left\{COV(L, L_i)\right\}^T \overline{C}^{-1} \tag{12}$$

the mean square error of an estimated quantity $L(\widetilde{T})$ will be

$$m_L^2 = \sigma_L^2 - H\{\mathrm{cov}_{(L, L_i)}\} H\, A m_X^2 (HA)^T \tag{13}$$

The associated error covariance estimates are equal to

$$\sigma_{PQ} = C_{PQ} - H\left\{\mathrm{cov}(L_Q, L_i)\right\}. \tag{14}$$

From (14) it is evident that the error covariance function depends on the signal covariance function. It also depends on the distribution and the accuracy adopted for the data used. The

computation of the error covariance functions of the gravimetric geoid in the Arctic Ocean is presented in the following sections.

In order to study the behavior of the error covariance functions two computations schemes were applied: (1) A regional computation using a signal covariance function computed from all available gravity anomalies and (2) A block wise computation, using individual signal covariance functions for each block and denser data distribution than that of the regional computation. In both cases error covariance functions were computed along meridians with equidistance equal to 0.1 degree.

Geoid model and covariance estimates in the Arctic Ocean using a regional covariance function

The geoid was computed using selected point gravity data compiled in the framework of the Arctic Gravity Project – ArcGP (Forsberg and Kenyon, 2004). An amount of 56,878 point gravity anomalies was used extracted from 10 gravity surveys, at a resolution of 15 km. These point data were distributed within the area bounded by $64^{o} \leq \varphi \leq 90°$, $-180^{o} \leq \lambda \leq 180°$ (Figure 1.20)

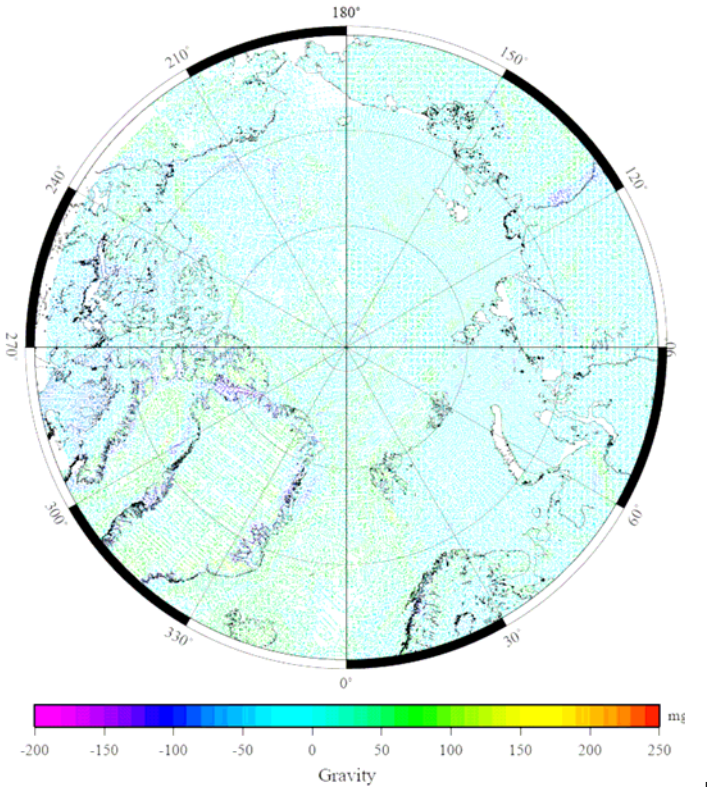

Fig. 1.20: The distribution of the 56,878 point gravity anomalies. Units mgal.

As a reference field the geopotential model EIGEN-CG03C (Förste et al., 2005) to degree 90 was used. The reduced gravity anomaly field is shown in Figure 1.21. In Figure 1.22 the empirical covariance function of the reduced gravity anomalies as well as its analytical model are shown.

Equation (6) with $A_i = 1$ was used to estimate biases of the gravity data. The resulted biases and their error estimation are shown in Table 1.2. It should be noted that because only a

subset of the data was used, and no terrain information was used on land, that these biases might in some cases be unrealistic.

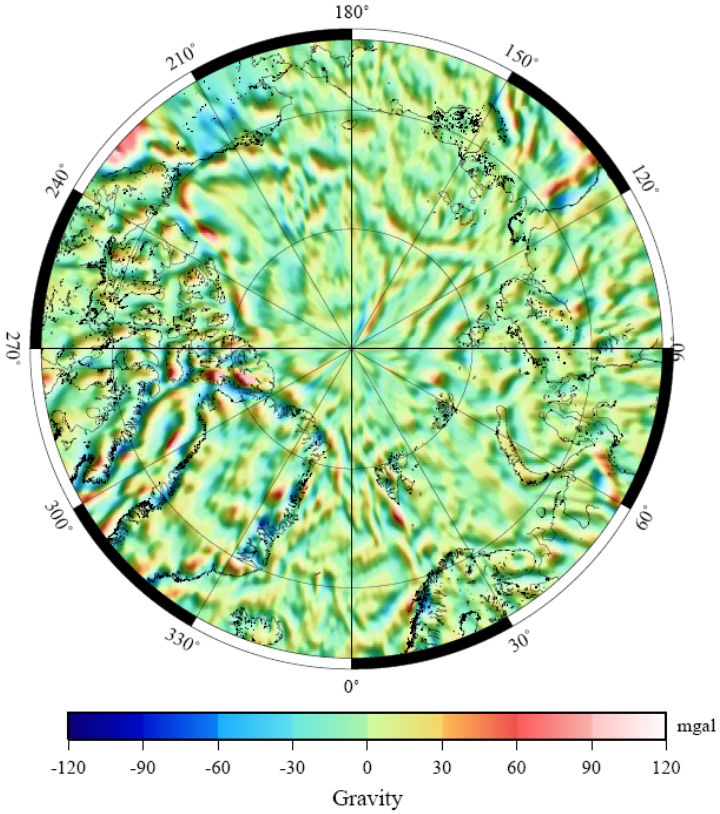

Fig. 1.21: The gravity anomaly field reduced to EIGEN-CG03C to degree 90

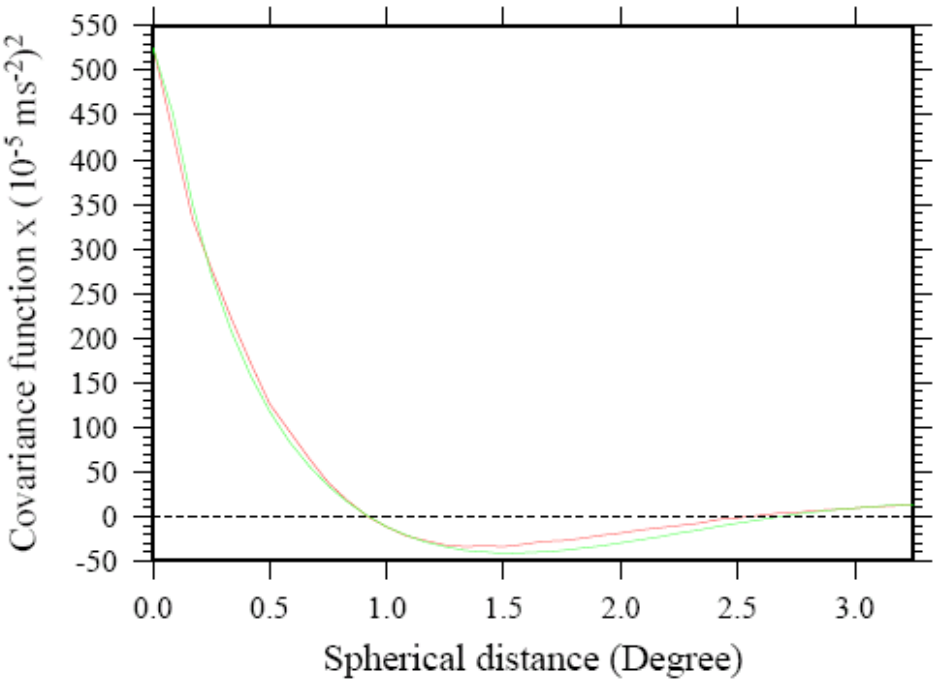

Fig. 1.22: Signal empirical (red) and model (green) regional covariance function of gravity anomalies in the Arctic Ocean after the removal of the contribution of EIGEN-CG03C to degree 90.

The geoid model resulted from this computation is shown in Figure 1.23. The error estimates of the geoid heights are shown in Figure 1.24. Error estimates greater than 25 to 30 cm correspond to areas with lack of data or with very poor data coverage.

Table 1.2: Results of bias estimation of the gravity data sets using LSC. The biases were estimated relative to the reference field used.

Internal no	Data set ID	Bias (mGal)	Error estimation (mGal)	Data type
1	1300006	0.373	0.074	Russian VNIIO grid data
2	1300010	-9.146	0.269	Alaska surface data
3	1300004	-1.149	0.075	Canada surface data
4	1300009	-0.424	0.118	Laxon/McAdoo altimetry
5	1300002	-3.756	0.239	NRL airborne 1992-96
6	1300008	-6.419	0.366	Scicex submarine data
7	1300003	-1.441	0.157	NRL airborne 1998-99
8	1300005	-2.106	0.096	Scandinavian surface data
9	1300001	0.531	0.185	DNSC airborne gravity
10	1300007	-1.409	0.166	NRL airborne Greenland

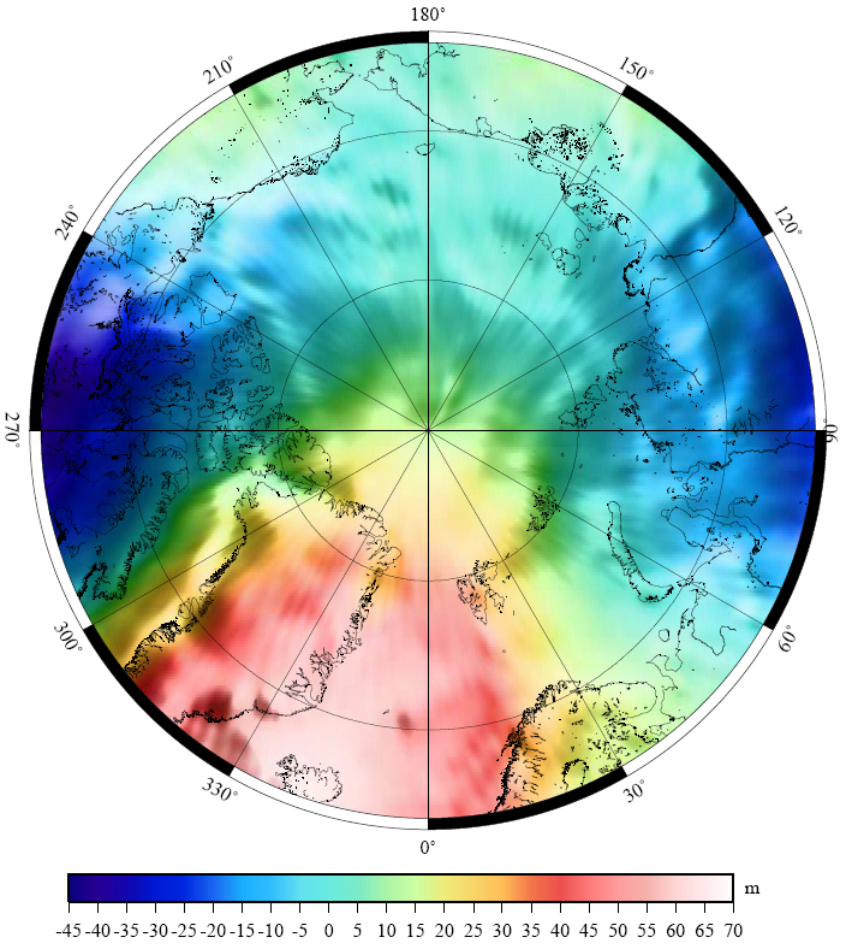

Fig. 1.23: Gravimetric geoid model from the regional computation. Units m.

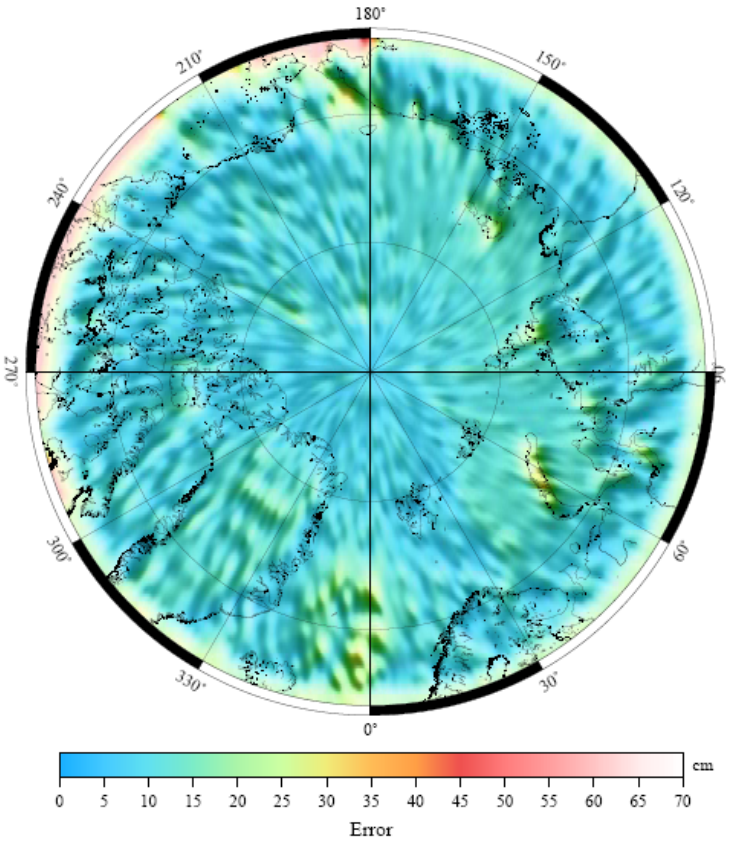

Fig. 1.24: Error estimation of the gravimetric geoid model resulted from the regional approach

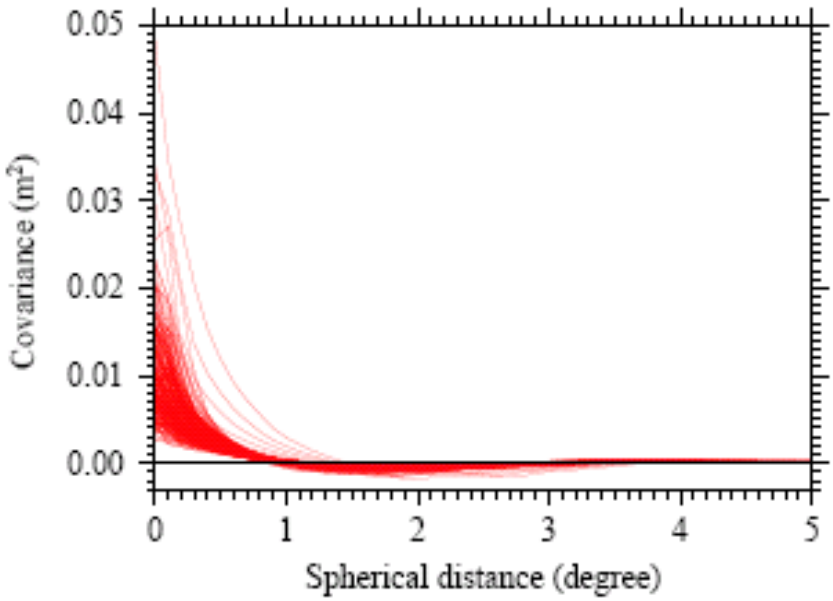

Fig. 1.25: Error covariance functions along the meridian of 15° computed from φ=64° to φ= 90°, with equidistance 0.1°.

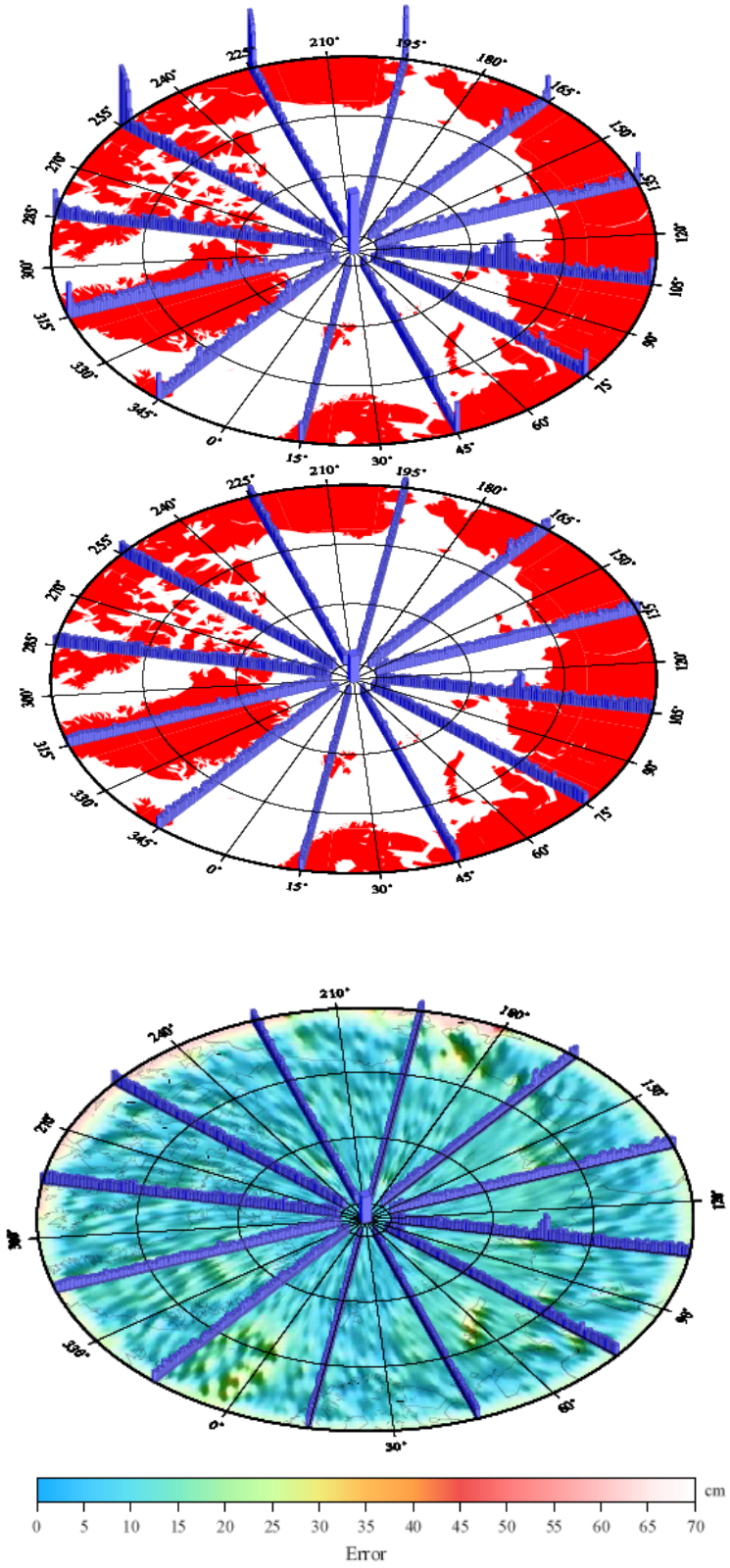

Fig. 1.26: Standard deviations (upper part) and Correlation length (middle part) of the correlated errors along meridians every 30º. The height of the central bar corresponds to 66 cm for the standard deviations and to 0.47º for the correlation lengths. Values with equidistance 0.2º are shown, up to latitude of 88º. Lower part is also the same correlation length of the error covariance (bars) as the middle part of this figure with the geoid errors (regional approach) as background (Figure 1.24).

Error covariance estimates with spacing 0.1º were computed along meridians every 30º, covering the latitudes 64º ≤ φ ≤ 90°. In Figure 1.25 the error covariance functions along the meridian of 15º are shown. The standard deviations (square root of the variances) and the corresponding correlation lengths of these covariance estimates are shown in Figure 1.26 (upper and lower part respectively). The correlation length was computed after a fitting of each error covariance function to the exponential model

$$\mathrm{cov}(\psi) = ae^{b\psi}, \tag{15}$$

where ψ is the spherical distance and a, b determinable coefficients. It should be noted that the correlation length was considered only for error covariance functions comprising at least 8 error-correlation values and for coefficients of determination > 0.9. Depending on the distances of the prediction points relative to data points there are cases where the value of the variance of the covariance function is lower than the value of the next class (see equation 14). In these cases, the definition of the correlation distance was avoided.

In Figure 1.26 it is shown that the error covariance estimates of geoid heights in the Arctic Ocean computed by LSC using a regional covariance function, resulted in standard deviations ranging from 5 to 66 cm, with correlation lengths ranging from 0.1º to 0.47º. Because the computation is carried out with a regional covariance function, it is reasonable to attribute the differences in the characteristics (standard deviation and correlation length) of the error covariance estimates to the data distribution and the error adopted for the data. Since the characteristics of the error covariance estimates are different even in areas having the same data accuracy, the data distribution is the main reason for the changes of the characteristics of the error covariance estimates. Indeed, from Figure 1.26 in view of Figure 1.20 it is obvious that standard deviations above 30 cm are related with areas with lack or poor data coverage.

The main conclusion from this regional computation is that the variance of the error covariance functions is anti-correlated with the data sampling. Dependence of the variance from the data accuracy assumption was not detectable.

Block-wise approach using local covariance functions

In order to study the dependence of the error covariance estimates on the local characteristics of the gravity field, the computations described in Section 3 were repeated block-wise. The advantage of the blockwise approach is that more data can be handled, and that the covariance parameters can be changed; the disadvantage is – as can be seen in the sequel – that there will be a risk of jumps and offsets between adjacent blocks.

For the blockwise computations, the area between the parallels 64º and 82º was divided in 6º x 30º blocks and the rest (82º to 90º) be divided to 8º x 90º (see Figure 1.28). Signal covariance functions were computed individually for each block. The standard deviation (square root of the variance) and the correlation length of the signal covariance function in each block are shown in Figures 1.28 and 1.29 respectively. The large changes of the standard deviation (from 9 to 52 mgal) as well as of the correlation length (from 0.12º to 0.48º) of these covariance functions, showed that the test area is suitable for studying the dependence on the local signal characteristics. Note that the standard deviation and the correlation length of the regional signal covariance function are 22.8 mgal and 0.28º respectively. However, besides the characteristics of the gravity field in each of the blocks, the error covariance estimates also depend on the data sampling as it is shown in the sequel.

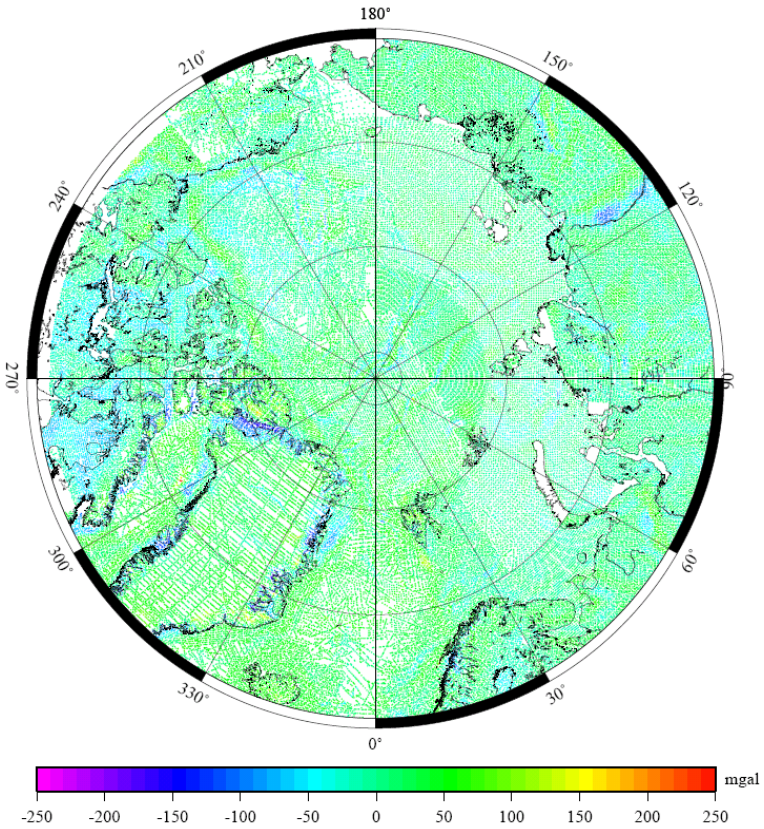

Fig. 1.27: Distribution of the data points used in the block-wise approach (91,382 point gravity anomalies). Colours show free-air anomalies in mgal.

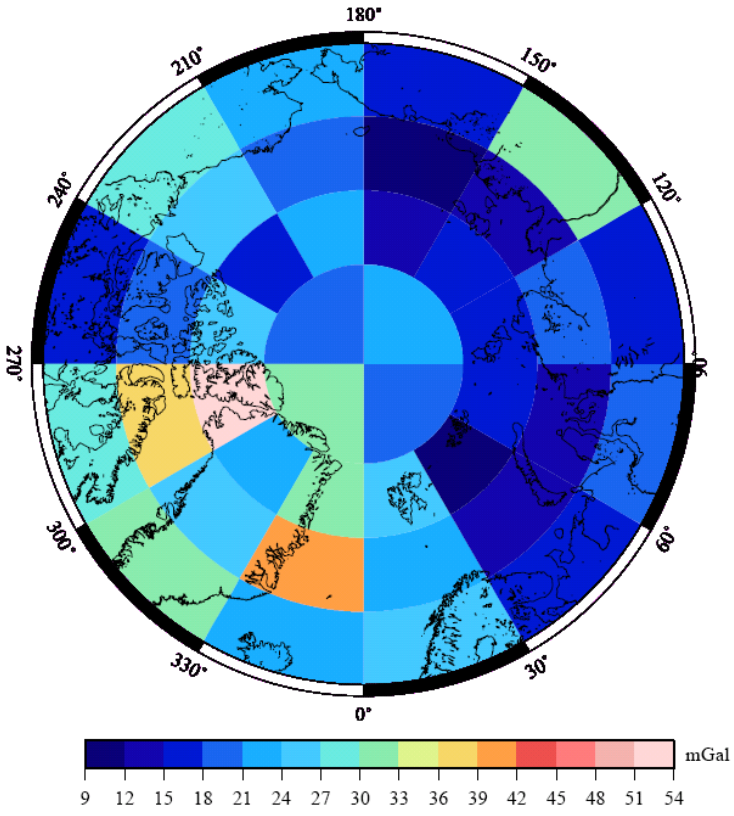

Fig. 1.28: Standard deviation per block of the reduced gravity anomalies. Unit mgal.

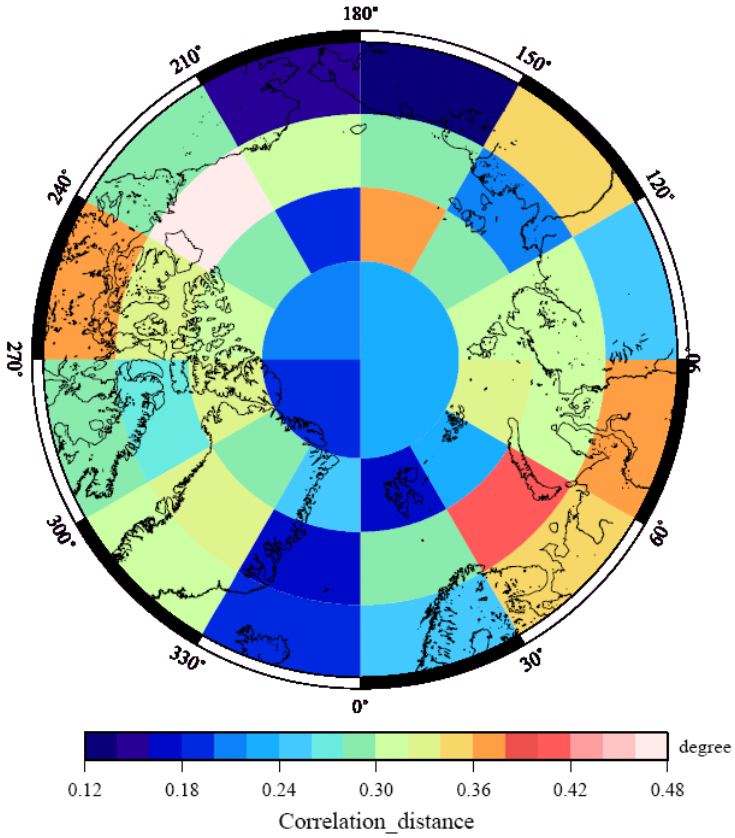

Fig. 1.29: Correlation length of the signal covariance functions per block.

Using the individual covariance functions the gravimetric geoid as well as the error covariance estimates were computed for each block separately. An overlapping zone of 1º in latitude and 2º or 3º in longitude around each block was used in order to avoid omission effects.

The gravimetric geoid model computed in this way is shown in Figure 1.30, and the error estimates of the geoid heights are shown in Figure 1.31. Note that the same accuracy for the gravity anomalies aswas adopted also in these individual computations. This also applies to the new points added for the block-wise computation, because a common error was adopted for each gravimetric survey and the additional data are coming from the same surveys.

However, as it was expected, the geoid model in Figure 1.30 shows much more details than that of Figure 1.23, since about 61% more point gravity anomalies were used in the block-wise approach. The error estimates of the geoid heights (Figure 1.31), shown that errors above 30 cm are related to areas with lack of or poor distribution of point gravity data.

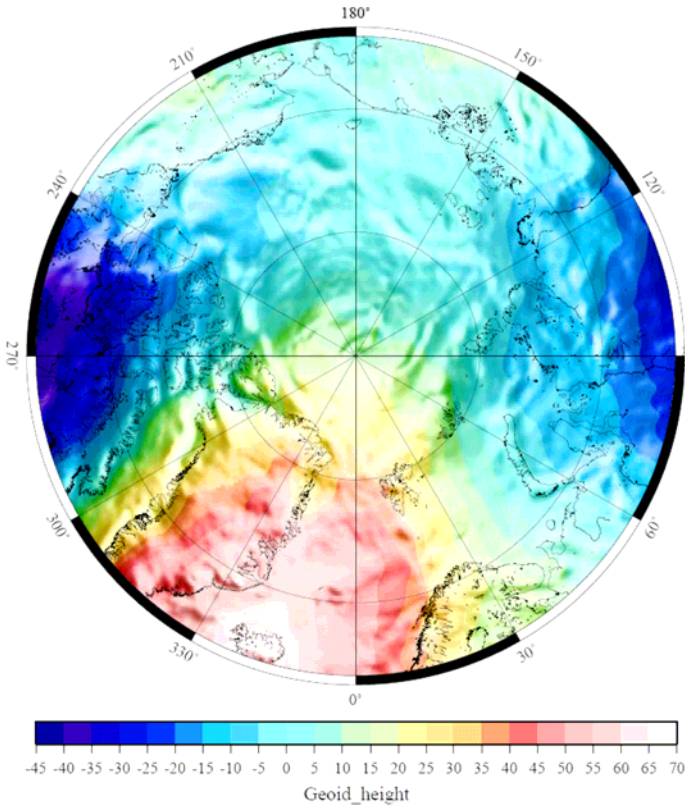

Fig. 1.30: Gravimetric geoid model of the Arctic Ocean computed block-wise. Unit m.

To check for inconsistencies in the geoid heights between the blocks a new representation of the block-wise computed geoid was plotted, using isolines with an equidistance of 1 m (Figure 1.32). Each block was plotted individually in this representation. In Figure 1.32 discrepancies of the order of the error estimates of the geoid heights are shown at the borders of some blocks.

The characteristics (standard deviation=square root of the variance and correlation length) of the block-wise computed error covariance estimates are shown in Figure 1.33. The missing values of correlation length, mainly at the beginning of each block (Figure 1.33, lower part) are due to the procedure used for its computation, which is the same as in the regional approach.

The two collocation solutions – regional and blockwise – are compared in Figure 1.34. The statistics of the differences is the following: Mean diff.= 0.0 m, std.dev. = 0.25 m, min. diff. = -1.5 m, max. diff. = 2.0 m. The large differences are seen to be concentrated in the more rough gravity field regions, e.g. off Eastern Greenland. Aliasing of point gravity data in rough topography will be a major source off errors (more data was used in the blockwise computation than the regional computation). Figure 1.35 shows the similar comparison for a block-wise computation, where the data were corrected for the estimated collocation biases from the regional computation. The statistics of the differences is now changed to: Mean diff.= 0.0 m, std. dev. = 0.25 m, min. diff. = -1.5 m, max. diff. = 2.7 m. It is seen that the changes in parts of the Arctic Ocean are quite large.

In Section 2.1 the effect of the collocation biases will be shown on the FFT geoid solutions, and in Section 3.5 the resulting MDT's from the different geoid models are compared.

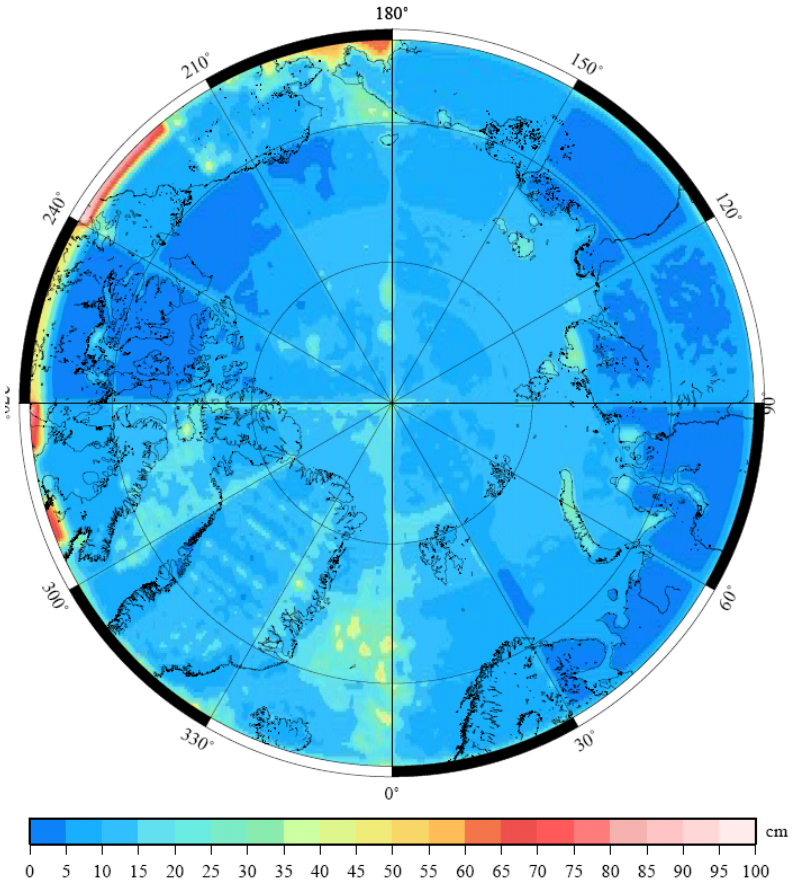

Fig. 1.31: Error estimates of the gravimetric geoid computed block-wise. Unit cm.

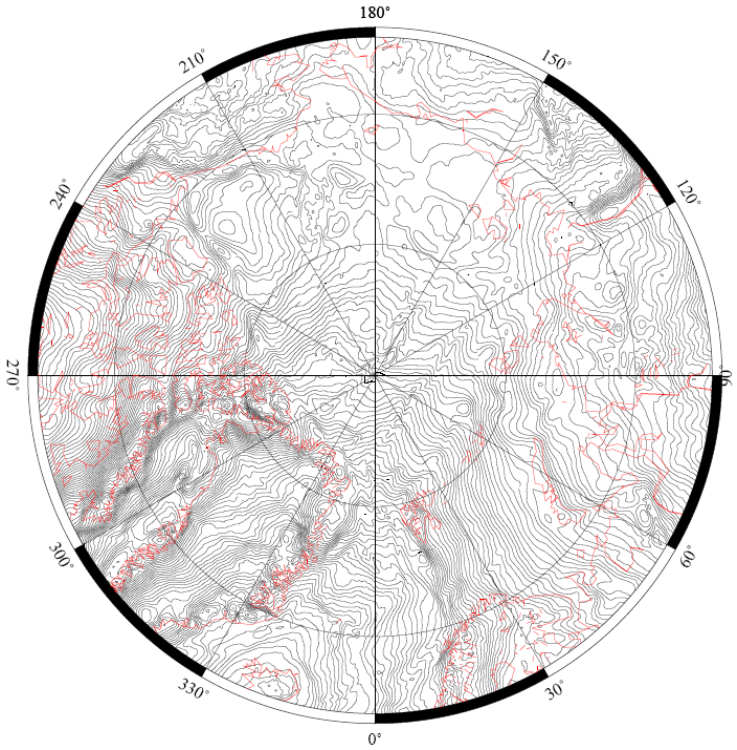

Fig. 1.32: The block-wise computed geoid in the Arctic Ocean. The equidistance is 1 m. Each block was plotted individually. Inconsistencies within the estimated errors are visible in some cases, between neighbouring blocks.

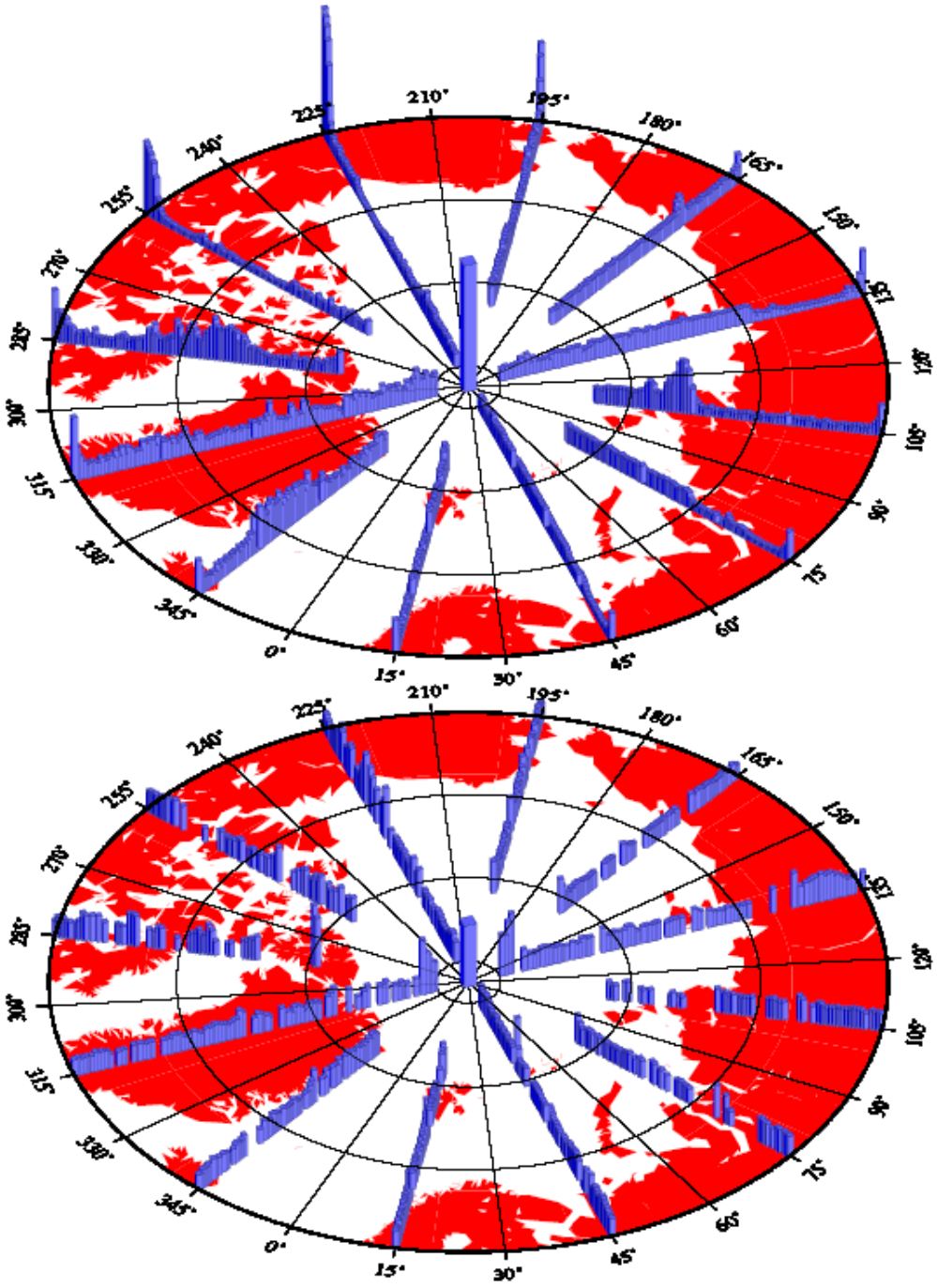

Fig. 1.33: Standard deviation (square roots of the variance) (upper part) and correlation length (lower part) of the error covariance functions along meridians every 30º. The height of the central bar corresponds to 86 cm for the standard deviations and to 0.79º for the correlation lengths. Values with equidistance 0.2º are shown, up to latitude of 88º.

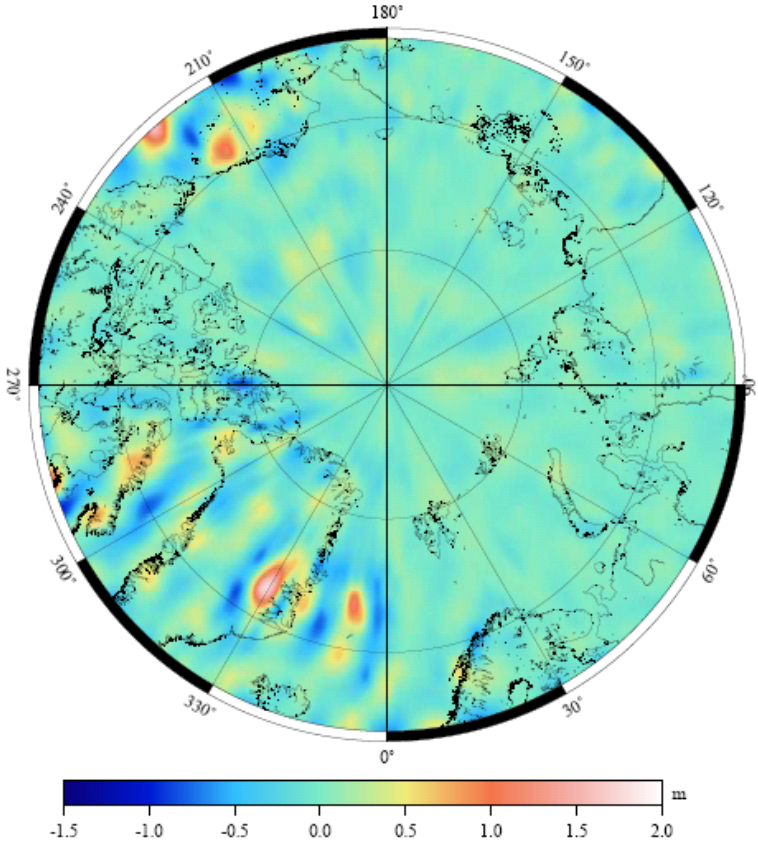

Fig. 1.34: Differences between regional and block-wise computed geoid using least squares collocation.

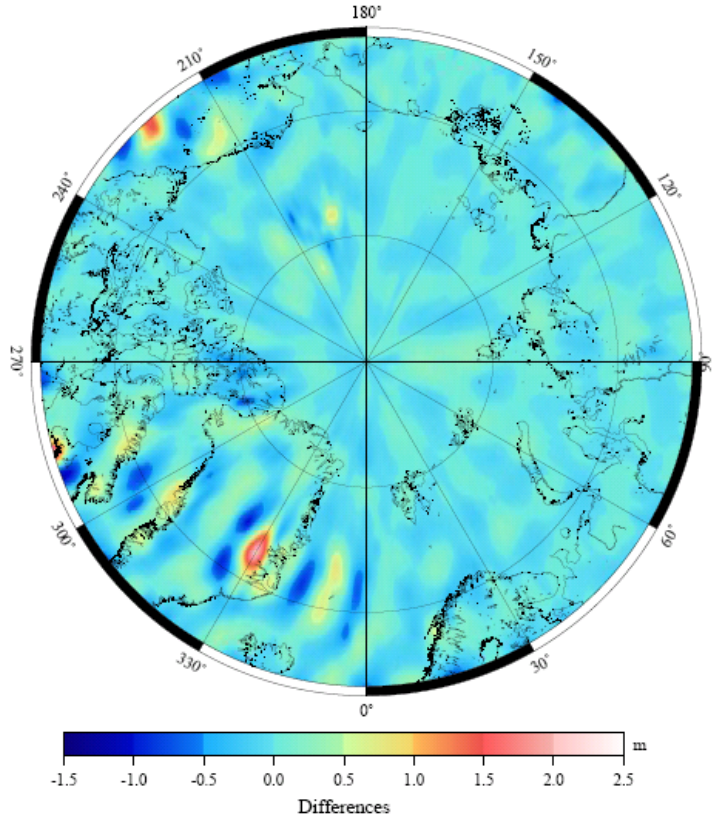

Fig. 1.35: Differences between regional and block-wise geoid, with bias correction applied to block data.

The values of the standard deviation range from 1 to 86 cm. Compared to the regional computation, larger values are shown in Figure 1.33, upper part, in areas where data are missing. This is due to the fact that in these blocks the variances of the signal covariance functions increased, while the data distribution was not improved (compare Figures 1.20 and 1.27). Neglecting these extreme cases the standard deviation is larger in blocks where the variance of the signal local covariance function was increased (compared to the regional one). For example, in the block bounded by $70^o \leq \varphi \leq 76°$, $270^o \leq \lambda \leq 300°$ the standard deviation was increased by a factor of 3.5 (from 12.5 cm in the regional approach to 44 cm here). The corresponding signal standard deviation increased by a factor equal to 1.6. On the other hand, in the block bounded by ($70^o \leq \varphi \leq 76°$, $90^o \leq \lambda \leq 120°$) the standard deviation was decreased (comparing to the regional approach) by a factor of 0.99, while the standard deviation in this block was decreased by a factor of 0.86. However, here the increase of the density of the data should be taken into account.

Furthermore, the standard deviation decreased in blocks with considerable increase of the correlation length of the local signal covariance function (e.g. in the blocks ($64^o \leq \varphi \leq 70°$, $60^o \leq \lambda \leq 90°$), ($64^o \leq \varphi \leq 70°$, $240^o \leq \lambda \leq 270°$), ($70^o \leq \varphi \leq 76°$, $210^o \leq \lambda \leq 240°$)) and increased in blocks with decreasing correlation length (e.g. in the block $70^o \leq \varphi \leq 76°$, $330^o \leq \lambda \leq 0°$).

The conclusion from these examples is that the variance of the error covariance estimates is correlated with the variance of the signal covariance function and anti-correlated with its correlation length.

With respect to the correlation length, values from 0.14 to 0.79 are shown in Figure 1.33 (lower part). In Figure 1.33 lower part, a significant increase of its value in several blocks is shown, probably correlated with the data-sampling. This conclusion is based on the fact that the increase of the correlation length close to the pole does not correspond to an increase of the standard deviation (see Figure 1.28) or of the correlation length (see Figure 1.29) of the local covariance function comparing to the regional one.

Conclusion to Section 1.4

Gravimetric geoid models and error covariance estimates of the geoid heights in the Arctic Ocean were computed by LSC, following two different computation schemes. A regional one using, a regional covariance function and a block-wise, using a local covariance function for each block. In both cased error covariance estimates with spacing 0.1° were computed along meridians, covering the latitudes $64^o \leq \varphi \leq 90°$.

The error covariance estimates from the regional approach resulted in standard deviations ranging from 5 to 66 cm, with correlation lengths ranging from 0.10° to 0.47°. Standard deviations above 25 to 30 cm are related to areas with lack of or poor data coverage. From the regional approach it was concluded that the standard deviation of the error estimates depends mainly on the density of the data. Dependence on their accuracy was not detected.

The gravimetric geoid model from the block-wise approach showed details not visible in the regional one, due to the denser data set used. The error covariance estimates resulted in standard deviations ranging from 1 to 86 cm, with correlation lengths ranging from 0.14° to 0.79°. The conclusion derived from the block-wise approach was that the standard deviation is correlated with the signal standard deviation and anti-correlated with the signal correlation length. The correlation length of the error covariance function seems to have a dependence on the density of the input data.

Combining the results from both computation schemes it could be concluded that the variance of the error covariance function is correlated with the signal variance and anti-correlated with the data sampling and the signal correlation length. Concerning the correlation length of the error covariance function, it seems to be correlated only with the data sampling. A direct comparison of results from the two approaches is not possible: the regional approach cannot use all the data, and are – in present software – limited to a stationary covariance function; the blockwise approach will have errors due to the limited area in use. Therefore a full error study of the complete Arctic gravity data set have not been possible.

The error covariance estimates, include valuable information (especially in the case of the block-wise approach) for the combination of the gravimetric geoid of the Arctic Ocean with other data for the determination of the sea ice free-board in the Arctic Ocean. On the other hand it shows that one can not compute one error-covariance function to be used in the whole area, but the error-covariances must be computed in a point by point basis.

1.5 Optimal combination of MSS and geoid

To calculate the best possible reference surface a mean sea surface (MSS) may be derived from a combination of multi mission satellite altimetry. Furthermore, the regional geoid which may have been updated using GRACE and recent airborne surveys, may contribute to further improvements of the mean sea surface, especially in areas covered by sea ice. The method described here is based on the work carried out in the GOCINA project (Knudsen et al., 2004, Knudsen, 1995).

Combining data sources

When different data types are combined it is important that it is done in a rigorous way and that the full signal/error content is taken into account. Else fatal inconsistencies between different data types may occur. Neglecting sea ice, the MSS consists of the geoid and the MDT, as expressed as

$$h = N + \zeta + \Delta h \tag{16}$$

where

h	is the mean sea surface ellipsoidal height
N	is the geoid height,
ζ	is the mean dynamic topography, and
Δh	is the measurement noise.

The geoid height is a quantity associated with the anomalous gravity potential T. Hence, N can be expressed in terms of a linear functional (or as in this case a linearized functional according to *Bruns' formula*) applied on T (γ is the normal gravity):

$$N = \mathrm{L_N}(\mathrm{T}) = \frac{\mathrm{T}}{\gamma} \tag{17}$$

At this point the important link between altimetry and gravimetry can be made, as gravity anomalies are associated with T too. They are expressed as

$$\Delta g = \mathrm{L}_{\Delta \mathrm{g}}(\mathrm{T}) = -\frac{\partial \mathrm{T}}{\partial \mathrm{r}} - 2\frac{\mathrm{T}}{\mathrm{r}} \tag{18}$$

The gravity data are used in the combination solution rather that the estimated geoid. Hereby the structure of the original data source, e.g. data distribution and their individual errors, are maintained and represented in the computations. Furthermore, remaining biases in the

individual gravity surveys may be taken into account. For the ship data such a bias should be considered. The air-borne data may be considered to be bias free.

In principle, the altimeter data should be used as described in Knudsen (1991, 1993). However, if a mean sea surface determination includes a very large number of data and those data have been combined using a rigorous method, it may decided to use such a mean sea surface with its associated errors in the combination solution. MDT information from ocean circulation models may be taken into account if reliable error estimates may be derived (See also Knudsen and Vest, 2005).

The combination of the mean sea surface heights and the gravity data is done rigorously using the optimal estimation technique called least squares collocation (LSC). Here the results in the following expression

$$x = C_x^T \left(\mathrm{C} + \mathrm{D}\right)^{-1} \mathrm{y} \tag{19}$$

An estimate of the *a-posteriori* error covariance between two estimated quantities, x and x', is obtained using

$$\hat{c}_{x'x} = c_{x'x} - C_x^T \left(\mathrm{C} + \mathrm{D}\right)^{-1} C_{x'} \tag{20}$$

where $c_{xx'}$ is the *a-priori* (signal) covariance between x and x' (see e.g. Moritz, 1980).

The elements of the covariance matrices of equations (20-21) are calculated according to the mathematical model of the observations. In this case, signals associated with the gravity data and the mean sea surface is considered.

The covariance values are obtained using the kernel functions. The kernel associated with the gravity field is derived using equation (20) and some *a-priori* variances. Then the covariance between T in the points P(φ,λ) and Q(φ',λ') is expressed as

$$K(\mathrm{P},\mathrm{Q}) = \sum_{\mathrm{i}=2}^{\infty} \sigma_{\mathrm{i}}^{\mathrm{TT}} \mathrm{P_i}(\cos\psi) \tag{21}$$

where σ_i^{TT} are degree variances and ψ is the spherical distance between P and Q. Hence, eq. (22) only depends on the distance between P and Q and neither on their locations nor on their azimuth (i.e. a homogeneous and isotropic kernel). Expressions associated with geoid heights and gravity anomalies are obtained by applying the respective functionals on K(P,Q), e.g. C_{NN}=L$_N$(L$_N$(K(P,Q))) (more on collocation by Sansò, 1986, Tscherning, 1986). Then

$$C_{NN} = \sum_{i=2}^{\infty} \left(\frac{1}{\gamma}\right)^2 \sigma_i^{TT} \mathrm{P_i}(\cos\psi) \tag{22}$$

$$C_{\Delta g \Delta g} = \sum_{i=2}^{\infty} \left(\frac{i\text{-}1}{R}\right)^2 \sigma_i^{TT} \mathrm{P_i}(\cos\psi) \tag{23}$$

$$C_{N\Delta g} = \sum_{i=2}^{\infty} \left(\frac{i\text{-}1}{\gamma R}\right) \sigma_i^{TT} \mathrm{P_i}(\cos\psi) \tag{24}$$

The kernel associated with the SST, equation (21), is expressed in a similar manner as the gravity fields as

$$C_{\zeta\zeta} = \sum_{i=1}^{\infty} \sigma_i^{\zeta\zeta} \mathrm{P_i}(\cos\psi) \tag{25}$$

The modeling of the covariance function associated with the gravity field is described in Knudsen (1987, 1988). This technique has been applied using empirical covariance values

calculated from marine gravity data reduced using a hybrid reference model consisting of the GRACE GGM01 model up to degree 90 and EGM96 from degree 91 to degree 360. As degree variance model a Tscherning/Rapp model (Tscherning & Rapp, 1974) was used. This expression has the advantage that the kernel can be evaluated using a closed expression instead of the infinite sum. The model is

$$\sigma_i^{TT} = \begin{cases} \varepsilon_i^{GRACE} & i = 2,...,90 \\ \varepsilon_i^{EGM96} & i = 91,...,360 \\ \dfrac{A}{(i-1)(i-2)(i+4)}\left(\dfrac{R_B^2}{R^2}\right)^{i+1} & i = 361,.... \end{cases} \tag{26}$$

where A = 1544850 m^4/s^4, $R_B = R - 6.823$ km were found in an adjustment. The error degree variances, ε_i, associated with the EGM96 model was multiplied by 0.25. The covariance function associated with gravity anomalies has a variance of (11.8 mgal)^2 and a correlation length (which is the distance where the covariance is 50 % of the variance) of 0.15°. The corresponding geoid height covariance function has a variance of (0.20 m)^2 and a correlation length of 0.26° (Degree variances and geoid covariance function are shown in Figure 1.36 and 1.37 respectively).

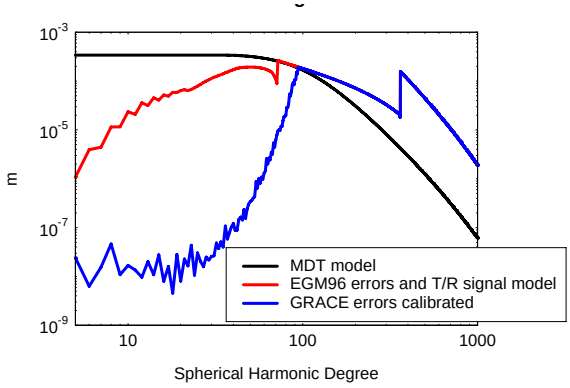

Fig. 1.36: Degree variances for the geoid with error variances from the GRACE and the EGM96 models (blue), EGM96 error variances (red), and MDT degree variance model (black).

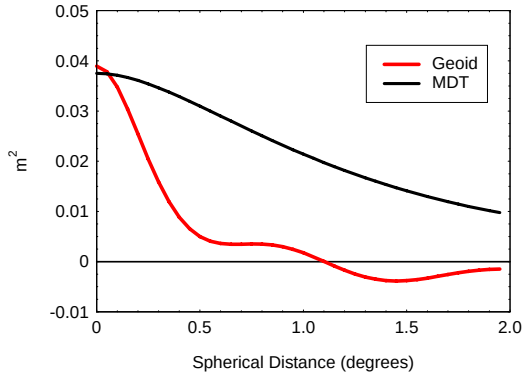

Fig. 1.37: Covariance functions associated with the geoid (red) and the MDT (black).

A determination of a covariance function model associated with the MDT was carried out using an empirical covariance function was determined and a degree variance model chosen. The degree variance model was constructed using 3rd degree Butterworth filters combined with an exponential factor. Hence, the spectrum of the MDT is assumed to decay similar to the geoid spectrum. Then the model was fitted iteratively to the empirical covariance values as described in Knudsen (1992, 1993). This resulted in the model:

$$\sigma_i^{ss} = b \cdot \left(\frac{k_2^3}{k_2^3 + i^3} - \frac{k_1^3}{k_1^3 + i^3} \right) \cdot s^{i+1} \tag{27}$$

where b = 6.3 10^{-4} m^2, k_1 = 1, k_2 = 90, $s = ((R\text{-}5000.0)^2/R^2)^2$. The variance and correlation length are (0.20 m)^2 and 1.3° respectively (Degree variances and covariance function are shown in Figure 1.36 and 1.37 respectively). The variance and correlation length of the current components are (0.16 m/s)^2 and 0.22° respectively.

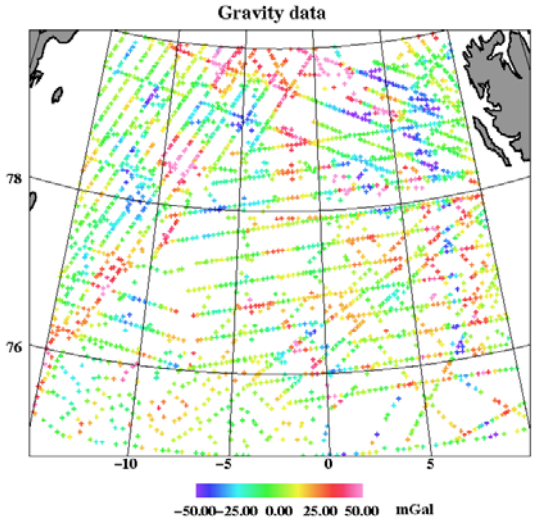

Fig. 1.38: Distribution of gravity data – both ship and air borne data – with color shading of individual values of residual gravity anomalies.

Results

The rigorous combination method has been tested in a partly ice covered region between Greenland and Svalbard (see Figure 1.38). As MSS observations the KMS04 MSS model by Andersen (2005) was used. It has been constructed using multi mission altimetry and represents a mean over the period 1993-2001. The data were selected with a spacing of 0.2 by 0.5 degrees. The gravity data from ship surveys as well as airborne surveys were used (Forsberg et al., 2004, Olsen, 2005). Those data were selected with a spacing of about 0.1 by 0.2 degrees (see Figure 1.38).

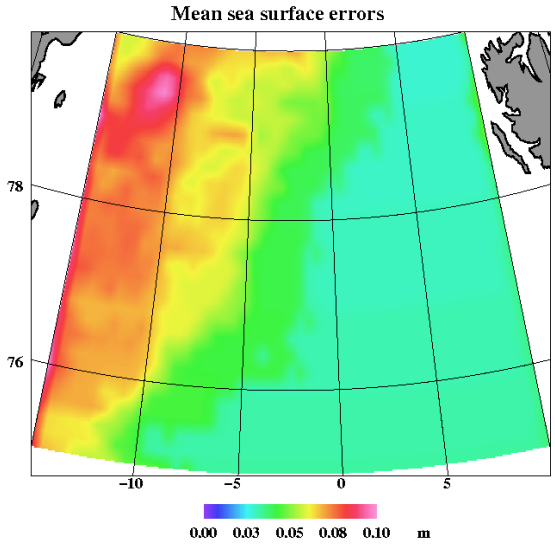

Fig. 1.39: Estimated errors of MSS based on MSS data only.

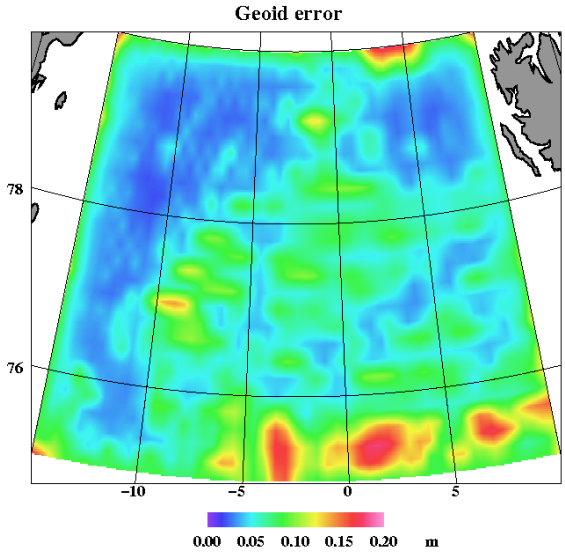

Fig. 1.40: Estimated errors of geoid based on gravity data only.

The method of least squares collocation was used to compute solutions with different input data sets: 1) MSS data alone, 2) Ship gravity data combined with the airborne gravity data, and 3) Gravity combined with MSS data. Observation errors were taken into account properly. Subsequently, for each solution error estimates associated with the MSS and the geoid heights were computed. The errors of the MSS based on MSS data alone are shown in Figure 1.39. The effects of sea ice on the computation of the MSS are clearly shown. In the ice covered areas the errors are significantly larger that in the ice free areas. The resulting geoid error maps based on gravity data alone is shown in Figure 1.40. The contribution of the airborne data is evident, especially in the North-western part of the region.

The results based on both data types are shown in Figure 1.41 and 1.42. The effects of combining the data sets are clear in both the estimated MSS errors and the estimated geoid errors. Especially in the estimated MSS errors it is evident that the MSS has been improved in the ice covered areas. In the ice free parts of the region the combination of the two data types has lead to an improvement of the geoid in areas with poor coverage of gravity data. Hence, the combination of MSS and gravity data has improved the estimation of both quantities.

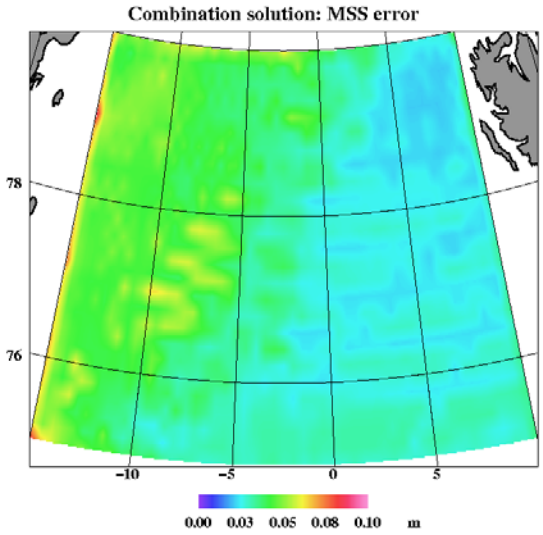

Fig. 1.41: Estimated errors of MSS based on MSS and gravity data combined.

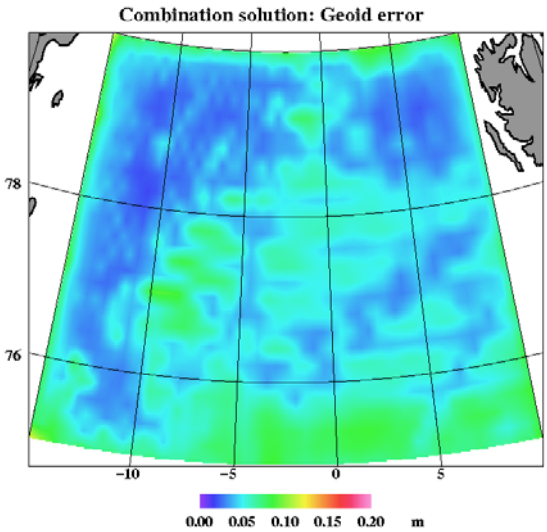

Fig. 1.42: Estimated errors of geoid based on MSS and gravity data combined.

Perspectives

The procedure for combining MSS and geoid information (the geoid through the gravity data) has been tested as described in the previous section demonstrating that both quantities may be improved. The challenge in modeling MSS in ice covered areas is to find procedures for extracting altimetry heights over ice free areas only. Altimeter data in such regions may represent partly the sea surface and partly the top of the sea ice. Such data need to be separated. Subsequently, the MSS should be determined using sea surface data combined with gravity data to provide the reference surface for the determination of sea ice thicknesses.

The procedure may be augmented to include sea ice thicknesses, or using its associated free board height, using

$$h = N + \zeta + F + \Delta h \tag{28}$$

where

h	is the sea ice surface ellipsoidal height,
N	is the geoid height,
ζ	is the mean dynamic topography
F	is the freeboard height, and
Δh	is the measurement noise.

Then a covariance function associated with the sea ice thicknesses is needed. For initial tests a covariance function similar to the MSS covariance function may be used. However, studies are needed to recover information about both the spatial and the temporal characteristics and statistical properties of the sea ice thicknesses to determine such a covariance function. Also the time varying component needs to be included to describe the instantaneous sea surface height as described in Knudsen (1991, 1993).

2 Geoid models and MSS

2.1 Updated geoid of Arctic region based on GRACE

The new Arctic Gravity Project geoid model has been determined by remove-restore spherical Fourier transformation methods with modified kernels. In the Fourier method the free-air gravity anomalies Δg are reduced for satellite (GRACE-GGM02S/EGM96) spherical harmonic model gravity anomalies

$$\Delta g' = \Delta g - \Delta g_{ref} \tag{29}$$

and subsequently transformed into reduced geoid heights N' by a convolution expression readily evaluated by two-dimensional spherical FFT

$$N' = S_{mod}(\Delta\phi,\Delta\lambda) * [\Delta g'(\Delta\phi,\Delta\lambda)\sin\phi] = F^{-1}[F(S_{ref})F(\Delta g')] \tag{30}$$

where S_{mod} is a modified Stokes' kernel

$$S_{\mathrm{mod}}(\psi) = S(\psi) - \sum_{n=2}^{N_2} \alpha(n) \frac{2n+1}{n-1} P_n \cos(\psi) \tag{31}$$

with modification coefficients α(n) being 0 for low degrees and 1 for high degrees, with a transition zone in a suitable harmonics band around the resolution of the GRACE data.

As reference field for the geoid determination a composite model of GRACE-GGM02S and EGM96 is used, so that GRACE is used exclusively until degree 100, then EGM96 from degree 110, and a linear transition in between. Due to the use of modified kernels, the effect of EGM96 is mainly to limit aliasing along the southern border.

We experimented with different kernel modification transition degrees (60-70, 80-90 and 100-110); we finally selected degree 80 as the preferred spherical modification degree, based on a visual inspection of ICESat sea ice features, and – especially – experience from many other regions (Scandinavia, UK, Malaysia and Mongolia), where experience has shown the higher spherical harmonic degrees of the GRACE models to be error-affected (with a particular, yet unresolved, tendency for N/S "error stripes"). These investigations are mainly based on analysis of continental geoids when compared to GPS leveling, and experience from the GOCINA project (Forsberg et al., 2004). No clear "optimal" modification numbers have yet been reported in the literature, and it is an area of active research among geodetic GRACE user groups.

Table 2.1 below shows some of the error statistics of the computed geoids, and Figure 2.1 and Figure 2.2 show the geoid and differences to earlier solutions. Figure 2.3 shows the magnitude of difference for kernel modifications 60-70 versus 100-110.

The geoid determination techniques are implemented in the GRAVSOFT software and have been used extensively for a host of other continental and marine geoid projects, e.g. recently in the North Atlantic/Greenland seas using GRACE reference fields as part of the GOCINA project (Forsberg at al., 1996, 2003, 2004).

Because the new ArcGP geoid was computed in the Topex system, an alternative FFT geoid was also computed with the EIGEN-CG03C reference field, complete to degree and order 360, in order to be consistent with the least-squares collocation runs of Section 1.4. These geoid computations were done in the WGS84 reference system. The mean geoid differences

in Table 2.1 reflect mainly the different reference systems used. The use of different geoid reference systems was mainly for historical reasons and the use of different software setups; unfortunately no common reference was selected prior to the rather large computations. At the north pole the difference between a geoid in WGS84 and Topex is roughly 0.9 m; the main effect is from the difference in the semi-major axis of the reference ellipsoids.

The alternative EIGEN-CG03C FFT computation was done both using the revised ArcGP grid directly, and with a corrected ArcGP grid, using the collocation estimated collocation data biases (cf. Section 1.4, Table 1.2). Since the ArcGP raw data were not available for these studies, an approximate correction was done for the biases through a gridding of the data biases, and the gridded biases were subsequently used to correct the ArcGP grid. The biases were only applied to the data sources over the Arctic Ocean, since biases over land areas are mainly coming from aliasing due to lack of terrain reductions in the collocation geoid computation.

Figure 2.4 shows the gridded gravity data biases, and Figure 2.5 the geoid effect of the biases (difference between FFT solutions without and without using the bias grid). The comparison to the collocation geoids is shown in Table 2.1, and plotted in Section 2.3, and the MDT comparison in Section 3.5. It is seen that the common reference field made the collocation and FFT approaches agree well in absolute level, but there is large discrepancies, likely due to thinned data used in the collocation, and terrain effects.

Table 2.1: Comparison of different geoid models. Unit: meter.

Geoids	**Mean**	**Std.dev.**	**Min**	**Max**
New ArcGP geoid (n=80) – ArcGP old	0.89	0.22	-1.56	3.82
New ArcGP geoid – ArcGP 2004 geoid	0.00	0.08	-0.63	1.97
New ArcGP geoid (n=100) – geoid (n=60)	0.00	0.11	-0.44	0.48
New ArcGP compared to ICESat (laser 2a)	-0.17	0.38	-1.51	3.74
Comparisons to EIGEN reference fields: New ArcGP geoid – EIGEN-CG03C	-0.07	0.25	-2.18	1.94
New ArcGP geoid – EIGEN-GL04C	-0.07	0.23	-1.94	2.03
EIGEN-CG03C versus EIGEN-GL04C	0.00	0.12	-0.40	0.37
Comparisons to collocation geoids: New ArcGP geoid – regional collocation solution (WP1.4)	-0.87	0.28	-4.31	0.75
New ArcGP geoid – blocked collocation	-0.88	0.30	-6.46	1.68
Comparisons to collocation geoids with the same ref.field (EIGEN-CG03C): Geoid from FFT – regional collocation	-0.01	0.28	-3.44	1.75
Geoid from FFT – regional collocation, using bias-corrected ArcGP grid	-0.01	0.29	-3.42	1.77
Geoid from FFT – blockwise collocation, without bias correction	-0.01	0.30	-5.61	2.61
Geoid from FFT – blockwise collocation, with bias correction	0.00	0.31	-6.50	3.18
Difference in FFT geoid with and without collocation gravity bias correction	0.00	0.03	-0.22	0.14

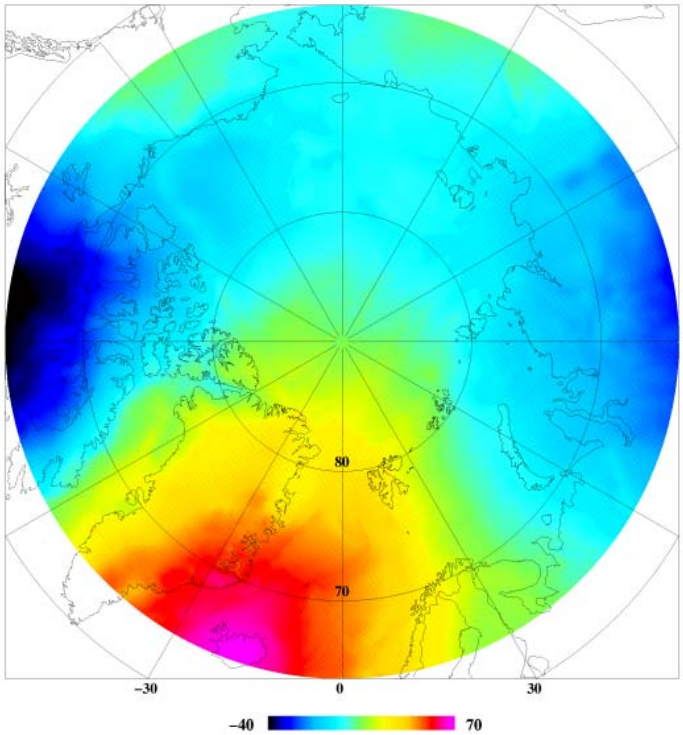

Fig. 2.1: New ArcGP geoid. Unit meter.

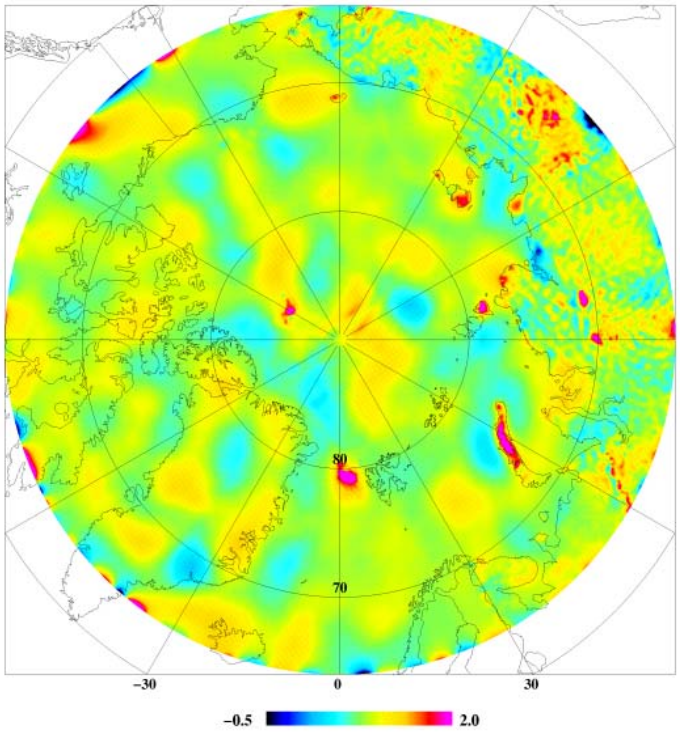

Fig. 2.2: Difference between new (Jan 2006) and old (Dec 2002) ArcGP geoid. Unit m.

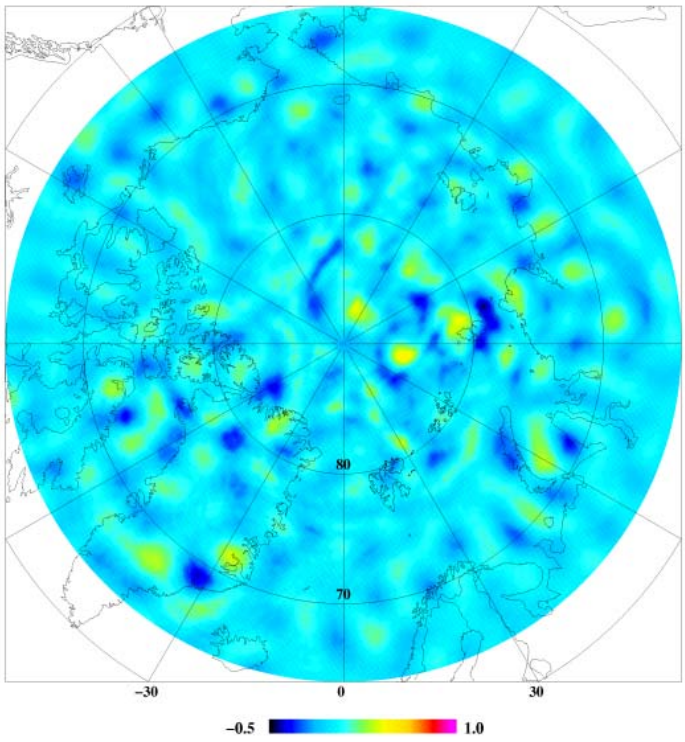

Fig. 2.3: Difference between FFT geoids computed with a low (60-70) and a high (100-110) degree of kernel modification. Unit m.

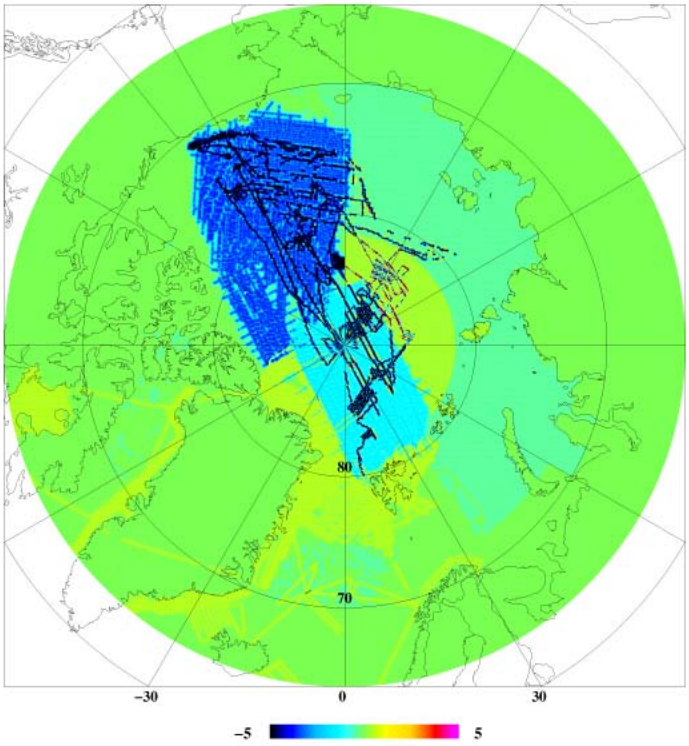

Fig. 2.4: Apparent ArcGP gravity data biases for the major Arctic Ocean surveys (NRL and Scandinavian airborne, Scicex submarine, Russian grid and ERS data) estimated by collocation, cf. Section 1.4. Unit mgal.

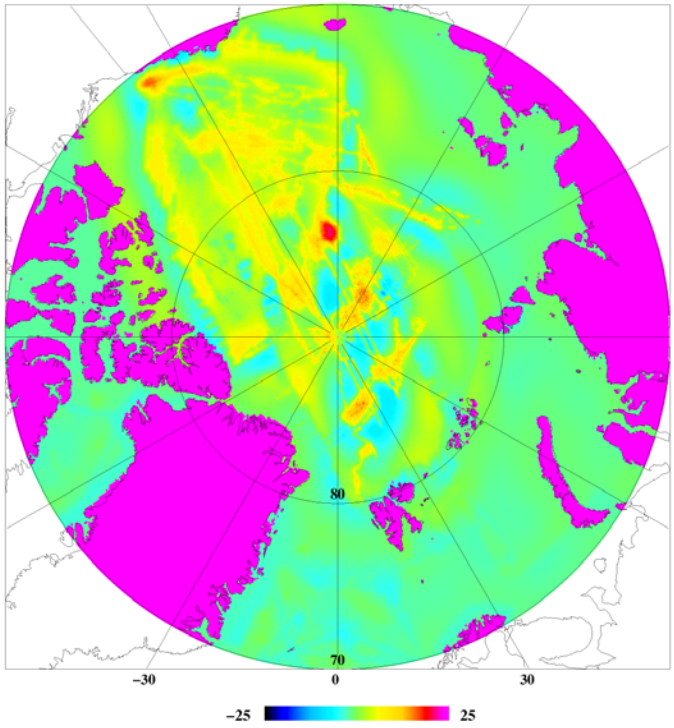

Fig. 2.5: Effect of gravity bias correction on the computed FFT geoid. Unit cm.

2.2 Error estimation of new geoid

The formal error estimates of the geoid were found and shown in Section 1.4 using least-squares collocation. Formal error estimates of the spherical FFT geoid computation of the Arctic Gravity Project grid are not available (a consequence of the method; so far no published FFT methods exist, which takes into account real data errors and correlations). Therefore the collocation error estimate may be viewed as an upper bound on the errors (the FFT errors are likely smaller, since much more data has been used, and terrain effects have been taken fully into account on land). Figure 2.6 below shows the error estimate from the detailed block-wise collocation runs.

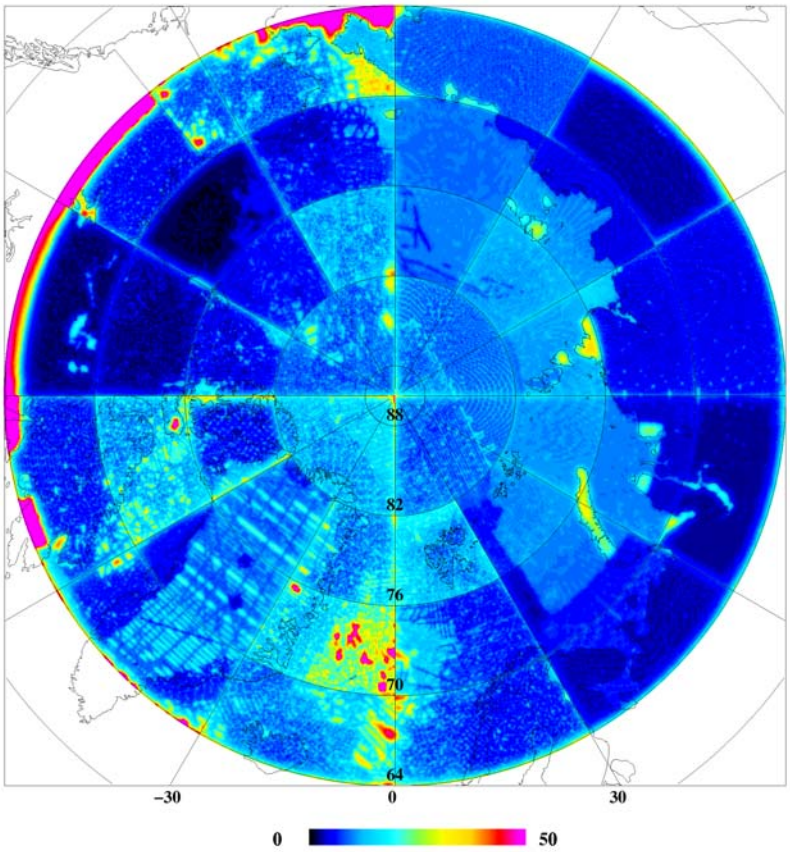

Fig. 2.6: Geoid errors (cm) of the blocked-collocation geoid estimation of Section 1.4.

2.3 Assessment of new and existing geoids

The different geoids for the region include the ArcGP spherical FFT solutions (corresponding to the December 2002 original ArcGP grid; the December 2004 interim grid; the January 2006 new grid), and the EIGEN-CG3C/GL4C used for collocation computation with biases and the "simple" approach to ICESat MSS estimation. To this come the two collocation geoids of Section 1.4 (regional solution and blocked solution). The Figures 2.7-2.9 below show intercomparisons of the geoids, with statistics of comparison shown in Table 2.1.

Within the Arctic Ocean the proper comparisons are at the 20 cm level r.m.s. Some of this difference is from the different GRACE models used, but also the different ways in which the long-wavelength information is treated (the FFT method only estimates geoid from local data above degree 80; collocation estimates will use the full spectrum of terrestrial data for the geoid estimate, and has estimated survey biases; and the EIGEN models are spherical harmonic expansions with no information beyond spherical harmonic degree 360).

It should be noted that because of the very large computational effort involved in the regional collocation solution for geoid and geoid error estimates, this computation is only available on a 1°-resolution grid. An offset in bias of around 90 cm for the collocation solutions is due to difference in the reference system (the ArcGP and EIGEN geoids are computed on the Topex ellipsoid, while the collocation error estimates use WGS84 ellipsoid).

Fig 2.10 shows a direct plot of all ICESat heights compared to the new, detailed ArcGP geoid, equivalent to the plots of Figure 1.12 using the EIGEN-CG4C spherical harmonic model. On

the qualitative level and at the small illustration scale these plots appear to be quite similar. Comparisons of more solutions to ICESat results are done in Section 3.5 where derived MDT's are compared. A detailed assessment of the different geoids cannot be done except by judging the realism and noise of the derived MDT and ice thickness fields. Given the superior resolution, the ArcGP geoid will be the primary geoid to be studied in the sequel.

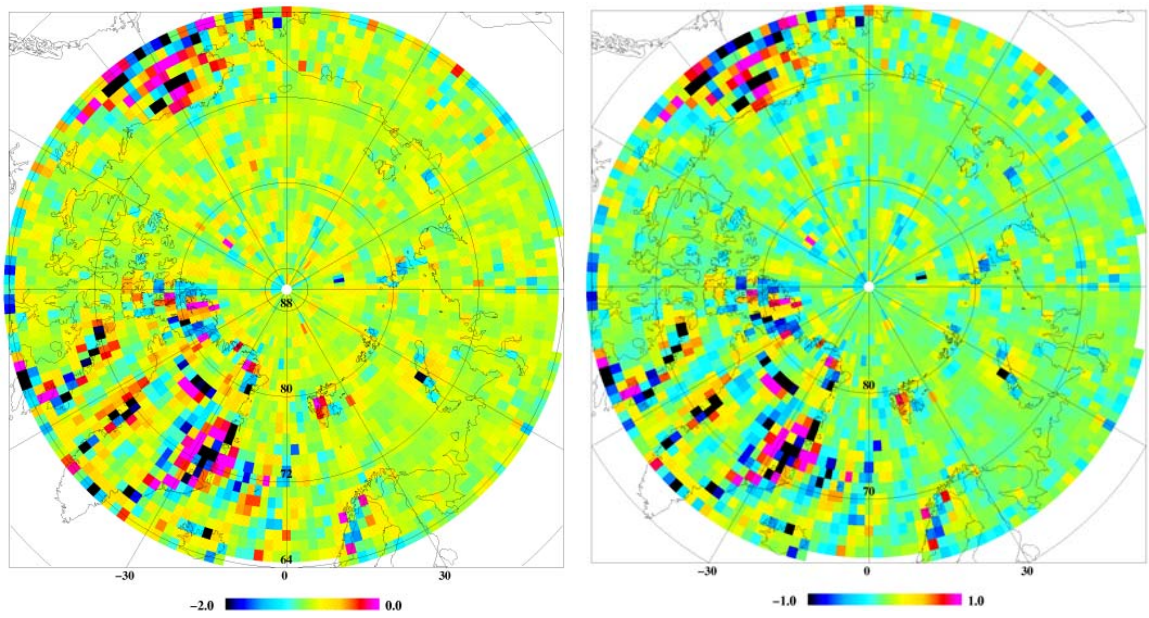

Fig. 2.7: Comparison of regional collocation solution to new spherical FFT solution. Left: ArcGP geoid, right: geoid using EIGEN-CG03C and bias-corrected Arctic Ocean gravity data. Since the collocation solution did not use terrain reductions on land, major differences are expected here, primarily due to terrain aliasing of the relatively sparse collocation data set. Units: meter.

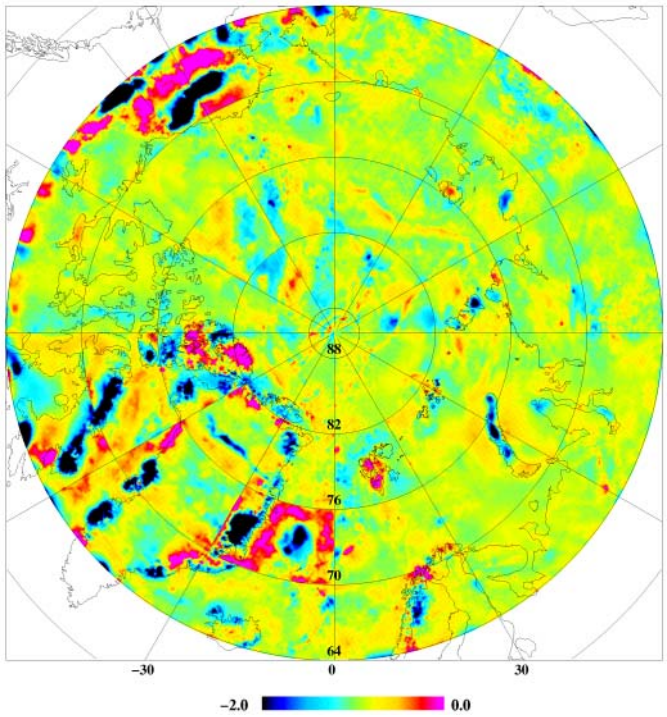

Fig. 2.8: Comparison of the collocation blocked solution to the ArcGP spherical FFT solution. Unit: m.

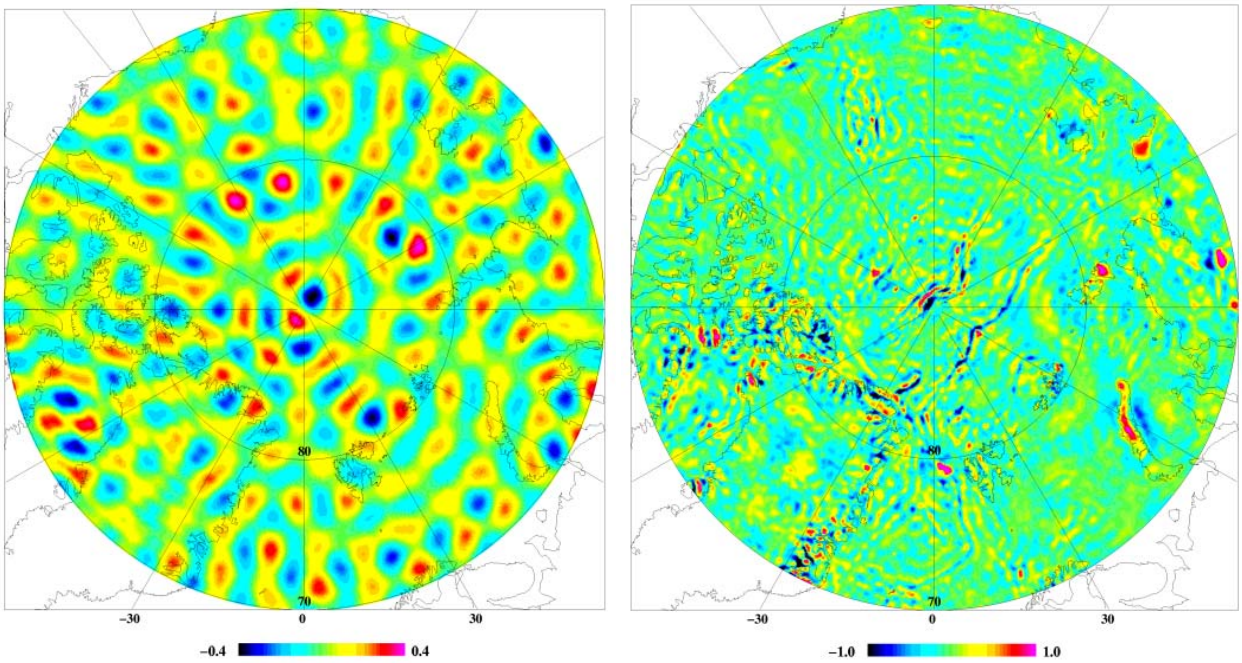

Fig. 2.9: Comparison of the EIGEN geoids: Left: Difference EIGEN-CG3C versus EIGEN-GL4C; right: difference New ArcGP geoid versus EIGEN-GL4C. Units: meter.

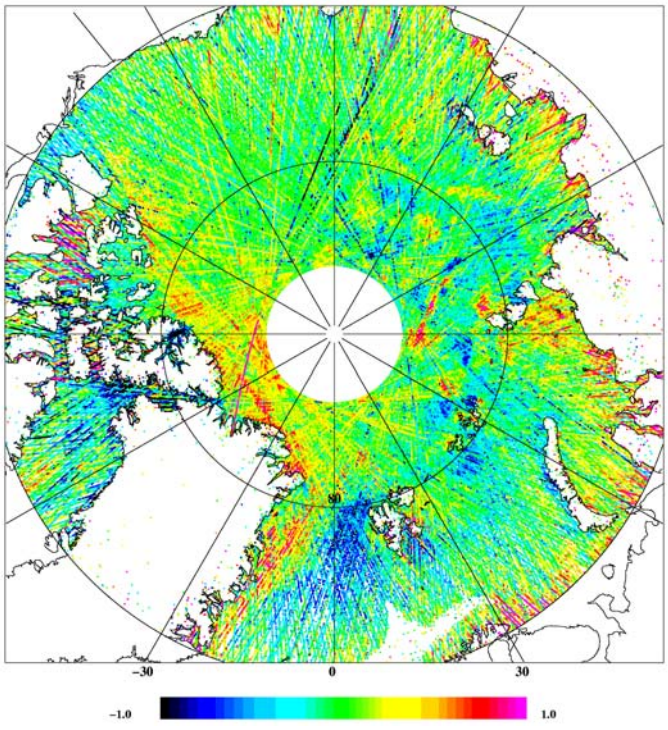

Fig. 2.10: Example of comparison of the ArcGP geoid model to the raw ICESat measurements of surface height, for the new ArcGP geoid. Units: m. It is seen that plots of h-N gives an apparent sea ice signature, with thick ice north of Greenland, but also illustrates the trackiness in the raw data.

2.4 Development of a composite MSS grid from ERS and ICESat

The 7 ICESat periods analyzed in Section 1.3 resulted in a series of quite different MSS grids, a consequence of the differences in data density, and the errors associated with the lowest level filtering. Figure 2.11 shows the 7 ICESat MSS fields, shown here with the ArcGP geoid subtracted (i.e., represented as MDT fields). The MSS grids have been derived from the selected "lowest levels" in the ICESat measured heights, at a resolution of approximately 0.2°. The IB correction has been applied, and a cross-over adjustment subsequently applied to remove some of the trackiness apparent from Figure 2.10. The ICESat MSS for each observation epoch, and the combined ERS MSS, are compared both to the ArcGP and to ERS in the overlap band 79-81.5°N in Table 2.2. Biases in the different ICESat epochs are apparent, and also clearly seen in the difference plots 2.11. These biases are likely due to calibration problems with the ICESat lasers, but as outlined in Section 1.3, and illustrated by the airborne lidar comparison, the lowest-level filtering procedure may additionally be a source of biases.

Table 2.2: Comparison of mean ERS and ICESat epoch MSS to the new ArcGP geoid. Unit: m.

.

Comparison (in area north of 77.5 N)	ArcGP geoid (WGS84)		ERS in overlap 79-81.5 N	
	mean	std.dev.	mean	std.dev.
Laser 1 (March 2003)	-0.48	0.21	-0.21	0.35
Laser 2A (Oct. 2003)	-0.57	0.17	-0.30	0.34
Laser 2B (March 2004)	-0.29	0.19	-0.03	0.34
Laser 2C (June 2004)	-0.25	0.19	0.06	0.35
Laser 3A (Oct. 2004)	-0.60	0.20	-0.32	0.35
Laser 3B (March 2005)	-0.66	0.21	-0.37	0.35
Laser 3C (June 2005)	-0.24	0.23	-0.24	0.38
MSS from ERS 1995-2003	-0.32	0.37	-	-

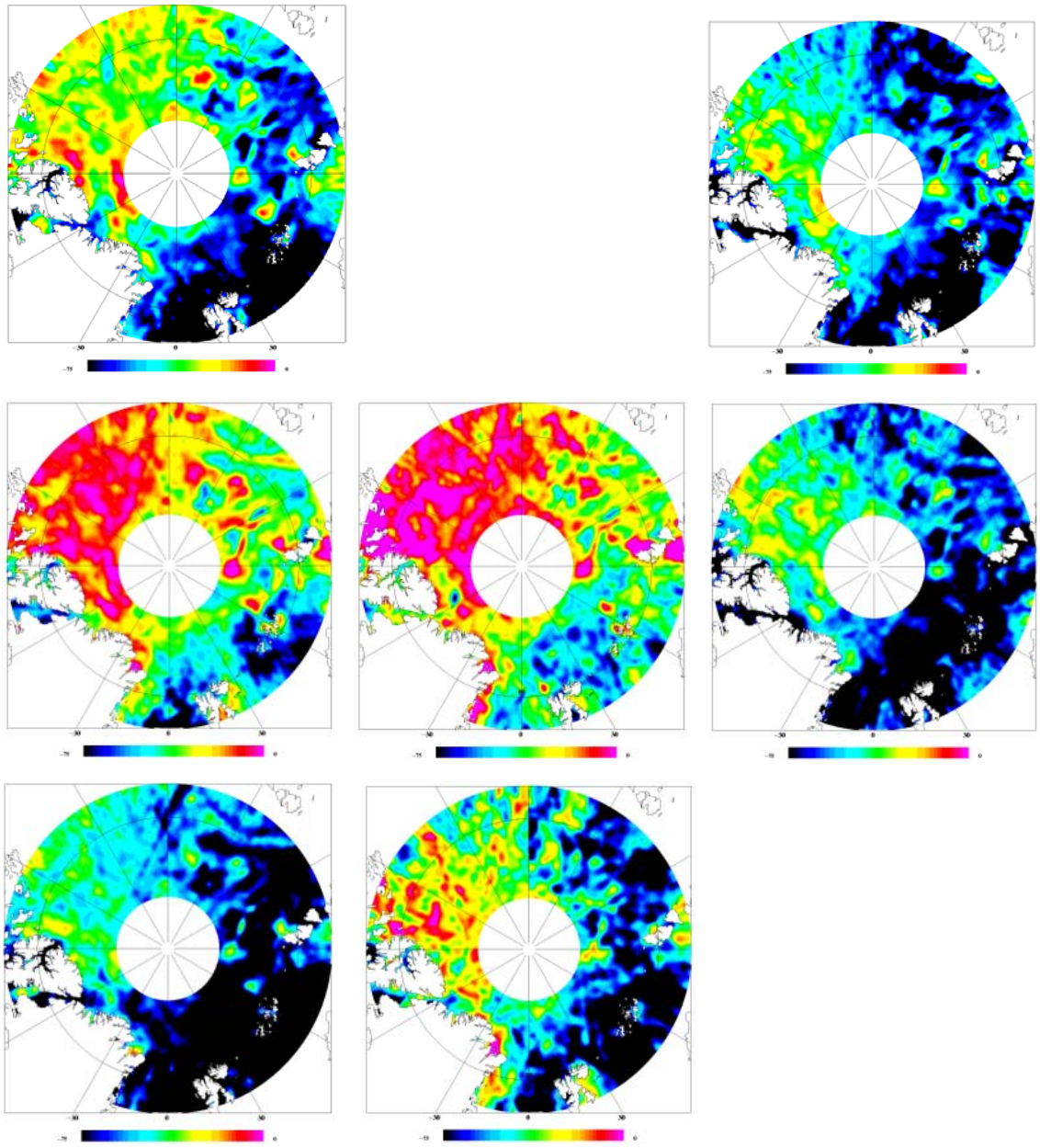

Fig. 2.11: MSS minus ArcGP geoid for the 7 analyzed ICESat epochs. Top row: 2003, middle row: 2004 and bottom row: 2005. Left: March, June and November (precise periods shown in Table 1.1)

Because of the apparent biases, it will be necessary in some way to fit the ICESat data to the ERS MSS. A composite MSS of the entire Arctic Ocean was constructed in the following way:

The ERS MSS, spanning the period 1995-2003, was used as a reference, and then the ICESat average MSS for the seven epochs 2003-5 was averaged and "draped" upon the ERS MSS. Finally the "hole" in the Arctic Ocean north of 86°N was filled with the new ArcGP geoid. The "draping" technique is essentially a collocation approach, where the difference

$$\varepsilon = SSH_{ERS} - SSH_{ICESat} \tag{32}$$

is modeled by a bias and a random function

$$\varepsilon = h_0 + s \tag{33}$$

where s is modeled by least-squares collocation, using a 2nd order Markov covariance function

$$s = C_{sx}C_{xx}^{-1}\underline{x} \tag{34}$$

Here $\underline{x}$ is a vector of observed difference values (typically differences at the overlap band). We used here a 2.5° overlap band, with differences as shown in Figure 2.12 for Laser 3B (March 2005). A correlation length of 30 km, and 25 cm a priori errors was used for ICESat/ERS, and 60 km / 20 cm for draping the ArcGP geoid across the polar gap.

The relatively large standard deviation of the ICESat-ERS overlap band is likely mainly due some relatively large differences along the coasts, but there also seem to be a more systematic tilt with lower values in the Eurasian basin compared to the Amerasian basin.

Figure 2.13 shows the MSS-geoid with and without the ICESat draping, and Figure 2.14 shows the final composite MSS. It is clear that this MSS is not consistent, in that it uses different averaging periods for ERS and ICESat; but it is probably the best, which can be done at present, as long as no more ICESat data are available.

The composite Arctic MSS will be the basic surface in the sequel, and used to compare the different MDT models.

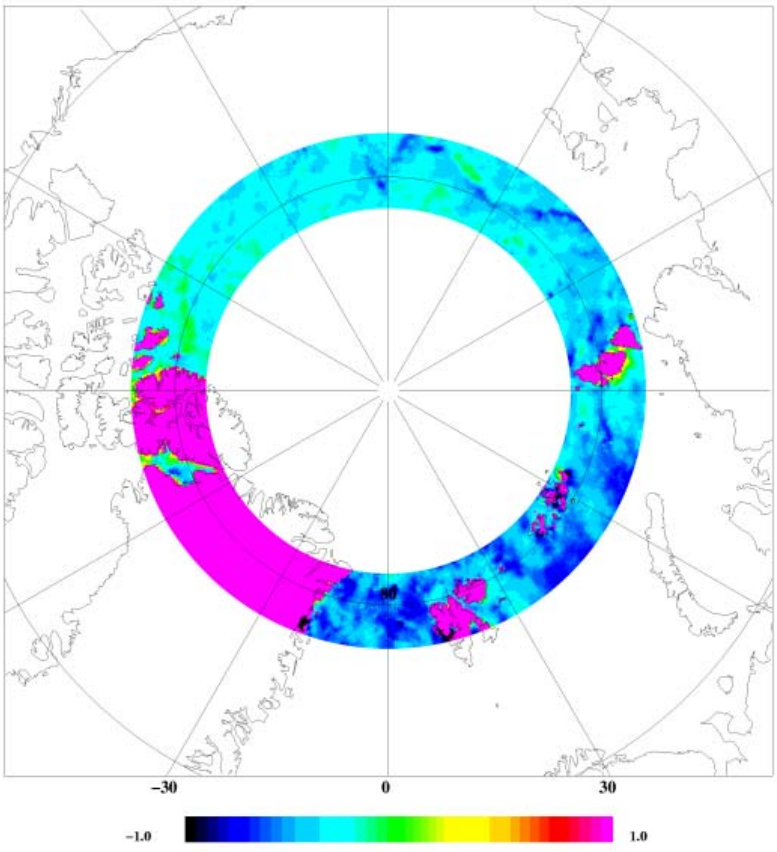

Fig. 2.12: Difference between ICESat (March 2005) and ERS for the overlap band 79-81.5 °N.

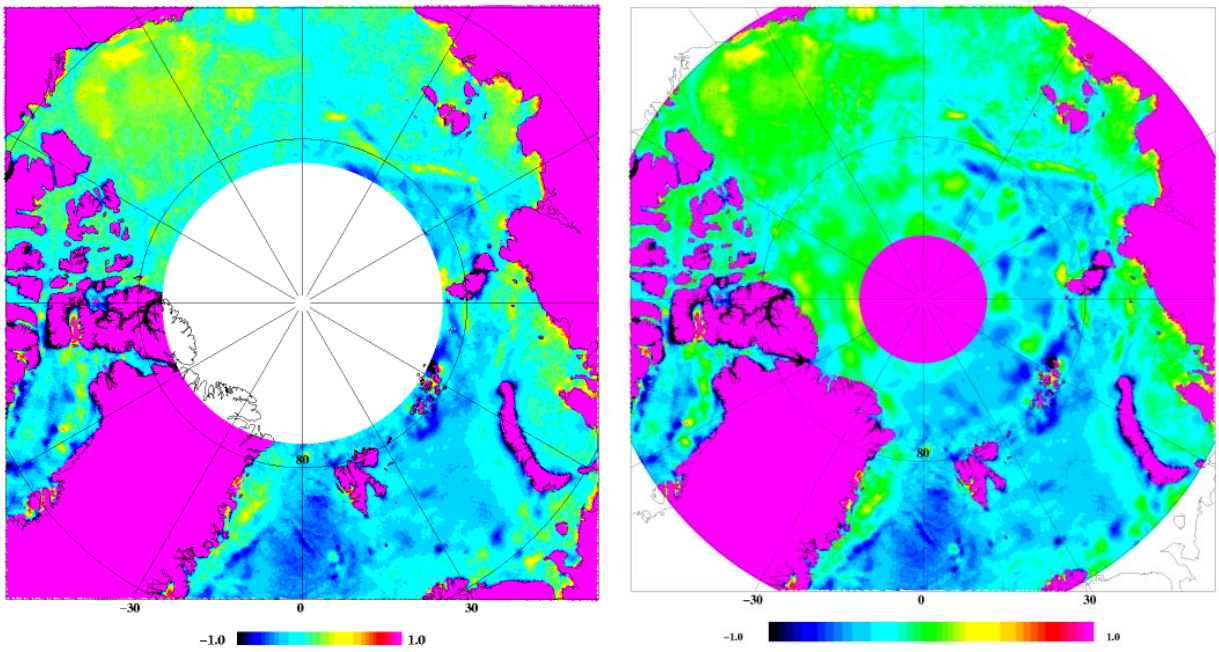

Fig. 2.13: ERS MSS – geoid (left) and draped ERS+ISESat minus geoid (right). Unit m.

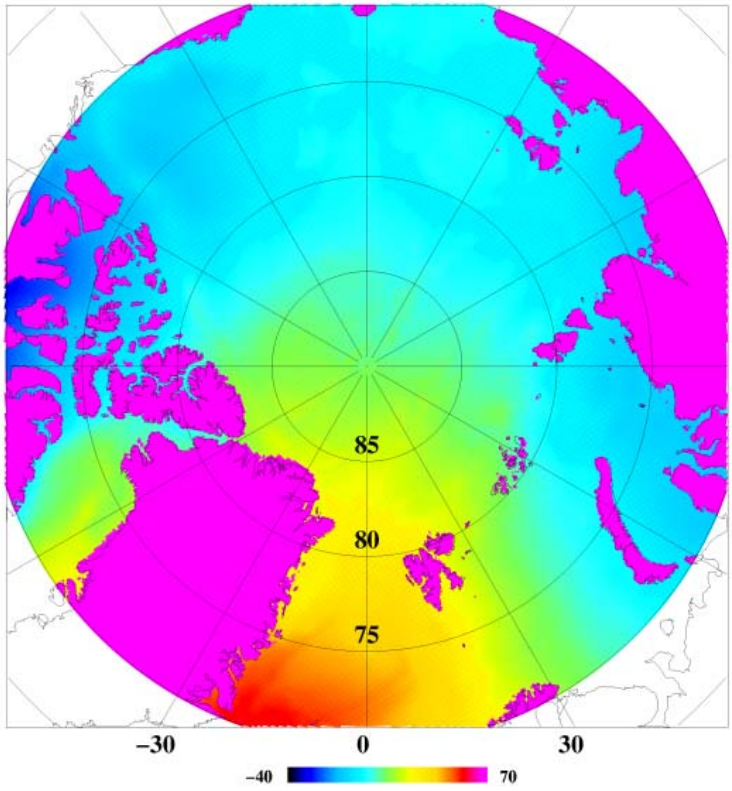

Fig. 2.14: Composite MSS from ERS and ICESat, with ArcGP draped in around the north pole. Unit m.

3 Mean Dynamic Topography and Tides

3.1 Temporal variability of the Dynamic Topography in the Arctic Ocean; results from the MICOM global hindcast integration

The Dynamic Topography (DT) for the Arctic region is extracted from a free run hindcast simulation of a global version of the Miami Isopycnic Coordinate Ocean Model (MICOM, see Bleck et al. 1992). Detailed description of the model components and the set-up is given in Gao et al. 2005 and references therein.

In the horizontal, a local orthogonal grid system with one pole over North America and one pole over western part of Asia was adopted (Bentsen et al. 1999). The horizontal grid scale varies between 25 and 100 km, with approximately 40 km resolution for the Arctic region.

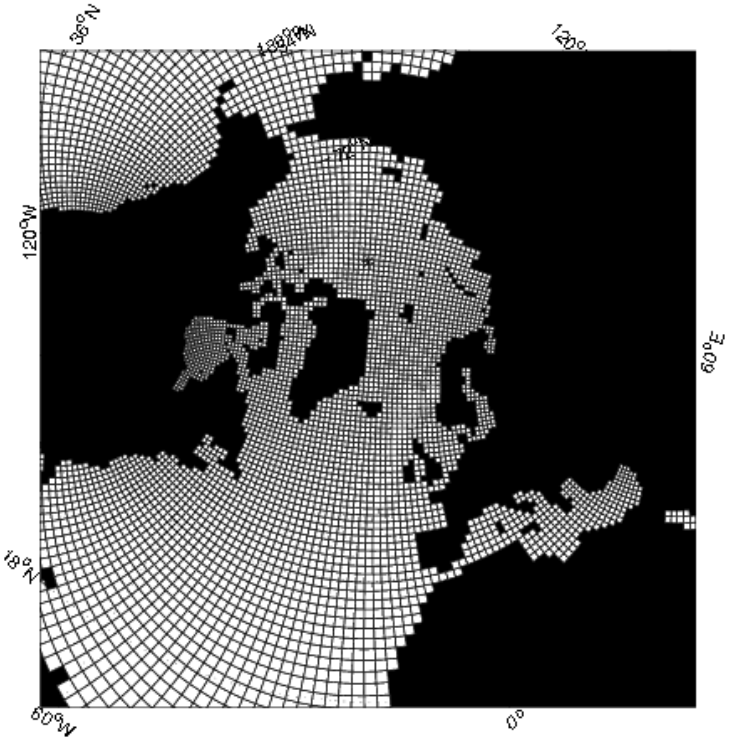

Fig. 3.1: MICOM grid configuration. The model run was performed with doubled resolution in both dimensions. Each displayed cell contains four cells of the model grid.

The DT from MICOM is interpolated to a 0.25° × 0.5° grid for the region 64°N-90°N, 180°W - 180°E. The method used for the interpolation is a weighted average of neighbouring points with the weights given as linear function of the distance to the target point, see Figure 3.1.

In detail the method is as follows:

For the target point (λ_0,φ_0) a neighbourhood is defined by all points (λ_i,φ_i) in a maximum distance of d_{max} from (λ_0,φ_0) with distances $d_1 \le d_2 \le \ldots \le d_n$ and according DTs $\zeta_1,\zeta_2,\ldots,\zeta_n$. The nearest n_{max} points (or all, if $n < n_{max}$) are weighted depending on their distance d_i from the target point as

$$w_i = \frac{d_{\max} - d_i}{\sum_{j=1}^{\min\{n,9\}} d_{\max} - d_j}, \text{ with } \sum_{i=1}^{\min\{n,9\}} w_i = 1 \tag{35}$$

so that the interpolated DT gets to

$$\varsigma_0 = \sum_{i=1}^{\min\{n,n_{\max}\}} w_i \varsigma_i \tag{36}$$

The parameters d_{max} and n_{max} are chosen as 60 km and 9, respectively.

Interannual to decadal variability for the period 1992-2003

A general description of the variability in Dynamic Topography (DT) on inter-annual timescales results from an analysis of annual mean fields for the years 1948 to 2005. For the Arctic Mediterranean north of 64°N four regions with high variability of 10 cm and more emerge (Figure 3.2).

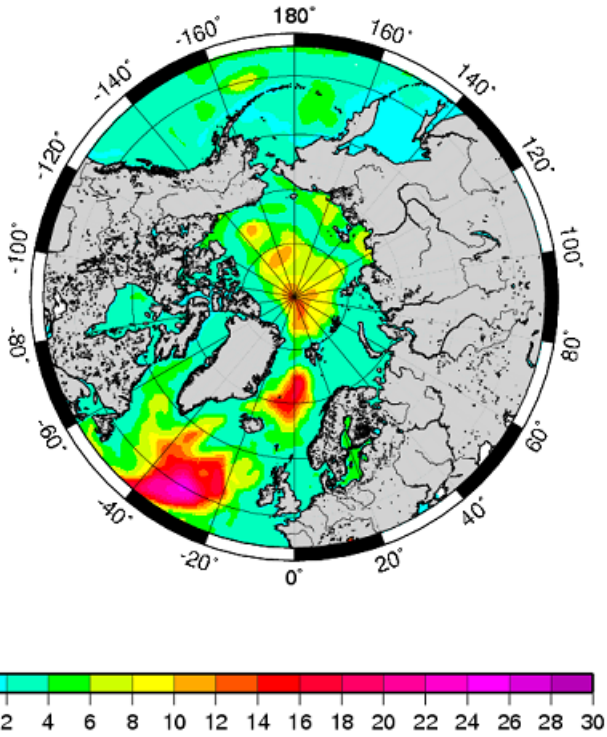

Fig. 3.2: Standard deviation of annual mean Dynamic Topography from MICOM global hindcast simulation for the period 1948 to 2005, in cm. The dynamic topography itself is shown in Section 3.3.

The highest variability is found in central parts of the Nordic Seas with core values exceeding 15 cm. The other three regions are located in the Arctic Ocean. North of 80°N, where the variability is generally high, two centres are prominent: One in the Amundsen Basin (~12 cm) and one with slightly smaller amplitude in the northern Canada Basin. In addition in a comparatively small area in the centre of the Canada Basin variability also reaches 10 cm.

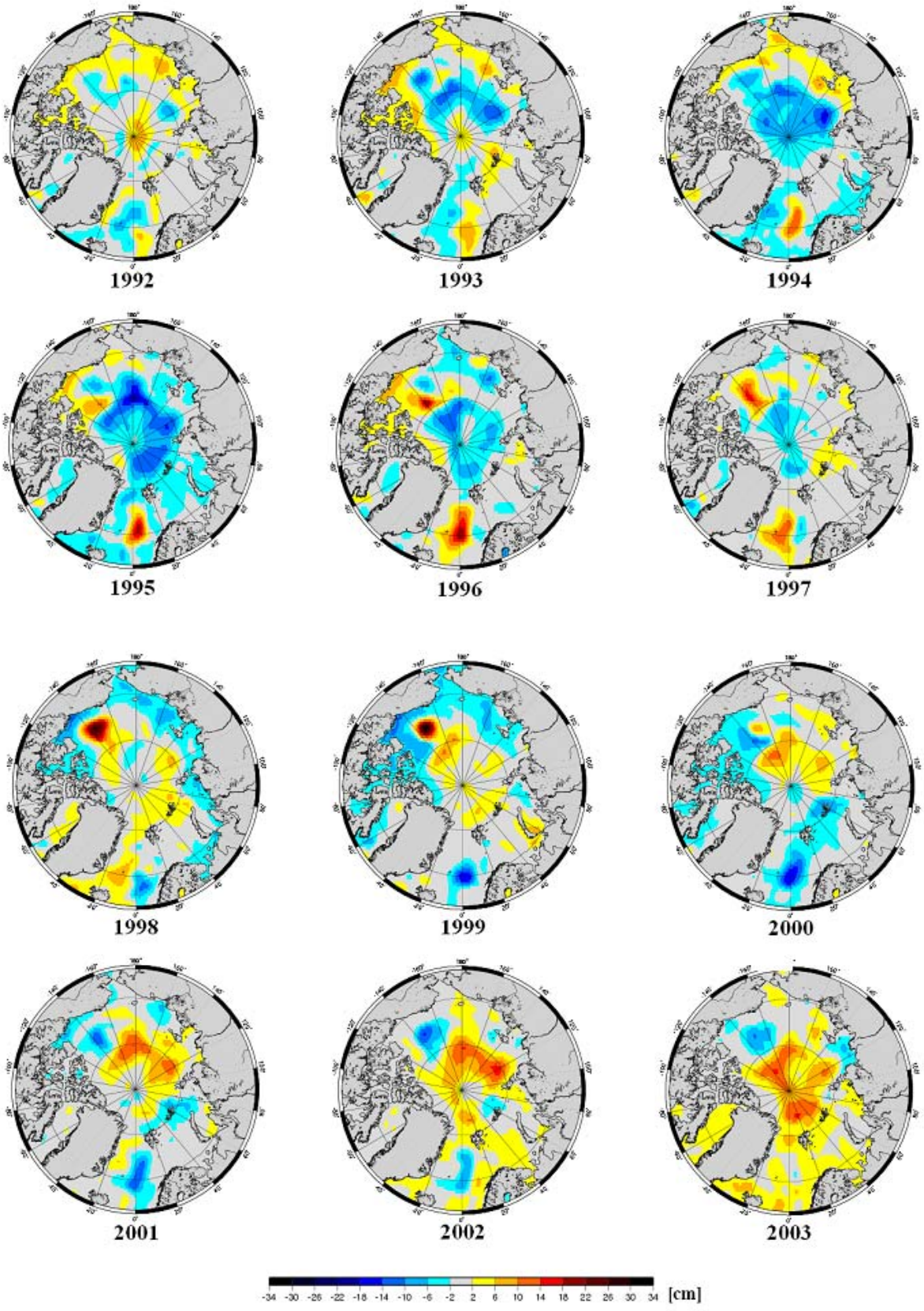

Fig. 3.3: Annual mean anomaly in Dynamic Topography relative to the reference period 1992-2003. Unit cm.

Figure 3.3 displays the annual mean anomaly DT for the years 1992 to 2003 as compared to the mean DT for the whole period. The areas with strong inter-annual to decadal variability in the period 1992 to 2003 coincide largely with the areas of strong variability in the annual mean DT indicated in the last section.

In the central Nordic Seas a roughly ten years cycle is found with increasing DT until 1995/ 1996 and decreasing values until year 2000. After that the DT increased to average values in 2003. The peak to peak difference in DT exceeds 30 cm east of Jan Mayen Island.

The deep Basins of the Arctic Ocean despite the southern part of the Canada Basin show a long term variability starting with average values in 1992 to low values in 1994 and 1995 highest values in 2002 and 2003. The 8 years increasing trend from 1995 to 2003 accounts overall roughly to 20 cm, reaching 30 cm in some areas. In the central Canada Basin the most prominent feature is a very strong positive anomaly found in 1998 and 1999 reaching 30 cm in 1999 while in the rest of the 12 years period mainly a negative anomaly is found.

Monthly variability for the period 2003-2004

Part of the variability found in the monthly mean DT is explained by a seasonal signal. The MICOM hindcast simulation for the full integration period from 1948 to 2005 is used to calculate a mean seasonal cycle. From this it emerges that the amplitude of the seasonal cycle values below 2 cm for roughly half the area north of 64°N and does not exceed 10 cm despite east of New Siberian Islands in the East Siberian Sea (see Figure 3.4).

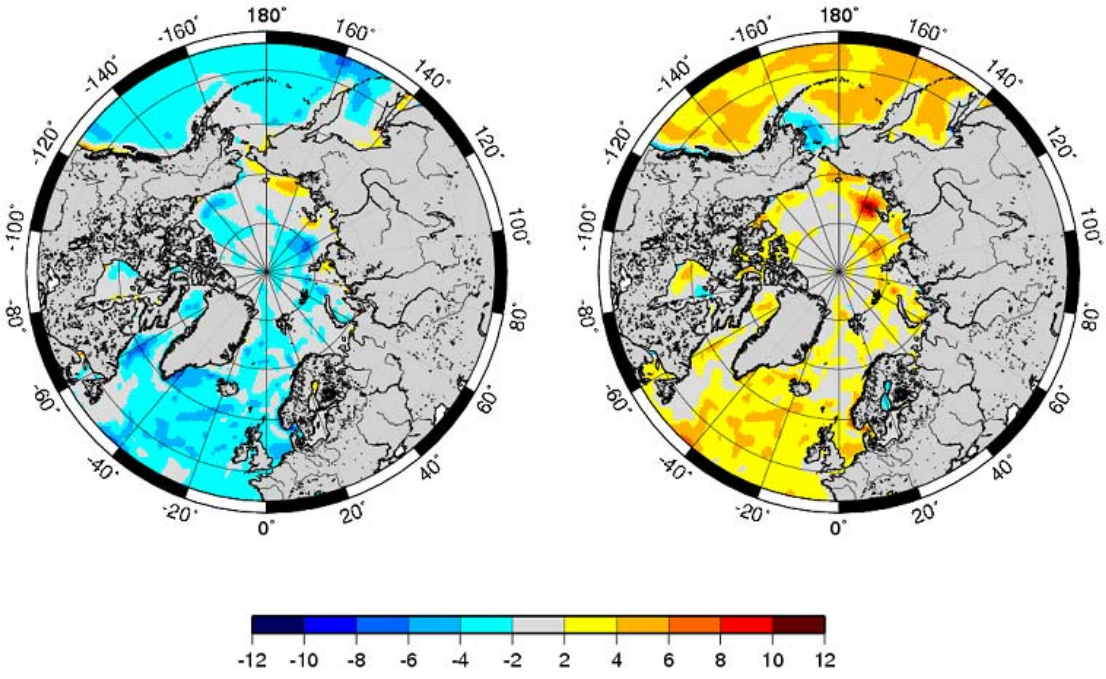

Fig. 3.4: Mean anomaly in Dynamic Topography for March (left) and September (right) compared to the mean field for the period 1948-2005 from MICOM global hindcast simulation.

In general the monthly variability exceeds essentially the mean seasonal cycle for most part of the area (see Figure 3.5).

The most striking feature is the high variability on the Siberian Shelf. High values are found from July to September 2003 and again in December 2004. Low values are found in April and May 2004. Values are in the order of 15 cm exceeding 20 cm in the parts of the East Siberian Shelf.

For the Canada Basin DT is generally low from April 2003 to May 2004 and high afterwards with roughly 20 cm between minimum and maximum values. No strong changes/ fluctuations are found in the Eurasian Basin. A positive signal builds up at North Pole starting February 2004, reaches about 20 cm in magnitude in June 2004. A signal is shifted successively from month to month and is seen as distinct feature until September 2004 found south of Alpha and Mendeleyev Ridges at the northern rim of the Canada Basin.

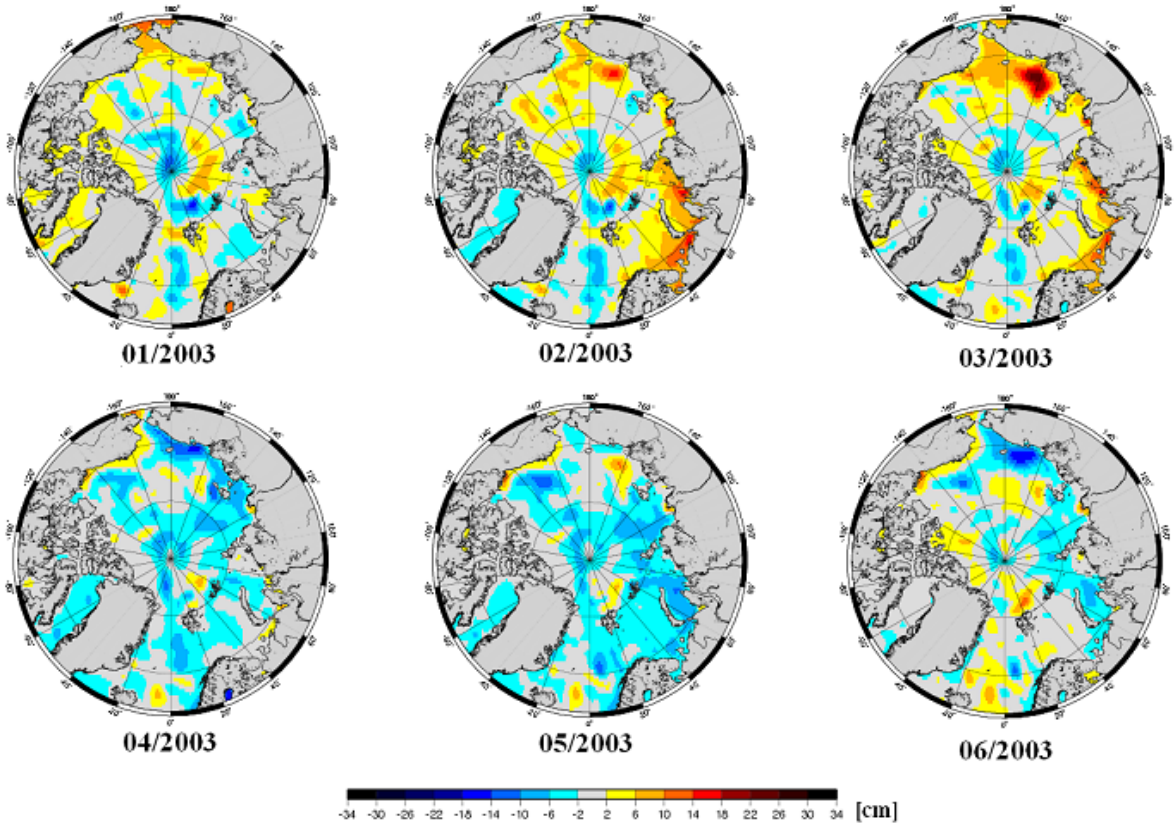

Fig. 3.5a: Monthly mean anomaly in Dynamic Topography relative to the reference period 2003-2004 for the months January to June 2003.

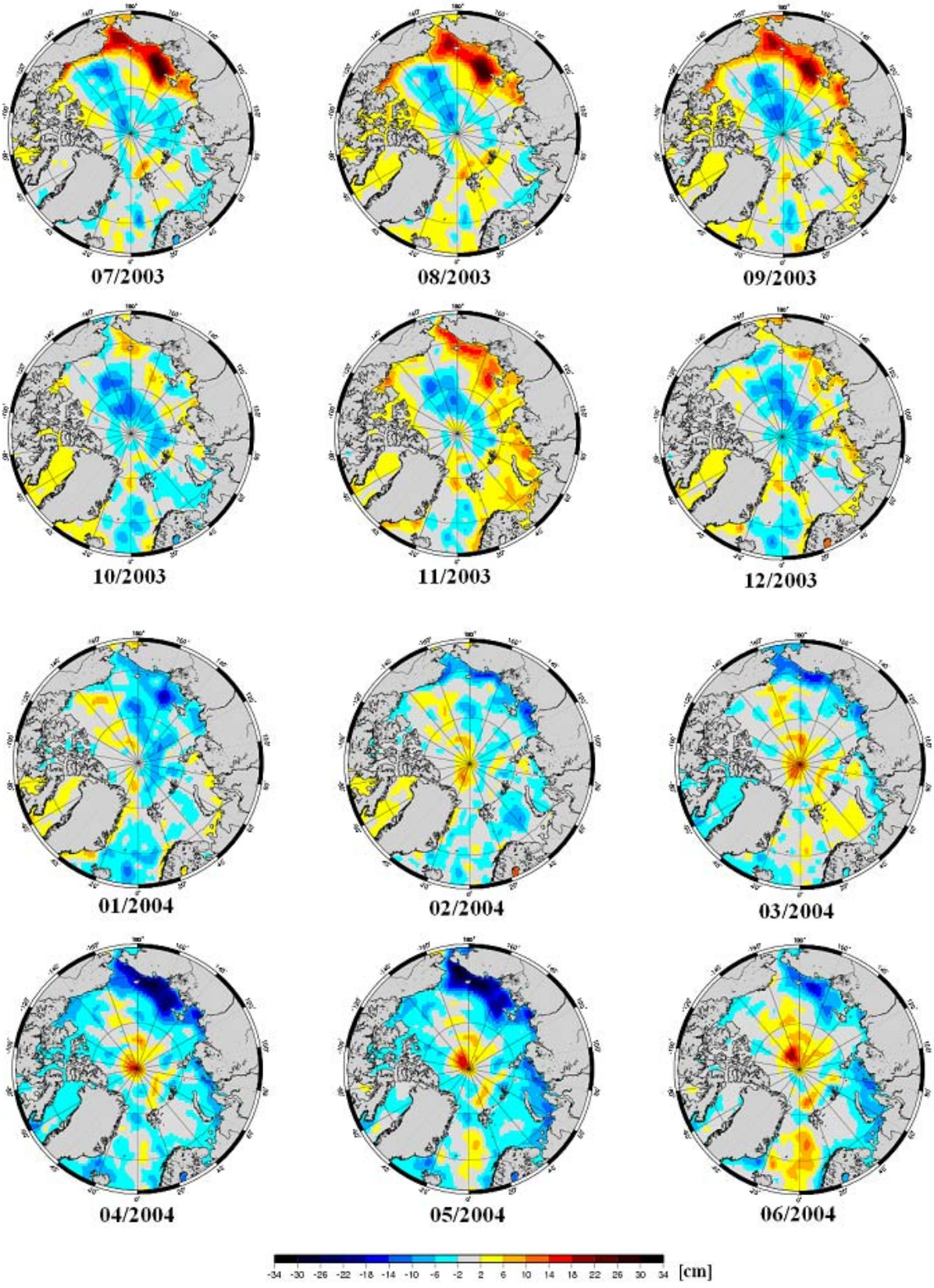

Fig. 3.5b: Continuation of Figure 3.5a for the months January to June 2004.

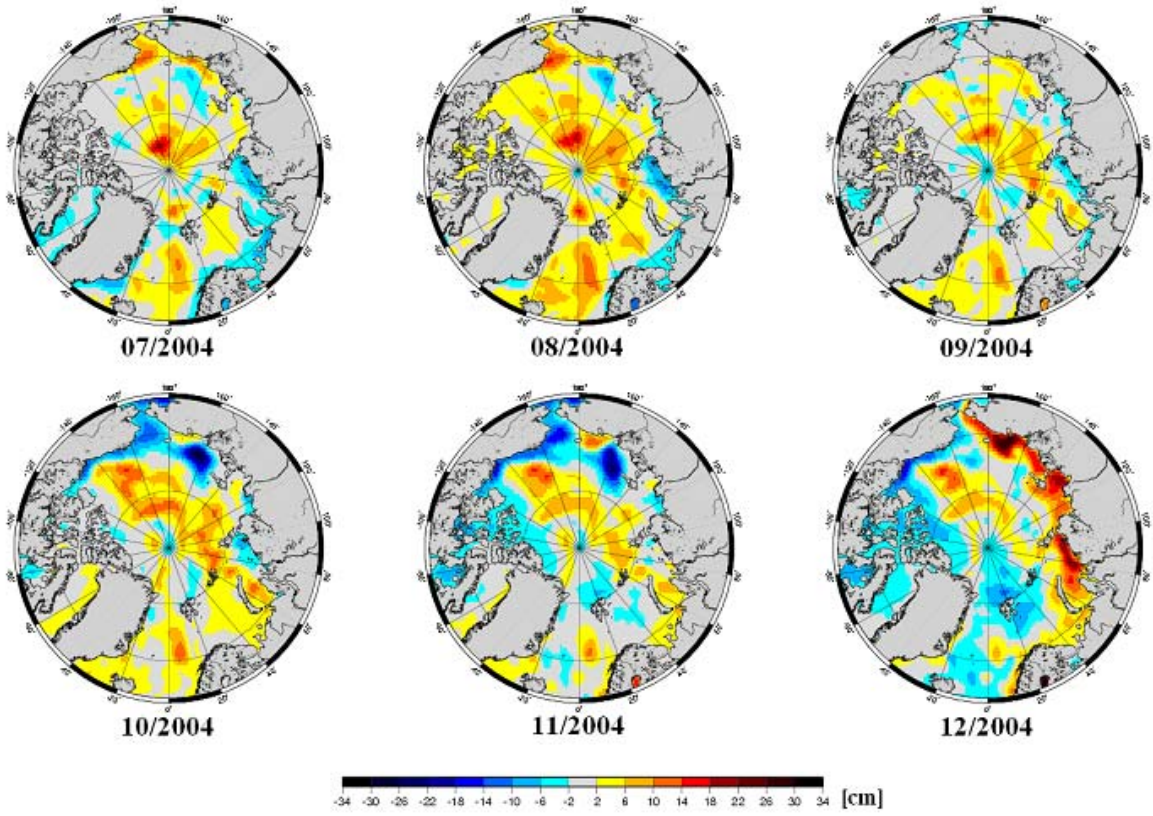

Fig. 3.5c: Continuation of Figure 3.5a for the months July to Dec 2004.

3.2 Recommendation of time/mean averaging

Running MICOM with a resolution of 2.4° x $\cos\theta$ (~50 km for θ = 80°N) and NCEP forcing the monthly dynamic topographies (DT) for the years 1992-2005 have been produced. From these fields the temporal and spatial characteristics are examined. It should be stated that the model resolution is not sufficient to resolve sub-basin structures at scales of less than 200-300 km.

Spatial variability

The spatial variability of the mean dynamic topography (MDT) structure is manifesting the large-scale pattern of the circulation on the Northeast Atlantic, the Nordic Seas and Arctic Ocean. In particular, there is roughly a 1 m difference between the minimum in MDT located south of Greenland connected with the recirculation branch of the North Atlantic Current and the distinct maxima located in the Canada Basin, along the northern shore of Canada and the Bering Strait.

Seasonal variability

The DT is generally highest in September – as expected – with an overall minimum in sea ice extent and correspondingly largest upper ocean absorption of short wave radiation in late fall. In contrast the lowest DT is found in March in result to maximum sea ice cover and thus larger albedo.

There is an order of magnitude reduction in the seasonal DT changes compared to the spatial variability in MDT. In terms of the seasonal variability changes along the Beaufort Sea are found with differences reaching up to 15 cm between September and March. In comparison the seasonal differences in the Nordic Seas and Arctic Basin respectively range between 5-10 cm and < 5 cm, both maintaining the same phase as for the Beaufort Sea. The northern Chukchi Sea and Siberian Shelf express a seasonal signal in DT of 15-20 cm. However, in contrast to the other regions, the highest DT is encountered in December and the minimum in April/May.

Interannual variability

The standard deviation of the annual DTs from 1992-2005 can be summarized as follows:

- Low variability between 1 to 3 cm in the Nordic Seas;
- Generally higher variability in the Arctic Ocean, in particular in the Canada Basin (9 cm), Nansen Basin (7 cm) and east of Severnaya Zemlia (7 cm).

During the 13 years time period from 1992-2005 the changes in the annual mean DT seem to be mostly manifested as a trend at the decadal time scale. For instance, at a scale of about 500 – 1,000 km in the Canada Basin the changes in annual mean DT reaches up to 30 cm from a minimum of -10 cm in 1996 to a maximum of + 20 cm in 2004.

This rise is not representing a general interannual change in the Arctic MDT, but is rather connected to an upstream regime shift in the circulation pattern and hydrology of the sub-polar gyre that took place in 1995/1996. In comparison the interannual changes between 1992-1996 and after 2004 are rather small with no trend.

In summary we conclude that on the 500 – 1,000 km spatial scale the Arctic Ocean inter-annual changes in MDT can undergo abrupt changes, from one regime to another, that results from significant shifts in the large-scale circulation pattern. It is therefore highly necessary to pay close attention to such shifts when the averaging period for the MDT is determined.

Based on the present knowledge of the circulation and hydrography of the northern North Atlantic, the Nordic Seas and the Arctic Ocean, the prime candidate for regime shifts are circulation changes in the North Atlantic Subpolar Gyre. These changes are then advected northward, occurring in the Arctic Ocean after 3-4 years. In the future, with gradually reduced sea ice extent caused by a warmer climate, it could be that regime shifts could also be triggered within the Arctic Ocean associated with abrupt reduction in the extent of sea ice (when passing the so-called “tipping-point”).

3.3 Additional MDT models: OCCAM, PIPS and UW

To provide additional data on MDT, and especially to get an qualitative estimate of differences between different models, three coupled ice-ocean models have been acquired; These models include Ocean Circulation and Climate Advanced Modeling Project (OCCAM) from the UK oceanographic center in Southampton, Polar Ice Prediction System (PIPS) from the US Naval Postgraduate School (NPS, W. Maslowski), and a model developed by the University of Washington here addressed as UW (Steele et al. 2004, and Morison et al. 2006). The different models all have very different resolutions and forcing fields, with PIPS being a high resolution 9 km eddy-resolving model, whereas MICOM, OCCAM and UW are lower resolution models at an average resolution around 40 km.

For OCCAM the original rotated lat/lon grid has been maintained, and data have been gridded directly. We use yearly averages covering 1995-1999 in this section, as well as monthly snapshots, March and October (from an old version in Section 3.5). MICOM MDT fields were provided as yearly averages 1995-2003. Similarly PIPS were provided as yearly samples from 1995 to 2003, but only as averages from March each year. PIPS also include data from October 2003, to show interannual variations. From University of Washington we received a MDT grid representing the period 1955-2006, as well as March and October 2003-2006.

Yearly samples of OCCAM, MICOM and PIPS MDT are shown in Figure 3.6, 3.7 and 3.8, respectively. The PIPS MDT is based on data from March only, and an example of seasonal variations (March and October, 2003) is plotted in Figure 3.10 (top). The UW MDT 1955-2006 is shown in Figure 3.9, and Figure 3.10 (bottom) illustrates MDT from March and October 2003 to show seasonal variability. The models have different reference levels, but the scales are given within the same interval (50 cm) of the various models.

It is seen that the main features of the MDT appears to be relatively stable during the decade, and only OCCAM show a weakening (~20 cm from 1995-1999) in the high North of Greenland and Canada. OCCAM, PIPS and UW seem to be pretty similar in the features with higher values along the coasts north of Greenland, Canada and eastern part of Siberia, but with a more distinctive Beaufort Gyre in UW also present in the last years of OCCAM. MICOM is dominated by a strong signal from the Beaufort Gyre in the Canadian Basin. Fram Strait and fresh water from the Bering Strait.

Table 3.1: Description of the different MDT models.

MDT Model	Resolution in Arctic	Atmospheric Forcing
MICOM	40 km	NCEP/NCAR
OCCAM	¼ x ¼ deg	ECMWF
PIPS	9 km	NOGAPS
UW	40 km	NCEP/NCAR

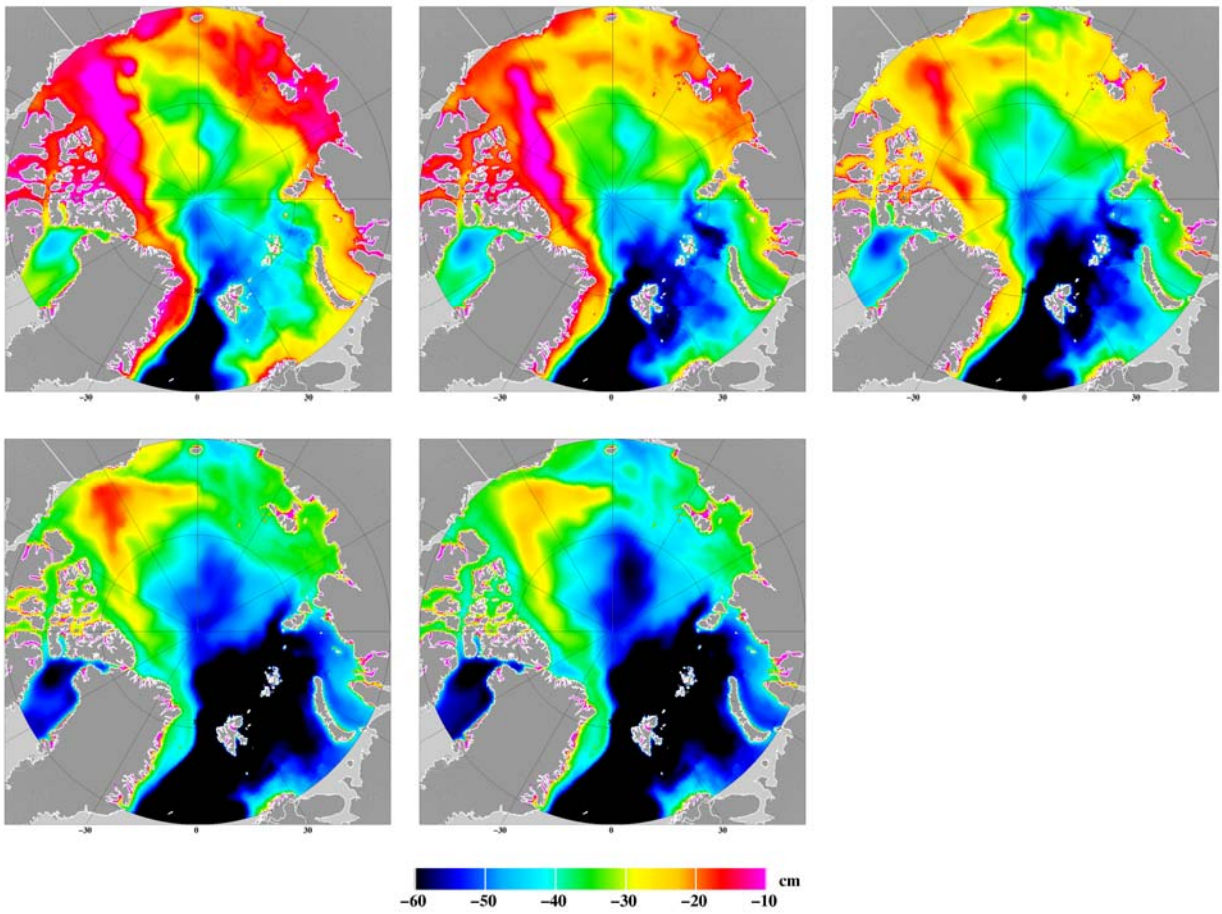

Fig. 3.6: Yearly averages of MDT from the OCCAM model 1995-1999, updated OCCAM version received February 2007

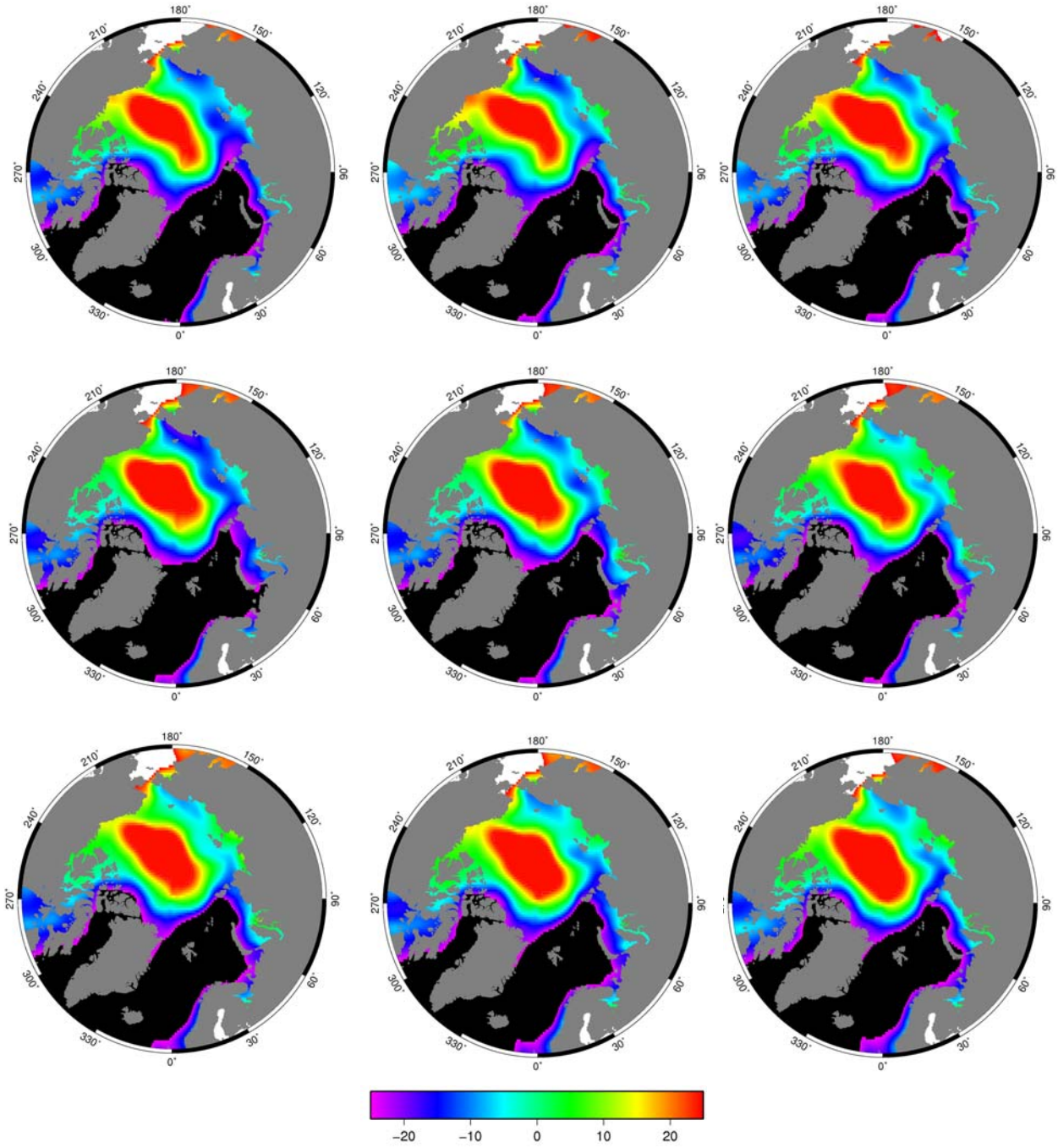

Fig. 3.7: Yearly averages of MDT from MICOM 1995-2003, in the same colour scheme as Figure 3.5. Unit cm

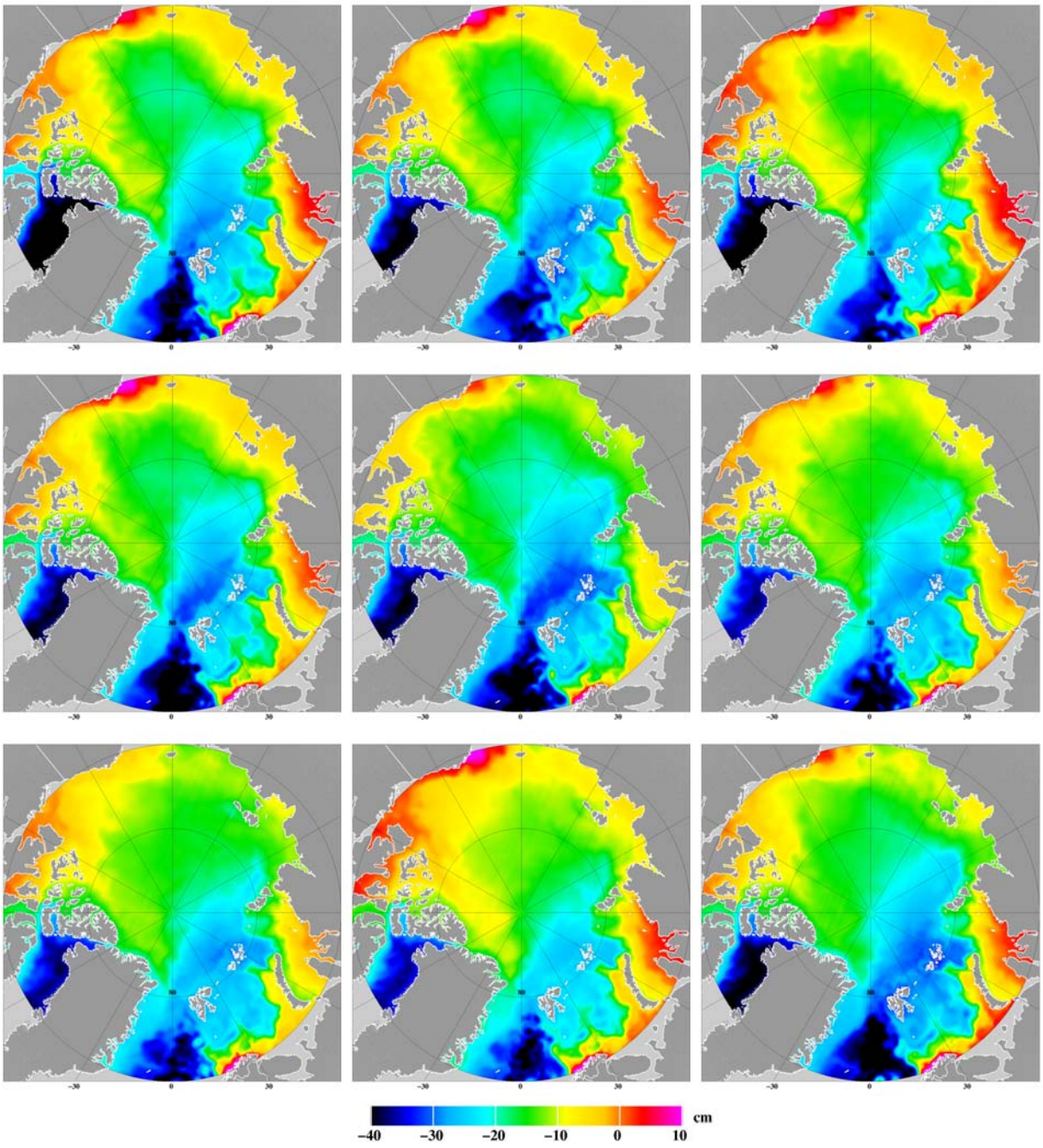

Fig. 3.8: Yearly MDT from PIPS 1995-2003 (every March), in the same color coding scheme as Figure 3.5.

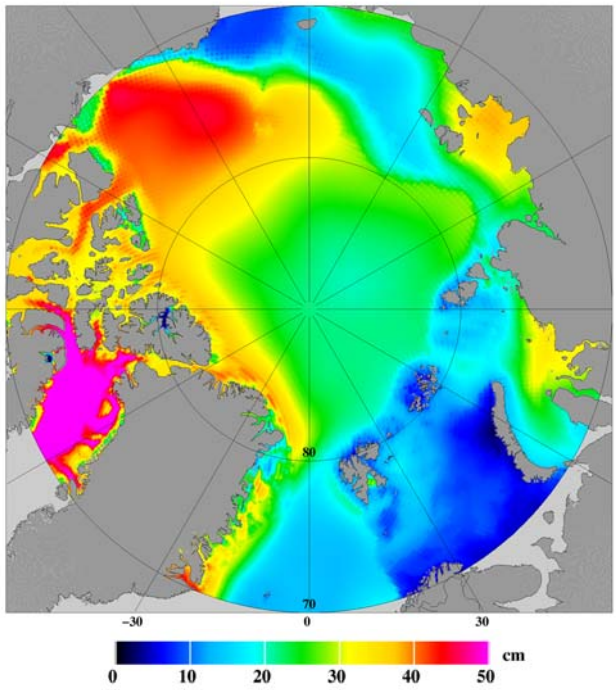

Fig. 3.9: Averaged DT from UW 1955 - 2006. Same colour range as Fig. 3.5.

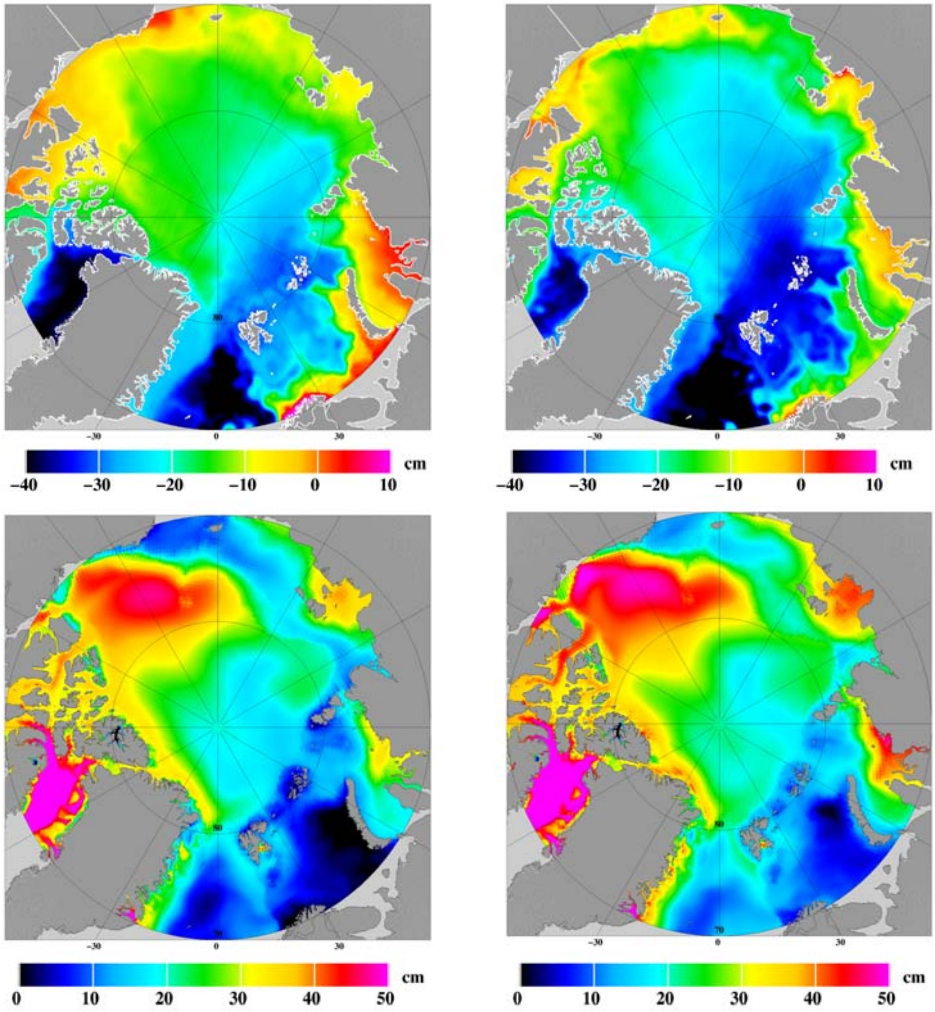

Fig. 3.10: Top: MDT from PIPS, and bottom MDT from UW for 2003 (left: March, right: October). A large seasonal change is apparent in both models.

3.4 Assessment of Arctic Ocean Tide Models

In order to correct ICESat and later CryoSat observations for the instantaneous ocean tides and loading, a number of tide models have been compared to assess their accuracy and discrepancies in different areas of the Arctic Ocean. The tide models analyzed include the global tide models CSR 4.0, GOT00.2, and AOTIM-5.

The individual tide model predictions are derived for every footprint (same time epoch and location) for three ICESat mission periods, a) September-November 2003, b) February-March, 2004, and c) September-November 2005. The results are expressed in terms of differences between different models for one particular time period in order to identify the spatial and temporal variations. Additionally the effect of sea ice on tides has been investigated by comparing the tide models with tide gauge records, altimetry data and sea ice concentrations obtained from SSM/I passive microwave sensor.

Introduction

In order to model and monitor the sea surface in the Arctic Ocean, the accurate prediction of the ocean tide signal is required. Specifically, this study requires amplitudes of ocean tides for the estimation of the mean sea surface and sea ice freeboard height. The term tide is used in two ways, “tide” describes the vertical movement of the sea surface due to astronomical forces, and “tidal currents” describe the accompanying horizontal movements of the ocean water. Here, the focus lies on the vertical “tide” and tidal currents are neglected due to their less relevant impact on our study and the less accurate prediction in areas with insufficiently mapped bathymetry.

Ocean tides can be obtained from a harmonic analysis of tide gauge records. Ocean tide models can be separated into two classes, i) hydrodynamic models, and ii) observation models. While the first class uses hydrodynamic equations and the knowledge of astronomical tide generating forces, the latter assimilates observations of the instantaneous sea surface for the estimation of ocean tide parameters. Today, most ocean tide models are hybrid models using both approaches to improve the model. Observations which can be assimilated in tide models predominantly come from satellite altimetry and tide gauges. While the first sensor provides nearly global and homogeneous spatial sampling, but low temporal sampling, tide gauges have a high temporal, but low spatial sampling. A combination of the two observation types are preferable, but involve certain limitations. These arise from the fact that tide gauges are located at the coast, and altimetry is prone to errors near the coast, e.g. within a perimeter of about 20-40 km from the coastline. Consequently, both data sets cannot be simply compared and validated. In addition, tidal currents (e.g. Kelvin waves) predominantly occur near the coast and in shallow waters where altimetry does not observe with high accuracy.

However, the primary objective, of the ArcGICE tidal study is to identify the best ocean tide model over open ocean. The best altimetry data set assimilated in ocean tide models come from the Topex/Poseidon mission launched in 1992. Due to the sun-synchronous orbit of ERS-1/2 and ENVISAT, their contribution is rather limited, since estimation of tidal solar components will be biased. None of the radar altimetry mission provide any coverage north of 81°N.

Another major concern arises from the fact that the Arctic Ocean is sea ice covered most of the year. Sea ice cover changes the dynamics of ocean tides and currents and has a damping effect on the ocean tide amplitudes. It can also lead to a phase lag of cotidal lines. Hence, the amphidromic system will change if sea ice is present.

The currently available global and regional ocean tide models (e.g. CSR, NAO, GOT, TOPX, AOTIM-5 etc.) do not assimilate altimetry data over sea ice. These models further do not consider tide-ice interaction such as friction (King and Padman, 2005). Consequently, Arctic Ocean tide models rely mainly on the available tide gauge records. As tide- sea ice interaction is important to consider in the Arctic ocean, a number of analyses were designed. The following questions are important for the assessment of Arctic ocean tide models:

- Does sea ice impact the amplitude and phase of ocean tides?
- Do tide gauge records and altimetry records agree?
- Do tide gauge records and ocean models in the Arctic agree?
- How do sea ice observations correlate with ocean tide observations from tide gauges and models?
- Is it possible to define a sea ice flag to account for the sea ice impact on ocean tides?

To quantify the tidal effects and their spatio-temporal resolution, we have focused on the Canadian arctic. The following datasets were collected and used in this study.

Tide Gauge Records (TGR):

TGR for 9 tide gauge stations in Canada were obtained from the Marine Environmental Data Services (MEDS) and the Joint Archive for Sea Level (JASL). The station names, their location and record lengths are listed in Table 3.2 and shown in Figure 3.11.

Table 3.2: Tide-gauge stations and data availability.

Station Name	Latitude	Longitude	Record Length
Prudhoe	70.40000	211.47333	Jul 1, 1993 - Oct 31, 2004
Churchill	58.76667	265.81667	Jan 1, 1940 - Dec 31, 2005
Alert	82.49186	297.68267	Nov 1, 1961 - Jul 31, 1979
Tuktoyaktuk	69.43826	227.00560	Nov 1, 1961 - Sep 30, 1991
Resolute	74.68333	265.11667	Nov 1, 1961 - May 31, 1977
Cambridge Bay	69.11667	254.93333	Nov 1, 1961 - Aug 31, 1981
Cape Parry	70.15000	235.33333	Aug 1, 1966 - Jul 31, 1981
Sachs Harbour	71.96667	234.75000	Sep 1, 1971 - Jul 31, 1982
Cornwallis	75.38333	236.05000	Nov 1, 1986 – Sep 30, 1994

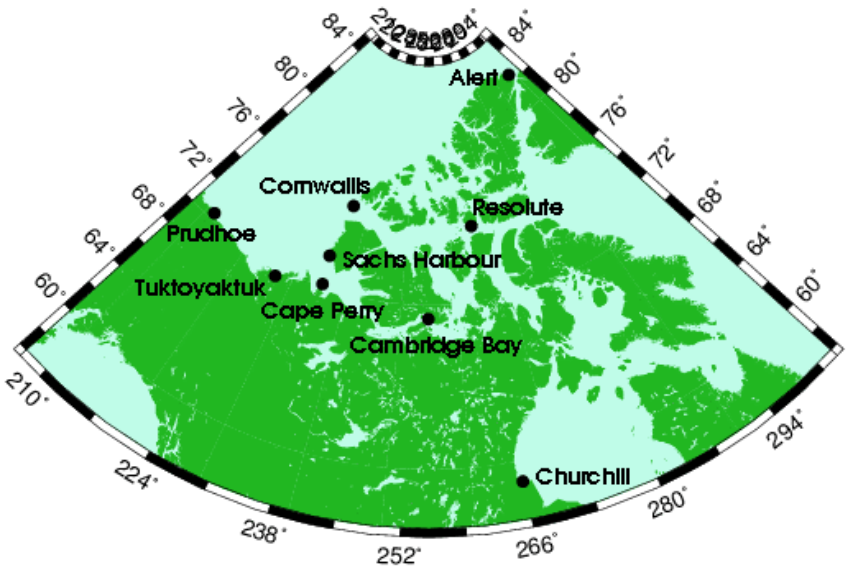

Fig. 3.11: Locations of Canadian tide-gauge stations used in this study.

Tide Models:

Ocean tide models that are evaluated in this study are CSR 4.0, GOT 00.2, TPXO6.2, AOTIM-5. The tidal predictions have been made with different software modules and depend on the particular realization. The differences, however, which are introduced by this fact do not exceed 1 centimeter.

CSR 4.0: The Center for Space Research global ocean tide model (CSR 4.0) was developed by Richard Eanes, at the University of Texas. It is an updated version of CSR 3.0 (Eanes, 1995) which was basically a long-wavelength adjustment of the FES94.1 (Le Provost et al., 1998) and AG95.1 (Anderson, 1995) models. CSR 4.0 is an empirical model obtained from the assimilation of 6.4 years of TOPEX/Poseidon (T/P) altimetry data with CSR 3.0 as the reference model. The corrections to the CSR 3.0 orthoweights (in 2 x 3 degree spatial bins) were computed using the T/P altimetry data. These corrections were smoothed by a convolution with a two-dimensional Gaussian for which the full-width-half-maximum was 2.3 degrees. CSR 4.0 follows the FES94.1 model beyond ± 66 latitude (as this is the cutoff for T/P data). Using the tidal orthoweights, tides can be synthesized for a particular latitude, longitude and time.

GOT00.2: The Goddard/Grenoble Ocean Tide Model (GOT00.2), an updated version of GOT99.2 model (Ray, 1999), was developed by Richard Ray at the Goddard Space Flight Center, NASA. It is a long wavelength adjustment of FES94.1 using 6 years of altimetry data and hydrodynamic models in shallow and polar seas. Since, T/P and ERS data (although not under ice shelf regions) were used in the assimilation process, it is likely improved compared to CSR 4.0 in polar regions above ± 66 degree latitude. The resolution of this model is 0.5 by 0.5 degrees. More details about the model development and comparisons of the model with tide gauge records can be found in Ray, 1999.

TPXO6.2: The TOPEX/Poseidon crossover solution version 6.2 (TPXO6.2) is a medium-resolution, $1/4^{o}$ x $1/4^{o}$ fully global assimilation model developed by Egbert and Erofeeva, 2002, at Oregon State University. It is a global model which best-fits, in a least-squares sense,

the Laplace Tidal Equations and along track averaged data from T/P and Jason. The methods used to compute the model are described in detail in Egbert et al. (2004), and Egbert and Erofeeva (2002). The model domain includes ocean cavities under floating ice shelves. The principal assimilated data set in this model is T/P altimetry, between +/-66^o latitude. However, ERS data and coastal and benthic tide gauge data from the Arctic (about 310 tide gauges) and Antarctica were also assimilated into the model. Bathymetry and resolution of global and local grids has also improved in version 6.2 of the TPXO model. Thus, TPXO6.2 is one of the most accurate global tidal solutions, particularly for high latitudes (King and Padman, 2005; King et al, 2005; Padman and Fricker, 2005).

AOTIM-5: The Arctic Ocean Tide Inverse Model (AOTIM-5, or denoted by PAD in the Figures) was developed by Padman and Erofeeva (2004) at Oregon State University. It is a regional high-resolution (5-km regular grid) linear dynamics and inverse model of the Arctic Ocean barotropic tides. This model assimilates coastal and benthic tide gauges (about 310 tide gauges) and T/P and ERS altimetry (about 364 cycles and 108 cycles respectively) for further improvements of the 4 dominant constituents M2, S2, K1 and O1. Data assimilation was done for 4 major constituents only: TG+T/P+ERS data for M_2 and O_1, TG+T/P for K_1 and TG only for S_2. This model is significantly better than other global models mainly in the Canadian Arctic Archipelago, Nares Strait, and the Baffin Bay and Labrador Sea, and can be explained by the higher resolution of the new model in these topographically complex regions.

Sea ice concentrations (SIC):
Maps of SIC were obtained from SSM/I passive microwave sensor (Comiso, 1990) and weekly ice charts (provided by Canadian Ice Services).

SSM/I: The National Snow and Ice Data Center (NSIDC), Boulder, Colorado provides SSM/I daily and monthly polar gridded SIC. SSM/I sea ice products are in polar stereographic projection, gridded at a resolution of 25 x 25 km, beginning 25 June 1987. Two sets of SSM/I SIC grids have been formulated. The first data set was generated using the NASA Team algorithm and the second using the Bootstrap algorithm (which was used in this study). The SSM/I-derived ice concentrations are daily total and monthly averaged ice fractions for both hemispheres. Both the NASA Team and Bootstrap data are provided in the Hierarchical Data Format.

Ice Charts: SIC were provided by Roger Pilkington from Canatec Associates, Calgary, Canada, using their Ice Statistics Program (ICE '06). ICE'06 was recently upgraded in November 2006 with a new worldwide ice data set (years 1972-2005). ICE '06 generates statistical output based on over 30 years of continuous weekly ice charts. The source data are in the SIGRID gridded ice format standard of the World Meteorological Organization (WMO). The nominal resolution of SIGRID is 25 km in latitude. While most of the tide gauge records begin in 1960's (Table 3.2), there are no SIC data available from SSM/I of Ice charts for this time.

Methods

Sea ice thickness over the last century has changed significantly, however, different ice thickness measurements show different trends, some even an increase in sea ice thickness. This is due to complex sea ice dynamics particularly in coastal areas, where the long-term ice thickness sites are located. Natural Resources Canada maintains a sea ice thickness database, results from these records are shown in Figure 3.12.

The annual cycle of sea ice cover is evident. Most stations observe sea ice for about 8 month per year. It is obvious that this must be taken into account in any analysis of sea ice cover and ocean tide modeling.

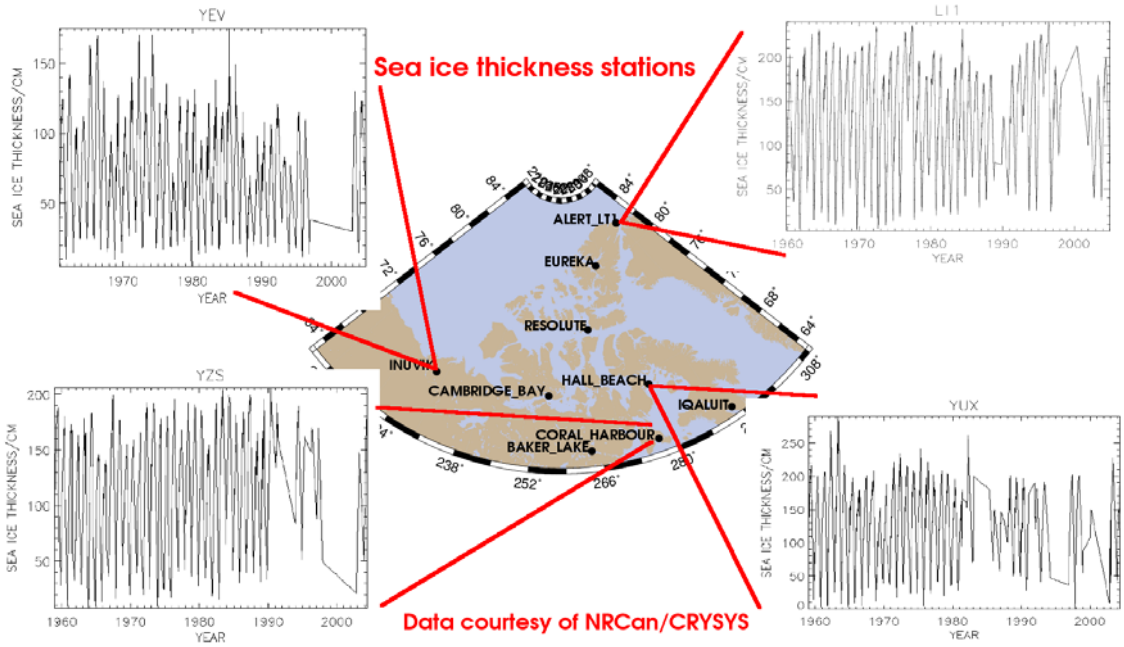

Fig. 3.12: Sea ice thickness at 4 sea ice monitoring stations in Canada.

Comparison of global and regional models in the Arctic

Figure 3.13 shows the differences between the three tide models (AOTIM-5, CSR4.0, and GOT00.2) for the entire Arctic, applied to the three ICESat epochs mentioned in the beginning of this section. It is obvious that the time period analysed has no impact on the differences identified between CSR4.0 and GOT00.2. This must be expected as both models have assimilated the same observations and rely on the same hydrodynamic equations. Minor differences likely occur due to a different numerical realization of the model. For this study, both models can be regarded as identical.

The differences of these two models with respect to AOTIM-5 are substantial and exceed 40 cm in coastal regions. The reason for the difference is likely the phase difference of the cotidal lines in these areas as the amplitudes have a similar magnitude compared to the differences in the Arctic. Focusing on the central Arctic ocean reveals that there are almost no differences, this is due to the fact that there are no observations available to constrain the model beyond the hydrodynamic model. The differences in coastal regions are of concern as they exceed the predicted freeboard heights in this area. The statistical information is presented in Table 3.3. The result of this study indicates that there are substantial differences between the regional model AOTIM-5, which is constrained by tide gauges, and the global

models, which assimilated altimetry data. As it is shown in Section 1.3, the estimated sea ice freeboard height maps also indicate that the AOTIM-5 model produces better or more realistic results. Using the CSR4.0 and GOT00.2 models results in regional patterns of unrealistic sea ice freeboard height, e.g. no ice at all, where ice is observed by SSMI or simply must be expected during the particular time of year. The AOTIM-5 model does not show such artifacts and must be regarded as the best tide model available in the Arctic at present.

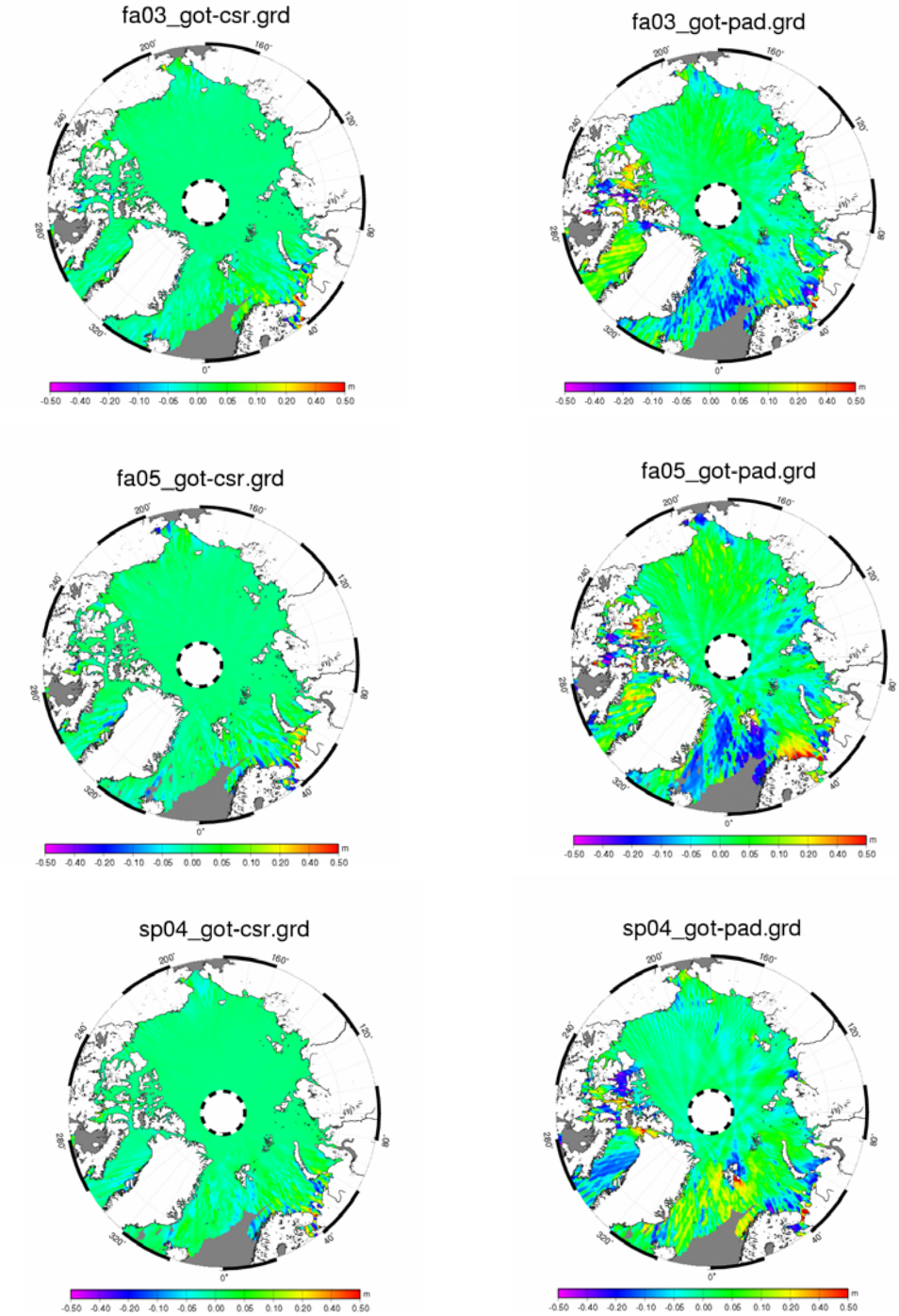

Fig 3.13: Differences of tide models at ICESat footprints in meters. Left: GOT00.2 -CSR4.0. Right: GOT00.2-AOTIM-5. Top: Sep-Nov 2003, Middle: Sep-Nov 2005, Bottom: Feb-Mar 2004.

The next section describes a comparison with tide gauges which confirms this assumption. However, the results are not strictly independent as the AOTIM-5 model assimilated tide gauge records.

Table 3.3: Statistics of the differences between tide models GOT00.2, CSR4.0, and AOTIM-5 for the three time periods discussed herein.

Time model	*min diff. [meter]*	*max*	*mean*	*std*	*rms*
2003 GOT-CSR	-1.03	0.94	-0.0002	0.028	0.028
2005 GOT-CSR	-0.77	0.73	0.0004	0.215	0.215
2004 GOT-CSR	-1.09	0.83	-0.0004	0.023	0.023
2003 GOT-AOTIM	-1.61	1.49	0.0001	0.086	0.086
2005 GOT-AOTIM	-1.14	2.56	0.0020	0.077	0.078
2004 GOT-AOTIM	-1.42	1.86	-0.006	0.081	0.082

Impact of sea ice on ocean tide records

Sea ice has a damping effect on ocean tides. Here, the major concern arises from the fact that all tide models, both regional and global, assimilate open water data from tide gauges and altimetry. In other words, the models are constrained by observations which do not include the sea ice – tide interactions. Consequently, tide models must perform less accurate in the presence of sea ice. In order to identify how the performance decreases and if there is a measurable effect, a number of tide gauges prone to sea ice cover have been selected. Hourly TWL were predicted for the tide-gauge stations listed in Table 3.2 using global and regional tide models - CSR 4.0, GOT00.2, TPXO6.2 and AOTIM-5. Tidal constituents were derived from the TGR of the same stations and the tide models using standard algorithms (Foreman, 1977). The four major constituents analyzed in this study are M2, S2, O1, K1 (similar to Andersen et al, 1995). Then, time-series of the tidal constituents were derived for each station using a three-month time period of TWL data. The time series consisted of 3-month windows which overlap at both ends by 1 month, in other words, the window is moved foreward by one month. The central month is used as the time reference in the time series. It is expected that the constituents show a correlation with sea ice coverage. However, as the models did not assimilate observations taken in sea ice conditions, it must also be expected that the models do not show such behaviour, unless the sea ice effects are included, e.g. by incorporating tide gauge records in the model assimilation. For every station, time series of sea ice concentrations were compared with the time-series of tidal constituents in order to analyze the effect of sea ice on tidal amplitudes. TWL from 9 tide-gauge stations are analyzed to study the effect of sea ice cover on ocean tides.

Results and Discussion

The results presented in this section contain data gaps and also gaps due to undefined areas for particular models. This must be considered in the interpretation of the results and does not mean that data has been masked out. The first tide gauge analysed is in Churchill, Manitoba, Canada. It is located at Hudson Bay, where tides can have significant amplitudes. The area exhibits an annual sea ice cycle and is located at latitude 58º which allows for a comparison with T/P data. The limitation of this site is that the regional AOTIM-5 model is not defined.

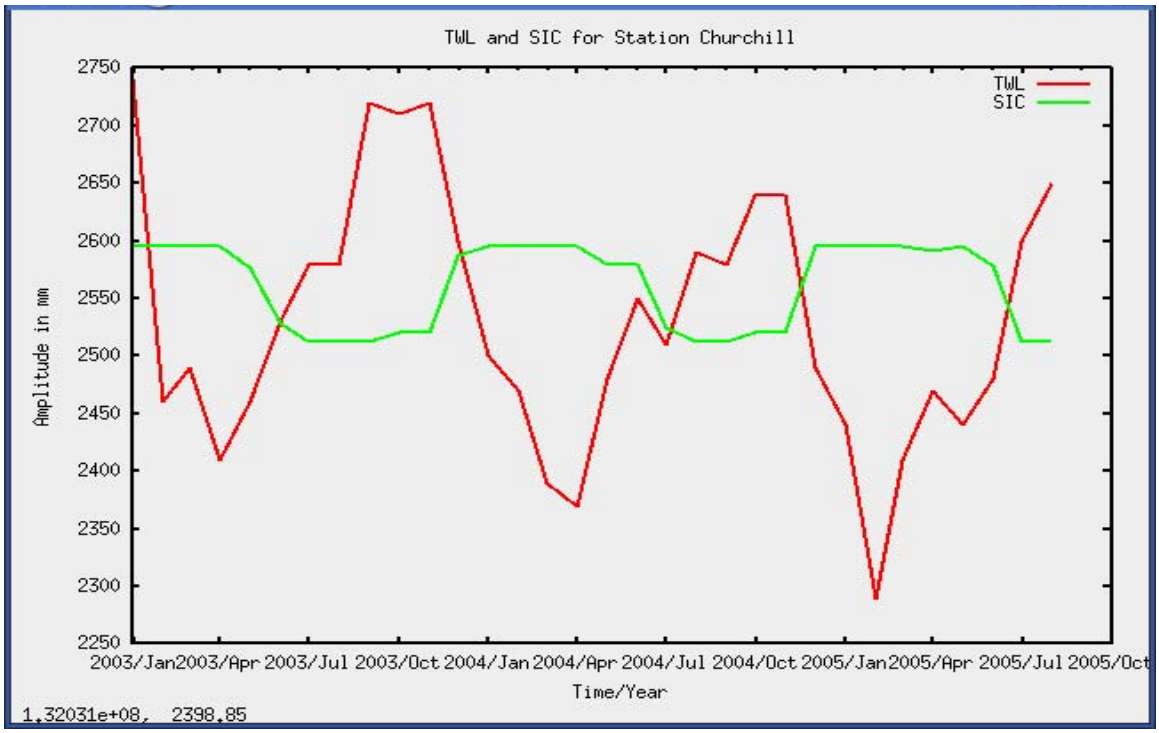

Fig. 3.14: Comparison of TWL and SIC for Churchill TGR.

Before splitting the TWL into constituents, the total TWL was compared to SIC. Three years between 2003 and 2006 were analysed. Figure 3.14 shows that TWL and SIC are negatively correlated. A minimum TWL is observed during winter months when there is a maximum SIC and a maximum TWL during summer months when ice-free conditions prevail.

In principle, this can be explained by the annual cycles in both sea ice and ocean tides. In order to prove that this is not a coincidence, individual tidal constituents were analysed to demonstrate that the effect originates from sea ice cover and not necessarily from astronomical tidal forces of annual periods.

All tidal constituents derived from TGR show a negative correlation with SIC similar to TWL (Figures 3.15 – 3.25) whereas the global tide models do not respond to the presence of sea ice.

These models do not show a decrease in amplitude when there is a maximum in SIC. This implies that tidal amplitudes will be overestimated during winter months.

Tidal amplitudes in general can be underestimated (Figure 3.15) or overestimated (Figure 3.16) by the global models when compared with the TGR. This is because the effect of sea ice cover on ocean tides is ignored in all global and regional ocean tide models. Presence of sea ice cover changes the tidal amplitude by up to 3% and the phase by about 1 hour (Kowalik and Proshutinsky, 1994). Although this change is small in the open ocean, locally it can occur at a wider range particularly in shallow water (Kowalik and Proshutinsky, 1994) (e.g., Figure 3.17). The difference between TGR and global models, including the high-resolution TPXO6.2 model, is particularly large at Churchill.

AOTIM-5 is found to perform best in terms of tidal amplitude prediction, if the TGR is considered true. As the model is not defined in Churchill, the comparison has been made in Alert. As expected, it is consistent with TGR because these data were already assimilated into this model (Figures 3.18 – 3.19). Although AOTIM-5 does not show the annual variability

inversely correlated with SIC, it has the same average amplitude as TGR. By adding ice-ocean frictional processes, this model could further improve.

Additional results from different constituents and tide gauge stations are presented in Figure 3.20 – 3.24.

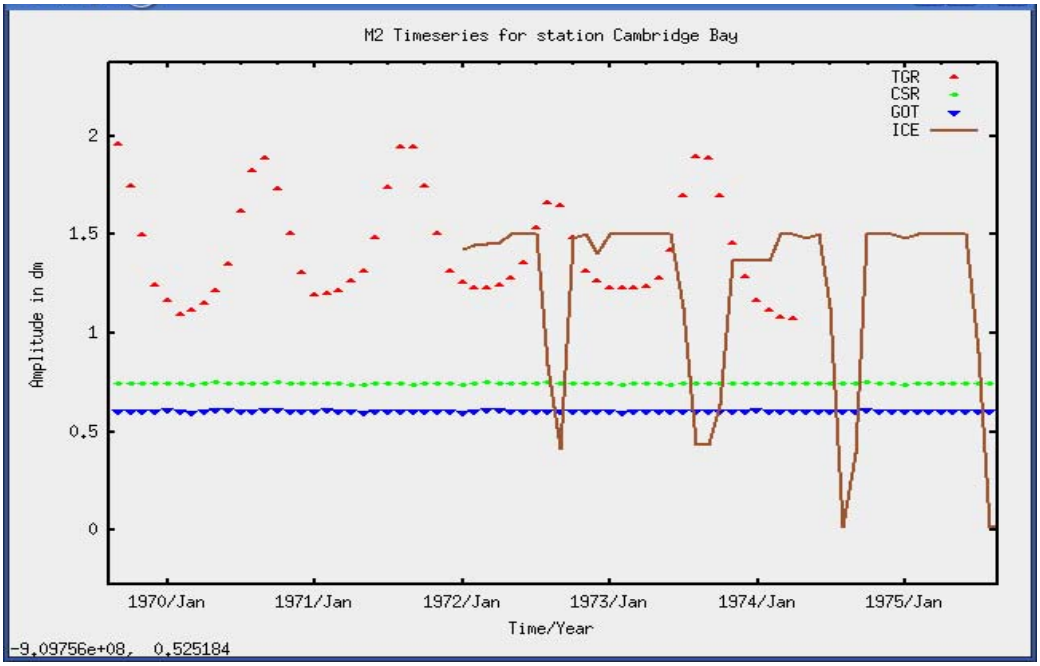

Fig. 3.15: Comparison of SIC and the M2 tidal constituent derived from TGR, CSR 4.0, GOT 00.2 for Cambridge Bay.

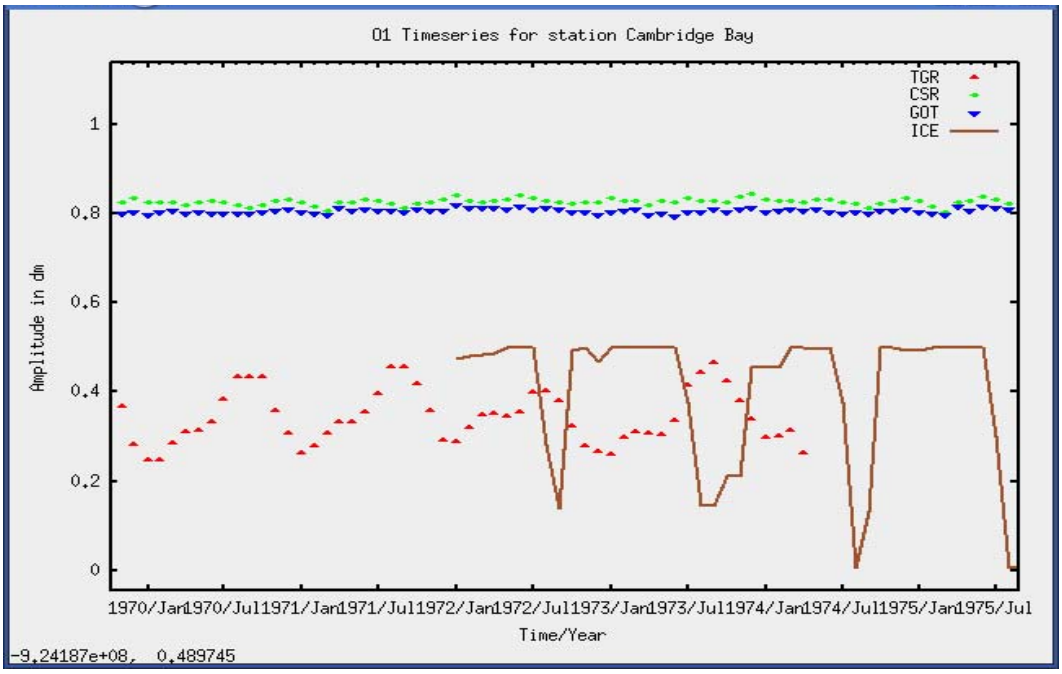

Fig. 3.16: Comparison of SIC and O1 tidal constituent derived from TGR, CSR 4.0, GOT 00.2 for Cambridge Bay.

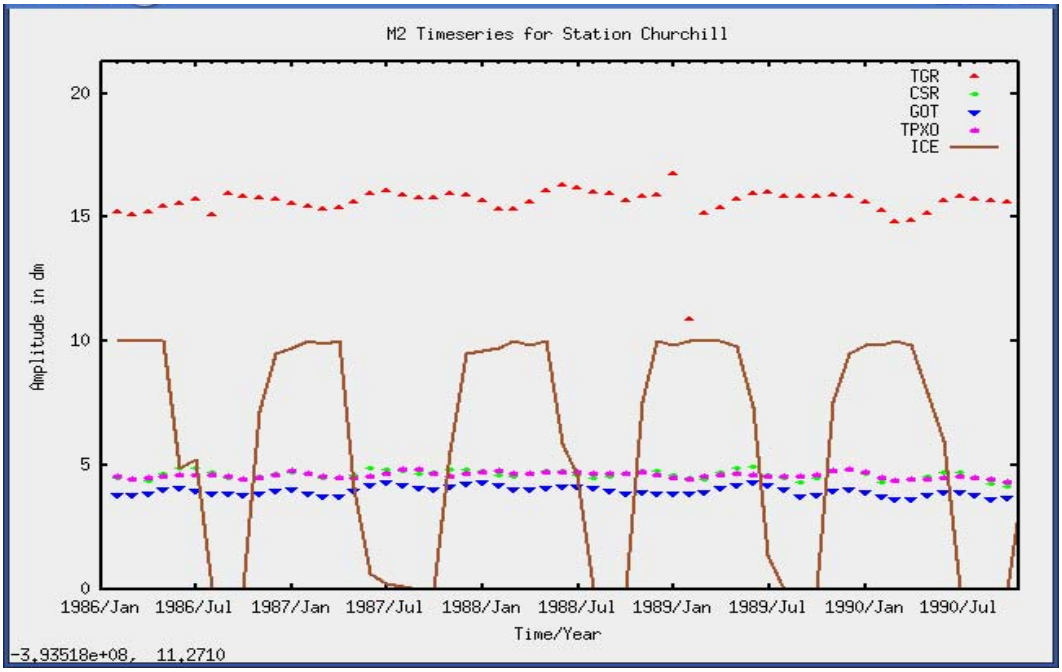

Fig. 3.17: Comparison of SIC and M2 tidal constituent derived from TGR, CSR 4.0, GOT 00.2, TPXO6.2 for Churchill.

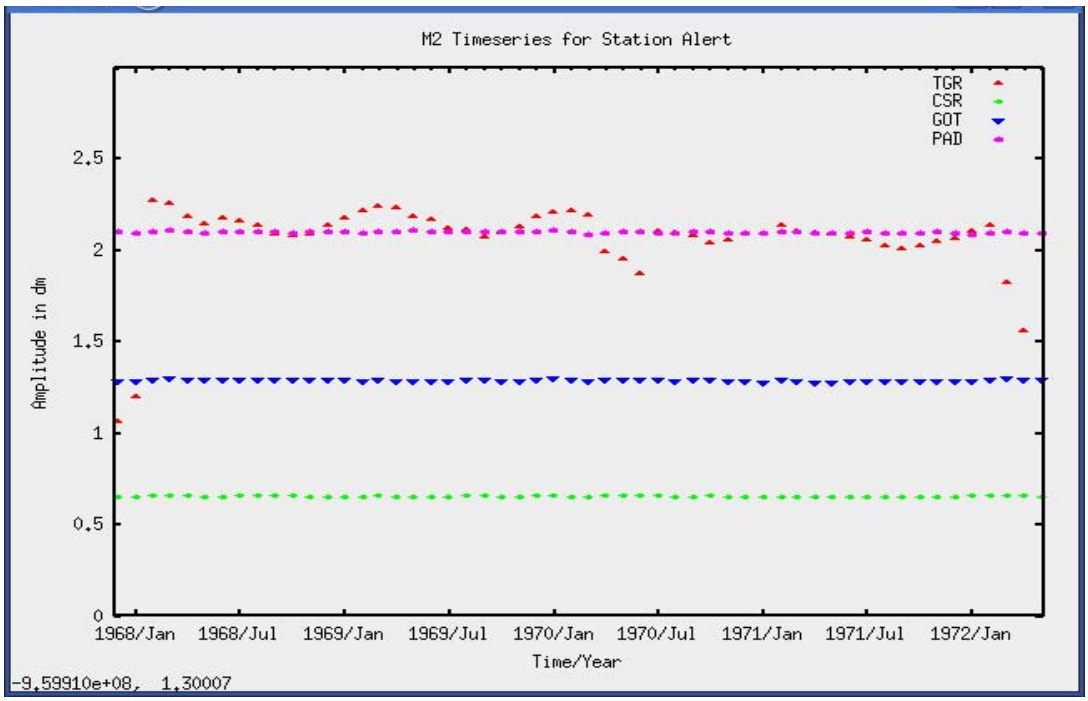

Fig. 3.18: Comparison of SIC and M2 tidal constituent derived from TGR, CSR 4.0, GOT 00.2, AOTIM-5 (PAD) for Alert.

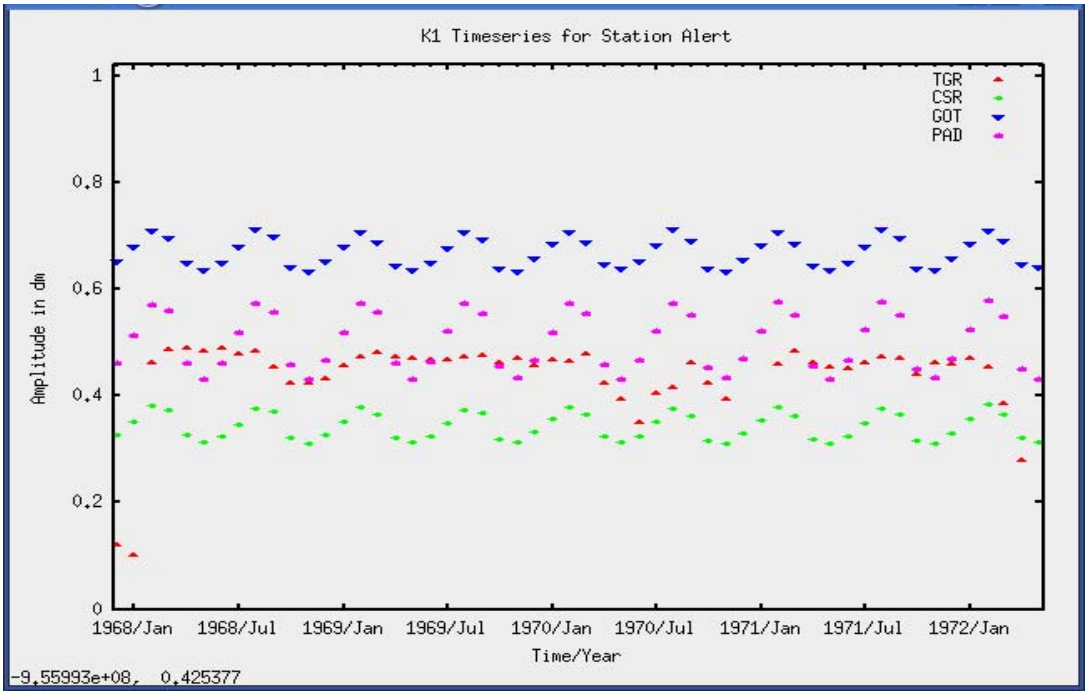

Fig. 3.19: Comparison of SIC and O1 tidal constituent derived from TGR, CSR 4.0, GOT 00.2, and AOTIM-5 for Alert.

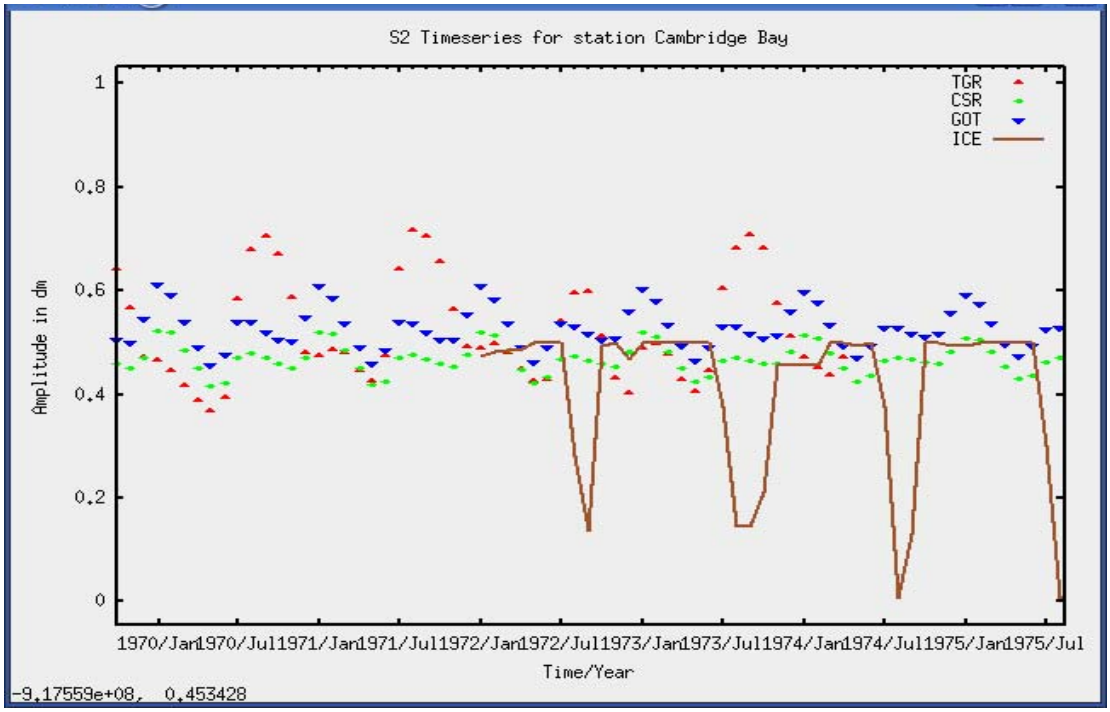

Fig. 3.20: Comparison of SIC and S2 tidal constituent derived from TGR, CSR 4.0, GOT 00.2 for Cambridge Bay.

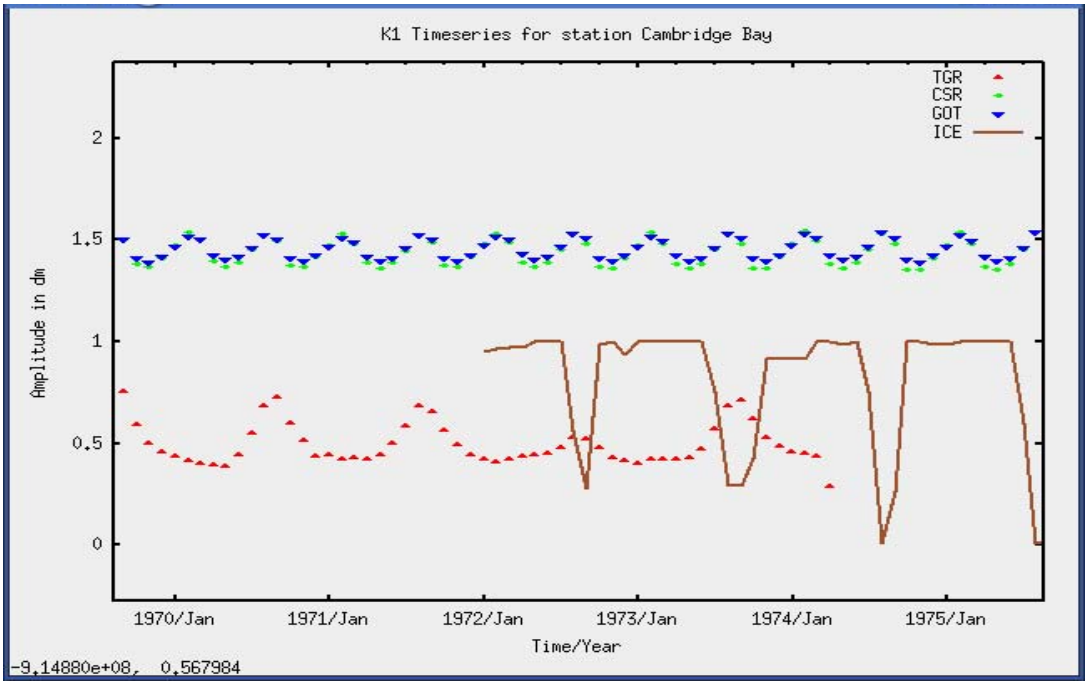

Fig. 3.21: Comparison of SIC and K1 tidal constituent derived from TGR, CSR 4.0, GOT 00.2 for Cambridge Bay.

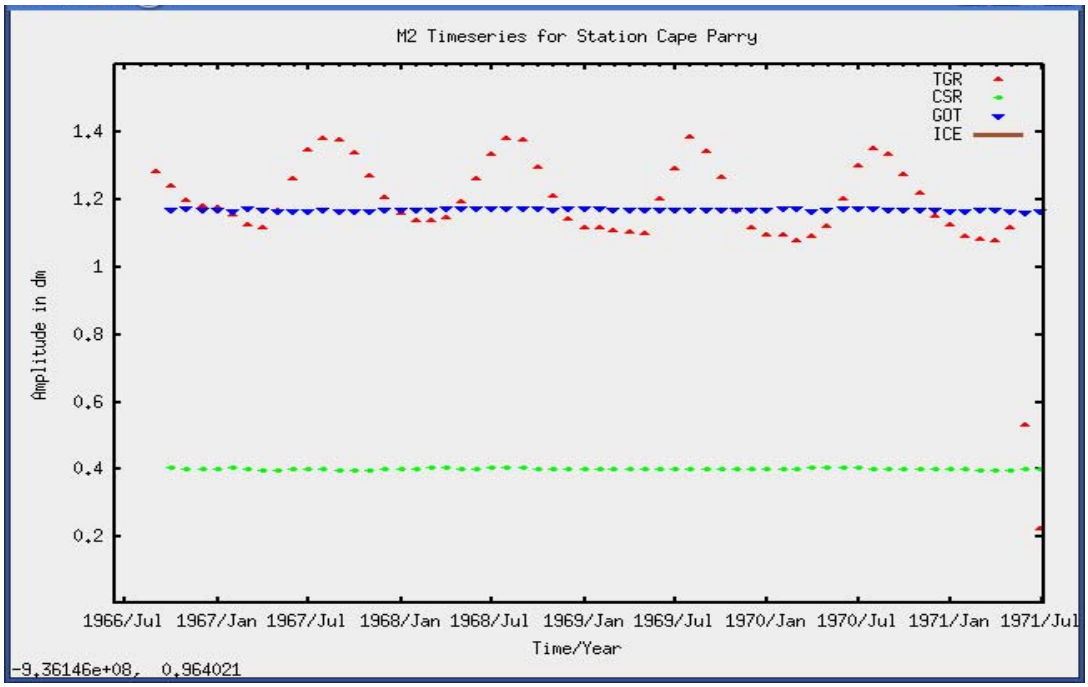

Fig. 3.22: Comparison of SIC and M2 tidal constituent derived from TGR, CSR 4.0, GOT 00.2 for Cape Parry.

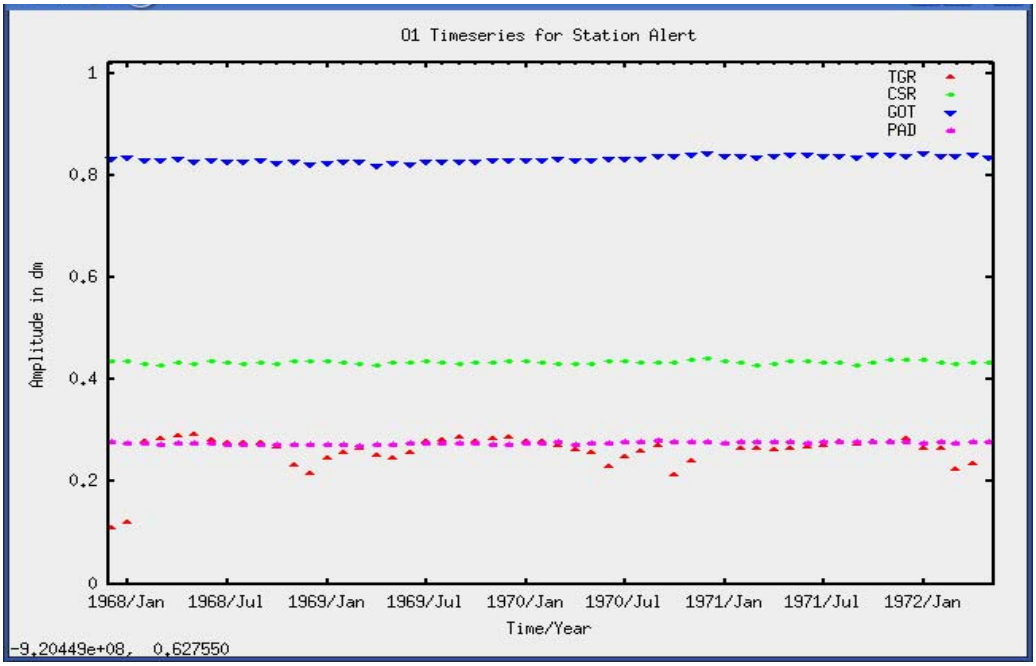

Fig. 3.23: Comparison of SIC and K1 tidal constituent derived from TGR, CSR 4.0, GOT 00.2, AOTIM-5 (PAD) for Alert.

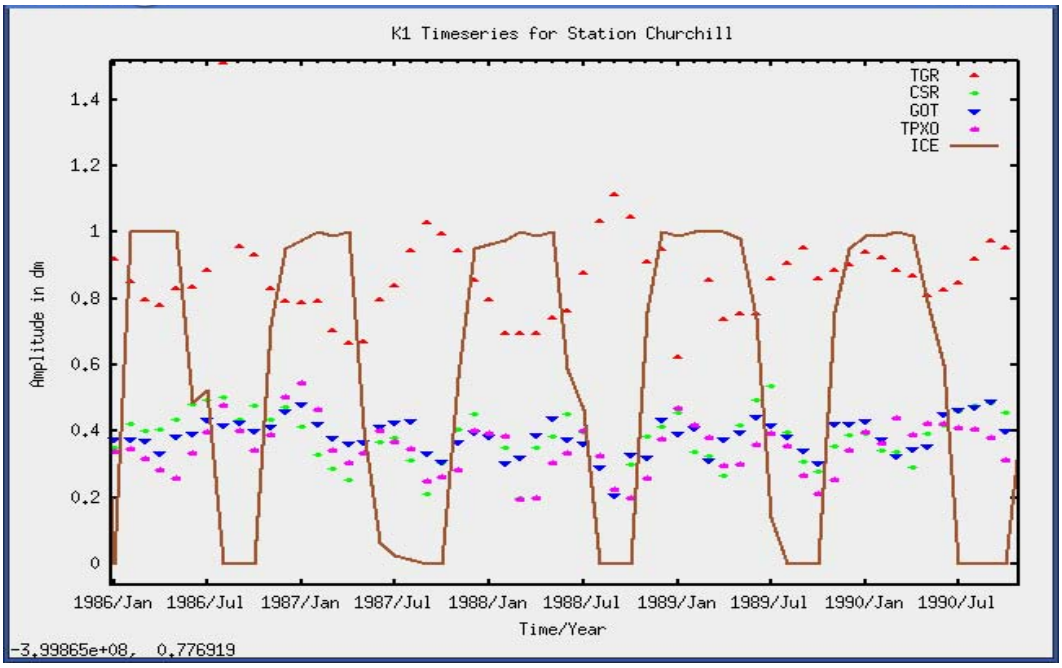

Fig. 3.24: Comparison of SIC and K1 tidal constituent derived from TGR, CSR 4.0, GOT 00.2, TPXO6.2 for Churchill.

Satellite altimetry

Satellite altimetry also provides a means to evaluate the global tide models. As a preliminary step, T/P data were compared with Churchill TGR and CSR 4.0, GOT 00.2, TPXO6.2 (Figure 3.25, Tables 3.4 – 3.5).

The difference between T/P data (within 50 km of Churchill) and global models is about 2 cm in mean and 15 cm in standard deviation (Figure 3.25, Table 3.4). The difference between T/P

data (within 100 km of Churchill) and global models is similarly about 2 cm in mean and 35 cm in standard deviation (Figure 3.25, Table 3.5). TGR and T/P data show large differences (Table 3.4 – 3.5) because the tide gauge station is on land and the closest altimetry data points are about 50 km offshore. Tides in this area change significantly within this 50 km distance. Padman and Fricker (2005) compared ICESat crossover elevations with global and regional tide models for the entire Ross Ice Shelf. R.m.s. differences between ICESat and regional model (RIS_2002) were about 20 cm and differences between ICESat and global models (FES 2004 and GOT 99.2) were about 30 cm, which is consistent with our results.

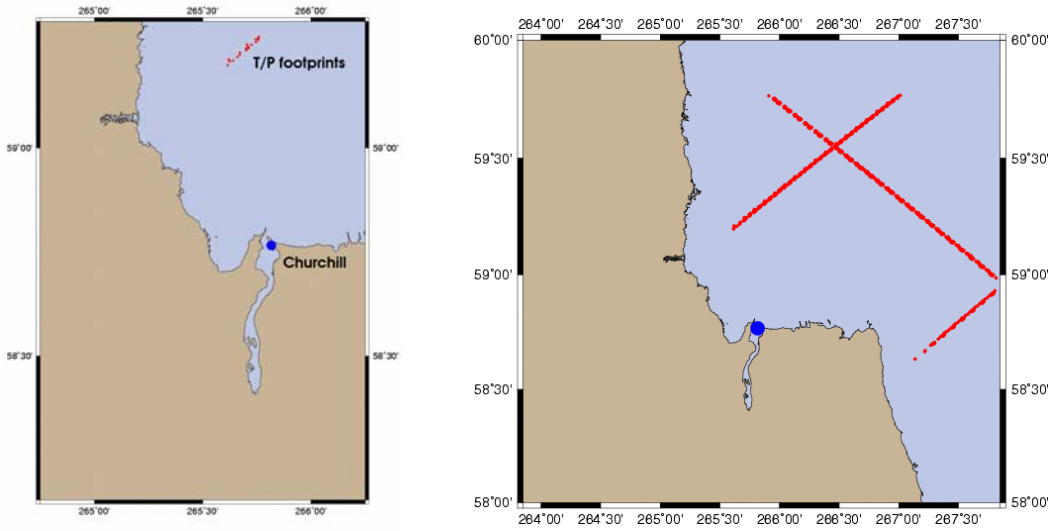

Fig. 3.25: Left: T/P data within 50-km radius. Right: Within a 100 km radius.

Table 3.4: Differences between T/P and global tide models within a radius of 50 km.

Differences	Mean (m)	Standard deviation (m)
T/P – TGR	-0.02	0.34
T/P – CSR 4.0	-0.02	0.16
T/P – GOT 00.2	0.02	0.14
T/P – TPXO6.2	-0.05	0.32

Table 3.5: Differences between T/P and global tide models within a radius of 100 km.

Differences	Mean (m)	Standard deviation (m)
T/P – TGR	0.01	0.53
T/P – CSR 4.0	-0.01	0.31
T/P – GOT 00.2	0.03	0.40
T/P – TPXO6.2	0.02	0.43

Conclusions

Ocean tides are affected by the presence of sea ice cover. Global models overestimate or underestimate tides as the ice-ocean frictional processes are ignored in the model development. The models perform well only in regions where nearby in-situ tide observations have been assimilated (Padman and Fricker, 2005). The accuracy decreases in other regions because i) altimetry data from winter months were not used in the model (Figure 3.26) ii) altimetry data not available for assimilation above 81° N/S before ICESat.

The comparison of individual constituents with SIC demonstrates that all constituents are affected by sea ice cover, although the magnitude varies. No model shows this variability and correlation with SIC. The AOTIM-5 model performs best as it predicts the tidal amplitudes in most constituents the best. Together with the results of the tide model comparison and the freeboard height estimation, it must be concluded that the AOTIM-5 model is the best model in the Arctic Ocean. However, there are significant limitations involved due to sea ice – tide interactions which are still not accounted for.

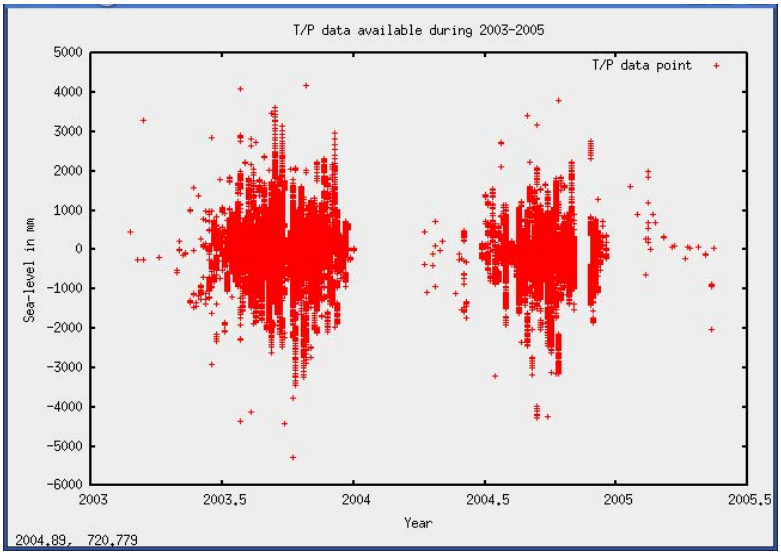

Fig. 3.26: T/P data available between 2003-2005 near Churchill. Winter month are not covered by observations.

Tide models can be improved by assimilating more altimetry data, gravimetric data, GPS records, and by adding the ice-ocean interactions (King and Padman, 2005). Kowalik and Proshutinsky (1994) constructed a tide model (14 km resolution) by numerically solving a set of equations that describe the dynamical ice-tide interaction. Kowalik and Proshutinsky (1994) were unable to produce the phase lag and amplitude change due to presence of sea ice because the bathymetry in narrow bays could not be reproduced accurately with the 14 km resolution. AOTIM-5, with a 5 km resolution, can overcome this problem if the ice-tide interactions would be added.

In conclusion, AOTIM-5 is currently the best ocean tide model available for the Arctic Ocean. It could be further improved by adding ice-tide interactions similar to Kowalik and Proshutinsky model (1994). In the meantime, it is suggested that an empirical function could be developed which accounts for the damping of tidal amplitudes. If sea ice is present, the amplitudes of the tide model must be corrected. It is clear that this approach is not a final solution, but would at least account for most of the sea ice – tide interactions for studies using tide models as a geophysical correction term. One example is this project, where ocean tides represent corrections to achieve better freeboard height estimates and gravity data.

The major findings of this tidal study are in summary:

- Ocean tides are affected in all tidal constituents by sea ice cover.
- Sea ice concentration is inversely correlated with tidal amplitudes.
- The AOTIM-5 model predicts the tidal amplitudes best.
- No tide model accounts for sea ice effects.
- An empirical sea ice flag and correction term is suggested to over come the problem until next generation tide models are developed.

3.5 Comparison of oceanographic MDT grids to MSS-geoid

The oceanographic MDT models of Section 3.1 and 3.3 should in principle resemble the MDT generated from space/geoid methods by MDT = MSS – N. Figure 3.27 below shows the difference between the ArcGP geoid, and the composite ERS-ICESat MSS of Section 2.4. For comparison the PIPS average MDT for March 1995-2003 is shown in Figure 3.28.

It is seen that the overall features of the MDT signal from the oceanographic models are reproduced, with high values toward the Canada side, and low values north of Russia in continuation of the MDT low in the Greenland/Norwegian Seas. The offset in mean values is probably a consequence of inconsistent datum systems, and likely effects from differences in application of the permanent pole tide corrections.

In Figure 3.29 the "remote sensing" MDT of Figure 3.27 is shown low-pass filtered with a Gausssian filter of 1.0° resolution, together with the similar MDT derived using the EIGEN-GL04C geoid. The difference between the filtered MDT based on ArcGP and EIGEN-GL04C is relatively minor (as it should be, since the earlier version ArcGP data were included in EIGEN-GL04C). The ArcGP MDT appears to be more smooth, especially north of Greenland and Canada.

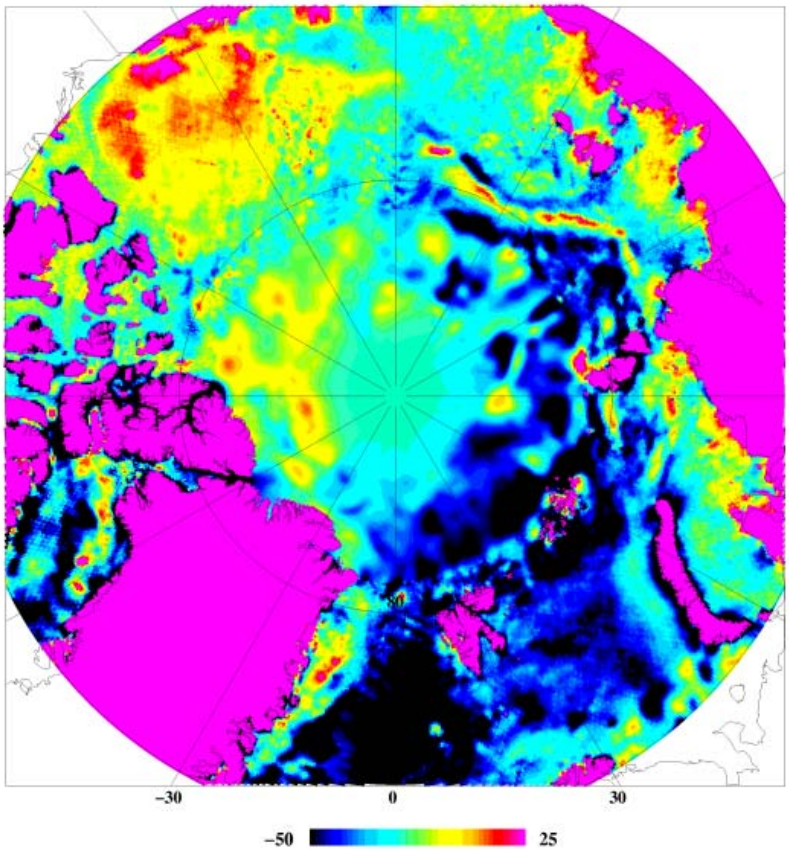

Fig. 3.27: MDT determined from the composite Arctic Ocean MSS from ERS and ICESat, and the ArcGP geoid. No filtering applied. Units: cm.

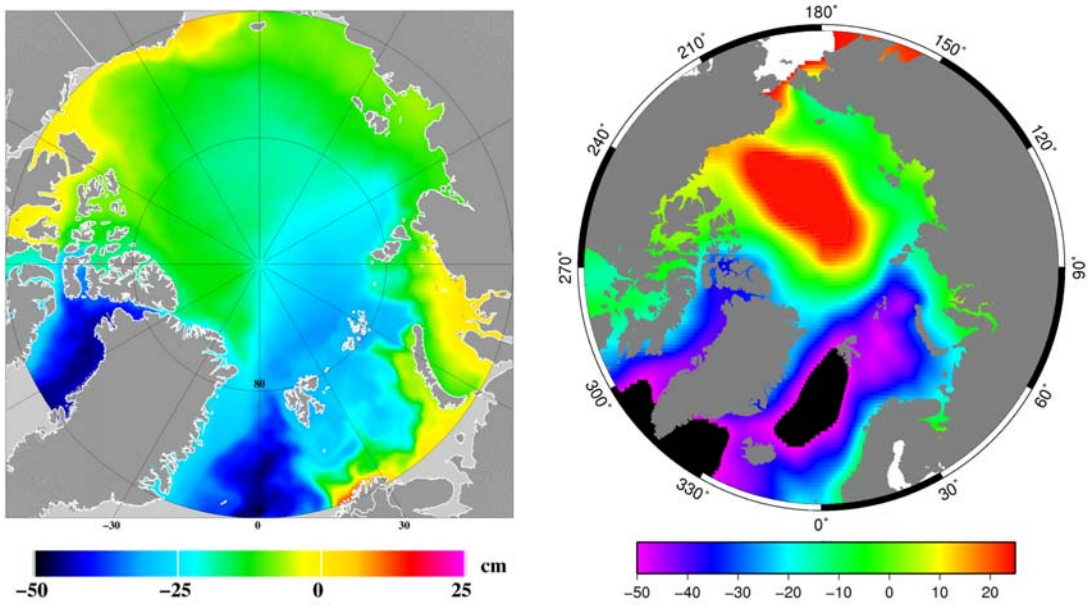

Fig. 3.28: MDT from PIPS (left) and MICOM (right) for the period 1995-2003 (PIPS average is for March only). Unit: cm. The large difference between the oceanographic models is evident.

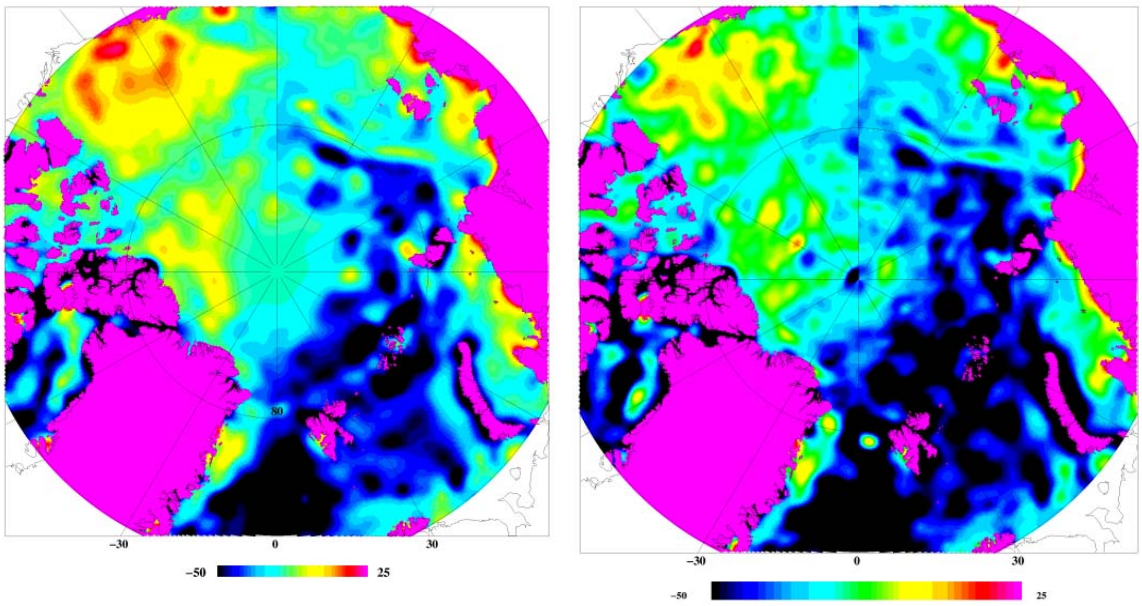

Fig. 3.29: Low-pass filtered MDT from remote sensing: MDT from MSS with ArcGP geoid (left) and EIGEN-GL4C (right). Unit: cm.

Figures 3.30 and 3.31 shows the comparison of the MDT derived from the collocation geoid estimates, and the MDT derived from the FFT geoids with EIGEN-CG03C with and without correction for data biases, estimated by collocation, cf. Section 1.4. The composite MDT used for Figures 3.30 and 3.31 is based on an earlier ICESat MSS, determined only for the laser 1 and 2A periods. It is seen that the collocation geoid has some problems due to the blocks or the insufficient density of prediction points, but the main MDT features are the same as for the FFT solution. Concerning the effect on taking the gravity data biases into account or not in the FFT method, the impact on the MDT estimation seems minor.

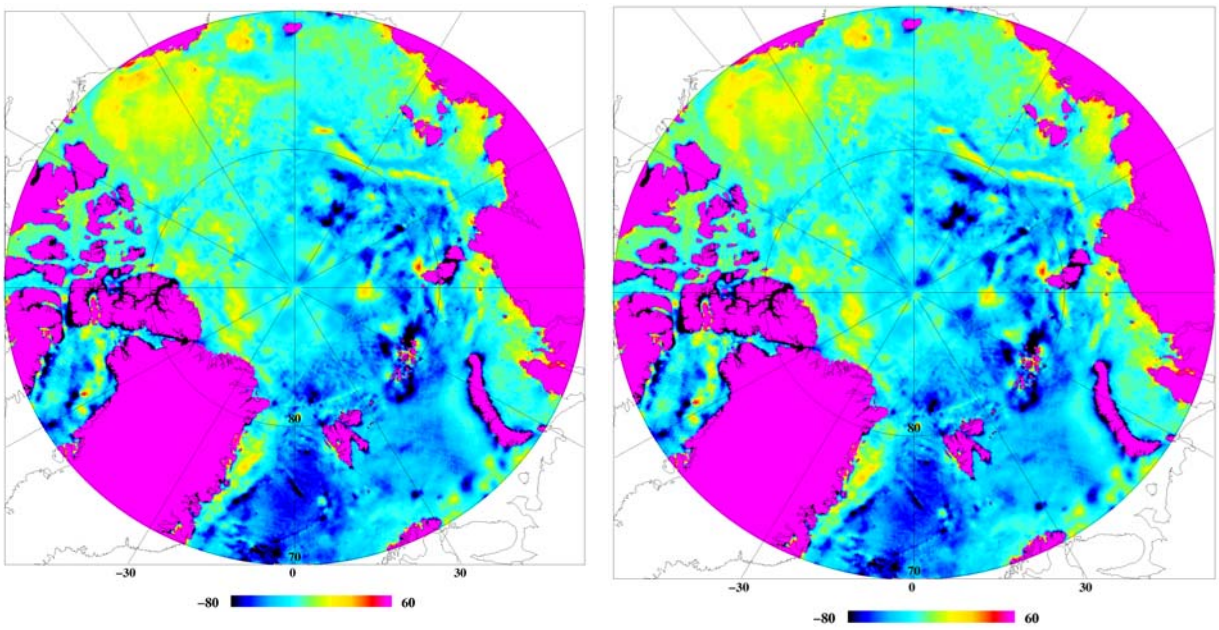

Fig. 3.30: Left: MDT from the FFT solution using the EIGEN-CG03C as reference field (based on an earlier version on the ERS/ICESat MSS). Right: Same MDT but with survey bias correction.Unit cm.

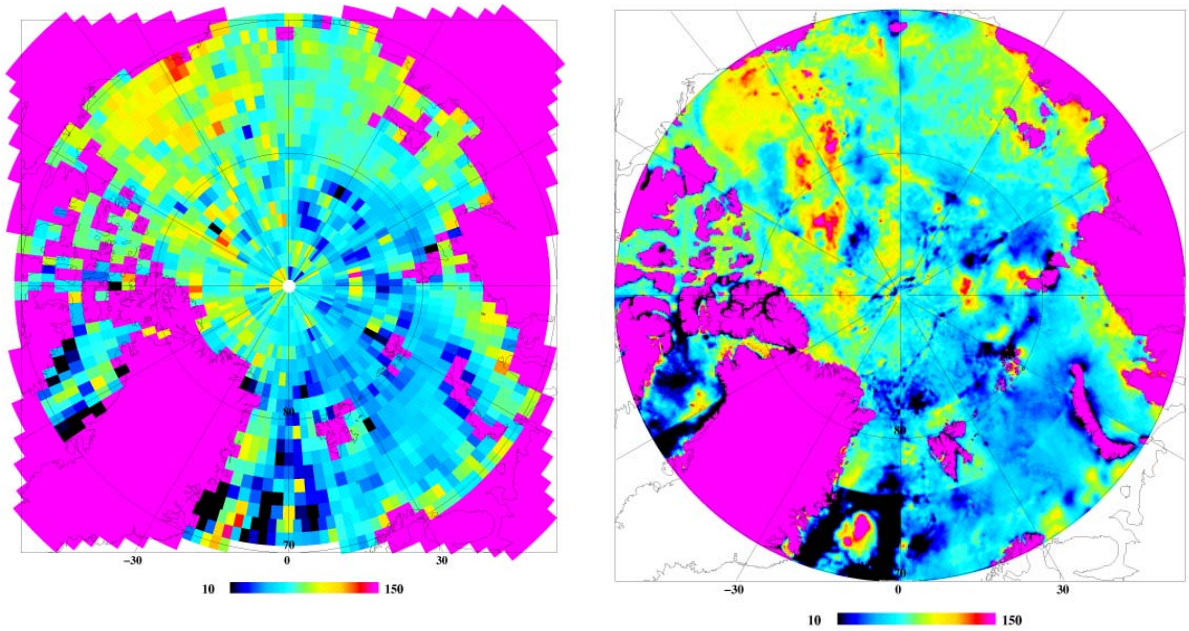

Fig. 3.31: MDT from the combination of ERS-ICESat MSS and the collocation geoids. Left: regional solution; right: block solution. These solutions show the same general features, but has some apparent bias problems for the blocked solution. Units: cm.

Overall, comparing to the oceanographic MDT results of Section 3.1 and 3.3, it is clear that the "remote sensing" altimetry/geoid MDT estimation is consistent with the independent MDT data, and the potential of the space-based methods for MDT determination therefore highlighted. The ability to map changes in the MDT, and thus the underlying ocean circulation, could in principle provide new constraints on oceanographic models of the region. This could again provide insight into the basal melting process of the sea ice, since the changing inflow of Atlantic and Pacific waters is believed to be a major source of currently observed sea ice thickness changes.

3.6 Recommendation for combined use of all data

Radar or laser altimeter observations in the Arctic region measure to the sea ice surface or to the sea surface. The sea surface height surface ellipsoidal height at a time t and location (φ,λ) can as earlier mentioned be written like

$$h^i(t) = N + \zeta + F(t) + h(t) + n \tag{37}$$

In the case of open water the equation reduces to

$$h^s(t) = N + \zeta + h(t) + n \tag{38}$$

where

h^i	is the sea ice surface ellipsoidal height,
h^s	is the sea surface ellipsoidal height,
N	is the geoid height,
ζ	is the mean dynamic topography
F	is the free board height,
$h(t)$	is the dynamic topography, and
n	is the measurement noise.

The sum of the geoid and the mean dynamic topography is the mean sea surface height so

$$h^i(t) = MSS + F(t) + h(t) + n \tag{39}$$

The challenge of using altimetry for sea ice or freeboard monitoring in the Arctic region is to use the altimetric data over a variety of zones ranging from open ocean where the freeboard is zero (F(φ,λ) = 0) to partly ice-covered regions (F(φ,λ,t) is variable) to permanently ice-covered regions (F(φ,λ) ~ constant). This is further complicated, as both radar altimetry (ERS-1, ERS-2, ENVISAT, CryoSat-2) and laser altimetry (ICESat, ICESat Follow On) can be used. The laser is more inclined to reflect and map the top layer of the snow on top of the sea ice compared to the radar which reflects from top of the sea ice. Furthermore, the laser has such small footprint (70 m compared with kilometers for radar) that the laser more frequently reflected from leads between the sea ice.

The determination of an accurate mean sea surface is a critical step in monitoring sea ice in the Polar Regions, as the mean sea surface can be used as reference. In the simplified case where data are averaged over a certain period and there is no sea ice present, the dynamic topography will integrate to zero and the h^s will become the Mean Sea Surface and the equation above will reduce to MSS = ζ + N. For the MSS the Geoid contributes with more than 90% of the magnitude in most locations, and geoid observations are consequently highly important. And the MSS can be determined from either satellite altimetry alone or from combining gravity observations and hydrodynamic MDT information which does not involve satellite altimetry. Determining MSS from altimetry alone, has some advantages over the other approach. However, it requires, in principle, that the averaging period is infinite, otherwise interesting climatic signal might be absorbed in the averaging. Similarly it requires knowledge about which surface reflects the radar signal (water or ice)

In this simplified case of time averaged observations a method for combining several data sources (exemplified with the MSS and the geoid) was described in Section 1.5. The outcome was that both quantities may be improved by combining the two observations and carrying out an optimal combination.

In the presence of sea ice, average height of the satellite observations will be called $H^i = \zeta + N + F$. Assuming that the sea ice or the freeboard is constant in time the freeboard can be mapped from $F = H^i - \zeta - N$. Here the estimation of the freeboard, the geoid and the MSS can be combined and all quantities can be improved using optimal combination techniques (Section 1.5) using (Equation 14). However, a covariance function associated with the sea ice freeboard is needed. However, studies are needed to recover information about both the spatial and the temporal characteristics and statistical properties of the sea ice thicknesses to determine such a covariance function, which has not been attempted.

The assumption that the combined quantities (MSS, geoid, freeboard) should be constant surfaces in time (taken over infinite timeseries), is an approximation, but in most cases the recommendation and the experience is that error committed by this assumption is small compared with other error sources in the Arctic region.. However, if the time varying component needs to be included to describe the instantaneous sea surface height one might use methods as i.e. described in Knudsen (1991, 1993).

In the more general case sea ice thickness or the freeboard monitoring can be obtained through monitoring of the geoid, the mean dynamic topography, and the dynamic sea surface height using

$$F(t) = h^i(t) - \zeta - N - h(t) \tag{40}$$

The recommendations for combined use of all the various data types available in the Arctic region, will consequently, follow the recommendation for each quantity in this equation.

Dynamic height

The largest contributors to the time variable component of the dynamic sea surface height is the tides followed by air pressure and wind generated signals in the open ocean. In most regions of the world the tidal signal contributes up to 80% of the time varying signal of the sea surface height observations. Also errors in the tidal models might map into the Mean Sea Surface particularly for the ERS+ENVISAT satellites (Section 1.2). We can estimate large fraction of dynamic topography can be obtained from accurate tidal models. The conclusions and recommendations are to use the Arctic Ocean tide model AOTIM-5 by L. Padman at Oregon State University. This model is currently the best ocean tide model. However, ocean tide are still inaccurate in the Arctic Ocean and in several localized regions the difference between investigated models are as large as the tidal range itself and ranges up to decimeter level.

Tide models are currently being improved. However, this is a complicated task because the only satellite data available is sun-synchronous (ERS, ENVISAT), which is unsuited for tidal prediction. However, tides can also be improved by assimilating other types of altimetry data, gravimetric data, GPS records, and by adding the ice-ocean interactions (King and Padman, 2005) and new series of hydrodynamic assimilations models adding the sea ice into the modeling of the ocean tide models is currently developed by one of our collaborators, Koji Matsumoto from the National Astronomical Observatory in Japan.

The air pressure can be determined using NCEP fields and existing formulas by i.e. Kwok et al. (2004) and Forsberg and Skourup (2005), and the High Frequency Variability can be determined using i.e. the French MOG2D model (Lyard et al.)

Mean Dynamic Topography

In the project, a comparison of four different oceanographic models for the determination of the MDT have been used: These models are the MICOM, OCCAM, PIPS and UW models, showing some differences, but also some common features, and giving a good understanding of the expected nature of the errors associated with MDT models. However, both the mean of these models as well as their accuracy is needs to be improved in the future to reach the accuracy of some other observables.

Geoid modeling

Significant new development in the determination of the Arctic geoid has been obtained. New gravity data and new satellite data have been used to generate an improved geoid model and a comprehensive determination of error covariance functions has been carried out, using a very large data set (55,000 points). The Arctic geoid has also been improved using data from the new satellite mission GRACE. In the future, GOCE level-2 products may be used to compute an improved geoid in the Arctic Ocean. Both the spherical harmonic coefficients and the gravity gradients may be used. The use of the gravity gradients will primarily help in reducing the error in the region south of 84º latitude. Also variance-covariance information associated with the coefficients will be available for the geoid estimation process.

Altimetric Sea Ice observations

The satellite providing the most accurate long term mean sea surface observations is the joint TOPEX/POSEIDON providing uninterrupted observations for nearly 15 years. This satellite is however not available north of 66°N. In this region the ERS-2 provides the next best option having 8 years of uninterrupted observations. However, the ERS-1, ERS-2 and ENVISAT satellites have the disadvantage that they only cover regions up to 82°N and secondly the ranging degrades in the presence of sea ice.

Consequently, the satellite altimetry must be augmented with ICESat up to 86° N. ICESat observations does on the other hand only provide sporadic mean of selected monthly periods (see Table 1.1 in Section 1.3). Furthermore ICESat has a known pointing problem as well as a minor saturation problem (solved in more recent versions) which makes the satellite less accurate in monitoring the mean that the ERS-2 satellite. Consequently the ICESat observations should be referenced to the ERS-2 altimetric observations, as was done in the composite MSS constructed in Section 2.4.

With the availability of CryoSat data from 2009 the polar region will be covered with high-precision radar altimetry data up to 88°N, so that the need for ICESat data might be less, and a merged CryoSat / Envisat data series might provide the necessary framework for providing a highly consistent altimeter MSS and freeboard data set.

4 ”Smart” Mean Sea Surface Estimation

4.1 Development of smart sea surface height interpolator for retrieval of sea ice thickness

Introduction

In order to compute sea ice freeboard and hence sea ice thickness from satellite radar altimetry data, the sea surface height must be accurately determined at each ice floe location so it can be removed from the floe height to leave the freeboard. This is done by measuring the sea surface height at surrounding lead locations and interpolating the sea surface height beneath the floes.

The current method used in sea ice thickness retrievals for ERS-2 data at UCL involves fitting a straight line through sea level anomalies measured in the leads up to 46.75 km either side of the floe location. The sea level anomalies are obtained by removing a mean sea surface computed from 4 years of ERS-2 data from the sea surface heights obtained from the satellite. Both the lead density and the properties of the sea level anomaly signal will vary both temporally and spatially, however the interpolator width remains fixed.

In this study the properties of the sea surface height signal are investigated using models of the tides, dynamic topography and geoid error. Real lead and floe locations from six cycles of ERS-2 data are combined with the simulated sea surface height signals from the models to test various interpolation schemes. The ultimate aim is to develop a smart interpolator which always performs the optimal interpolation using knowledge of the lead density and properties of the unmodelled sea surface height signal to be interpolated.

Method

Figure 4.1 illustrates the general method used to investigate the properties of various interpolators under different conditions. A sea surface height signal is generated using an appropriate combination of models. A file is generated with the modelled sea surface height placed at each floe and lead location from a real cycle of ERS-2 data. Gaussian random noise is then added to the sea surface heights at the lead locations. A floe location in chosen and for a range of interpolator widths the following properties are measured:

a) The error in interpolating the sea surface height at the floe by fitting a least squares linear interpolator to the lead locations.
b) The error in interpolating the sea surface height at the floe by fitting a least squares quadratic interpolator to the lead locations.
c) The 95% confidence interval for the least squares linear fit computed from the number of lead locations used and the RMS error in the fit.

The 95% confidence interval, C, for a set of n data points of the form (x_i, y_i), is computed as follows:

$$C = t_{.025}\, s \sqrt{\frac{1}{n} + \frac{x_0^2}{\sum x_i^2} + 1}$$

$$s^2 = \frac{\sum_i e_i^2}{n-2}$$

$$x_0 = x - \left(\frac{\sum x_i}{n} \right) \tag{41}$$

where $t_{.025}$ is 95% T-distribution percentile for (n-2) degrees of freedom, n is the number of points used in the least squares fit, s^2 is the residual variance, and e_i is the distance of each point, y_i, from the line of best fit. The interpolation is calculated at point x.

For an interpolation to be regarded as valid, at least 3 leads must occur within the span of the interpolator, with at least one on either side of the floe.

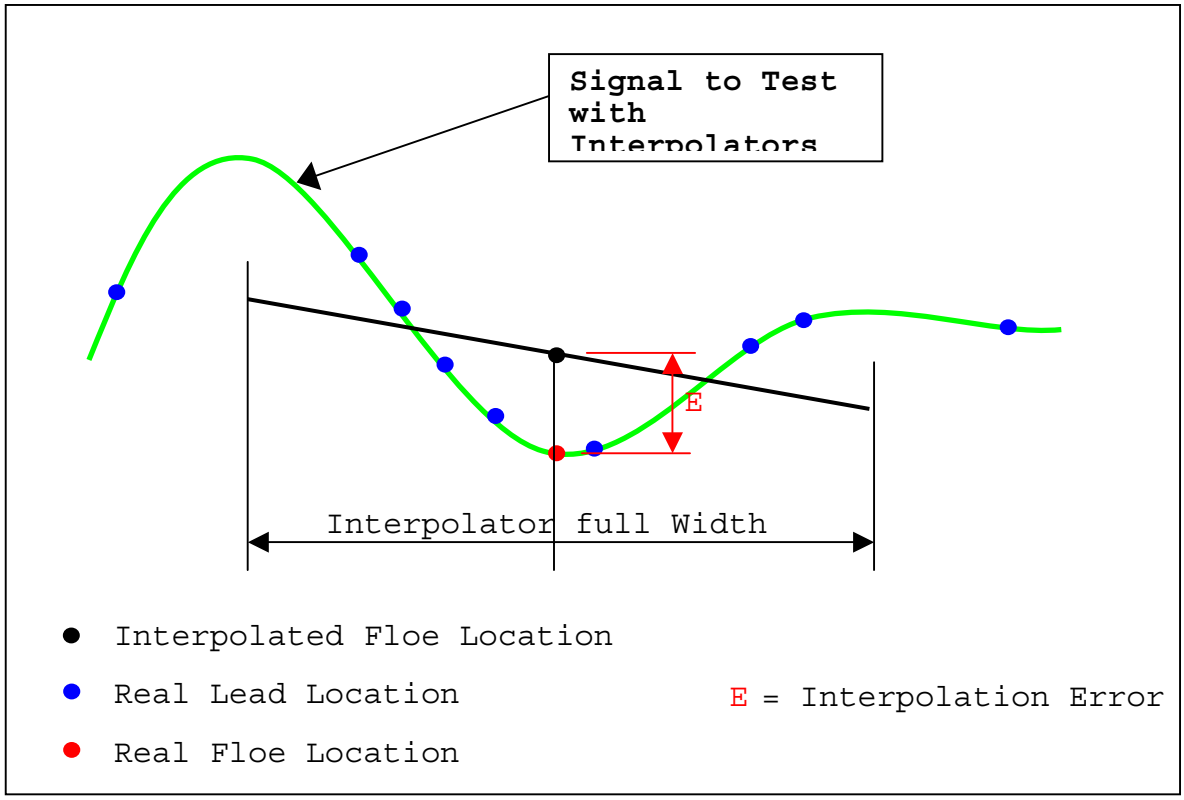

Fig. 4.1: Method used to investigate interpolator properties. At each floe location the linear interpolation error E is measured as a function of the interpolator full width W. Also measured as a function of W are the quadratic interpolation error and the 95% confidence interval for the linear interpolation.

Figure 4.2 shows the typical variation of the three properties above at a few individual floe locations along a single arc of ERS-2 data. The lead sampling and nature of the signal to be interpolated vary so rapidly from floe to floe that little can be deduced from measurements at a single floe location. Moreover, designing an interpolator which changes width from floe to floe, based on measurements only at one floe location, would produce extremely unstable results. To overcome this problem the three properties above are averaged over complete cycles, and then in 1 degree latitude by 5 degree longitude boxes within each cycle to see how they vary both temporally spatially.

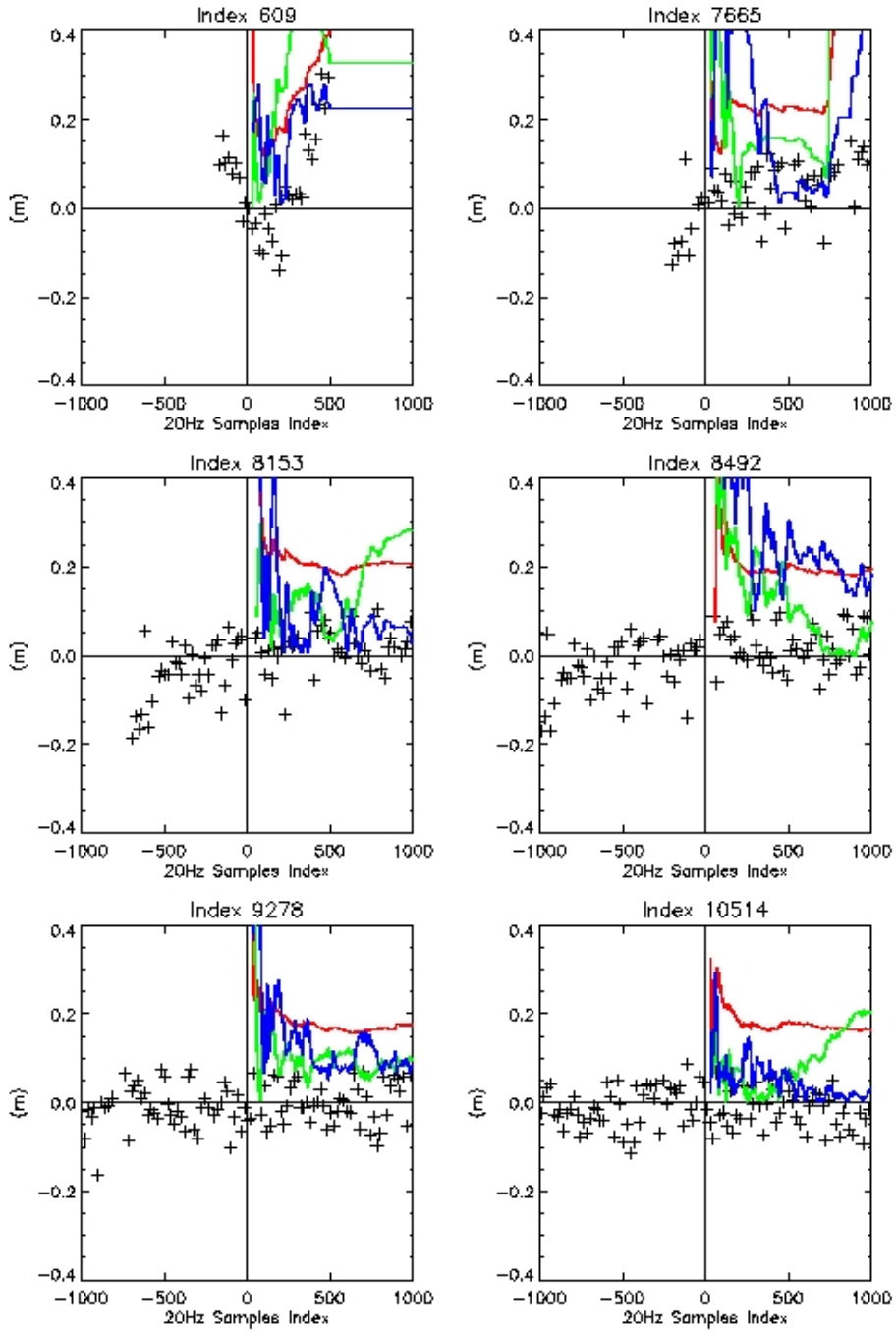

Fig. 4.2: Variation of Interpolation Metrics from Floe to Floe. The floe location is in the centre of each plot at (0,0) and the lead locations are marked with crosses at their correct height and distance from the floe. The red, green and blue lines are all scaled to fit the plot. The red line shows the change in 95% confidence interval in the linear fit with increasing interpolator width. The green line shows the absolute error in the linear fit and the blue line shows the absolute error in the quadratic fit. As an example, the position of the blue line at 500 samples shows (scaled) the absolute error in the interpolation at the floe location using a quadratic fit to all data within ±500 20 Hz samples of the floe location.

Table 4.1 shows the signal used in each run of the interpolator test and the questions which the run attempts to answer.

Table 4.1: Signals used in individual runs of the interpolator and the properties of those signals.

Signal	**Property**
OCCAM dynamic topography model. MICOM dynamic topography model. Estimate of error in dynamic topography models.	*What is the optimum interpolator width and interpolation method for the dynamic topography error signal? Does it vary spatially and temporally? Is much gained by removing a modelled dynamic topography before interpolation?*
GOT00 tidal model. Padman tidal model. Estimate of error in tide models.	*What is the optimum interpolator width and interpolation method for the tidal error signal? Does it vary spatially and temporally? Is much gained by removing a modelled tide before interpolation?*
The ArcGP geoid.	*What is would be the error in the estimated freeboard if geoid variations were neglected? The comparison also shows another way to look at the geoid variability.*
Estimate of the range of geoid error signals possible based on signals generated with both the minimum and maximum correlation length and minimum and maximum standard deviation expected in the Arctic geoid error signal.	*What is the optimum interpolator width and interpolation method for the geoid error signal?*
Error in the sea surface height by combining the estimates of the error in the geoid, tidal and dynamic topography signals.	*For unmodelled sea surface height, what is the optimum interpolator width and interpolation method? How does it vary spatially and temporally? Based on this, how would one design a smart interpolator?*

4.2. Validation of "smart" MSS estimation

Generation of Real Lead and Floe Locations

The real lead and floe locations are taken from cycles 79 to 84 or ERS-2 data which span the winter of 2002/2003. The exact times of these cycles of data are shown in Table 4.2.

Table 4.2: Start and end dates associated with five ERS-2 cycles which span the winter of 2002/2003.

Cycle	**Start Date**	**End Date**
79	04-NOV-2002	09-DEC-2002
80	09-DEC-2002	13-JAN-2003
81	13-JAN-2003	17-FEB-2003
82	17-FEB-2003	24-MAR-2003
83	24-MAR-2003	28-APR-2003
84	28-APR-2003	02-JUN-2003

Generation of Dynamic Topography Signal and Estimate of Dynamic Topography Error

The following two models of Dynamic Topography were used in the test runs with the interpolators:

a) The Miami Isopycnic Coordinate Ocean Model (MICOM, see Dynamic Topography section in this report)
b) The Ocean Circulation and Climate Advance Modelling project (OCCAM, see Dynamic Topography Section in this report) from the National Oceanography Centre in Southampton, UK.

No OCCAM/MICOM data was available for the 2002/2003 winter so the data from the nearest month in the 1999/2000 winter was used (Table 4.3).

Table 4.3: Dates of the dynamic topography model data utilised in this study.

Cycle	OCCAM / MICOM Data
79	November 1999
80	December 1999
81	January 2000
82	March 2000
83	April 2000
84	May 2000

Figure 4.3 and Figure 4.4 show the OCCAM and MICOM model values for the months listed above.

To estimate the Dynamic Topography Error signal, the difference between the OCCAM and MICOM models at each satellite location was used. Figure 4.5 shows this estimated error signal at each lead location for all cycles. Note that the amplitude of the error signal shown here is of the same order of magnitude as the individual OCCAM and MICOM signals.

Generation of Tidal Signal and Estimate of Tidal Error

The following two tide models were used in the test runs with the interpolators:

a) The Arctic Ocean Tidal Inversion Model (AOTIM-5, see Padman and Erofeeva, 2004). This model is referred to here as the Padman model. See Tides section in this report.
b) The GOT00 Model (Ray, 1999). See Tides section in this report.

As with the dynamic topography, the tidal error signal was estimated by using the difference between the two tidal models at each satellite location. Figure 4.6 shows the RMS difference between the two models at each lead location for the various cycles, binned on a 5 degree longitude by 1 degree latitude grid. Note how similar the two models are in the Beaufort Sea.

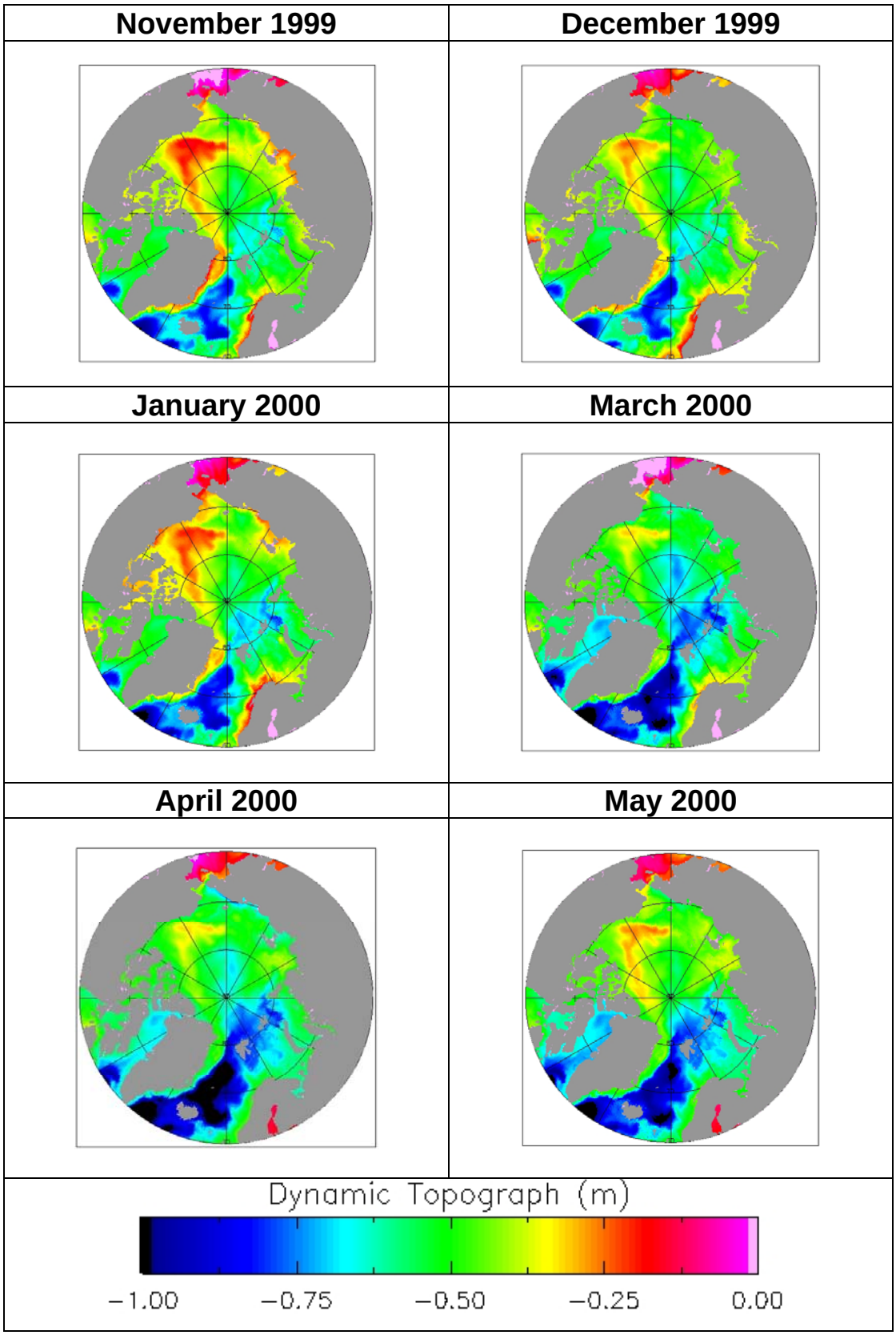

Fig. 4.3: OCCAM Model Dynamic Topography Values Used

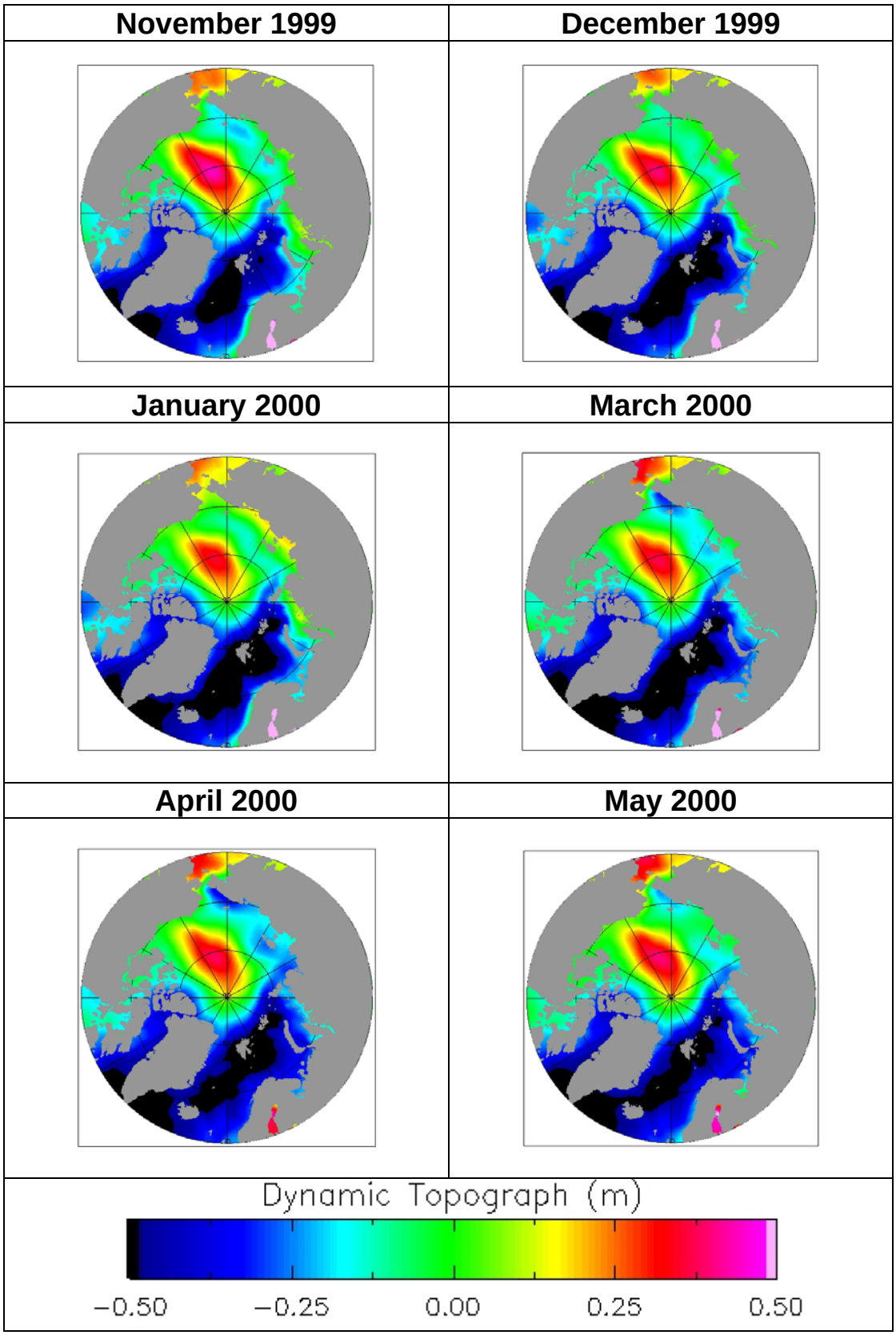

Fig. 4.4: MICOM Model Dynamic Topography Values Used

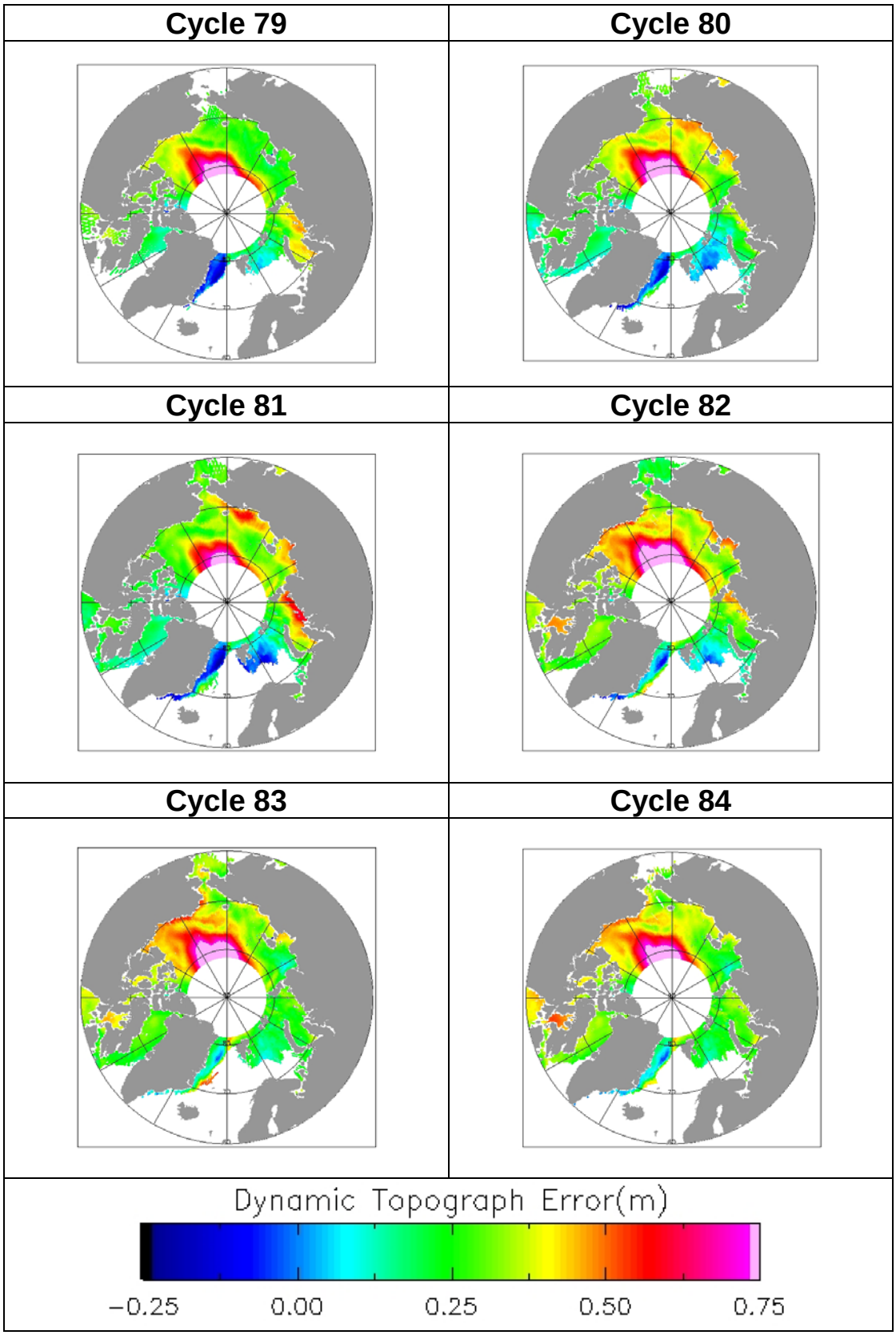

Fig. 4.5: Estimate of Dynamic Topography Error at Lead Locations

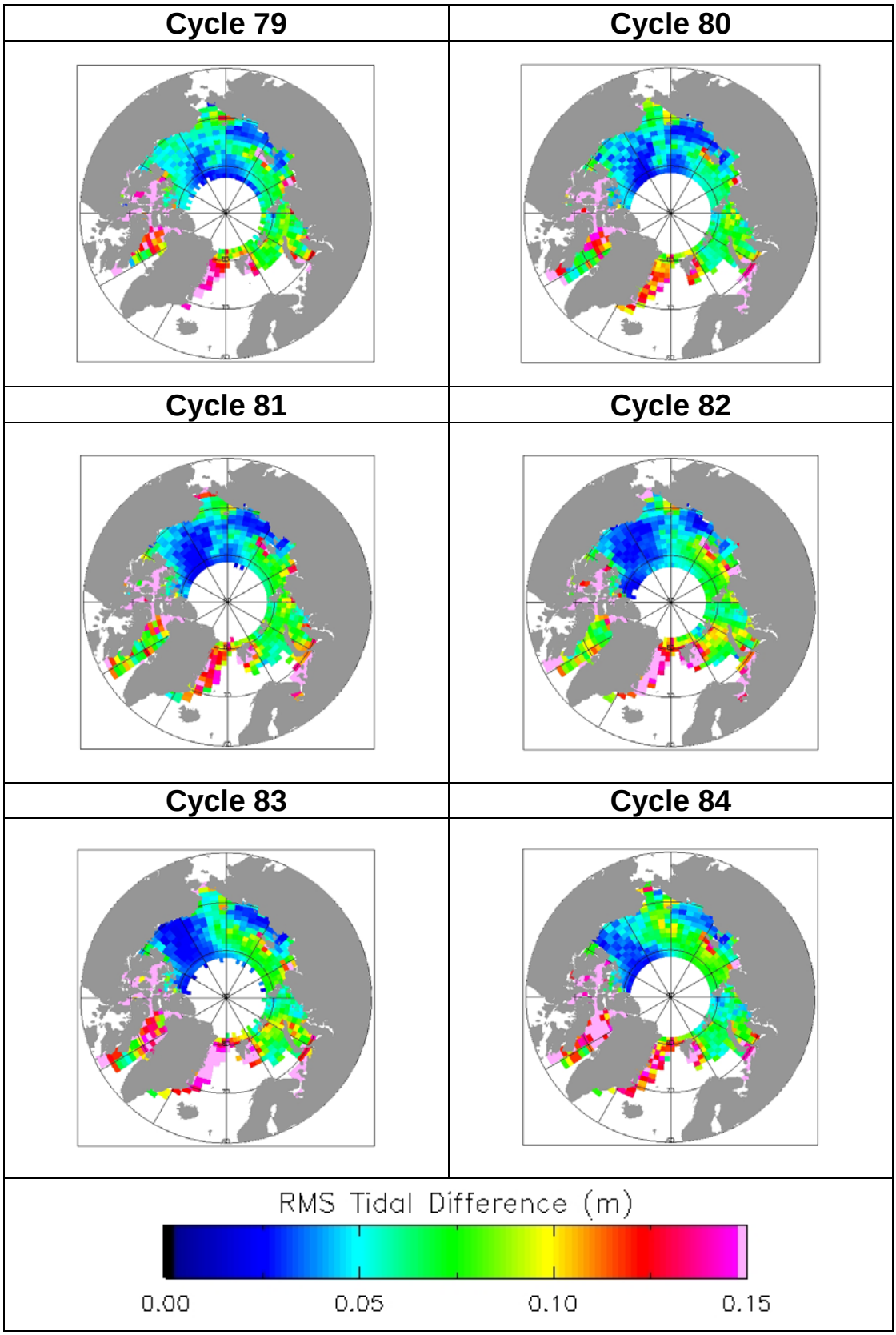

Fig. 4.6: RMS Difference between GOT00 and Padman Tidal Models.

Generation of ArcGP geoid interpolation errors for the actual lead locations

When using the "smart" interpolator directly on the ArcGP geoid grid, with no noise added, a measure is obtained of the errors in using or not using the geoid prior to using the estimator.

Figure 4.7 shows the geoid interpolation error when using the smart interpolator, i.e. the difference between the actual geoid value at the each floe location , and the interpolated value for the lead positions. The results were analysed for 6 ERS cycles, but are only shown in Figure 4.7 for cycle 81, for three different interpolator widths (100 km, 200 km and 300 km). It is seen that for the short (100 km) interpolation width, the geoid interpolation error is relatively small (less than 10 cm), but for the larger widths the interpolation error is large, and the use of an apriori geoid model essential.

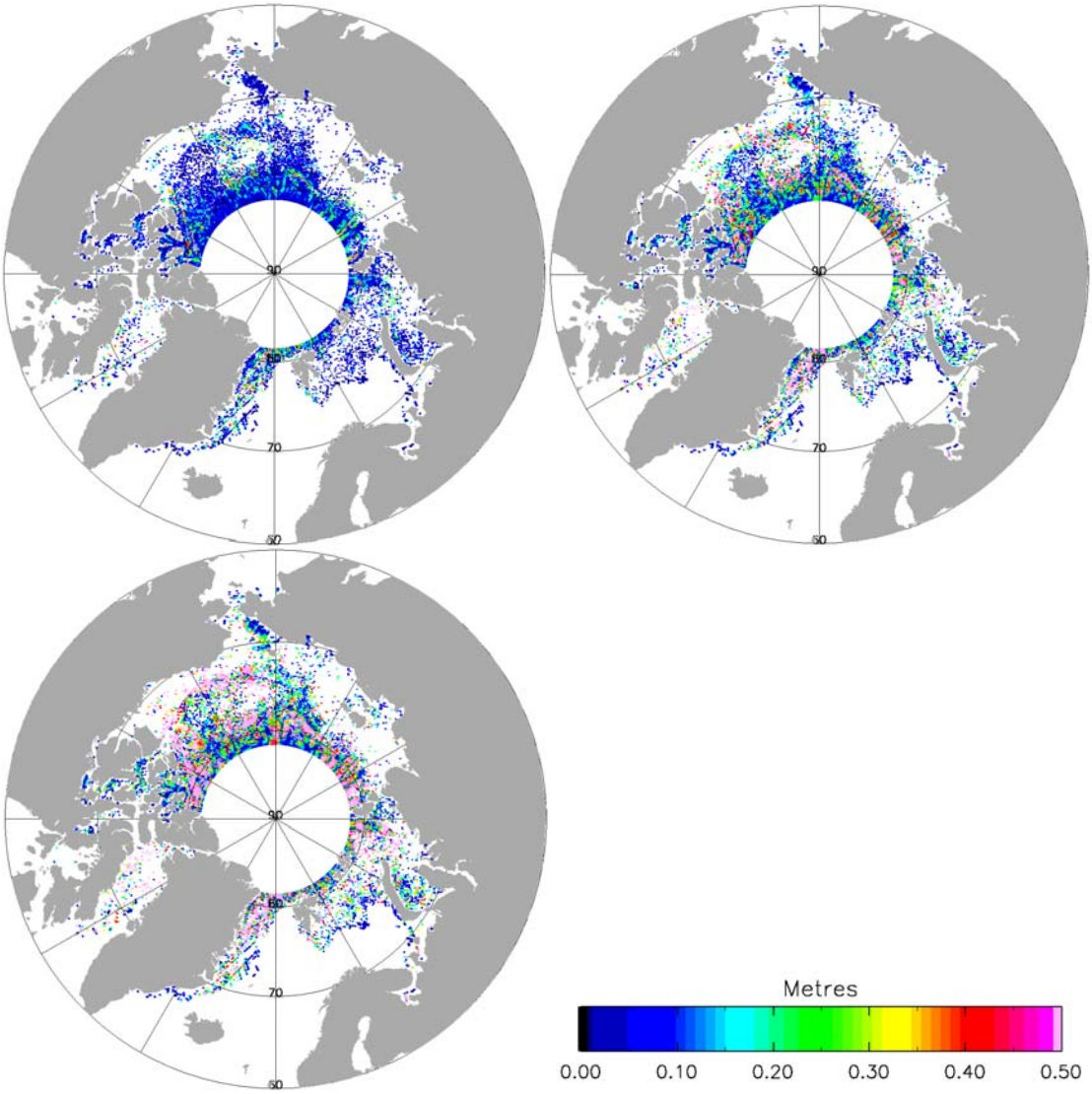

Figure 4.7. Geoid interpolation errors at floe locations from "smart"interpolation from lead locations, ERS cycle 81. Top left: 100 km interpolator width, top right: 200 km, lower left: 300 km.

Simulation of the Arctic Geoid Error

We generated profiles of geoid error using errors in line with the computed error covariances of Section 1.4, shown in Figure 4.8. In order to generate these profiles we first generated a sequence of Gaussian random numbers, whose distribution had prescribed mean and standard deviation. A portion of such a sequence is illustrated in Figure 4.9 (a).

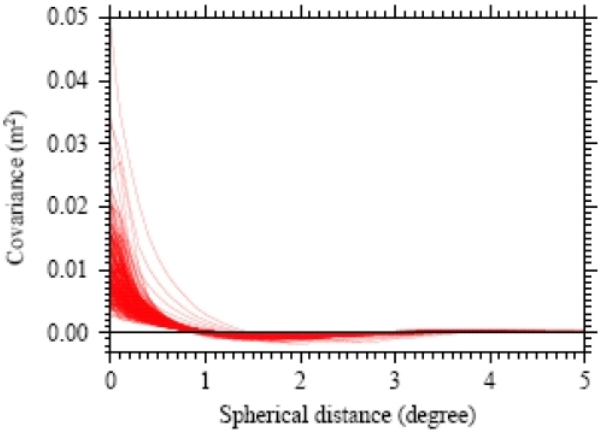

Fig. 4.8: Used error covariance functions along the meridian of 15° computed for latitudes between 64° and 90°, with equidistance of 0.1°, cf. Section 1.4.

The error covariance function of the random number series however did not correspond to the computed error covariances. We therefore prescribed an autocorrelation function, called the desired autocorrelation function (DACF), which represented the calculated error covariance functions (Figure 4.8).

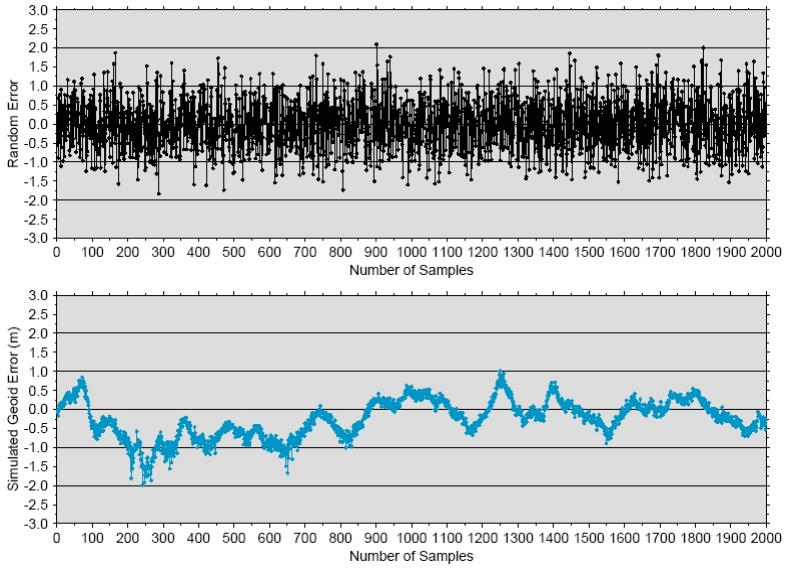

Fig. 4.9: (a) A portion of an initial Gaussian random number sequence which has a mean of 0 cm and a standard deviation of 66 cm. (b) The re-sequenced random number series representing a profile of geoid error with a standard deviation of 66 cm, correlation length of 0.47°, and a covariance function that coincided with computed values.

The correlation coefficients, r_k, at lags k, of the DACF were of the form

$$r_k = e^{-\frac{SS}{R}k} \tag{42}$$

where R is the correlation length of the simulated geoid error and SS is the sample spacing. The DACF (red) and the initial autocorrelation function of the Gaussian random number sequence (blue) are illustrated in Figure 4.10

We computed the autocorrelation function of the time series following *Box and Jenkins* (1976). The data consist of n samples x_i, for $i = 1, 2,..., n$. The autocorrelation coefficients at lags $k = 1, 2,..., K$ are defined as

$$r_k = \frac{\sum_{i=1}^{n-k}\left(x_i - \bar{x}\right)\left(x_{i+k} - \bar{x}\right)}{\sum_{i=1}^{n}\left(x_i - \bar{x}\right)^2} \tag{43}$$

where K is the maximum lag. In this analysis, we set the maximum lag as follows

$$K = \frac{6 * R}{SS} \tag{44}$$

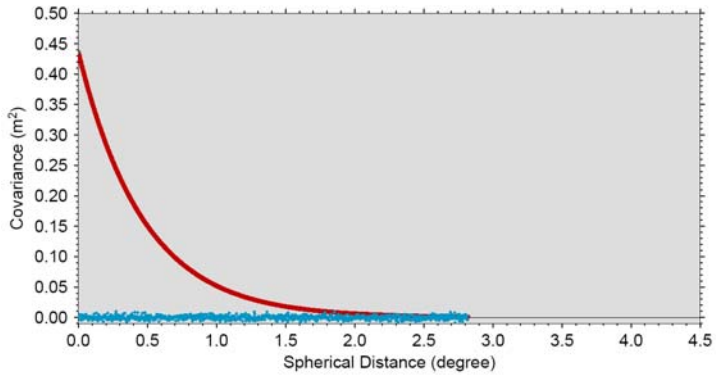

Fig. 4.10: The error covariance functions of the desired autocorrelation function (red) and the Gaussian random number series (blue).

Using a technique known as stochastic minimisation (*Hunter and Kearney*, 1983), the sequence of Gaussian random numbers was subsequently shuffled until the actual autocorrelation function (AACF) coincided with the DACF. The stochastic minimisation technique works in the following manner. First the AACF of the sequence is calculated using (43) and compared to the DACF using the sum squares criterion

$$SS_i = \sum_{k=0}^{K}\left[AACF_i(k) - DACF(k)\right]^2 \tag{45}$$

Two samples in the sequence are then randomly chosen and the values of these samples are interchanged. After the interchange, the AACF is recalculated and compared to the DACF using (45). If the sum squares value is less than the previous sum squares value, then the interchange is preserved, otherwise the values are restored to their previous positions. The stochastic minimisation process continues until the DACF and the AACF converge, i.e. SS <

some small value[1]. Upon convergence of the DACF and the AACF, the Gaussian random number series has been re-sequenced so that both the standard deviation and the error covariance function correspond to the computed values (Figure 4.8) and the series represents a realistic profile of geoid error (Figure 4.9b). Figure 4.11 shows the DACF (red) and the AACF (blue) of the profile of geoid error.

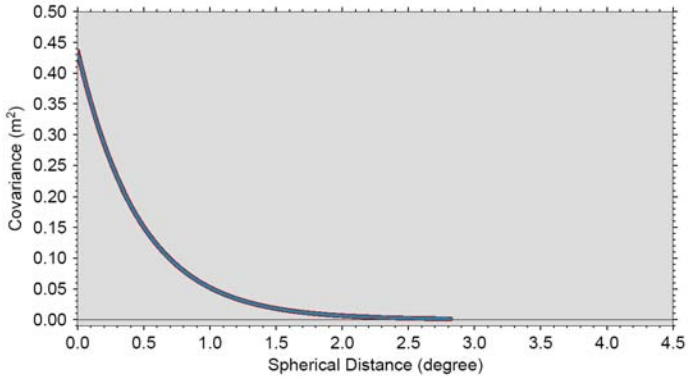

Fig. 4.11: The error covariance functions of the desired autocorrelation function (red) and the re-sequenced Gaussian random number series after stochastic minimisation, which represents a profile of geoid error (blue).

Table 4.4: Characteristics of the simulated profiles of geoid error.

Simulated Profiles of Geoid Error			
	Mean Error (cm)	Standard Deviation of Error (cm)	Correlation Length (°)
Profile 1	0	5	0.1 (11.10km)
Profile 2	0	5	0.47 (52.17km)
Profile 3	0	66	0.1 (11.10km)
Profile 4	0	66	0.47 (52.17km)

We simulated the geoid error profiles for a number of different conditions and these are outlined in Table 4.4. The correlation lengths and standard deviations used correspond to the minimum and maximum values reported in Section 1.4 for covariance estimates of the Arctic Ocean calculated using a regional covariance function.

Discussion of results

Interpolation of the Dynamic Topography Error Signal.

The red lines in Figure 4.12 shows the change in RMS interpolation error as a function of interpolator width using a linear interpolator for the 6 cycles of ERS-2 data. The four red lines in ascending order in the plot are for 2 cm, 5 cm, 10 cm and 20 cm of random noise. The results for each cycle are reasonably similar. The minimum point on each line shows the interpolator width for which the linear interpolation error is a minimum, i.e. the optimum width of the interpolator. The location of the minimum is highly dependent on the level of random noise, occurring at a wider interpolator width the higher the noise level. The blue lines show the equivalent 95% confidence interval (scaled to fit on the same axes). Unlike the RMS interpolation error, this does not need the value of the dynamic topography error at the floe location to compute, and hence could be computed using real satellite data if the signal in the satellite data were purely unmodelled dynamic topography. Unfortunately the minimum

[1] In this analysis we consider the DACF and the AACF to have converged when SS $\leq$ 0.002 and the stochastic minimisation process is subsequently halted.

does not occur at the same point as the RMS error curve and hence could not be used to determine the optimum interpolator width in real data.

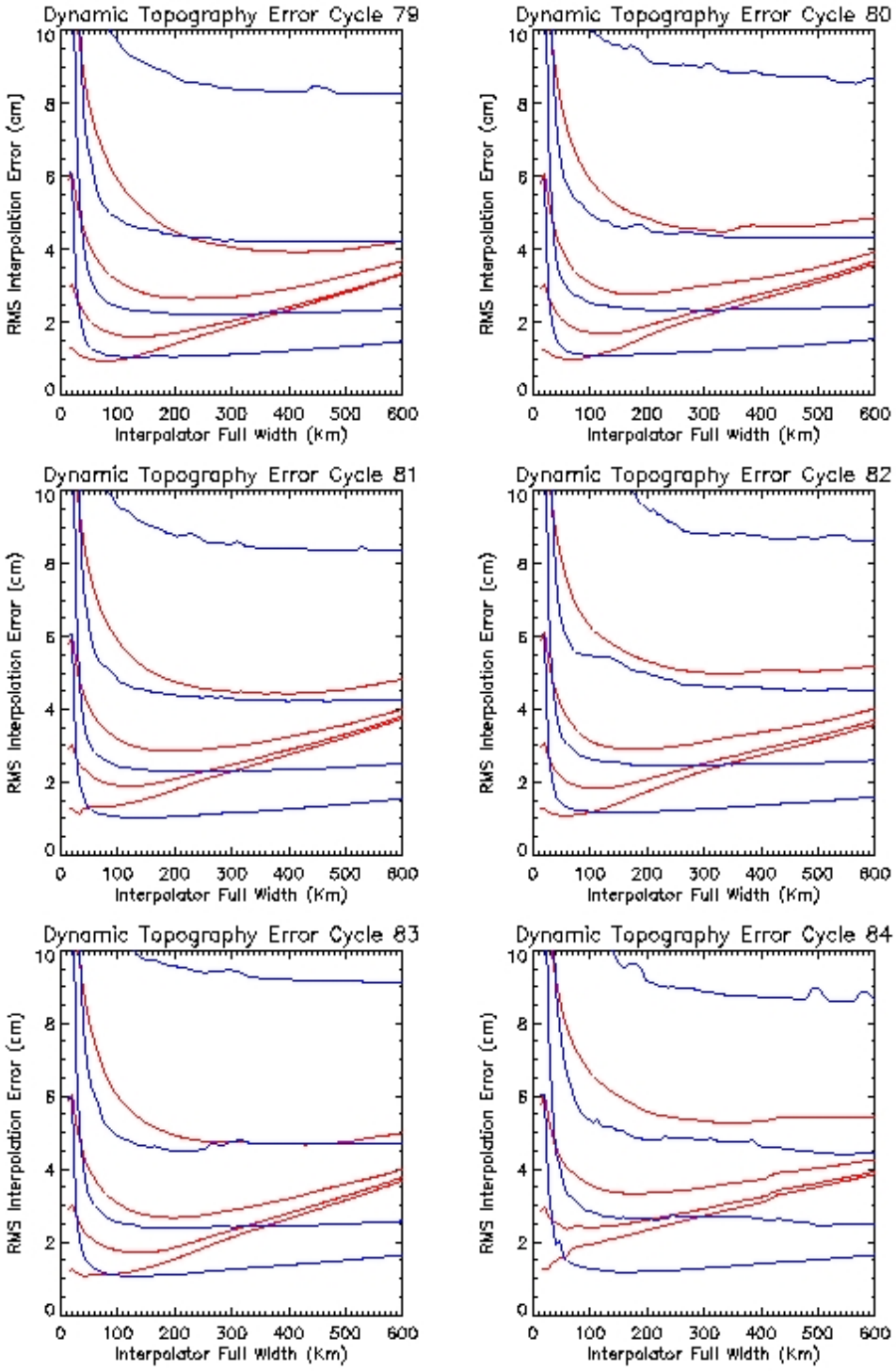

Fig. 4.12: Interpolation of Residual Dynamic Topography Signal. Comparison of RMS linear interpolation error (red) with scaled 95% confidence interval (blue). RMS random noise of 2cm, 5cm, 10cm, and 20cm added.

Figure 4.13 shows the same RMS error curves in red as above, but compares them with the RMS error if a quadratic fit is used in the interpolation instead of a linear fit. The optimum interpolator width using the quadratic fit occurs at a wider point. Unfortunately the RMS error

in the quadratic fit at the optimum width is no lower than when using the linear fit, so no reduction in noise is achieved. There could however be an

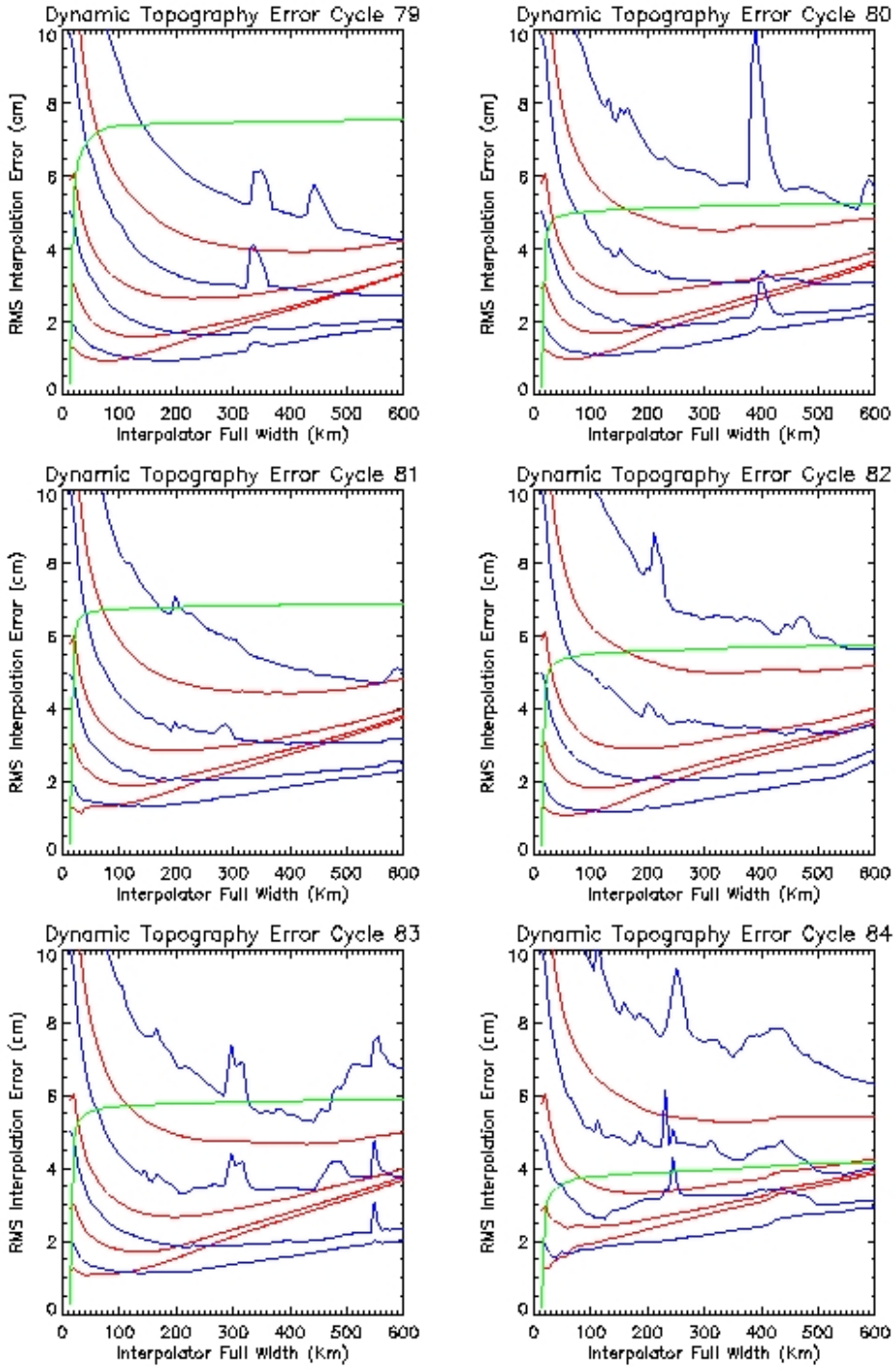

Fig. 4.13: Interpolation of Residual Dynamic Topography Signal. Comparison of RMS linear interpolation error (red) with RMS quadratic interpolation error (blue). Number of successful interpolations is shown in green. RMS random noise of 2cm, 5cm, 10cm, and 20cm added.

advantage to having the optimum width at a wider point if the number of successful interpolations increases as a result. The green line on each plot shows the number of successful interpolation for each interpolator width (scaled to fit the plot). At widths of 50 km or more, very few more successful interpolations occur as a result of using a wider

interpolator, again giving the quadratic interpolator no real advantage over the linear one. In view of the higher stability of a linear fit, there is no real reason to use a quadratic fit instead.

Figure 4.14 compares the RMS error interpolating the dynamic topography error signal with the RMS error of interpolating the pure OCCAM and MICOM signals. This is to show the difference in the interpolation statistics if the dynamic topography is still present in the sea surface height, compared with if an attempt has been made to remove it with a model. The plots show that interpolation fit to the dynamic topography error signal is about the same as for the MICOM model and higher than for OCCAM. This indicates that there is no real advantage in removing a modelled dynamic topography signal from the sea surface height prior to interpolation because the uncertainty in the model is as high as the values in the model itself. In a way this is obvious from the comment in section 2.2 where the uncertainty in the models was seen to be of the same order as the model values themselves.

Finally Figure 4.15 and Figure 4.16 show the minimum point of the RMS linear interpolation error curve (i.e. the optimum interpolator width) for all 6 cycles and two levels of noise, when the curves are averaged in a 1 degree latitude by 5 degree longitude box. Qualitatively they show that the optimum interpolator width is spatially and temporarily variable, however in view of the size of the difference between the two models used to create the curves and maps, nothing further should be inferred from them.

Interpolation of the Tidal Error

The results from the runs interpolating the tidal signals are very similar to those discussed above. Figure 4.17 shows in red the change in RMS interpolation error as a function of interpolator width using a linear interpolator for the 6 cycles of ERS-2 data. In ascending order the four red lines are for noise levels of 2 cm, 5 cm 10 cm and 20 cm random noise. As with the dynamic topography error, the location of the minimum and hence the optimum interpolator width is highly dependent on the level of random noise. It occurs at a wider point the higher the noise level. The results are quite similar from cycle to cycle. As before the behaviour of the 95% confidence interval in the linear fit does not mimic the observed RMS error in the linear fit and hence could not be used as a proxy for the RMS error curve with real data if the sea surface height were due only to unmodelled tides.

Figure 4.18 compares using a linear fit to the tidal error signal with a quadratic fit. As with the dynamic topography, the minimum RMS error in the fit occurs at a wider interpolator width using the quadratic fit, but the RMS error at the minimum is no lower for the quadratic fit and in this case is occasionally higher (see cycle 84). Since the number of successful interpolations does not increase much with an interpolator wider than 50 km, and the behaviour of the quadric fit is rather more unstable than the linear fit, there is no real advantage in using a quadratic fit over a linear fit to the tidal error signal.

Figure 4.19 is to show what advantage there is in removing a tide model prior to interpolation. It compares the RMS error in the linear fit when interpolating the tidal error signal with the RMS error if the sea surface height were due only to the Padman or GOT00 tides. The fit to the residual tidal error signal is no better than to the Padman or GOT00 models by themselves indicating that removing a tide model does little to improve the performance of the interpolator.

Finally Figure 4.20 and Figure 4.21 show the minimum point of the RMS interpolation error curve for the linear fit (i.e. the optimum interpolator width) for all 6 cycles and two noise levels, when the curves are averaged in a 1 degree latitude by 5 degree longitude box. The plots do indicate that in some areas like the Beaufort Sea, where our estimate of the tidal error shows it is likely to be small, the optimum interpolator width is considerably wider than in

areas where the error in the tide model is likely to be high. If the sea surface height signal were only due to unmodelled tides, such plots could form the basis of a look-up table to determine the optimum interpolator width.

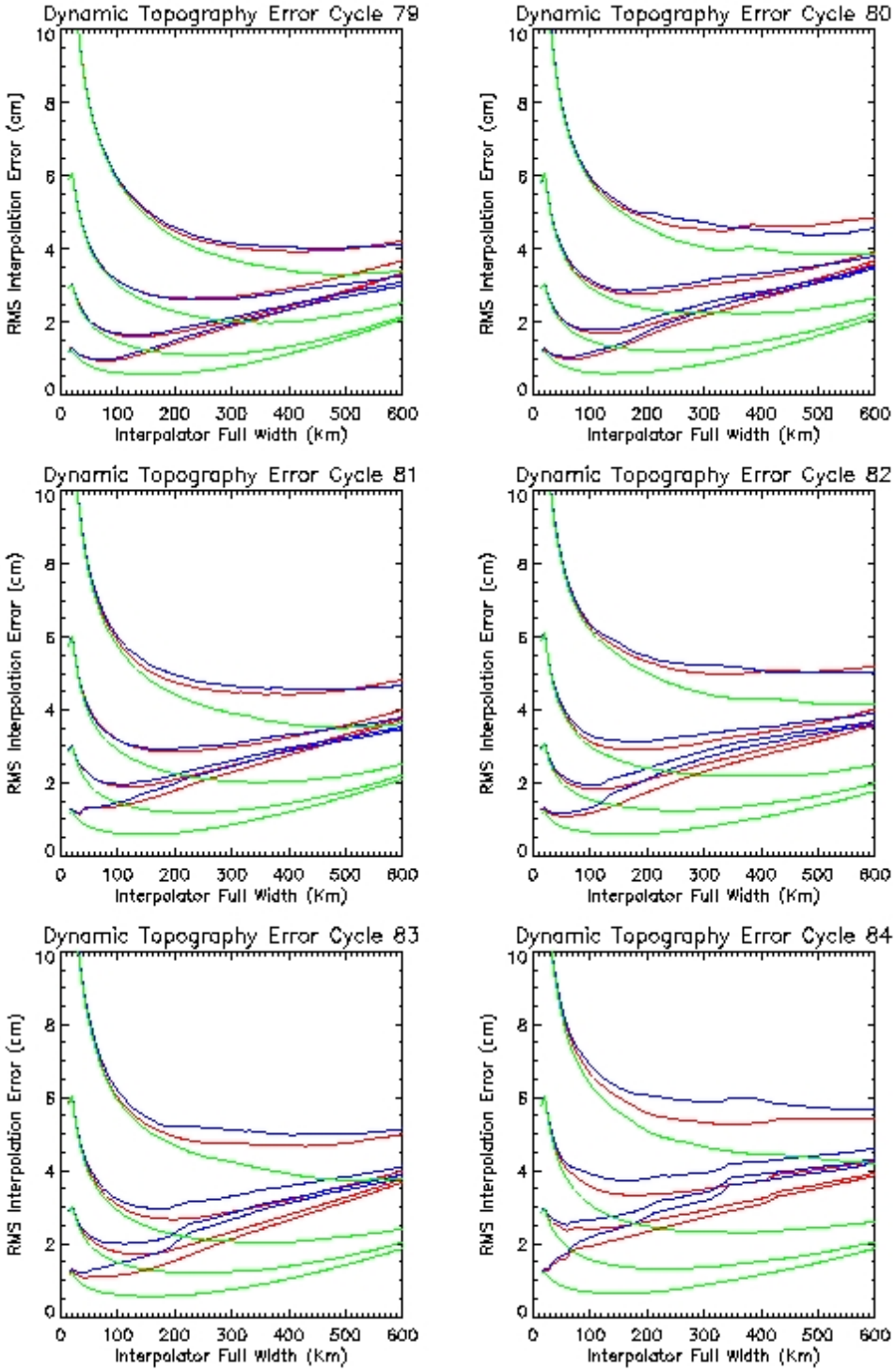

Fig. 4.14: Interpolation of Residual Dynamic Topography Signal. Comparison of RMS linear interpolation error of the dynamic topography residual (red) with actual dynamic topography signals from the OCCAM (blue) and MICOM (green) models. RMS random noise of 2cm, 5cm, 10cm, and 20cm added.

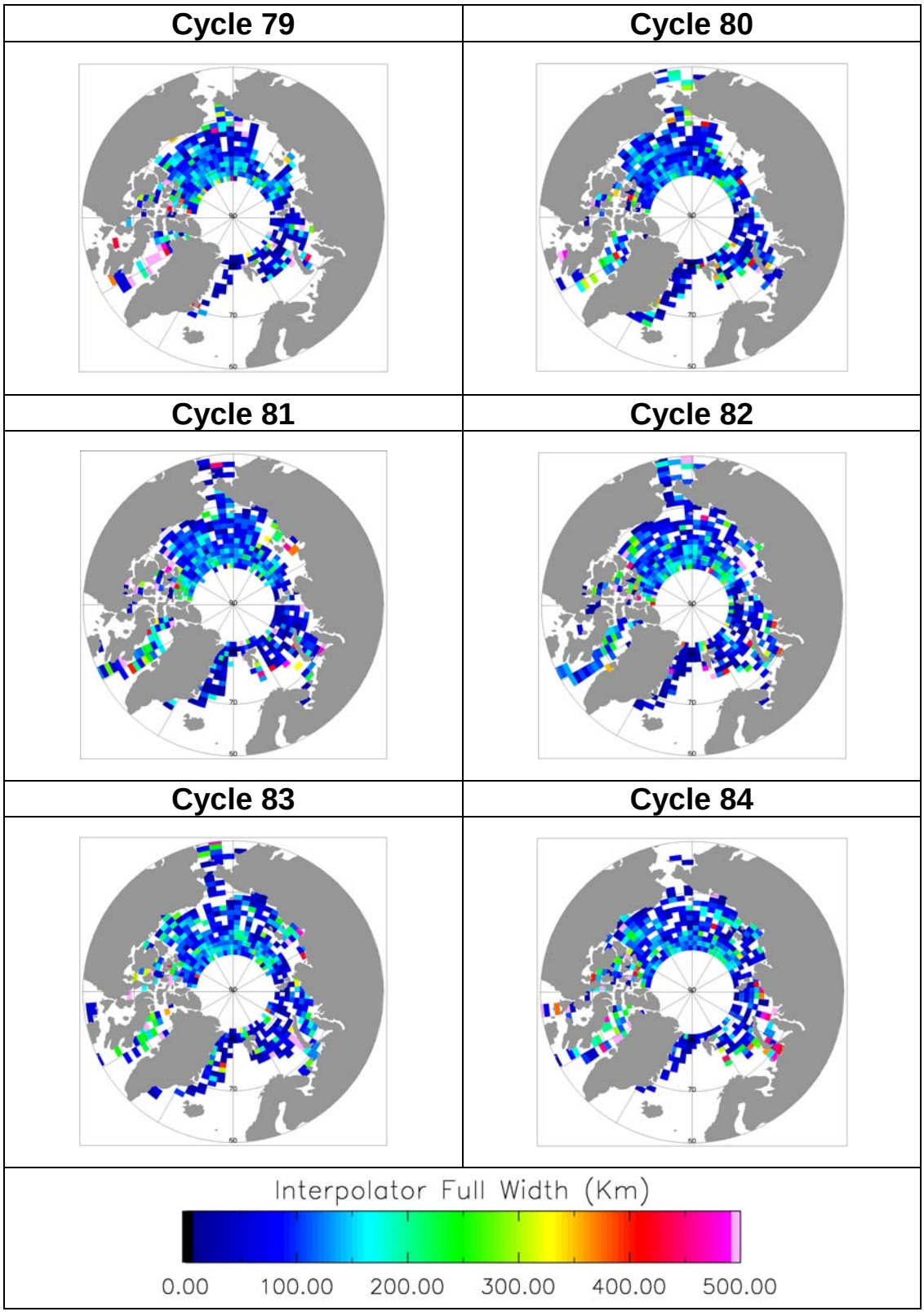

Fig. 4.15: Optimum Interpolator Width for Dynamic Topography Error with 2cm RMS Random Noise.

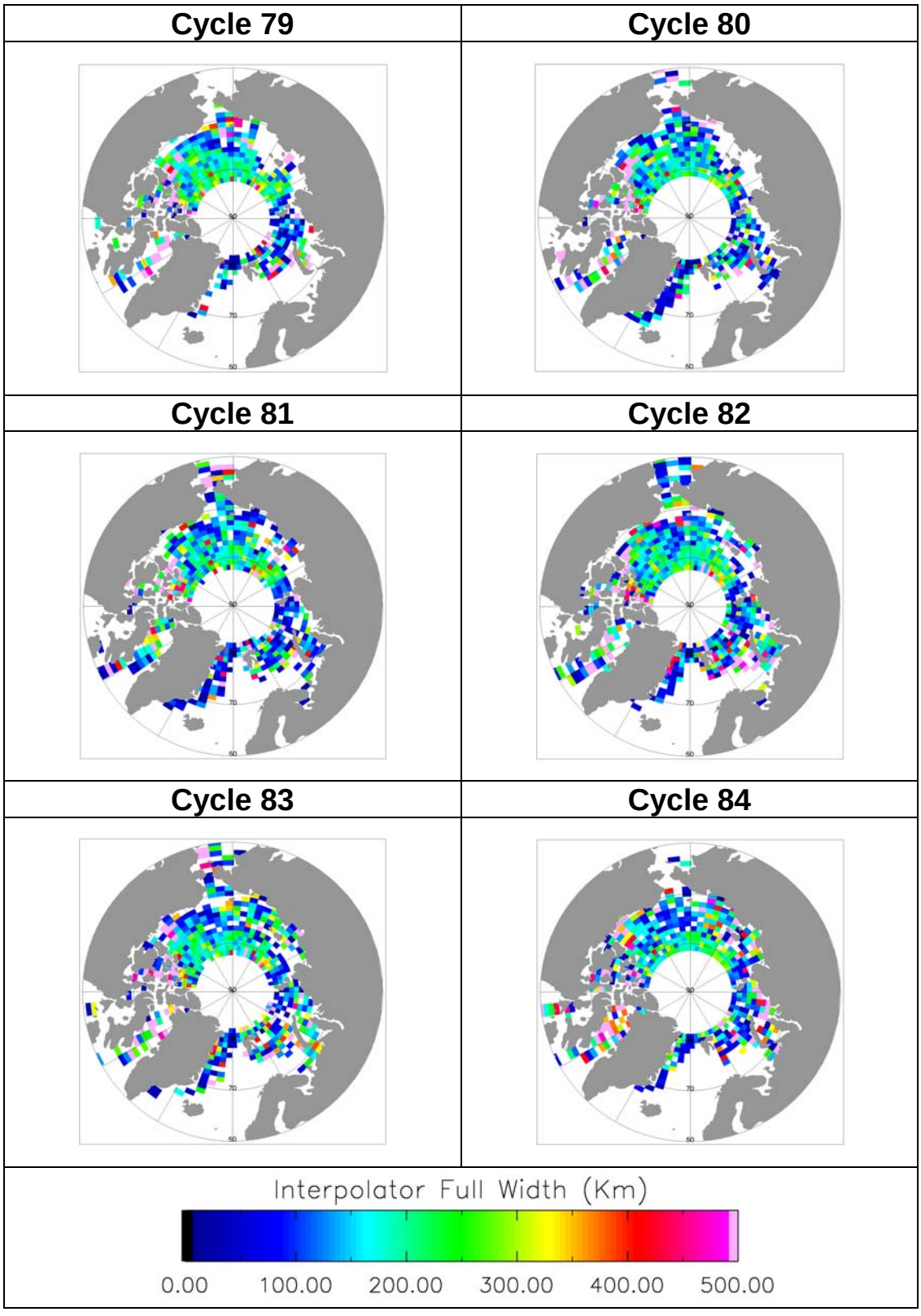

Fig. 4.16: Optimum Interpolator Width for Dynamic Topography Error with 5cm RMS Random Noise

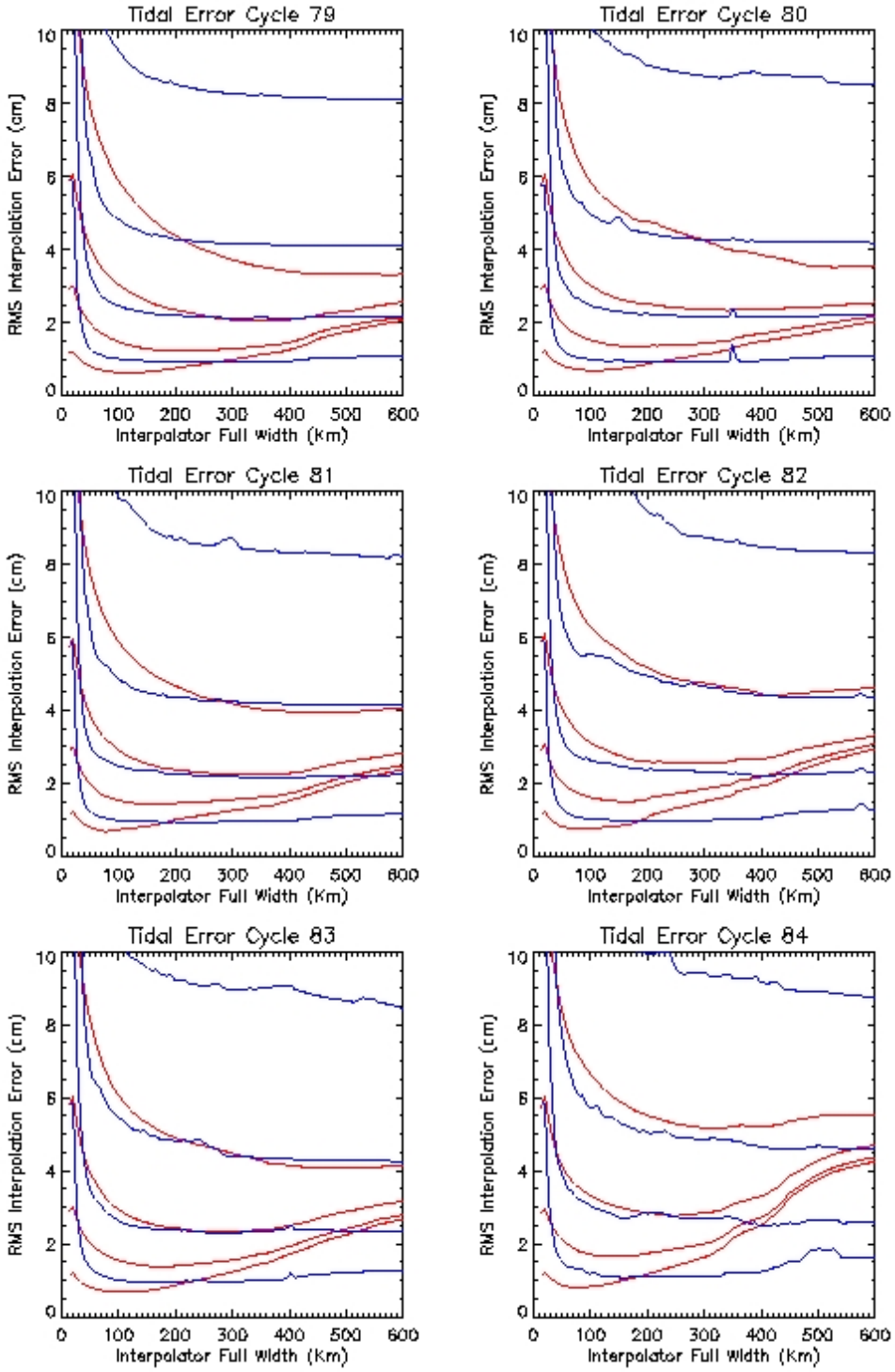

Fig. 4.17: Interpolation of Residual Tidal Signal. Comparison of RMS linear interpolation error (red) with scaled 95% confidence interval (blue). RMS random noise of 2cm, 5cm, 10cm, and 20cm added.

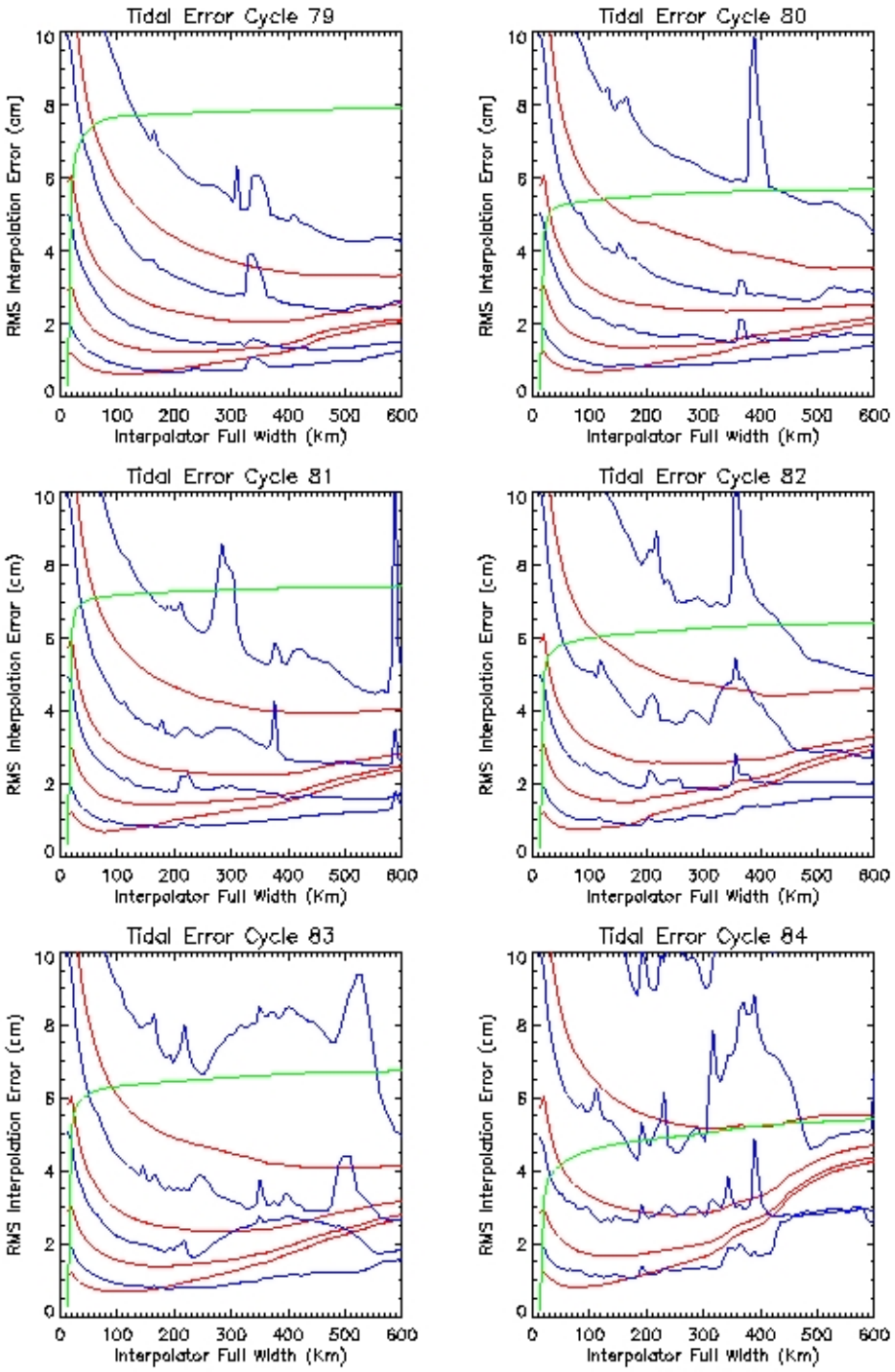

Fig. 4.18: Interpolation of Residual Tidal Signal. Comparison of RMS linear interpolation error (red) with RMS quadratic interpolation error (blue). Number of successful interpolations is shown in green. RMS random noise of 2cm, 5cm, 10cm, and 20cm added.

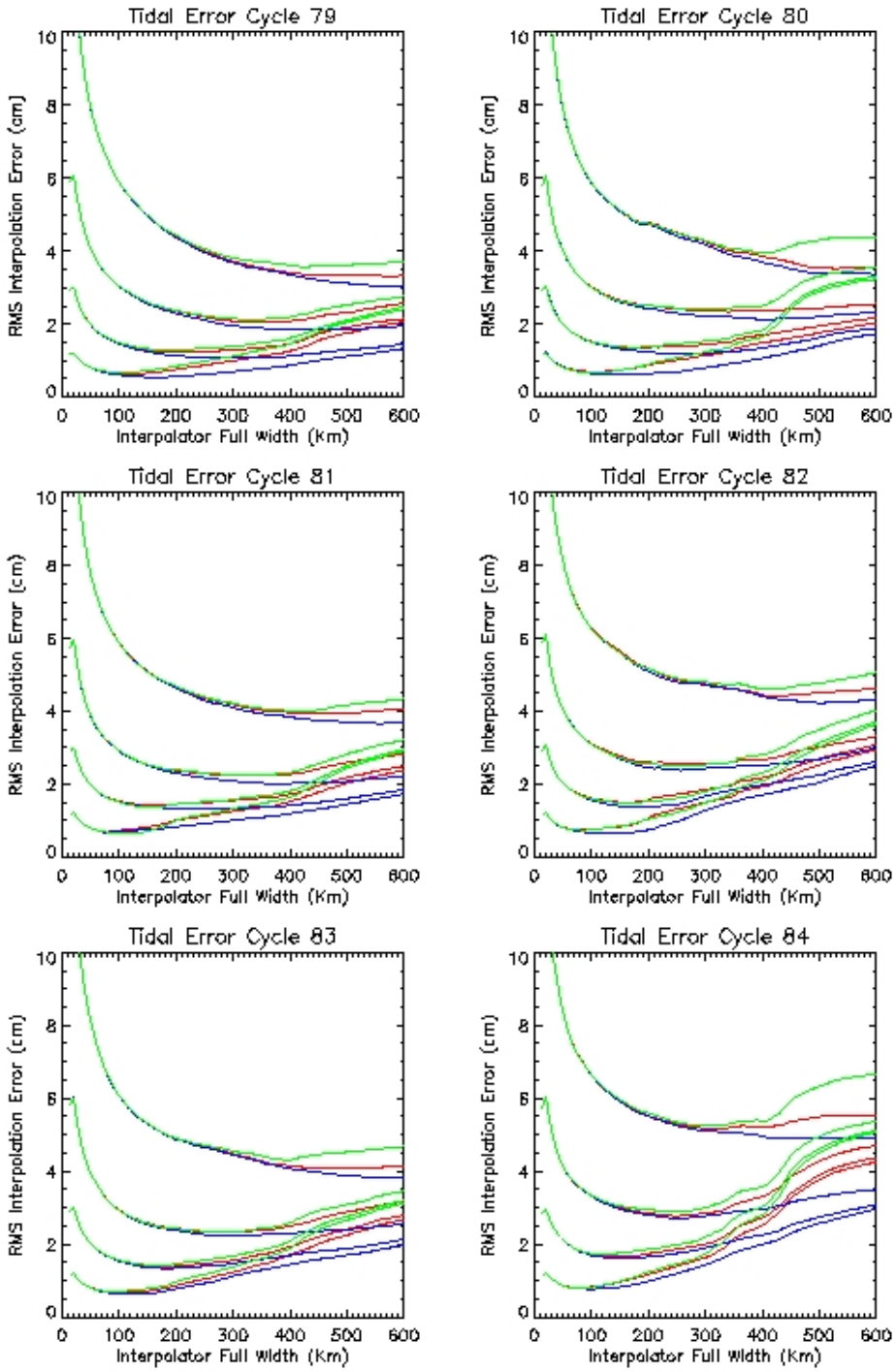

Fig. 4.19: Interpolation of Residual Tidal Signal. Comparison of RMS linear interpolation error of tidal residual (red) with actual tidal signals from Padman (blue) and GOT00 (green) models. RMS random noise of 2cm, 5cm, 10cm, and 20cm added.

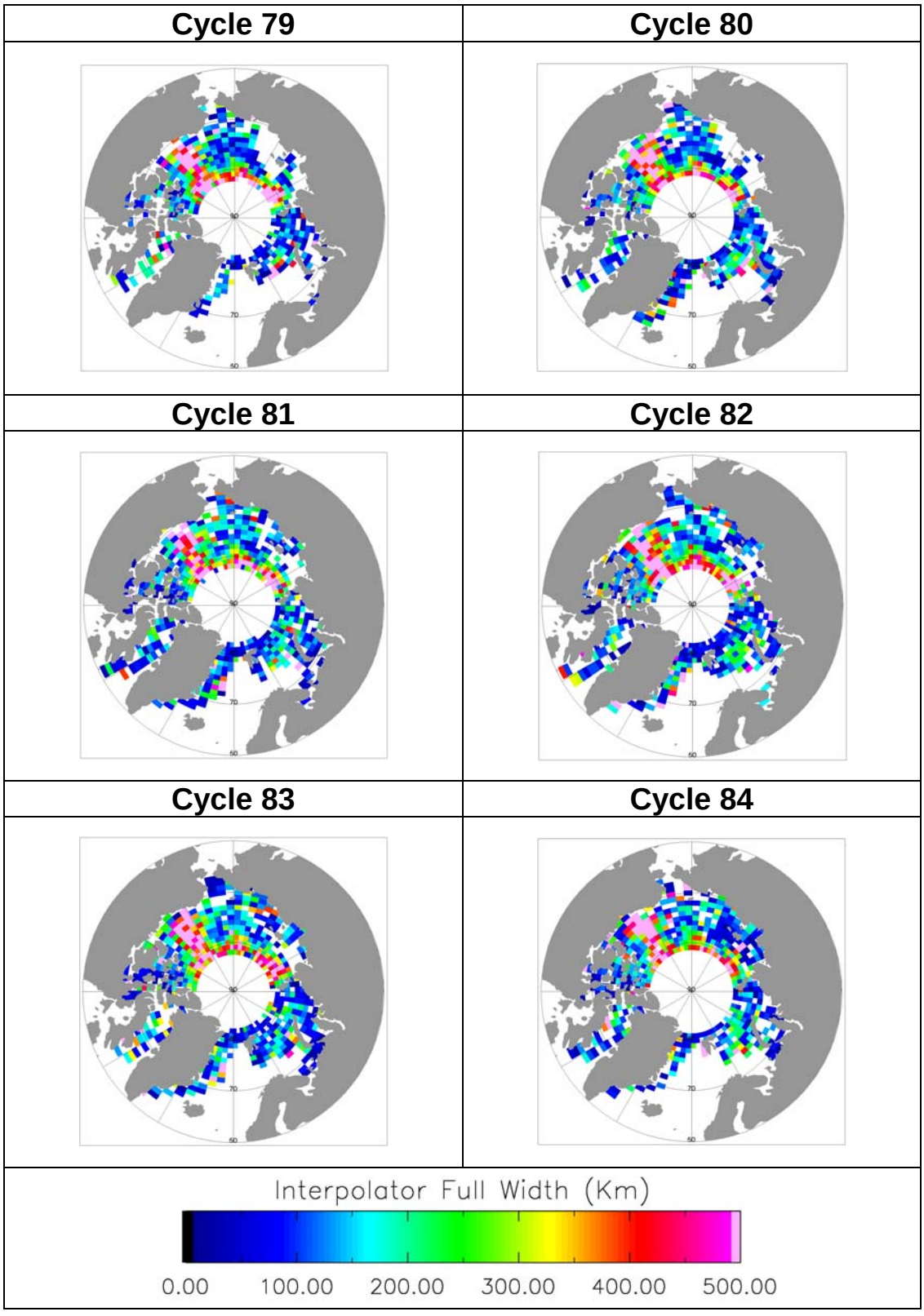

Fig. 4.20: Optimum Interpolator Width for Tidal Error with 2cm RMS Random Noise.

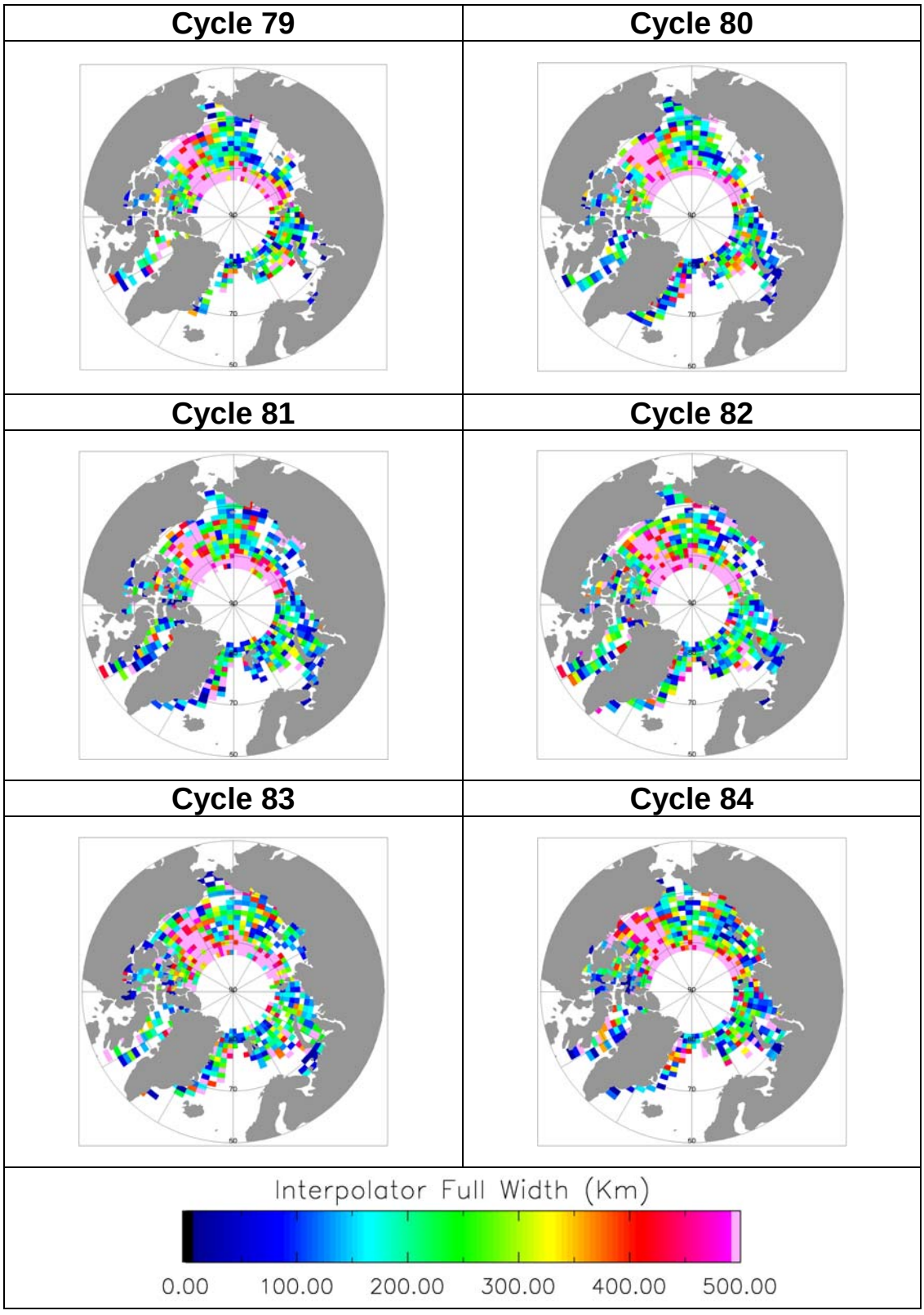

Fig. 4.21: Optimum Interpolator Width for Tidal Error with 5cm RMS Random Noise.

Interpolation of the Geoid Error.

All interpolation tests were run on the simulated geoid error signals mentioned in Section 2.4. For each test two values for the correlation length (11.10 km and 52.17 km) and standard deviation (5 cm and 66 cm) were used representing the extremes believed to be encountered in the Arctic. In all cases the behaviour of the 95% confidence interval (not shown) with increasing interpolator size did not correspond to the behaviour of the RMS error in the linear fit, and as with the tides and dynamic topography were discounted as being of any use. Figures 4.22 to 4.25 compare the RMS error in the linear fit with the RMS error in the quadratic fit for all combinations of correlation length and standard deviation. As before with each of these figures, six cycles are shown with four different levels of random noise levels per cycle. With standard deviation set at 66 cm (Figure 4.22 and Figure 4.23), the random noise level does not affect the result and all four curves overlay each other. The RMS error in both the quadratic and linear fit just grows the wider the interpolator. Although in both figures the narrowest interpolator would give the smallest interpolation error, the number of successful interpolations would be drastically reduced. In these two cases it would be better to set the interpolator width just past the point at which the number of successful interpolations begin to level off i.e. above 50 km. There seems to be a small advantage in using the quadratic fit, however since these are the only result that shows this in this study, and in view of the instability of the quadratic fit seen in other results, it is would probably still be better to use a linear fit. With the standard deviation set at 5cm (see Figure 4.24 and Figure 4.25) the quadratic fit returns to being unstable and not particularly advantageous. In these two cases, using a random noise level of 2 cm, the RMS error in the linear fit again just grows as the interpolator widens. At higher random noise levels however, the behaviour is more complex. In Figure 4.24 where the large correlation length is used, a minimum is seem in the RMS linear interpolation fit using 5 and 10 cm of random noise, however at 20 cm random noise the RMS error just falls as the interpolator width increases. In Figure 4.25 where the correlation length is at its minimum, the RMS error in the linear fit either grows or falls depending on the noise level. Finally Figure 4.26 shows the spatial behaviour of the minimum point in the RMS error in the linear fit with the correlation length and standard deviation set at 52.17 km and 5 cm respectively, and a random noise level of 5 cm. This is about the only curve where a minimum is seen (see the second from bottom red curve in Figure 4.24). It should be remembered that only the lead density is truly affecting the spatial behaviour of the minimum because the geoid error signal is just generated with a fixed set of parameters for the whole of the Arctic.

The ideal interpolator for the geoid error should be at the minimum of the relevant curve seen in Figure 4.22 to 4.25 but should always be larger than about 50 km so the maximum number of output points is achieved. The behaviour of the curves depends crucially on the noise level and error statistics of the geoid signal. If it were known accurately how these vary spatially over the Arctic a look up table could be designed to choose the optimum width.

Interpolation of the Total Error.

The dynamic topography and tidal error estimates were combined with the 4 simulated geoid error signals mentioned above (correlation length = 11.10 km and 52.17 km, and standard deviation = 5 cm and 66 cm) to get a set of four estimates of the combined total error in the sea surface height signal. With the standard deviation set at 66 cm in the geoid error signal, the geoid error totally swamps the total error and the results (not shown) are identical to those in Figure 4.22 and Figure 4.23 above. Figure 4.27 and Figure 4.28 show the RMS error in the linear and quadratic fits using a standard deviation = 5 cm and the two different correlation lengths, again for six cycles and four noise levels per cycle. The curves strongly resemble those for the geoid error for small interpolator widths (Figure 4.24 and Figure 4.25) but the RMS error in the linear fit rises more rapidly at higher interpolator widths producing a more pronounced minimum. Figure 4.29 shows the spatial behaviour of the minimum of one of

these curves. As with the geoid error, the ideal interpolator for the total error should also always be larger than about 50 km so the maximum number of output points is achieved, but after that depends crucially on the noise level and error statistics of the geoid signal. Again, were it known accurately how these parameters vary spatially over the Arctic, a look up table could be designed to chose the optimum width.

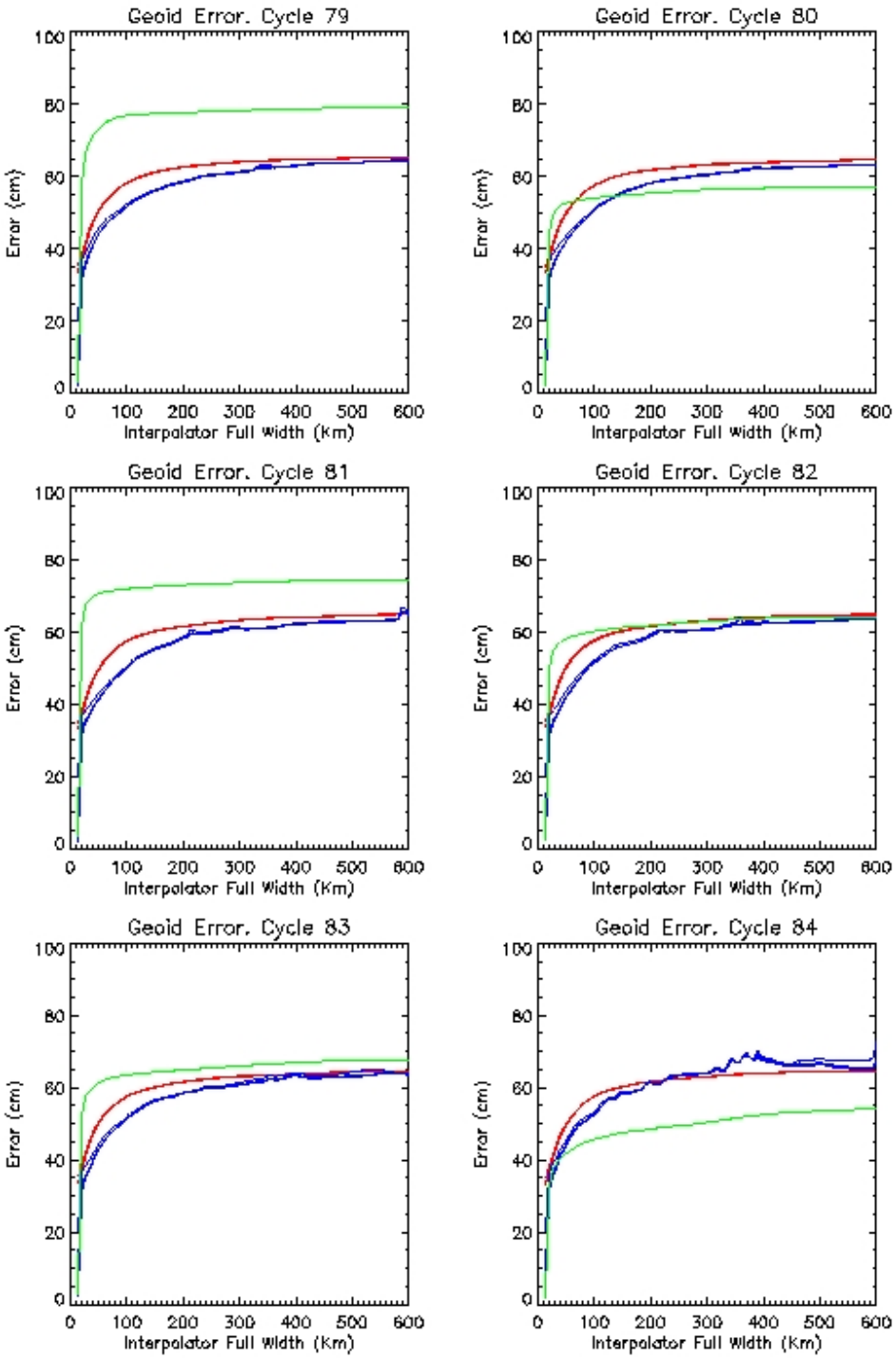

Fig. 4.22: Interpolation of Geoid Error Signal with Correlation Length = 11.10 km and Sigma = 66 cm. Comparison of RMS linear interpolation error (red) with RMS quadratic interpolation error (blue). Number of successful interpolations is shown in green. RMS random noise of 2cm, 5cm, 10cm, and 20cm added.

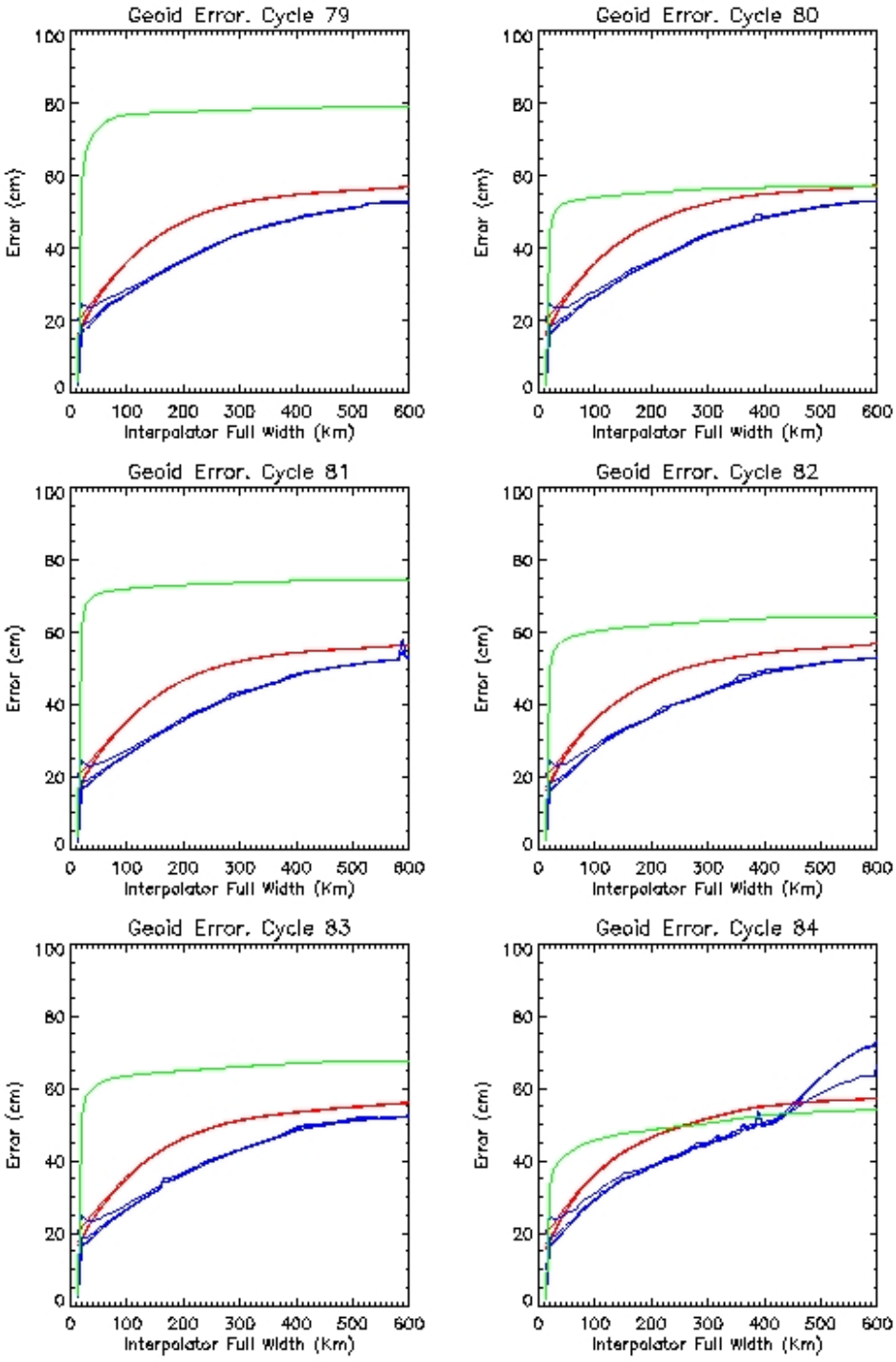

Fig. 4.23: Interpolation of Geoid Error Signal with Correlation Length = 52.17 km and Sigma = 66 cm. Comparison of RMS linear interpolation error (red) with RMS quadratic interpolation error (blue). Number of successful interpolations is shown in green. RMS random noise of 2cm, 5cm, 10cm, and 20cm added.

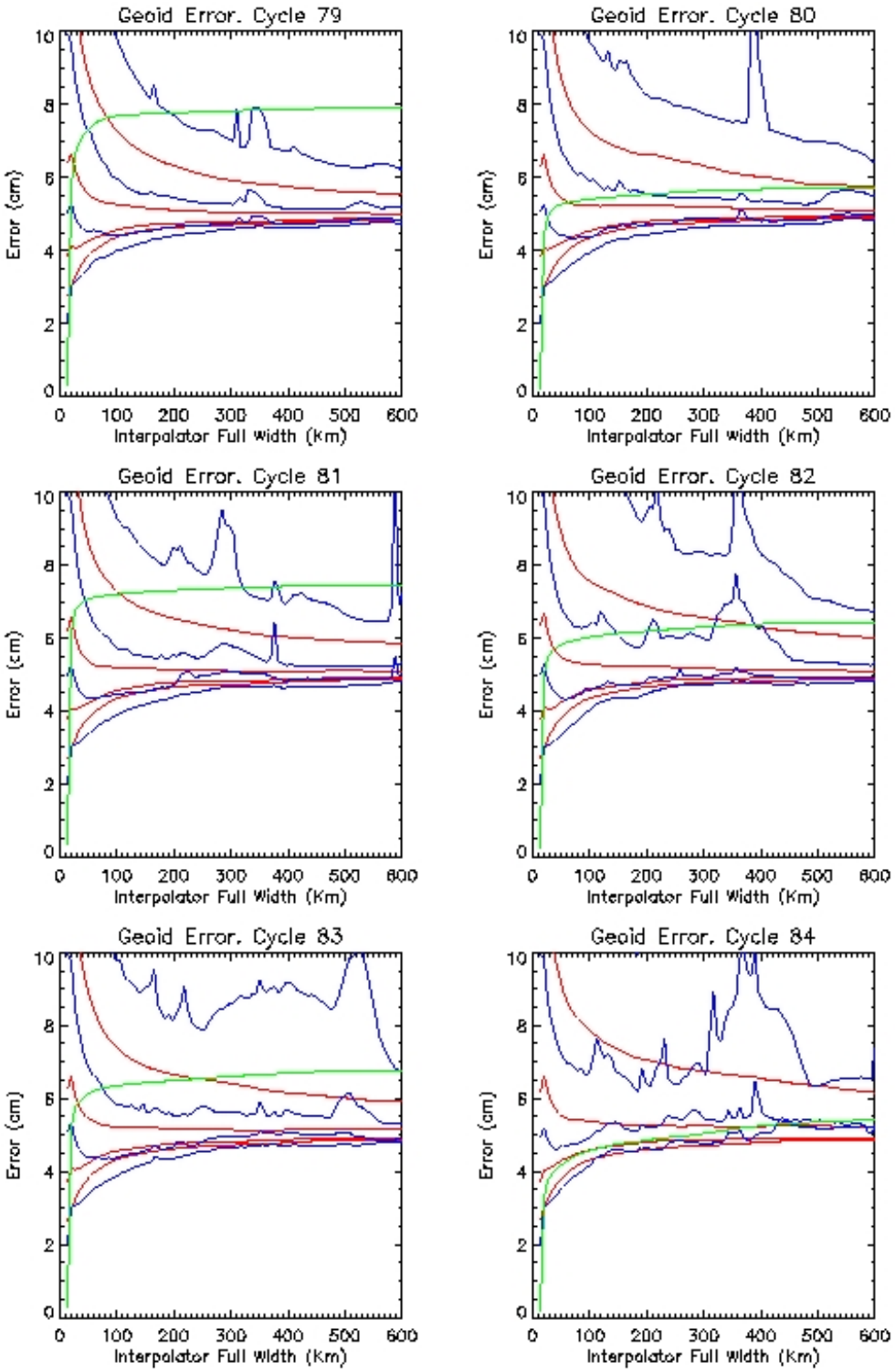

Fig. 4.24: Interpolation of Geoid Error Signal with Correlation Length = 11.10 km and Sigma = 5 cm. Comparison of RMS linear interpolation error (red) with RMS quadratic interpolation error (blue). Number of successful interpolations is shown in green. RMS random noise of 2cm, 5cm, 10cm, and 20cm added.

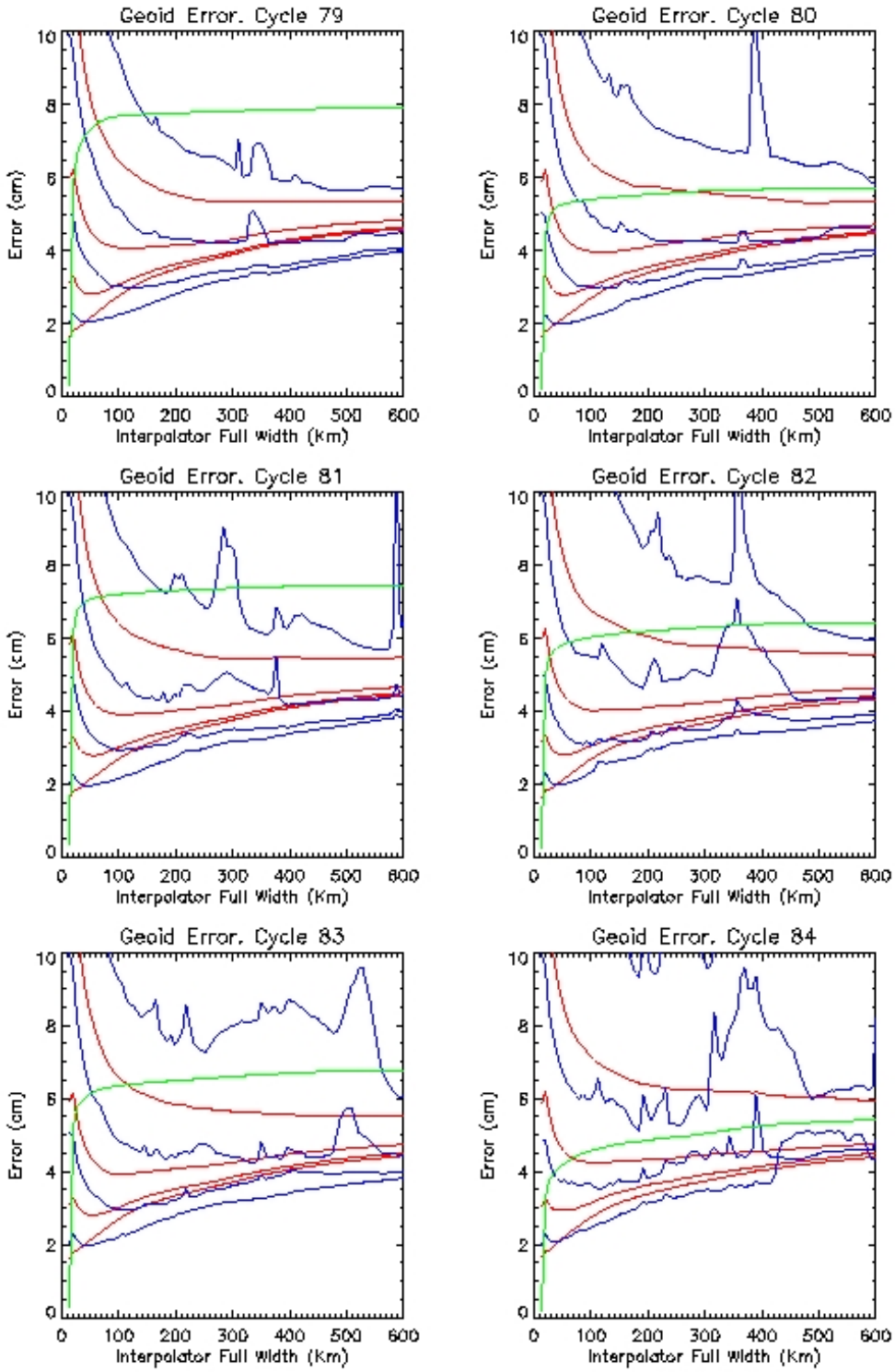

Fig. 4.25: Interpolation of Geoid Error Signal with Correlation Length = 52.17 Km and Sigma = 5 cm. Comparison of RMS linear interpolation error (red) with RMS quadratic interpolation error (blue). Number of successful interpolations shown in green. RMS random noise of 2cm, 5cm 10cm and 20cm added.

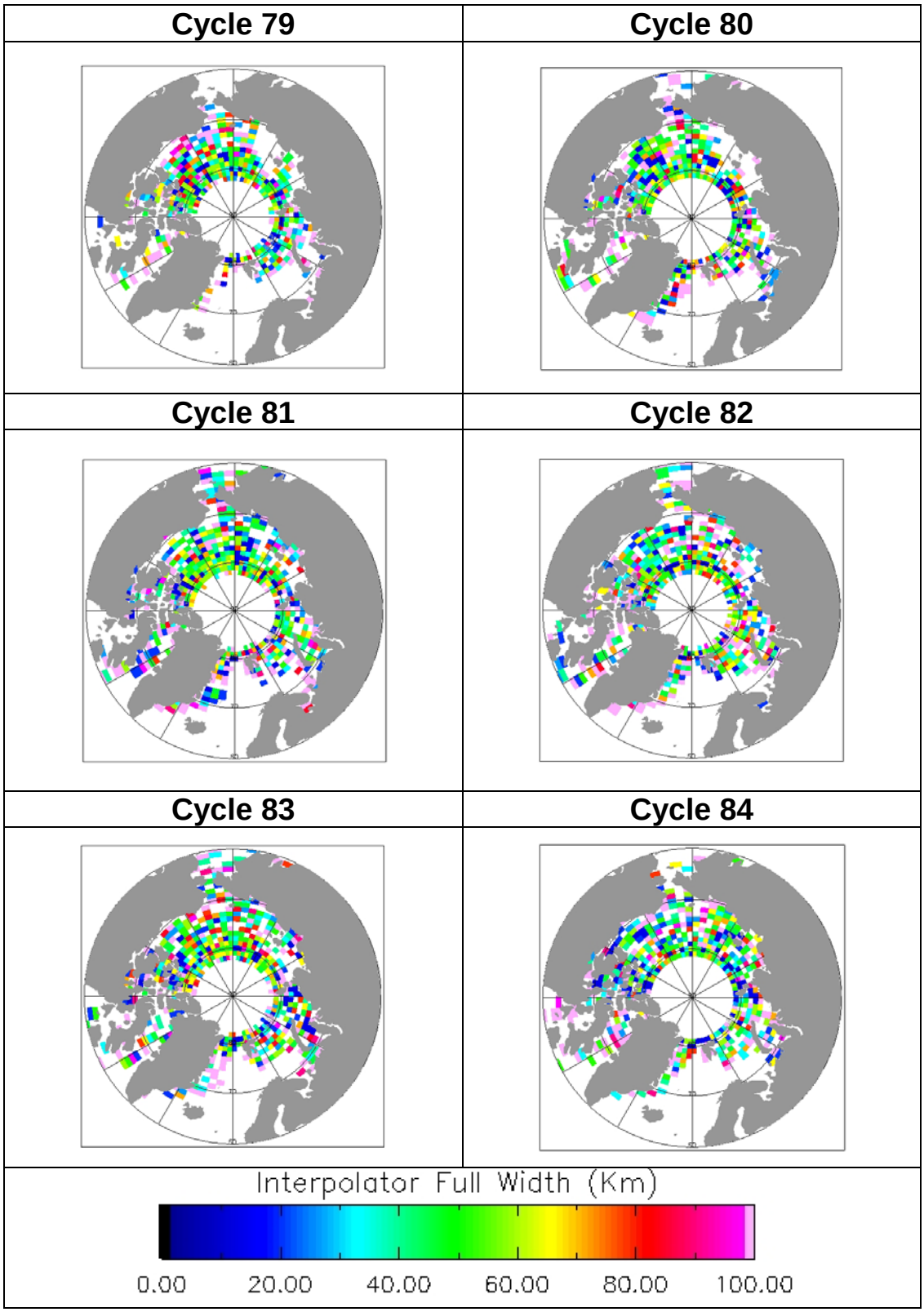

Fig. 4.26: Optimum Interpolator Width for Geoid Error (S. Dev. of 5cm and correlation length of 52.17 km) with 5cm RMS Random Noise.

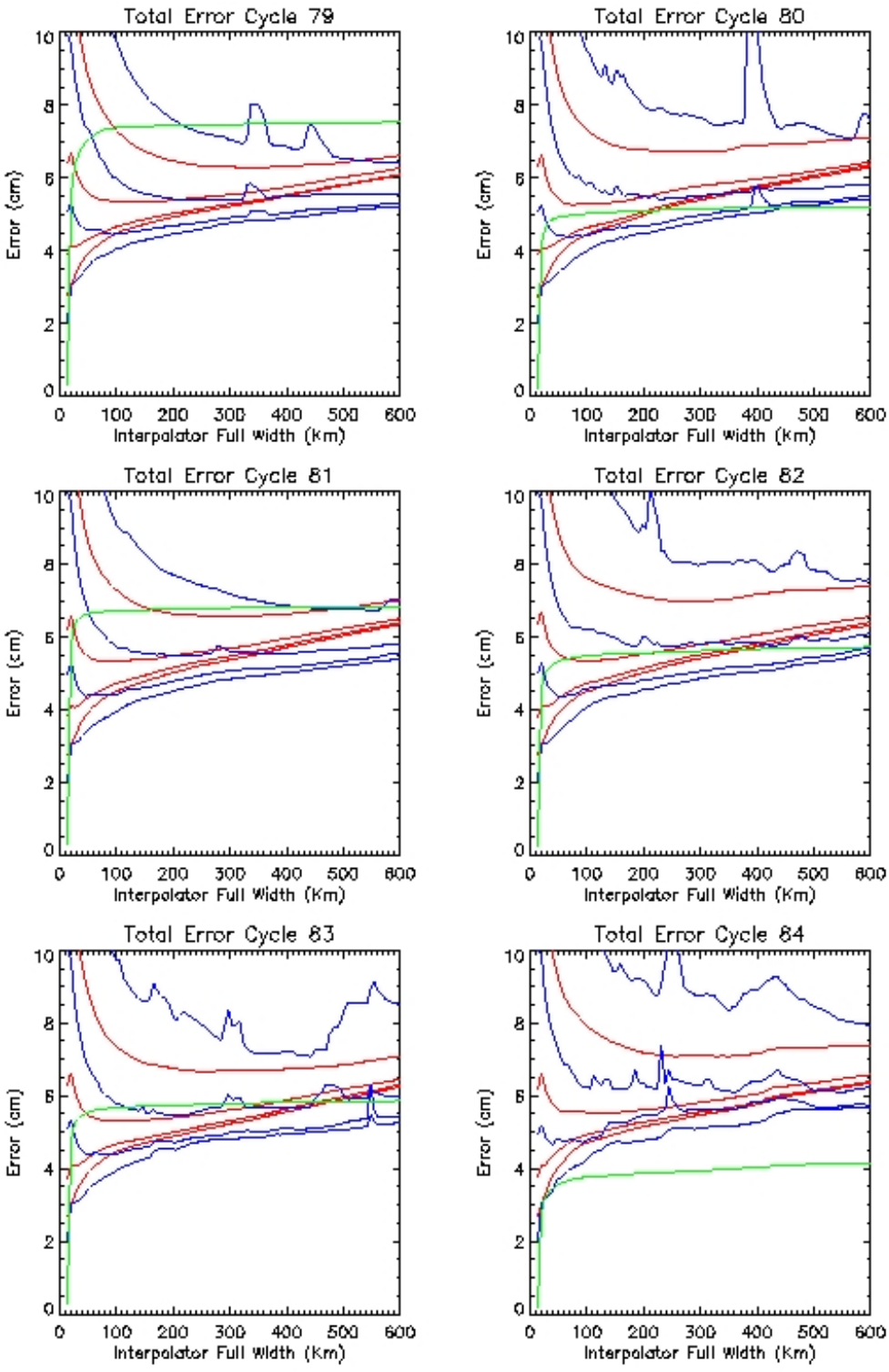

Fig. 4.27: Interpolation of Total Error Signal with Correlation Length = 11.10 km and Sigma = 5 cm. Comparison of RMS linear interpolation error (red) with RMS quadratic interpolation error (blue). Number of successful interpolations is shown in green. RMS random noise of 2cm, 5cm, 10cm, and 20cm added.

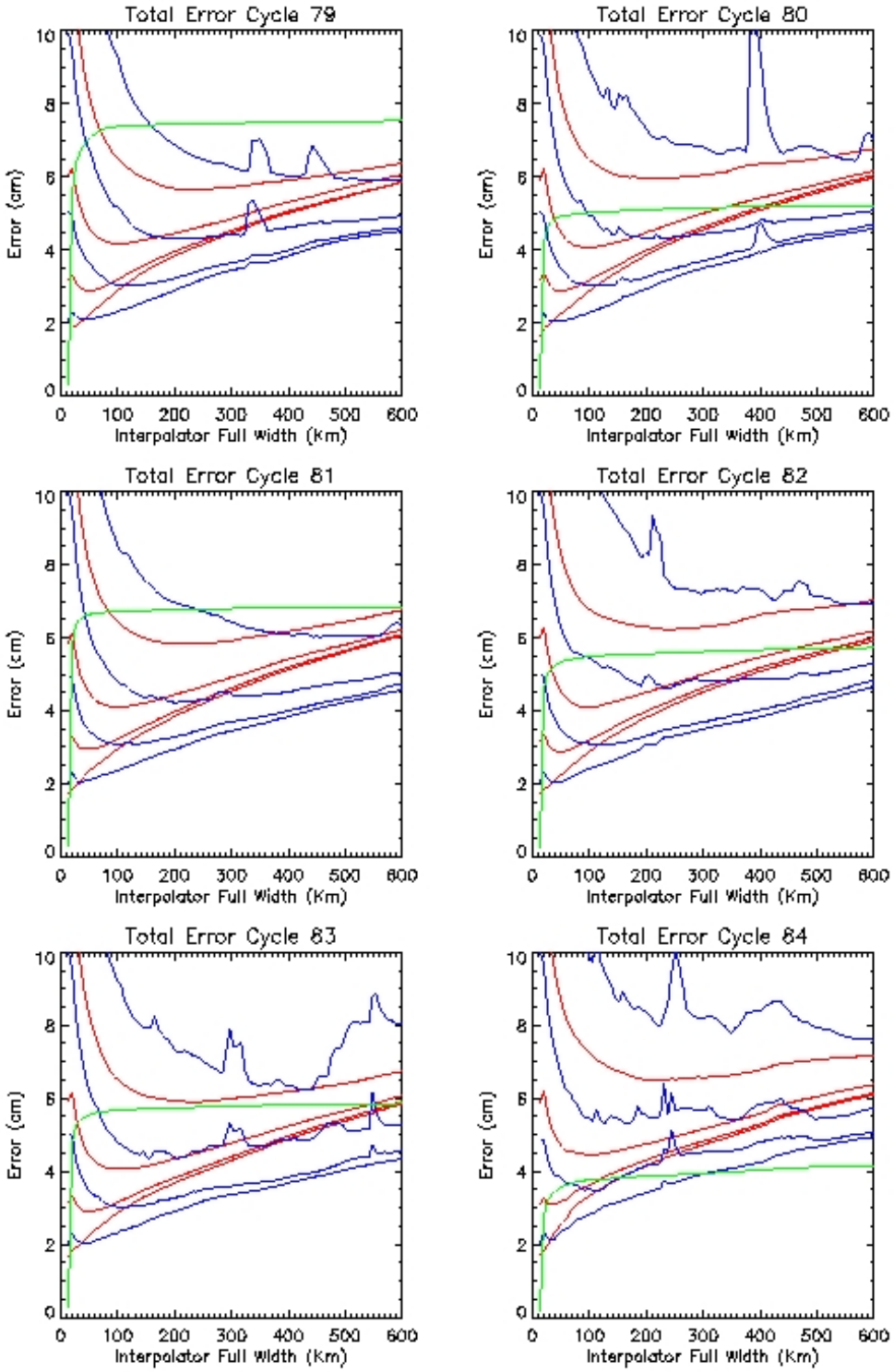

Fig. 4.28: Interpolation of Total Error Signal with Correlation Length = 52.17 Km and Sigma = 5 cm. Comparison of RMS linear interpolation error (red) with RMS quadratic interpolation error (blue). Number of successful interpolations shown in green. RMS random noise of 2cm, 5cm 10cm and 20cm added.

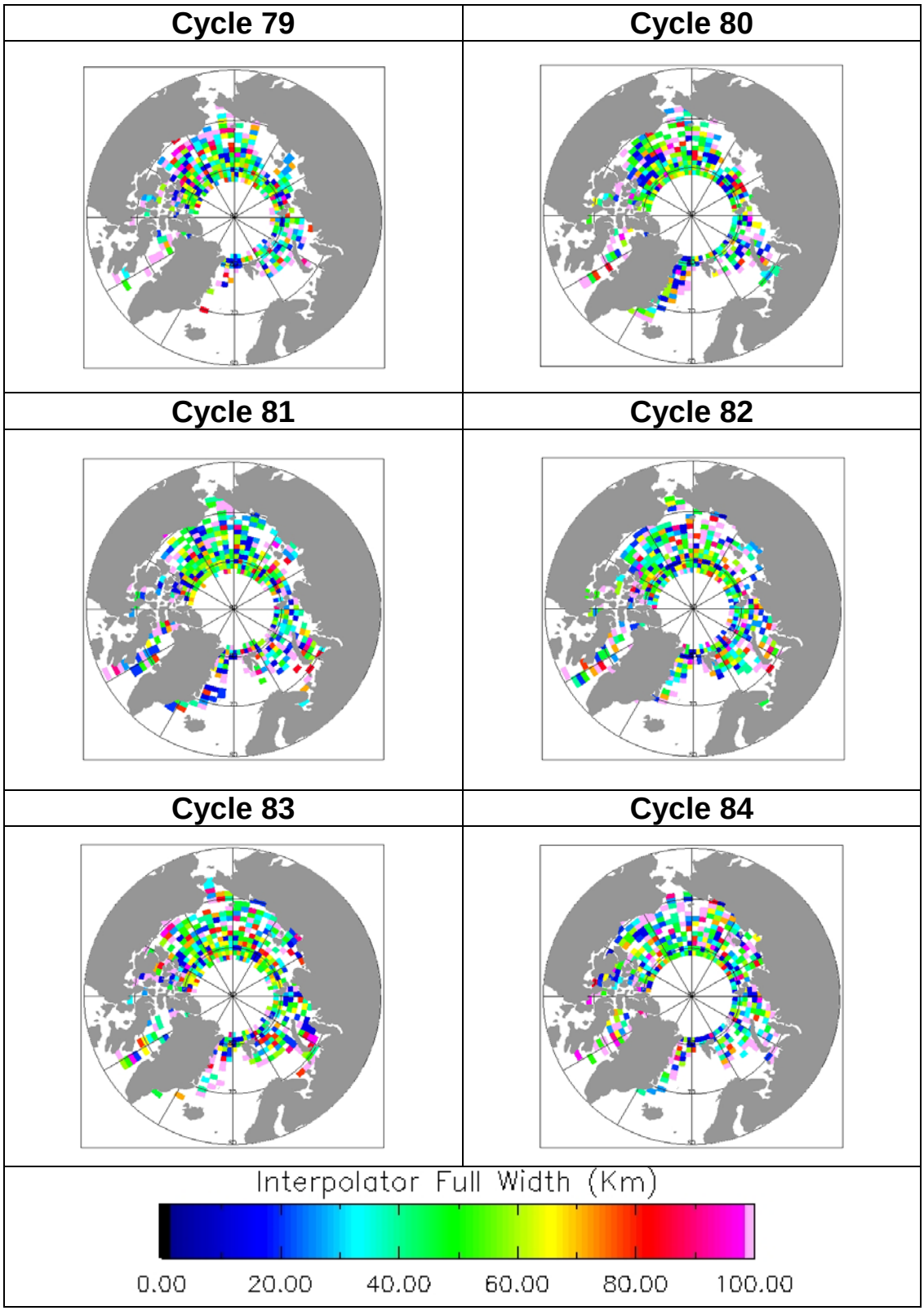

Fig. 4.29: Optimum Interpolator Width for Total Error (Geoid Error has S. Dev. of 5cm and correlation length of 52.17 km) with 5cm RMS Random Noise.

Conclusions Regarding Development of Smart Interpolator

It would be hard to design a smart interpolator which works solely based on the incoming data without any extra knowledge about the statistics of the errors in the sea surface height signal. The 95% confidence interval, the only of the metrics considered here which uses no knowledge of the real signal height at the floe location, does not mimic actual measurements of interpolation error with varying interpolator width. This is probably because of the non Gaussian behaviour of the error signals. Moreover, even if it did, the rapid change in the behaviour of the error verses interpolator width curves from floe to floe would produce something very unstable.

Only in one or two situations was a slight advantage seen in using a quadratic fit to the lead heights, and in view of this and the generally more unstable behaviour of the quadratic fit, a linear fit would be better in all cases. The poorer performance of the quadratic fit may well be due to its ability for contorting to fit the outliers better, causing a poorer fit in general.

With the current level of uncertainty in the dynamic topography models there is no real advantage in removing the dynamic topography signal prior to interpolating the sea surface height. The interpolation statistics show no real advantage to removing a tidal error signal prior to interpolation. We do however have more confidence in the spatial behaviour of the tidal error over the Arctic so if the sea surface height error were due solely to tidal error, the results in Figure 4.20 and 4.21 could form the basis of a look-up table for the optimum interpolator width.

In reality the interpolation statistics of the geoid error dominate those of the total error and hence are crucial in designing the smart interpolator. This interpolator should use a linear fit to the data and never be narrower than 50 km full width so as not to compromise the number of successful interpolations. Its optimum width should be at the minimum of the RMS fitting error versus width curve. Since the behaviour of these curves depend crucially on the geoid error statistic and noise level, detailed maps of these over the Arctic would be required to build a look up table for the optimum interpolator width. Until this is done, a fixed width of about 100 km would seem a good all round compromise.

4.3 Recommendations for inclusion of GOCE data

Introduction

In this note we will discuss the inclusion of GOCE data in the determination of the Arctic geoid.

The GOCE satellite level 2 products will be produced of the High Level processing Facility, (HPF).

The main products of importance for ARCGICE are, cf. (GOCE product Handbook):

EGM_GCF_2 the spherical harmonic series
EGM_GVC_2 the associated error-covariance matrix,
EGG_NOM_2 gravity gradients in the gradiometer reference frame (GRF).
EGG_TRF_2 gravity gradients in a local North-oriented frame.
SST_PSO_2 precise science orbit, including rotation matrix information.

All these data may contribute to the determination of an enhanced geoid and enhanced estimates of associated error-estimates and error correlations. The problems of the rotation of gradients in the GRF for the EGG_NOM_2 product can in principle be solved in least squares

collocation by using the GRF for the individual observations and the associated (different) covariances; there is no need to transform to a local level frame.

Use of the spherical harmonics coefficients

The spherical harmonic coefficients may be directly used in the geoid computation in the so-called remove-restore step. The variance-covariance matrix must be used so that the error information is correctly propagated into the geoid error-estimates and error-covariances.

At the moment only the error-variances of the estimated coefficients are used in order to produce so-called error-degree-variances. The use of the full variance-covariance matrix is complicated, and its integration into the geoid-estimation process is difficult, mainly because of the sheer size of the computational effort, and the limitations of existing software. The planned GOCE User Toolbox System (GUTS) could possible facilitate the software part of this (but not the large size of the equation system).

On the other hand the covariance function of the residual gravity anomalies (obtained in the remove-restore process) will include some information related to the coefficient errors.

The coefficients may also be used to improve the identification of biases in individual gravity surveys as described in Section 1.4 (Table 1.2).

Use of the gravity gradients

The gravity gradients include the same information as the spherical harmonic coefficients in areas of moderately varying gravity. In areas with larger gravity variations (such as over trenches) they may include extra information.

Such areas may be identified by computing the difference between observed values and values of the gradients computed from the spherical harmonic series.

In these areas the gravity gradients may directly be used in the geoid estimation using such methods as Least-Squares-Collocation (LSC). The use may, however, require changes in existing software, where spherical approximation is used. On the other hand, the availability of ground gravity data is important for “tuning” the “downward” continuation inherent in a process where data at satellite altitude is combined with data on the ground.

Conclusion

The level 2 GOCE products may be used to compute an improved geoid in the Arctic Ocean. Both the spherical harmonic coefficients and the gravity gradients may be used. The use of the gravity gradients will primarily help in reducing the error in the region south of 84^{o} latitude.

The optimal use may require improvements in existing software especially so that the variance-covariance information associated with the coefficients can be properly propagated into the geoid estimation process.

5 Synthesis report of benefits of combining all data

5.1 Synthesis report of benefits of combining all data

In this section we summarize the benefits of including corrections for the various components of sea surface height prior to the application of the sea surface height interpolator to estimate the 'unobserved' elevation beneath an ice elevation measurement.

Usefulness of Geoid information

The geoid is obviously the dominant term in the variation of the SSH, and removal of this main field will make estimation of all other quantities – freeboard height, tides and MDT – more easy, and make it more robust to detect and reject outliers in the altimetry data. The results of Chapter 4 show that errors in a-priori knowledge of geoid will be the dominant error in sea surface height retrieval, primarily due to the short scale of the signal error. An examination of the geoid error covariance shows that it is closely related to the signal covariance and is therefore highly non-stationary on a regional basis in the Arctic. In addition the error covariance has been estimated by least squares collocation of a variety of spaceborne, airborne, surface and sub-surface gravity data and may not be reliably determined from the data source itself.

Although the inclusion of GOCE data may prove valuable in reducing the overall errors if, as appears, the primary error is at short wavelengths, then the accurate determination of the higher frequency components is critical. It would seem likely that within the first few months of the CryoSat mission that sufficient data may be gathered to generate a high resolution MSS, which may provide an additional source of high frequency geoid information, which could be used to base further estimates of sea surface height, analogous to the processing of ERS and Envisat for sea ice freeboard. However, since CryoSat is on an essentially non-repeat orbit (attempted repeat cycle is yearly), such an MSS from CryoSat specular returns would have to interpolated by some smooth assumptions, which are more valid when the a main reference geoid have been pre-subtracted from data.

The combination of the CryoSat MSS and a reference geoid, based on GOCE and possibly improved with additional Russian data, not yet incorporated in ArcGP, therefore seems to be an optimal choice.

Usefulness of Mean Dynamic Topography

The project explored a number of models of Mean Dynamic Topography (MDT) in the context of using model data to reduce the uncertainties in sea surface height retrieval. Although on an annual time-scales two of the models (OCCAM and MICOM) show similar patterns this is substantially different from the PIPS and UW models. At monthly timescales even the OCCAM and MICOM models show differences which are similar or larger in magnitude to the actual dynamic topography signal. Since there is no current mechanism or even consensus on which models might provide the best estimate of MDT we can only assume an uncertainty that is equal to the difference between model estimates. Until uncertainties in MDT are significantly reduced therefore we do not recommend their inclusion in sea surface height retrieval for freeboard determination. The MDT is, however, a quantity of great interest by itself, and it is clear from the present determination of MDT in Section 3 that CryoSat will have a great potential to determine an MDT for the Arctic Ocean, when combined with a best possible geoid model, thus providing an independent method for validating oceanographic models.

Usefulness of Tidal Corrections

Tidal corrections to altimetry data are essential when attempting to use altimetry at the few cm accuracy level. Comparisons between the different tidal models shows large differences in the marginal seas, e.g. the Fram Strait and Baffin Bay, whereas central Arctic Ocean tides are more well-represented, but still with large differences between models.

Experiments were carried out to test the accuracy of the operational SSH interpolator with and without tidal correction for the ERS data area. In general at the shorter scale interpolator widths there is little difference in accuracy when the tidal correction is switched on or off, indicating that the interpolator removes most of the tidal error that is not properly modelled (WP4). Unlike the geoid and MDT the tidal correction showed a significant regional pattern in terms of optimal interpolator width. If tidal were shown to be dominant in the sea surface height retrieval then a case may be made to implement a regionally varying interpolator width.

Usefulness of an adaptive and/or second order interpolator

Given the non-stationarity of errors on the geoid and MDT, and the limited confidence in the error co-variance estimates, experiments were carried out to determine whether an adaptive interpolator width driven by an estimate of the goodness of fit could be implemented. These experiments showed that in most cases this technique were not successful in optimizing the interpolator width due to the non-Gaussian nature of the error signal.

A second order interpolator was also employed and although this gave a very marginal improvement in the number of successful interpolations this was at the expense of highly non-linear behaviour at longer interpolation distances.

5.2 Plan for development of Arctic geoid using GOCE

GOCE is designed to measure the geoid to an accuracy of 1 cm at a resolution of 100 km. This improved geoid knowledge will reduce the dominance of the geoid in the total sea surface height error modelled here, and together with GRACE ensure that the absolute position of the geoid in space is known to 1 cm. To get the full geoid signal at high resolution, the existing data sets in the Arctic Ocean can be improved by GOCE data, by estimation of data biases (like in Chapter 1) for both airborne and Russian data sets. Giving the underlying density of data, typically at 15-20 km, this means that a geoid accuracy of 5 cm is possible for the actual geoid. When CryoSat is operational, MSS heights from CryoSat can be high-pass filtered, and merged with the information from the terrestrial gravity to provide a broad-band geoid accuracy of 2-5 cm (with some luck and after sufficient open water lead data have been collected from CryoSat), analogous to the estimation of open ocean MSS and geoid from altimetry.

Apart from providing an improved reference surface for MDT and freeboard estimation, such an accurate geoid would also be very useful for recovering a detailed gravity anomaly field across the Arctic Ocean at accuracies of the 2-3 mgal level, useful for regional geophysics and hydrocarbon exploration.

To improve the ArcGP gravity data and geoid, the following is planned over the coming few years:

- Collect additional, hitherto available Russian gravity data for the areas covered by ERS-altimetry in the present ArcGP compilation, notably the inner Russian shelf areas north of Siberia where Russian gravity maps of scale 1:1.000.000 will be available for circum-arctic gravity compilation project.
- Check all existing data sets for biases by least-squares collocation using GRACE and GOCE long-wavelength gravity fields, combined with improved altimetry gravity solutions from ICESat and ERS, e.g. as currently being prepared for the EGM07 global geopotential solution.
- Optimally merge ICESat gravimetry with surface gravimetry in regions where surface gravity data coverage is of poor resolution (especially in the Russian side of the Arctic Ocean)
- Conduct additional airborne gravity surveys in regions of high variability or interest (e.g., Fram Strait), or as individual tie lines to check and validate other data sources.

To fully utilize a potential cm-geoid of the Arctic Ocean, reference system issues are essential to be resolved. The satellite orbits of e.g. CryoSat must, e.g., be in a well-described tidal system (tide-free) consistent with the tidal system used for construction of the geoid (zero-tide). The differences in treatment of the permanent pole tides are in the 10-15 cm order of magnitude, and thus highly significant.

Conclusions

This report has outlined the current state in the determination of the Arctic geoid, tides, mean sea surface heights (MSS) and mean dynamic topography (MDT), and has both qualitatively and quantitatively investigated the order of magnitude of the variations of these quantities in time and space. The role of the variations in each of the quantities have been quantitatively investigated using a simple linear interpolator scheme, based on actual ERS data locations of sea ice leads and floes, along the same principles as the planned operational CryoSat sea ice freeboard estimator.

For the geoid, new gravity data and new ICESat data have been used to generate an improved Arctic Gravity Project (ArcGP) geoid model, with extensive studies of covariance and error-covariance functions done on large subsets (55,000 points) of the actual point data underlying the ArcGP grid. This is the first time to our knowledge such comprehensive error studies are carried out. Despite the large differences in tectonics, the shape of the covariances and error covariances across the Arctic are relatively similar and uniform, averaged models may be used, except for a variance scaling.

For tides, a large number of comparisons were done between models and to in-situ tide gauge data in northern Canada. Many of the existing state-of-the-art tidal models perform relatively poorly in the Arctic region, mainly due to the lack of altimetry data. We have found that the AOTIM-5 model of Padman et al performs the best in the Arctic Ocean and adjacent sea areas, but significant improvements are needed to get tidal corrections sufficiently accurate to match the future accuracy of CryoSat in the marginal seas. In the central part of Arctic Oceans tides are generally small and models perform reasonably similar here (but so far no independent validation, e.g. by GPS or bottom pressure transducers, to our knowledge has been done). It has been found that the presence of sea-ice damps the amplitudes of the tides; a more quantitative investigation how a damping function could be implemented in practice has not been done yet.

To estimate an Arctic Ocean-wide MSS, ERS and ICESat has been used together for the first time to generate a quasi-consistent surface extending to 86°N, patched to the pole by a draping of the ArcGP geoid across the remaining polar gap. Major problems in how to determine a reliable MSS from ICESat (and thus a corresponding sea ice freeboard) still remains to be solved; there is no easy way to discriminate between leads and ice floes in laser data. The MSS model is to be improved as the processing of ICESat data is developed, especially with enhanced lowest level filtering algorithms, and more ICESat data is made available to the scientific community. For an improved MSS it is also essential that the epochs of the surfaces from ERS, Envisat and ICESat are identical, since the MSS shows yearly and secular variations linked to changes in underlying ocean currents, temperatures etc.

We have studied and compared four different oceanographic models for MDT: MICOM, OCCAM, PIPS (W. Maslowsky, Naval Postgraduate School) and UW (M. Steele, APL/Washington) as a function of time and space. Models differ quite significantly, but also agree on some common features. It appears that at the 5-10 cm level it could be feasible to describe the errors associated with MDT models, and thus – in the long term – operationally use an MDT model together with a geoid to determine a theoretical SSH as a function in both time and space.

We have in the ArcGICE study for the first time estimated a “remote sensing” MDT from combination of the MSS and the geoid, illustrating the potential use of CryoSat and GOCE in combination for monitoring the Arctic Ocean MDT, and provide independent data for validating the oceanographic models.

For the operational estimation of seaice freeboard heights, we have as a spin-off from the MSS determination for ICESat also generated 7 epochs of ICESat freeboard fields using a lowest level filtering method, and further explored the direct determination of freeboard heights using geoid only for new release-26 ICESat data. Generally these freeboard fields are consistent with the expected distribution of first-year and multi-year ice, as e.g. evidenced from Quikscat; however, large errors remain.

CryoSat will obviously be more efficient in determining sea ice freeboards due to the specular returns over leads. A major part of the present report if focused on the simulation of the operational CryoSat freeboard estimator, using a linear fit procedure for local MSS estimation with a varying width of interpolation – the "smart" interpolator. We have investigated in detail whether the width of this linear fit operator could be changed adaptively using apriori information on errors in geoid, tides and MDT, but results have not been very conclusive and it appears that in most cases a standard estimation procedure with a constant operator width might provide more or less equivalent results to the "smart" (adaptive) approach. However, it should be pointed out that the major limiting factor is the adaptive approach is the geoid error; with the improved geoid information from GOCE this conclusion might change. It should also be stressed that the adaptive estimator actually helps in the case of the tides. The investigations were done for real data in the ERS domain (i.e., south of 81°N), and whether conditions are different in the more northern areas, especially the heavy pack ice north of Ellesmere Island and Greenland, remains to be seen.

Monitoring changes in Arctic MDT and sea ice freeboard by remote sensing would be an important contribution to global change studies, and hopefully the work of the present project would serve as a useful background document for preparation of such monitoring. A long-term operational scheme should in principle go hand-in-hand with geoid change monitoring (from e.g. GRACE follow-on or a future laser interferometry mission), as geoid in the long term will also change due to tectonics, glacial-isostatic changes, and changes in ocean bottom pressure.

Recommendations and Future Outlook

The present study shows that a geographically variable interpolation tool could be implemented – in the present case through simply changing the width of the lead interpolator based on some kind of geographical lookup table. We therefore recommend

* *That the CryoSat processor lead interpolation, used for the estimation of freeboard, is designed so that a variable interpolator width can be used.*

Along with such a flexible Cryosat processor, a methodology should also be developed to routinely estimate the altimeter signal variances and covariances along the tracks, and relate these to the model variances of the different fields (sea-ice, geoid, MDT and tides). In the present study it has been briefly outlined how an integrated collocation-based approach in principle could be used for the simultaneous estimation of e.g. freeboard and MDT; such an approach, applied more consistently, have the potential to assign errors to MSS, gravity and tidal sources in a one-step process.

The MSS surface, the fundamental basis for recovering the freeboard heights by Cryosat, needs to have a formal error estimate. Because statistics of this error are non-stationary and non-Gaussian, there is a need for

* *Further development of a scheme for generating representative MSS error statistics.*

An investigation of tidal uncertainties has also shown that tidal model corrections can be very different, and none of the current models take sea-ice cover into account in a proper way. It appears from our comparisons in the Arctic that Padman's AOTIM-5 model is presently the best choice, but it is obvious that

** Further developments are needed on an improved Arctic tidal model. Until such a model is available, CryoSat should use AOTIM-5 for tidal corrections.*

An improved model of the Arctic Ocean tides, taking into account the damping of tides by sea-ice, would clearly need more data, especially along the Arctic shores, but also e.g. by central Arctic Ocean tide gauge information from ocean bottom pressure gauges and drifting geodetic GPS buoys.

Comparisons between the different oceanographic MDT models indicate there is a very large discrepancy between models. There is therefore an urgent need in the oceanographic modeling community to get more consistent results, or at least understand the limitations of the various models as a function of e.g. the grid size, the representation of fresh-water inflow, e.g. from the Siberian rivers etc. Obviously Arctic Ocean oceanographic in-situ data have until now been extremely limited; during the International Polar Year much more data will be acquired, and it is recommended that

** Oceanographic in-situ data are assimilated into Arctic Ocean oceanographic models as soon as possible*

In the long-term perspective, with the geoid modeled to cm accuracy from GOCE and GRACE, satellite orbits and radar ranges accurate to cm, and improved tidal and MDT models also accurate at the cm level, it should be possible in principle to directly use altimetry to measure the actual location of the sea-ice surface, and thus provide a routine and direct observation approach for long term monitoring of sea-ice freeboard (and MDT). Future satellites such as the GMES Sentinel-3 mission and the laser ICESat follow-on could attain such a goal in the 2010-2020 decade, especially when reference system issues are properly and consistently addressed. This is very much work in progress in geodesy, and is currently being implemented in GGOS – the Global Geodetic Observing System.

There is therefore a continuous need to

** Develop an improved Arctic geoid model, incorporating more GRACE and – especially – GOCE data, as well as new airborne gravity data.*

The GOCE data will bring a major improvement in the Arctic geoid, with geoid accuracies at 1 cm over 100 km. This will allow enhanced detection of biases in terrestrial gravity data, and this potentially also improve the geoid at shorter wavelengths. The use of GOCE gravity gradients would also contribute to improved resolution, and especially be useful in the vicinity of the polar gap of GOCE (86°N).

However, fundamental questions relate to the *datum* of oceanographic models: The MDT is in principle obtained by integration of hydrodynamic equations from a level of no motion. Such a level of no motion could be e.g. at 2000 m depth (currently proposed by some oceanographic groups as a standard for GOCE comparisons), leaving some uncertainty how to handle more shallow seas and shelf areas. It should be investigated

** What is the impact on the reference level on the "absolute" MDT from oceanographic models, and what is the quantitative impact of a deep level of no motion in shallow areas?*

Since the ultimate goal is to use e.g. a combination of CryoSat and GOCE for the direct measurement of MDT, we need to have a consistent reference system to be able to compare results. The definition of a proper global vertical datum (W_o), defining the geoid reference system, as well as the proper handling of the permanent pole tide, is an integrated part of such a consistent geodetic reference system.

Acknowledgements

The authors of this report wish to thank Rory Bingham, Proudman Oceanographic Laboratory, UK, for help in providing the OCCAM data; Wieslaw Maslowski, Naval Postgraduate School, Monterey, USA, for providing the PIPS data; M. Steele, University of Washington, for providing epochs of the UW Arctic Ocean model. Arctic Gravity Project point data for the collocation experiments of this report have been provided by S. Kenyon, US National Geospatial-Intelligence Agency, J. Brozena, US Naval Research Laboratory, B. Coakley, Univ. of Fairbanks, M. Veronneau, NRCan, A. Zayonchek, VNIIO, St. Petersburg, G. Demianov, Tsniigaik, Moscow and several others. We acknowledge the feedback and inspiration on several occasions from M. Drinkwater and M. Kern, ESA contract supervisors. ICESat data used for these studies were provided by NSIDC and the ICESat science team.

The work of the present project has been sponsored by the European Space Agency through GSP Study Contract 18753/05/NL/CB.

Arctic Sea Ice, 88°N 130°E, April 2007

References

Andersen, O.B.: MSS improvements and errors. Proceeding from the GOCINA Workshop, Luxemburg, 2005, Cahiers du Centre Europeen de Geodynamique et de Seismologie, in press.

Andersen, O. B.: Shallow water tides on the Northwest European Shelf from TOPEX/Poseidon Altimetry. J. Geophys. Res., 104 (C4), 7729-7741, 1999.

Andersen, O.B. Global Ocean Tides from ERS1 and TOPEX/POSEIDON Altimetry, J. Geophys. Res., 100, 25249-25259, 1995.

Andersen, O. B., P. L. Woodworth, and R. A. Flather: Intercomparison of recent ocean tide models, J. Geophys. Res., 100(C12), 25,261–25,282, 1995.

Bentsen M., G. Evensen, H. Drange, and A. D. Jenkins: Coordinate transformation on a sphere using conformal mapping. Monthly Weather Review, No. 127, pp. 2733-2740, 1999

Bleck, R., Rooth, C., Hu, D. and L. T. Smith: Salinity-driven thermohaline transients in a wind- and thermohaline-forced isopycnic coordinate model of the North Atlantic. J. Phys. Oceanogr. 22, 1486–1515, 1992.

Box, G. E. P. and G. M. Jenkins (1976), Time Series Analysis: Forecasting and Control (Revised Edition), 575pp., London, Holden-Day.

Brown, R.D. and P. Cote: Interannual variability of landfast ice thickness in the Canadian High Arctic, 1950-89. Arctic, 45(3):273-284, 1992.

Childers, V. A., D. C. McAdoo, J. M. Brozena, and S. Laxon: New gravity data in the Arctic Ocean: Airborne and ERS gravity compared. J. Geophys. Res., 106,8871 – 8886, 2001.

Comiso, J.: updated current year. DMSP SSM/I daily polar gridded sea ice concentrations, June to September 2001. Edited by J. Maslanik and J. Stroeve. Boulder, CO: National Snow and Ice Data Center. Digital media, 1990.

Copley, J. The great ice mystery. Nature, 408, 634-636, December 7, 2000.

Dalå, N.S., R. Forsberg, K. Keller, H. Skourup, L. Stenseng, and S. M. Hvidegaard: Airborne lidar measurements of sea ice north of Greenland and Ellesmere Island 2004. GreenICE/SITHOS/CryoGreen/A76 projects, Final Report. Technical Report, Danish National Space Center, 2005.

Eanes, R.: "The CSR 4.0 Global Ocean Tide Model", ftp://ftp.csr.utexas.edu/pub/tide, 2002.

Eanes, R. J.: Diurnal and semidiurnal tides from TOPEX/POSEIDON altimetry, Eos Trans. AGU, 75(16), 108, 1994.

Egbert, G. D., and S. Y. Erofeeva: Efficient inverse modeling of barotropic ocean tides, J. Atmos. Oceanic Technol., 19(2), 183–204, 2002.

Egbert, G. D., R. D. Ray, and B. G. Bills: Numerical modeling of the global semidiurnal tide in the present day and in the last glacial maximum, J. Geophys. Res., 109, C03003, doi:10.1029/2003JC001973, 2004.

Forsberg R., H. Skourup, O. B. Andersen, P. Knudsen, S. W. Laxon, A. Ridout, J. Johannesen, F. Siegismund, C. C. Tscherning, D. Arabelos, and A. Braun: ARCGICE: Combination of Spaceborne, Airborne and In-Situ Gravity Measurements in Support of Arctic Sea-Ice Thickness Mapping, Midterm Report, 67pp., March 2006.

Forsberg, R. and H. Skourup: Arctic Ocean Gravity, Geoid and Sea-ice Freeboard Heights from ICESat and GRACE. Geophyscial Research Letters, vol. 32, L21502, doi:10.1029/2005GL023711, 2005.

Forsberg, R., A. Olesen, A. Vest, D. Solheim, R. Hipkin, O. Omang, P. Knudsen: Gravity Field Improvements in the North Atlantic Region. Proc. GOCE Workshop, ESA-ESRIN, March 2004.

Forsberg, R. and S. Kenyon: Gravity And Geoid in The Arctic Region – The Northern Polar Gap Now Filled. 6 pp., Proc. GOCE Workshop, ESA-ESRIN, March 2004.

Forsberg, R., G. Strykowski, J.C. Illife, M. Ziebart, P.A.Cross, C.C. Tscherning , P. Cruddace, K. Stewart, C. Bray and O. Finch: OSGM02: A new geoid model of the British Isles. Proceedings of the 3rd meeting of the International Gravity and Geoid Comission, GG2002, Aug. 26 - 30, 2002, Thessaloniki, I. Tziavos (ed.), Editions Ziti, pp. 132-137, 2003.

Forsberg, R.: Downward continuation of airborne gravity – an Arctic case story. Proc. International Geoid and Gravity Commission meeting, Univ. of Thessaloniki, pp. 51-56, 2002.

Forsberg, R., D. Solheim and J. Kaminskis: Geoid of the Nordic and Baltic area from gravimetry and satellite altimetry. Proc. Int. Symposium on Gravity, Geoid and Marine Geodesy, Tokyo, pp. 540-548, Sept. 1996.

Förste, C., F. Flechtner, R. Schmidt, U. Meyer, R. Stubenvoll, F. Barthelmes, R. König, K.H. Neumayer, M. Rothacher, Ch. Reigber, R. Biancale, S. Bruinsma, J.-M. Lemoine, J.C. Raimondo, A New High Resolution Global Gravity Field Model Derived From Combination of GRACE and

CHAMP Mission and Altimetry/Gravimetry Surface Gravity Data, Presented at EGU General Assembly 2005, Vienna, Austria, 24-29, April 2005

Gao Y., Drange H., Bentsen M., O. M. Johannessen: Tracer-Derived Transient Time of the Eastern Waters in the Nordic Seas. Tellus, 57B, 332-340, 2005.

Gloersen, P., C.L. Parkinson, D.J. Cavalieri, J.C. Comiso, and J. Zwally, Spatial Distribution of Trends and Seasonality in the Hemispheric Sea Ice Covers: 1978-1996, J. Geophys. Res. 104, 20,827-20,836, 1999.

GOCE Level 2 Product Data Handbook, Prepared by: The European GOCE Gravity Consortium EGG-C.GO-MA-HPF-GS-0110, (latest issue).

Haas, C. and H. Eiken: Interannual variability of summer sea ice thickness in the Siberian and Central Arctic under different atmospheric circulation regimes. J. Geophys. Res., 106 (C3), 4449-4462, 2001.

Heiskanen, W. A., and Moritz, H.: Physical Geodesy, W. H. Freeman, San Francisco, 1967.

Houghton, J.T., Y. Ding, J. D. Griggs, M. Noguer, P. J. van~der Linden, and D. Xiaosu: IPCC Third Assessment Report: Climate Change 2001. Cambridge University Press, Cambridge, England, 944 p, 2001.

Hunter I. W., and R. E. Kearney (1983), Generation of Random Sequences with Jointly Specified Probability Density and Autocorrelation Functions, Biol. Cybern., 47, 141-146.

Hvidegaard, S.M., and R. Forsberg: Sea-ice thickness from airborne laser altimetry over the Arctic Ocean north of Greenland, Geophysical Research Letters, vol. 29, no. 20, pp.1952-1955, 2002.

Kenyon, S., R. Forsberg, J. Brozena, and N. Pavlis: The contribution of the airborne gravimetry to the Arctic Gravity Project and future Earth gravity models. In: Weikko A. Heiskanen Symposium, Columbus, USA. The Ohio State University. October 1-5, 2002.

King M., and S. Aoki, Tidal observations on floating ice using a single GPS receiver, Geophys. Res. Lett., 30 (3), 1138, doi:10.1029/2002GL016182, 2003.

King, M. A., and L. Padman: Accuracy assessment of ocean tide models around Antarctica, Geophys. Res. Lett., 32, L23608, doi:10.1029/2005GL023901, 2005.

Knudsen, P.: The GOCINA project. Proceeding from the GOCINA Workshop, Luxemburgh, 2005, Cahiers du Centre Europeen de Geodynamique et de Seismologie, in press.

Knudsen, P., and A.L. Vest: Integrating gravimetry and altimetry by collocation. Proceeding from the GOCINA Workshop, Luxemburgh, 2005, Cahiers du Centre Europeen de Geodynamique et de Seismologie, in press.

Knudsen P., R. Forsberg, O. Andersen, D. Solheim, R. Hipkin, K. Haines, J. Johannessen & F. Hernandez. The GOCINA Project - An Overview and Status. Proc. Second International GOCE User Workshop "GOCE, The Geoid and Oceanography", ESA-ESRIN, March 2004, ESA SP-569, June 2004.

Knudsen, P.: Integration of Altimetry and Gravimetry by Optimal Estimation Techniques. In: R. Rummel and F. Sanso (eds.): Satellite Altimetry in Geodesy and Oceanography, Lecture Notes in Earth Sciences, 50, pp. 453-466, Springer Verlag, 1993.

Knudsen, P.: Estimation of Sea Surface Topography in the Norwegian Sea Using Gravimetry and Geosat Altimetry. Bulletin Géodésique, Vol. 66, No. 1, 27-40, 1992.

Knudsen, P.: Simultaneous Estimation of the Gravity Field and Sea Surface Topography From Satellite Altimeter Data by Least Squares Collocation. Geophysical Journal International, Vol. 104, No. 2, 307-317, 1991.

Knudsen, P.: Determination of local empirical covariance functions from residual terrain reduced altimeter data. Reports of the Dep. of Geodetic Science and Surveying no. 395, The Ohio State University, Columbus, 1988.

Knudsen, P.: Estimation and Modelling of the Local Empirical Covariance Function using gravity and satellite altimeter data. Bulletin Géodésique, Vol. 61, 145-160, 1987.

Kowalik, Z. and A. Yu. Proshutinsky: The Arctic Ocean tides, "The Polar Oceans and their Role in Shaping the Global Environment, AGU, Geoph. Monograph,137-158, 1994.

Kwok, R., G. F. Cunningham, H. J. Zwally, and D. Yi: ICESat over Arctic sea ice: Interpretation of altimetric and reflectivity profiles. Journal of Geophysical Research, vol. 111, C06006, doi: 10.1029/2005JC003175, 2006.

Kwok, R.: Annual cycles of multiyear sea ice coverage of the Arctic Ocean: 1999-2003. Journal of Geophysical Research, vol. 109, C11004, 2004.

Kwok, R., H.J. Zwally, and D. Yi: ICESat observations of Arctic sea ice: A first look. Geophysical Research Letters, vol. 31, L16401, 2004.

Kwok, R., Recent changes of the Arctic Ocean sea ice motion associated with the North Atlantic Oscillation, Geophys. Res. Lett, 27 (6), 775—778, 2000.

Kwok, R., and D. A. Rothrock: Variability of Fram Strait Flux and North Atlantic Oscillation, J. Geophys. Res., 104 (C3), 5177--5189, 1999.

Kwok, R., D. A. Rothrock, G. F. Stern, and H. L. Cunningham: Determination of Ice Age using Lagrangian Observations of Ice Motion, IEEE Trans. Geosci. Remote Sens., 33 (2), 392-400, 1995.

Laxon, S. W. and N. R. Peacock: Inter-annual, Seasonal and Regional variability in Arctic Sea Ice Thickness from satellite radar altimetry, submitted to J. Geophys. Res., 2004.

Laxon, S., N. Peacock, and D. Smith, High interannual variability of sea ice thickness in the Arctic region, Nature 425, 947-950, 2003.

Laxon, S., Seasonal and inter-annual variations in Antarctic sea ice extent as mapped by radar altimetry, Geophys. Res. Lett., 17 (10)}, 1553--1556, 1990.

Le Provost, C., F. Lyard, J. M. Molines, M. L. Genco, F. Rabilloud, A hydrodynamic ocean tide model improved by assimilating a satellite altimeter-derived data set, J. Geophys. Res., 103(C3), 5513-5530, 10.1029/97JC01733, 1998.

Manabe, S., M. J. Stouffer, R. J. Spelman, and K. Bryan: Transient responses of a coupled ocean-atmosphere model to gradual changes of atmospheric CO2. Part 1: Annual mean response, J. Clim., 4, 785--818, 1991.

Morison, J., M. Steele, T. Kikuchi, K. Falkner, and W. Smethie: Relaxation of central Arctic Ocean hydrography to pre-1990s climatology. Geophysical Research Letters, Vol. 33, L17604, doi:10.1029/2006GL026826, 2006.

Moritz, H.: Advanced Physical Geodesy. Herbert Wichmann Verlag, Karlsruhe, 1980.

Olsen, A.V.: Airborne gravimetry in the North Atlantic region. Proceeding from the GOCINA Workshop, Luxemburg, 2005, Cahiers du Centre Europeen de Geodynamique et de Seismologie, in press.

Padman L., H. A. Fricker: Tides on the Ross Ice Shelf observed with ICESat, Geophys. Res. Lett., 32, L14503, doi:10.1029/2005GL023214, 2005.

Padman, L. and S. Erofeeva: A Barotropic Inverse Tidal Model for the Arctic Ocean, Geophys. Res. Lett., 31(2), L02303, doi: 10.1029/2003GL019003, 2004.

Parkinson, C.L., Cavalieri, D.J., Gloersen, P., Zwally, H.J. and Comiso, J.C. Variability of the Arctic Sea Ice Cover 1978-1996, J. Geophys. Res., 104, 20,837-20,856, 1999.

Peacock, N.R., and S.W. Laxon, Sea Surface Height Determination in the Arctic Ocean from ERS Altimetry, J. Geophys. Res., 109 (c7), doi: 10.1029/2001JC001026, 2004.

Ray, R.D. A Global Ocean Tide Model from TOPEX/POSEIDON Altimetry : GOT99.2. NASA Technical Memorandum 209478, 1999.

Rind, D., R. Healy, C. Parkinson and D. Martinson: The role of sea ice in 2 x CO2 climate model sensitivity. Part II: Hemispheric dependence of sea ice thickness and extent, Geophys. Res. Lett., 24, 1491--1494, 1997.

Reigber, C., P. Schwintzer, R. Stubenvoll, R. Schmidt, F. Flechtner, U. Meyer, R. König, H. Neumayer, Ch. Förste, F. Barthelmes, S.Y. Zhu, G. Balmino, R. Biancale, J.-M. Lemoine, H. Meixner, J.C. Raimondo: A High Resolution Global Gravity Field Model Combining CHAMP and GRACE Satellite Mission and Surface Gravity Data: EIGEN-CG01C, Journal of Geodesy, in press 2005.

Rothrock, D., J. Zhang, and Y. Yu, The Arctic ice thickness anomaly of the 1990s: A consistent view from observations and models, J. Geophys. Res., 108, doi:10.1029/2001JC001208, 2003.

Rothrock, D., Y. Yu, and G. Maykut, Thinning of the Arctic sea-ice cover, Geophys. Res. Lett., 26, 3469-3472, 1999.

Sansò, F.: Statistical Methods in Physical Geodesy. In: Sünkel, H.: Mathematical and Numerical Techniques in Physical Geodesy. Lecture Notes in Earth Sciences, Vol. 7, 49-155, Springer-Verlag, 1986.

Schutz, B.E., H.J. Zwally, C.A. Shuman, D. Hancock, and J.P. DiMarzio: Overview of the ICESat Mission, Geophys. Res. Lett., 32, L21S01, doi:10.1029/2005GL024009, 2005.

Serreze, M.C., Maslanik, J.A., Scambos, T.A., Fetterer, F., Stroeve, J., Knowles, K., Fowler, C., Drobot, S., Barry, R.G. and T. M. Haran: A record minimum arctic sea ice extent and area in 2002. Geophys. Res. Lett., 30: 10.1029/2002GL016406, 2003.

Steele, M., J. Morison, W. Ermold, I. Rigor, M. Ortmeyer, and K. Shimada: Circulation of summer Pacific halocline water in the Arctic Ocean. Journal of Geophysical Research, Vol. 109, C02027, doi:10.1029/2003JC002009, 2004.

Tapley, B. D., S. Bettadpur, M. Watkins, and C. Reigber: The gravity recovery and climate experiment: Mission overview and early results, Geophys. Res. Lett., Vol. 31, No. 9, L09607, 10.1029/2004GL019920, 2004.

Tscherning, C. C.: Geoid determination by least-squares collocation using GRAVSOFT. Lecture notes "Int. School on the Use and Determination of the Geoid", Milano, pp. 135-164. Published by the International Geoid Service, October 1994.

Tscherning, C.C.: Functional Methods for Gravity Field Approximation. In: Sünkel, H.: Mathematical and Numerical Techniques in Physical Geodesy. Lecture Notes in Earth Sciences, Vol. 7, 3-47, Springer-Verlag, 1986.

Tscherning, C.C., and R.H. Rapp: Closed Covariance Expressions for Gravity Anomalies, Geoid Undulations, and Deflections of the Vertical Implied by Anomaly Degree Variances. Report no. 208, Dept. of Geodetic Science and Surveying, The Ohio State University, Columbus, 1974.

Tucker, W., Anderson, R., Newton, J., Wales, C., G. Newton, and T. Luallin: Accuracy of submarine ice draft measurements. In Thorndike, A., Parkinson, C., & Rothrock, D. (Eds.), Report of the Sea Ice Thickness Workshop, pp. B22--B24. University of Washington, Seattle, WA: Polar Science Center., 1992.

Wadhams, P. and N. R. Davis, Further evidence for ice thinning in the Arctic Ocean., Geophys. Res. Lett., 3973--3975, 2000.

Warren, S., I. Rigor, N. Untersteiner, V. Radinov, N. Bryazgin, Y. Aleksandrov, and R. Colony, Snow depth on Arctic Sea Ice, J. Clim. 12(6), 1814-1829, 1999.

Zwally, H.J., Schutz, B., Abdalati, W., Abshire, J., Bentley, C., Brenner, A., Bufton, J., Dezio, J., Hancock, D., Harding, D., Herring, T., Minster, B., Quinn, K., Palm, S., Spinhirne, J. and R. Thomas: ICESat's laser measurements of polar ice, atmosphere, ocean, and land. J. Geodynamics, 34: 405-445, 2002.

Technical Report Series

Danish National Space Center, Technical University of Denmark, Technical report series is an informal report series, published at irregular intervals. This publication is copyrighted and may therefore only be reproduced electronically or in other media if this corresponds to direct citation and includes a full reference to the publication, i.e. individual pictures or brief quotations from the text.

Danish National Space Center
Juliane Maries Vej 30
DK-2100 København Ø
Phone +45 3532 5700
Fax + 45 3532 2475
Mail office@space.dtu.dk
www.space.dtu.dk